Advances in Ab Initio Modeling of the Many-Body Effects of Dispersion Interactions in Functional Organic Materials

Advances in *Ab Initio* Modeling of the Many-Body Effects of Dispersion Interactions in Functional Organic Materials

A DISSERTATION PRESENTED
BY
MARTIN BLOOD ZWIRNER FORSYTHE
TO
THE DEPARTMENT OF PHYSICS

IN PARTIAL FULFILLMENT OF THE REQUIREMENTS
FOR THE DEGREE OF
DOCTOR OF PHILOSOPHY
IN THE SUBJECT OF
PHYSICS

HARVARD UNIVERSITY
CAMBRIDGE, MASSACHUSETTS

SEPTEMBER 2015

Dissertation Advisor: Professor Alán Aspuru-Guzik Martin Blood Zwirner Forsythe

Advances in *Ab Initio* Modeling of the Many-Body Effects of Dispersion Interactions in Functional Organic Materials

Abstract

Accurate treatment of the long-range electron correlation energy, including dispersion interactions, is essential for describing the structure, dynamics, and function of a wide variety of systems. Among the most accurate models for including dispersion into density functional theory (DFT) is the range-separated many-body dispersion (MBD) method [A. Ambrosetti *et al., J. Chem. Phys.* 2014, **140**, 18A508], in which the long-range correlation energy is computed from a model system of coupled quantum harmonic oscillators. In this work, we seek to extend the applicability of the MBD model by developing the analytical gradients necessary to compute MBD corrections to ionic forces, unit-cell stresses, phonon modes, and self-consistent updates to the Kohn-Sham potential. We include all implicit coordinate dependencies arising from charge density partitioning, as we find that neglecting these terms leads to unacceptably large relative errors in the MBD forces. Such errors would impact the predictive nature of *ab initio* molecular dynamics simulations employing MBD. We develop a new efficient implementation of the MBD correlation energy and forces within the Quantum ESPRESSO software package and rigorously test its numerical stability and convergence properties for condensed phase simulations. Additionally, we re-parameterize the MBD model for use with a wide variety of generalized gradient approximation exchange-correlation functionals. We demonstrate the efficiency and accuracy of these MBD gradient corrections for optimizations of isolated dispersively bound molecular systems, as well as representative condensed phase systems including adsorbed hydrocarbons, layered materials, and hydrogen-bonded crystals. Where highly accurate reference geometries are available, we find the DFT+MBD method significantly improves the predicted structures of these systems and consistently outperforms popular pairwise-additive DFT-D dispersion corrections. Though significant work remains in the benchmarking and testing of these contributions to the MBD model, we are optimistic that these methodological developments will enable many exciting discoveries of beyond-pairwise dispersive effects in organic materials.

Contents

I dedicate this dissertation to my niece Amalia Hope Forsythe-Pifer
who has valiantly persevered through the first months of life
while I have struggled to write these pages.

There are also many people to thank, without whom this thesis would not have happened. The constant support of my wife, Hannah Forsythe, has been an invaluable source of strength and inspiration. To all of my family, especially my parents, Ellen Forsythe and Alan Blood, my sister, Sadie Forsythe, and her husband, Chris Pifer, thank you for your love, patience, and support throughout my studies. I am especially grateful to my father-in-law, Dr. Gordon Bugbee, and my friend, Elias Sánchez-Eppler, for helping me to make steady progress with writing in the final weeks. To the "Cambridge Churchill gang," thank you for your ever present friendship and for many fine adventures together during these years of study.

Acknowledgments

First, I would like to sincerely thank my advisor, Prof. Aspuru-Guzik, for his support throughout my graduate studies, and especially for his confidence in me. I would also like to thank Prof. Cohen and Asst. Prof. Ni for serving as members of my thesis committee.

I owe a tremendous debt of gratitude to my co-worker and friend, Thomas Markovich, for collaborating closely with me on much of the work that is reported in this dissertation and for countless scientific discussions that have educated me greatly. I am also especially grateful to Samuel Blau and Prof. Peter Love for numerous discussions throughout my studies. Additional thanks are due to all of my colleagues in the Aspuru-Guzik group, but I am especially thankful to Tim Hirzel for software support, and to Dr. Dmitrij Rappoport, Dr. Edward Pyzer-Knapp and Asst. Prof. Johannes Hachmann for teaching me about various simulation techniques. I thank Dr. Eric Głowacki and Dr. Matthew White for their guidance in the study of organic semiconductors.

I would like to thank Prof. Alexandre Tkatchenko and Asst. Prof. Robert DiStasio for introducing me to the fascinating many-body dispersion model and for numerous discussions over the last few years. I also thank the participants of the 2015 Modeling Many-Body Interactions workshop. Their comments and questions helped shape my thinking about this work as I was writing. In particular, I had wonderful discussions with Jan Herman, Dr. Anthony Reilly, and Dr. Glenn Martyna about periodic convergence, with Nicola Ferri about self-consistency, and with Gregory Beran about three-body interactions.

I am grateful for the generous financial support of my graduate studies that has been provided by the Harvard Department of Physics, through the Purcell Fellowship, the An Wang Fellowship, the James Mills Peirce Fellowship, and Van Vleck travel grants, and also from the U.S. Department of Energy (DOE) Office of Science (SC) Graduate Fellowship Program, administered by ORISE-ORAU under Contract No. DE-AC05-06OR23100. I am particularly thankful for the opportunities that this fellowship program provided me for professional development, travel, and collaborative research. Portions of the work described in this thesis were also supported by funding from the STC Center for Integrated Quantum Materials under NSF Grant No. DMR-1231319.

This research used resources of the Odyssey cluster supported by the FAS Division of Science, Research Computing Group at Harvard University, the National Energy Research Scientific Computing Center (NERSC), a DOE Office of Science User Facility supported by the DOE Office

of Science under Contract No. DE-AC02-05CH11231, the Texas Advanced Computing Center (TACC) at The University of Texas at Austin, and the Extreme Science and Engineering Discovery Environment (XSEDE), which is supported by NSF Grant No. ACI-1053575. All opinions expressed in this dissertation are the author's and do not necessarily reflect the policies and views of Harvard University or the above funding bodies.

Further Acknowledgements by Chapter

Chapter 1 contains content that has been previously published in the following articles:

- Eric Daniel Głowacki, Halime Coskun, Martin A. Blood-Forsythe,* Uwe Monkowius, Lucia Leonat, Marek Grzybowski, Daniel Gryko, Matthew Schuette White, Alán Aspuru-Guzik, and Niyazi Serdar Sariciftci. "Hydrogen-bonded diketopyrrolopyrrole (DPP) pigments as organic semiconductors." Org. Electron. **15** (12), 3521 (2014).
- Dennis Sheberla, Lei Sun, Martin A. Blood-Forsythe, Süleyman Er, Casey R. Wade, Carl K. Brozek, Alán Aspuru-Guzik and Mircea Dincă. "High electrical conductivity in Ni_3(2,3,6,7,10,11-hexaiminotriphenylene)$_2$, a semiconducting metal-organic graphene analogue." J. Am. Chem. Soc. **136** (25), 8859 (2014).

Chapter 2 contains content that has been published in the following article: Martin A. Blood-Forsythe, Thomas Markovich, Robert A. DiStasio Jr., Roberto Car, and Alán Aspuru-Guzik. "Analytical nuclear gradients for the range-separated many-body dispersion model of noncovalent interactions." Chem. Sci. Accepted Manuscript (2015).

Chapter 3 contains content that will be submitted separately for publication as "Enabling large-scale simulation of many-body dispersion forces in condensed phase systems" with the following author list: Thomas Markovich, Martin A. Blood-Forsythe, Robert A. DiStasio Jr., Roberto Car, and Alán Aspuru-Guzik.

Chapter 4 contains contributions from Thomas Markovich, Xavier Andrade, Tim Hirzel, and Dasol Kim.

*All publications appear under my original surname.

Introduction

A sound description of many forms of matter requires a robust theoretical explanation of interactions at the atomic and molecular scales.[†] In an effort to explain the equation of state of non-ideal gases, Johannes van der Waals first proposed the idea of an attractive interaction between neutral atoms.[3] These eponymously named van der Waals (vdW) forces, encompass three separate interactions: orientation, induction, and dispersion. Orientation forces arise from the electrostatic interactions between charge distributions with permanent multipole moments and were first studied for dipole-dipole interactions by Willem Keesom.[4–7] Induction describes the forces between a permanent multipole and an induced multipole; at the dipole level, induction was first studied by Peter Debye in 1920.[8,9] Dispersion forces stem from the interaction between the instantaneous multipole moments of fluctuating charge distributions and were first described for fluctuating atomic dipoles by Fritz London in 1930.[10] A rigorous treatment of dispersion forces is often crucial for an accurate and reliable prediction of the structure, stability, and function of many molecular and condensed-phase systems.[1,11–13]

London's original description of dispersion interactions between noble gas atoms is based on a simple application of second-order perturbation theory, where the Coulomb interaction is treated with a multipole expansion (*i.e.* a Taylor series in R^{-1}, where R is the internuclear distance). The dispersion energy for the interaction of two atoms a and b that results from this calculation is

$$E_{ab}^{\text{disp}} = -\left(\frac{3}{2}\frac{I_a I_b}{I_a + I_b}\alpha_b\alpha_b\right)\frac{1}{R^6} = -\frac{C_6}{R^6}, \tag{1}$$

where I_a and I_b are the first ionization potentials of atoms a and b respectively, and α_a and α_b are the dipole polarizabilities. Collapsing the prefactor into the "C_6 coefficient" may be regarded as the more general expression since it does not rely on assumptions about the electronic structure of the two interacting bodies. In a similar fashion, the dispersion interaction between three dipoles may be computed with third-order perturbation theory, yielding the well known

[†]See Ref. 1 for an authoritative modern reference on the theory of intermolecular forces and Ref. 2 for a concise account of the history of the theoretical description of vdW interactions.

Axilrod-Teller-Muto "triple-dipole" or "three-body" term,[14,15]

$$E_{abc}^{\text{disp}} = C_9 \frac{3\cos\theta_1 \cos\theta_2 \cos\theta_3 + 1}{R_{ab}^3 R_{bc}^3 R_{ac}^3}, \tag{2}$$

where θ_i are the angles between the three bodies and R_{ij} are the relevant distances. Since the three-body term dies off more quickly with distance (going as R^{-9}), the pairwise interaction is often assumed to be sufficient.

Although each of the three types of vdW interactions are important, dispersion interactions are considered to be particularly influential for extended systems because polarizability tends to increase linearly with the system size[16–18] and the contribution of dispersion will never saturate. The potential for dispersion forces to act at long-range was realized when Hugo Hamaker extended the theory to macroscopic bodies and showed that the interaction between semi-infinite parallel slabs decays quite slowly (as d^{-2} in the non-retarded regime, where d is the slab separation).[19] A decade later, Hendrik Casimir and Dirk Polder analyzed the influence of electromagnetic retardation on dispersion forces[‡] and developed a simple integral relation between the dynamic dipole polarizability evaluated at imaginary frequency, $\alpha(\mathbb{i}\omega)$, and the C_6 coefficient.[21] In the 1950s, Evgeny Lifshitz developed a continuum theory of vdW interactions between simple geometric macroscopic bodies by deriving the interaction directly from Maxwell's equations, thus eliminating the approximations of pairwise interactions that had been made before.[22,23] Lifshitz and coworkers later re-derived this theory with a more rigorous treatment of quantum electrodynamics.[24]

Due to their long-range and scaling with system size, dispersion interactions can prove especially impactful in modeling interactions in nanostructured systems where reduced dimensionality can create large polarizable surfaces.[25,26] Given their importance, improving the accuracy and efficiency of techniques for representing these interactions has been a long standing area of focus in chemistry and physics. Although the Lifshitz theory is tremendously successful and is still being applied today,[27] at the nanoscale this continuum treatment breaks down. Therefore, it is often necessary to compute dispersion interactions using simple two-body models, such as classical Lennard-Jones potentials[28] used in forcefields, or pairwise models based on effective dipolar interactions as originally proposed by London. In recent years, considerable attention has returned

[‡]See Ref. 20 for an elegant interpretation of the Casimir-Polder potential as an interaction between dipoles that are induced by vacuum fluctuations of the electromagnetic field.

to the issue of non-additivity and many-body effects in dispersion interactions.[26,29–33]

Dispersion interactions are inherently quantum mechanical in nature since they originate from collective non-local electron correlations. Consequently, they pose a significant challenge for electronic structure theory and often require sophisticated wavefunction-based quantum chemistry methodologies for a quantitatively (and in some cases qualitatively) correct treatment. Many highly accurate wavefunction-based methods, such as coupled cluster, are capable of accurately capturing dispersion but their computational cost makes them prohibitively expensive for molecular systems with more than ~ 100 atoms, or for condensed phase systems. Over the past decade, this challenge has been addressed by a number of approaches seeking to approximately account for dispersion interactions within the hierarchy of exchange-correlation functional approximations in Kohn-Sham density functional theory (DFT),[34–88] which is arguably the most successful electronic structure method in widespread use today throughout chemistry, physics, and materials science.[89] See Refs. 69, 74, and 90 for comprehensive reviews of dispersion methods in DFT and Ref. 91 for a detailed analysis of the physics behind the most popular models. Much of the success of DFT is due to the accuracy that is provided by approximate exchange-correlation functionals with very simple forms. However, the long-range and highly delocalized nature of dispersion interactions, makes semi-local density functional theory (DFT) unsuitable for a complete picture. One prominent failing of standard functionals is their inability to describe long-range electron correlations. Indeed, density based dispersion corrections can largely reduce the errors of their parent functionals when considering interaction energies.[73,76,92] As such, the number of dispersion corrected DFT studies has increased dramatically in recent years. An estimate of this trend is provided in Figure 1.

The numerous approaches to correct for dispersion in DFT may broadly be divided into four levels of approximations, I, II, III, and IV, which will be discussed below. Our classification follows the schemes introduced in the reviews by Grimme (Ref. 74) and Klimeš and Michaelides (Ref. 90). At level I are methods that bind dispersively interacting systems at short range, but do *not* describe the correct long-range asymptotics or give the correct shape of binding curves, such as the local density approximation (LDA). Slightly more reliable, but still asymptotically incorrect, are the class of highly-parameterized functionals that have been trained to reproduce the potential minima of weak interactions (*e.g.* the "Minnesota functionals"[51]). Nevertheless, such functionals can be quite accurate for general chemistry problems such as thermochemistry and reaction barriers. Within pseudopotential based electronic structure methods, dispersion may also be

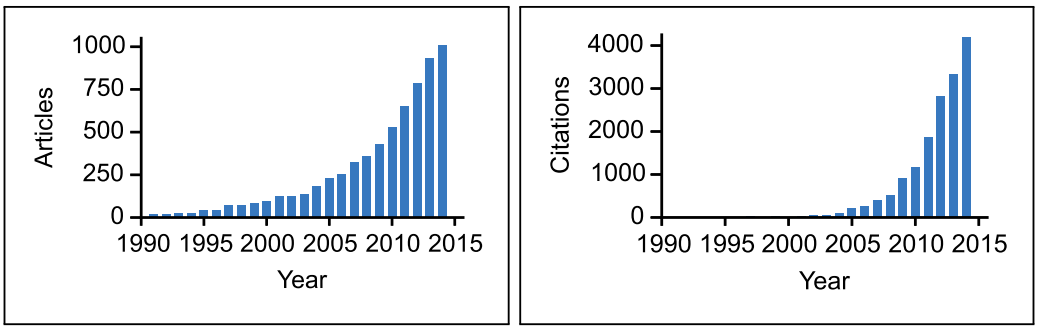

Figure 1: The number of dispersion corrected DFT studies has greatly increased in recent years. **Left:** An estimate of these trends is provided by tracking the number of papers whose topics contain either "DFT" or "density functional theory" and either "dispersion", "van der Waals", or "vdW". **Right:** An alternative estimate is provided by the aggregate number of citations to the seminal works in the field (Refs. 34–36,39,42–49,56,57,59,60,62–64,66,71–73,80,85). (Data from the Web of Knowledge, August 2015. Years: 1990-2015.)

modeled by adding in correcting one-electron effective potentials (variously called DCACP,[43] LAP[57] and DCP[59,60]), however these approaches suffer from the need for careful fitting and a lack of transferability.

The second level of approximation, II, covers the class of pairwise-additive dispersion methods (generally termed "DFT-D") based on a pairwise summation over generalized interatomic London (C_6/R^6) dispersion contributions:

$$E_{\text{disp}} = -\sum_{ab} \frac{C_6^{ab}}{R_{ab}^6}. \tag{3}$$

DFT-D methods are subdivided into two categories, which we will distinguish as II(a) and II(b), in recognition of the fact that some methods, level II(b), account for the local chemical environment, while level II(a) methods do not. DFT-D methods are extremely popular, largely due to their simplicity and low computational cost, thus making them worthy of a slightly more thorough discussion. These methods suffer from three principle shortcomings. Firstly, the C_6/R^6 dependence is only the leading term in the expansion of the dispersion energy, neglecting both many-body effects (such as the ATM three-body term) and higher-order terms (such as C_8/R^8 interactions). Secondly, the C_6 coefficients must be tabulated, either from experimental data such as ionization potentials and polarizabilities,[39–41,44] or by deriving them from theoretical approximations.[49,54,66,93–95] The third failing of early DFT-D methods was that the C_6 coefficient was kept constant, and thus unable to account for the influence of the local chemical environment. The most popular DFT-D methods where proposed by Grimme in 2006 and 2010 and are known as

DFT-D2[49] and DFT-D3[66] respectively. The popularity of these methods is difficult to overstate, *e.g.*, the four seminal papers[44,49,66,77] on these methods each received 270-1,300 citations in 2014 alone (Data from the Web of Knowledge, August 2015.). Judging from the rate of citations to other popular dispersion methodologies we estimate that Grimme's method is used in $> 65\%$ of studies employing dispersion inclusive DFT methodologies (see Figure 2). Another difficulty with simple C_6/R^6 corrections is that the dispersion correction must be damped out at short-range to prevent it from diverging. The damping function must be chosen carefully for each exchange-correlation functional because the short-range behavior of the exchange-correlation potential (particularly the repulsive exchange) will dramatically impact the shape of the binding energy curve.

DFT-D schemes that seek to account for the local chemical environment are considered level II(b) (these methods are sometimes classified as a separate level of approximation, see *e.g.* Ref. 90). Failing to do so when assigning C_6 coefficients is a serious failing, *e.g.* the C_6 coefficient of a carbon atom can differ by up to 35% depending on its hybridization state.[41] Several schemes have been proposed to address this problem, all of which exploit the concept that the polarizability of an atom is proportional to its volume.[16] In developing DFT-D3, Grimme *et al.* accounted for the variation of C_6 coefficients with hybridization states by interpolating between precomputed reference values based on the number of neighboring atoms each atom has. The Tkatchenko-Scheffler (TS) scheme[62] exploits the proportionality between atomic volume and polarizability more explicitly by rescaling reference C_6 coefficients for isolated atoms by the effective atom-in-a-molecule volumes that are extracted from a partitioning of the molecular charge density. Perhaps the most computationally involved DFT-D method is the exchange-dipole moment (XDM) model of Becke and Johnson.[46–48,50,52,52,73,75,76] The XDM model extracts C_6 coefficients by first scaling the atomic polarizabilities in a fashion similar to the TS model. Subsequently, the dipole moment associated with the region of depleted charge around an electron, known as the exchange-correlation hole, is averaged thereby accounting for the anisotropic charge density of the local chemical environment. The XDM model suffers from high computational cost, with limited benefit over simpler density dependent models such as TS.

The third level of approximation, III, is provided by non-local correlation functionals. These functionals compute a non-local correction that is added to the correlation energy of a typical local or semi-local functional:

$$E_{\mathrm{c}}^{\mathrm{nl}} = \int\int \mathrm{d}\mathbf{r}\mathrm{d}\mathbf{r}'\rho(\mathbf{r})\Phi(\mathbf{r},\mathbf{r}')\rho(\mathbf{r}') \tag{4}$$

where $\rho(\mathbf{r})$ is the Kohn-Sham density, and $\Phi(\mathbf{r}, \mathbf{r}')$ is a non-local kernel chosen to yield the correct $\mathcal{O}\left(1/|\mathbf{r} - \mathbf{r}'|^6\right)$ asymptotic behavior as well as reducing to the appropriate form for homogeneous charge densities. In the 1990s, several approaches were proposed, but were of limited use due to the restriction to non-overlapping regions of electron density.[34–36] By far the most widely used non-local correlation functional is the vdW-DF method proposed in 2004 by the groups of Langreth and Lundqvist.[42] Although the original vdW-DF method suffered from several problems, such as overestimating equilibrium distances for dispersion bound complexes and predicting too large dispersion energies, and was very computationally costly due to the double integration, refinements of the choice of exchange potential improved its accuracy (termed vdW-DF2).[72] A related model was proposed by Vydrov and Van Voorhis (now commonly termed VV10) which substantially improved both the accuracy and computational efficiency of the non-local correlation functional.[61,64,71,96–98] Subsequent work has greatly improved the computational efficiency of both vdW-DF2[63] and VV10,[85] enabling their widespread adoption in both planewave and Gaussian-type orbital (GTO) quantum chemistry software packages. Both vdW-DF2 and VV10 now offer self-consistent or non-self-consistent implementations, though the vastly greater computational cost of computing these non-local corrections self-consistently is usually deemed to be unwarranted given the accuracy of applying them as *a posteriori* corrections.[99] The primary advantage of non-local correlation functionals is that they do not depend on reference C_6 coefficients or atomic polarizabilities, but the added computational cost is not always justified given that the best DFT-D methods are often competitive on benchmark tests. A more serious criticism is that they rely on the assumption that the dispersion energy is pairwise additive, and thus the dispersion energy is constant without regard to whether or not a dielectric material separates the two bodies. For quantitate comparisons of different dispersion inclusive DFT methods we refer the reader to the many excellent reviews on this subject.[74,90,100–102]

The fourth and final level of approximation, IV, regards the inclusion of beyond-pairwise, or many-body, interactions. Many-body effects become increasingly important in the condensed phase,[103] so even if one were to construct a perfect pairwise interaction potential from high-level wavefunction calculations, the properties of solids and liquids would deviate.

Although pairwise-additive methods are capable of reliably describing the dispersion interactions in many molecular systems, it is now well known that both quantitative and qualitative failures of pairwise-additivity can occur, as demonstrated recently in the binding energetics of molecular trimers[104] and host-guest complexes,[105,106] conformational energetics in polypeptide α-helices,[107]

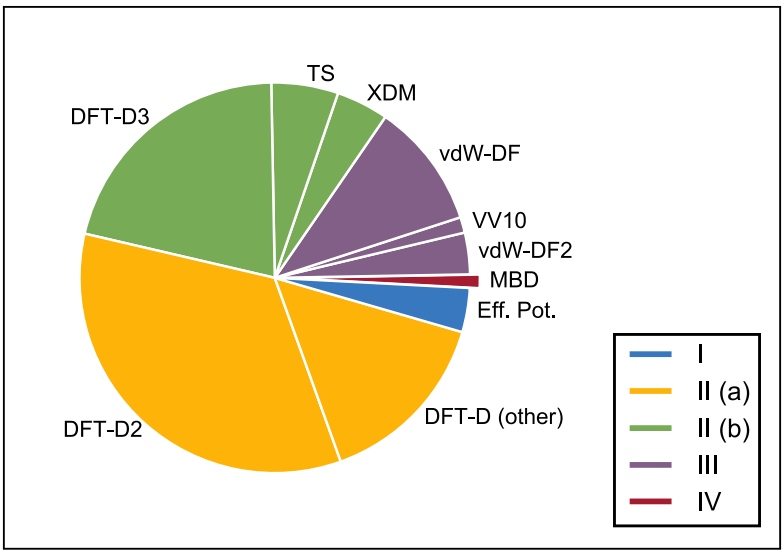

Figure 2: Estimate of the relative popularity of different DFT+vdW correction schemes discussed herein based on the total number of citations to the seminal works on those methods. (Effective Potential methods: Refs. 43,57,59,60, DFT-D (other): Refs. 39,44, DFT-D2: Ref. 49, DFT-D3: Ref. 66, TS: Ref. 62, vdW-DF: Refs. 42,72, VV10: Refs. 71, XDM: Refs. 46–48, MBD: Ref. 80) Methods are colored according to their level of approximation. (Data from the Web of Knowledge, August 2015. Years: 1990-2015.)

cohesive properties in molecular crystals,[108–110] relative stabilities of (bio)-molecular crystal polymorphs,[111–113] adsorption at metal surfaces,[114,115] and interlayer interaction strengths in layered materials,[26,116,117] to name a few. In each of these cases, the true many-body nature of dispersion becomes important, whether it is due to beyond-pairwise contributions to the dispersion energy, such as the three-body Axilrod-Teller-Muto term,[14,15] electrodynamic response screening effects,[80,91,114,115,118,119] or the non-additivity of the dynamic polarizability.[120] Since beyond-pairwise effects can have either attractive or repulsive contributions to the dispersion energy,[30,106,121] their inclusion can sometimes yield results that are qualitatively very different from the predictions of pairwise methods. The usual pairwise sum of C_6R^{-6} terms fails especially for metallic systems, or those with reduced dimensionality in which long-wavelength charge fluctuations can easily occur.[29] As such, incorporating an appropriately non-local many-body description of dispersion interactions into *ab initio* simulation methodologies becomes increasingly important as nanostructured materials are investigated for their exotic electronic properties and application in nanoscale devices.

Principally, two approaches have been suggested for modeling these many-body effects: (a) the use of the adiabatic-connection fluctuation-dissipation (ACFD) theorem[35,84,122,123] to evaluate the

exact correlation energy in the so called random phase approximation (RPA),[91,124,125§] or (b) the use of an effective Hamiltonian which describes a simpler model system of coupled oscillators whose many-body correlation energy can be solved exactly. Both of these approaches are actually revivals of ideas that were once popular in the physics literature. Indeed, the RPA was originally discarded as a poor starting place for constructing density functionals due to its problematic short-range behavior (*e.g.* see Ref.[126]) and extreme computational cost (even treating simple unit cells like graphite is challenging).[91] Nevertheless, ACFD-RPA correlation has proven to give very accurate lattice constants and elastic moduli for many crystals, including soft layered materials that typically prove challenging for other dispersion methods,[127–130] and is attracting renewed interest as a framework for constructing approximate correlation functionals.[131–133]

The effective Hamiltonian models of dispersion that have recently been revived are closely related to Langbein's model of coupled quantum harmonic oscillators (QHOs),[134,135] and Bade's model of coupled quantum Drude oscillators (QDOs).[136] Similar models have been revived or re-discovered many times (cf. Ref. 31 for a review on this subject and Refs. 137–139 for a modern revival of coupled QDOs and Ref. 140 for a coupled plasmon approach.). Just as the TS method assigns C_6 coefficients using effective atom-in-a-molecule volumes, these oscillator models both require coarse-graining the electron density to assign the polarizabilities of the atom-centered oscillators. Building on the successes of the TS method, Tkatchenko *et al.*[80,81,87,88,141] constructed one of the most successful models for incorporating many-body effects into DFT, called the many-body dispersion (MBD) model, in which the correlation energy is modeled at short-range by a semi-local density functional and the long-range correlation energy is approximated after the method of Langbein, using the zero-point energy of a model system of quantum harmonic oscillators fully coupled to one another in the dipole approximation. This method provides a cheap *ab initio* scheme for treating systems where pair-wise theories fail. The MBD model has consistently enabled improved qualitative and quantitative agreement with experimental results and wavefunction-based benchmarks.[80,81,141] Notably, MBD correctly predicts the experimentally known relative stabilities of polymorphs of molecular crystals such as glycine[111] and aspirin,[112] which pairwise methods are unable to do. Beyond these demonstrated successes, one of the most compelling features of the MBD model is that the correlation energy obtained from diagonalization of the coupled oscillator Hamiltonian is provably equivalent to the full ACFD-RPA correlation energy of a system of localized screened isotropic QHOs.[84,88] This equivalence gives additional

[§]In the quantum chemistry literature this is often called the direct RPA (cf. Ref.[123]).

tools for analyzing the approximations that are made in the theory and grounds the method within the wider context of ACFD-RPA approximations to the correlation energy. Refs. 87, 119 and 142 offer recent perspectives on the role of non-additive dispersion effects in molecular materials and the key successes of the many-body dispersion model.

0.1 Outline of the Dissertation

The principle contributions of this dissertation are in extending the applicability of the MBD model by developing analytical forces, unit-cell stresses, phonon corrections, and self-consistency, and by parameterizing MBD for use with a wide variety of exchange-correlation functionals. In each chapter we will provide examples of these methods applied to different physical systems, taking care to provide thorough details about the computational methodologies used in each case. Although it is less precise to do so, within the field of quantum chemistry (specifically the subfield that researches DFT), the terms vdW interaction and dispersion are often used interchangeably while induction effects are sometimes referred to simply as polarization. In recognition of this, we will occasionally use the terms "DFT+vdW" or "vdW inclusive DFT" to indicate DFT methodologies that include a correction for dispersion effects. Except where otherwise appropriate, all equations will be provided in Hartree atomic units ($\hbar = m_e = e = 1/4\pi\epsilon_0 = 1$). Glossaries of symbols, abbreviations, and unit conversions are provided in Appendix A.

In Chapter 1, we seek to motivate these contributions to the MBD model by examining two examples of material specific studies in which the ability of DFT to model non-covalent interactions significantly impacts the predicted properties of advanced functional organic materials. We focus on organic electronics materials since the structure and properties of organic semiconductors are heavily impacted by non-covalent interactions. In Chapter 2, we provide a detailed introduction to the MBD model before developing the analytical energy gradients needed to apply MBD corrected forces in structural optimizations. The developed methodology provides an accurate and efficient scheme for geometry optimizations of systems with inter-, intra-, or supra-molecular dispersion interactions, and the resulting geometries are shown to agree well with high-level wavefunction theory references. We pay particularly close attention to the implicit nuclear coordinate dependence arising from the partitioning of the charge density, an issue that has largely been ignored in prior treatments of the MBD model. In Chapter 3, we discuss the details of our new, efficiently parallel implementation of the MBD energy and analytic gradients,

which has enabled their application to larger simulations of condensed phase materials. This chapter highlights our efforts to improve the numerical stability and computational efficiency of the MBD algorithm as it applies to periodic systems.

In Chapter 4, we present three areas of recent, and ongoing, development work. First, we parameterize the MBD range-separation parameter to enable the use of a wide variety of exchange-correlation functionals. Secondly, we derive the analytical MBD Hessian to enable future studies of dispersion corrected phonon modes. Finally, we extend the MBD model to self-consistently update the charge density, thereby enabling dispersion corrected band-structure calculations and excitation spectra. Though significant work remains in the benchmarking and testing of these contributions to the MBD model, we are optimistic that these methodological developments will enable many exciting discoveries of beyond-pairwise dispersive effects in organic materials.

1

Dispersion Inclusive Density Functional Theory: Applications in Advanced Organic Materials

1.1 Introduction

The development of high-performance organic semiconductor materials has been the focus of significant research in the fields of chemistry and physics for more than 50 years, but for many years these materials were seen as a research curiosity, unable to compete with traditional semiconductor technologies.[143] In the late 1980s, Tang and van Slyke demonstrated an efficient low voltage thin film organic light emitting diode (OLED),[144] which sparked a revolution in the use of organic thin films for new optoelectronic devices. Today, organic semiconductors are a multibillion dollar industry, and displays based on OLEDs are available in consumer phones and televisions. However, significant barriers to manufacturing and commercializing organic electronics materials remain, both in terms of device efficiency and stability, and in 'scaling-up' from the research laboratory to industrial application.[145]

The fundamental promise of organic materials lies in the ability to modify chemical structure in a nearly infinite manner to control the properties of the resulting films. The key to exploiting this promise of 'rational design by chemical modification', is to understand the electronic structure of these materials since subtle changes in structure and composition can result in dramatic alterations of bulk properties.[143] Central to this challenge is understanding the relationships between intermolecular packing and charge-transport or optoelectronic properties.[146] However, understanding and controlling this relationship between chemical structure, bulk morphology, and the resulting properties has proven exceptionally challenging for many materials.

In part, this is because organic molecular materials are held together by weak non-covalent interactions, which makes them especially prone to polymorphism and leads to sensitive

dependence on processing conditions and substrate properties. This has led to many strategies for controlling thin film structure, such as nanoconfinement,[147] solution-shear processing,[148] tempalting with self-assembled monolayers,[149] or using hydrogen- and halogen-bonding to assist crystal engineering,[150–152] to name a few. Such techniques have led to an ever expanding catalog of high-performance organic semiconductor materials, but many organic molecular materials still face poor stability.

Alternatively, by using covalent linkages to form crystalline porous polymers from organic building blocks, it is possible to create structures with topologically predesigned skeletons; these materials are called coordination polymers, or more recently metal-organic or covalent-organic frameworks.[153–157] However, even coordination polymers face the challenge of rationally modifying properties while maintaining the desired structure since it is in no way guaranteed that tuning the organic linker will preserve the desired topology.[157] In the domain of organic electronics, these materials have typically been poor conductors since the linking groups are usually insulators with little π-conjugation.[158] In the quest for metal-organic frameworks (MOFs) with high-conductivity[158–161] or novel electronic properties,[162] two-dimensional conjugated MOFs have emerged as an attractive material class. Just as with organic molecular crystals, the interlayer structure of these materials is dominated by van der Waals interactions.

In this chapter we will examine two examples of the role that non-covalent interactions play in determining the structure and transport properties of novel organic electronics materials and highlight the need for van der Waals inclusive density functionals when studying such materials. These brief forays into single material studies are simply meant to highlight the kinds of problems that one might wish to model in studying organic semiconductor materials, and the challenges that arise for current approaches to treating non-covalent interactions in density functional theory. Since understanding of a material's properties must be derived from a model of its structure, we first discuss an example of the theory-aided structure determination of $Ni_3(HITP)_2$, a novel high-conductivity metal-organic framework reported by Sheberla *et al.* in 2014.[160] Next, we discuss a simple model of charge transport that has proven useful in explaining the behavior of different polymorphs and structural families of organic semiconductors and apply it to understanding the role of hydrogen-bonding in the charge transport of diketopyrrolopyrrole pigments.[163]

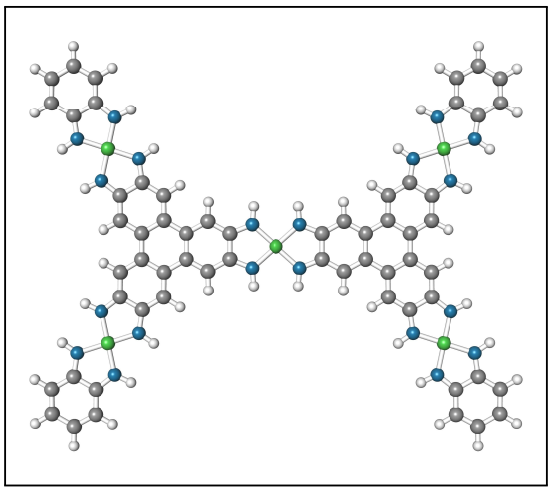

Figure 1.1: Hydrogen terminated molecular fragment used to construct the model unit-cell of $Ni_3(HITP)_2$. Nickel atoms are shown in green, carbon in grey, sulfur in blue, and hydrogen in white.

1.2 The Structure of $Ni_3(HITP)_2$: a 2D Metal-Organic Framework

Largely due to the exciting properties of graphene, there has been considerable interest in recent years in exploring the exotic electronic properties of two-dimensional (2D) materials. Motivated by semiconductor-based device applications, there has been considerable effort to identify 2D materials with non-zero bandgaps, primarily in two material classes: transition metal chalcogenides such as MoS_2, and 2D coordination polymers. Covalent-organic framework materials are attractive due to the ability to prepare them with "bottom-up" solution-based processing methods and their structural tunability. Recent efforts to synthesize high-conductivity covalent metal-organic frameworks have focused on square-planar metal ions bridged by fully conjugated aromatic organic moieties such as dithiolenes.[164–166] Inspired by these approaches researchers in the Dincă group at MIT synthesized a new metal-organic framework $Ni_3(HITP)_2$ (HITP = 2,3,6,7,10,11-hexaiminotriphenylene), which demonstrated very high electrical conductivity, vastly exceeding that of previous conductive MOFs. The material was synthesized by linking $Ni(isq)_2$ (isq = *o*-diiminobenzosemiquinonate) moieties into 2D sheets.

Elemental analysis and X-ray photoelectron spectroscopy (XPS) supported the expected chemical structure. The material demonstrated relatively high crystallinity, with clear powder X-ray diffraction (PXRD) peaks at 2θ of 4.7°, 9.5°, 12.6°, and 16.5°, indicative of long-range order within the *ab* plane. A weaker, broad peak at $2\theta = 27.3°$ was interpreted as a [001] reflection

corresponding to poorer long-range order in the c axis, as is typical for covalently linked layered materials, with an interlayer spacing of ~ 3.33 Å. According to the classification scheme of Koo et al. $Ni_3(HITP)_2$ is a topology **A** framework having a ternary connector with a binary linker.[167] This topology has 6-fold symmetry. Previous reports of 6-fold symmetric COFs have demonstrated a wide range of stacking arrangements.[168–173] For a hexagonal layered material like this there are two common structures: a staggered AA^{-1} layering like graphite, or an eclipsed AA arrangement with adjacent sheets lying exactly on top of one another. For a hexagonal framework like this though, there are two different types of staggering that one might consider, (i) staggering of the hexagonal pore ($+\frac{1}{3}\mathbf{a} + \frac{2}{3}\mathbf{b}$ shift of one plane relative to the other), (ii) staggering of the benzene ring ($\sim \frac{1}{16}$ unit cell shift in the ab plane). We refer to the first as fully staggered (AA^{-1}), and the second as parallel-displaced (AB) stacking.

Simulations of the PXRD spectra indicated that an eclipsed (AA) or parallel-displaced (AB) stacking in the c direction was more likely than a fully staggered (AA^{-1}) structure. However, the PXRD spectrum was unable to conclusively determine the structure. Ni K-edge extended X-ray absorption fine structure (EXAFS) analysis revealed a spectrum that better agreed with a simulated spectrum of the AB parallel-displaced stacking than the fully eclipsed AA.

To resolve the uncertainty in the structure of the $Ni_3(HITP)$ material, we performed molecular mechanics (*i.e.* forcefield) and DFT calculations on numerous stacking arrangements. The large aromatic organic bridging structure provided considerable surface area for attractive $\pi - \pi$ dispersion interactions, while the typical oxidation states of square-planar Ni indicated that the metal center was likely to be charged, adding a significant repulsive penalty to the eclipsed structure. We started our investigation with the construction of a model unit-cell. The PXRD spectrum indicated a likely spacegroup of P6/*mmm*, with $a = b \simeq 21.75$ Å and $c = 3.33$ Å. We optimized a hydrogen-terminated molecular fragment, shown in Figure 1.1, using the B3LYP functional in a 6-31G(d) basis set[174] with Grimme's atom-pairwise third generation dispersion correction[66] and a Becke-Johnson damping scheme (D3BJ).[77] In the optimized geometry the Ni atoms formed two isosceles triangles with side lengths of 10.926 Å and 10.933 Å and angles of 59.96° and 60.02°. This structure was then converted into fractional coordinates using a cell length $a = b = 21.86$ Å, determined from the Ni–Ni distances of the optimized fragment. Since we do not expect a 2D sheet of this material to have these squeezed angles, the unit cell was forced into P6/*mmm* symmetry in Avogadro using a threshold of 1.7 pm (*i.e.*, the maximum adjustment of any coordinate to force this symmetry was 1.7 pm). An interlayer spacing of 3.3 Å was enforced

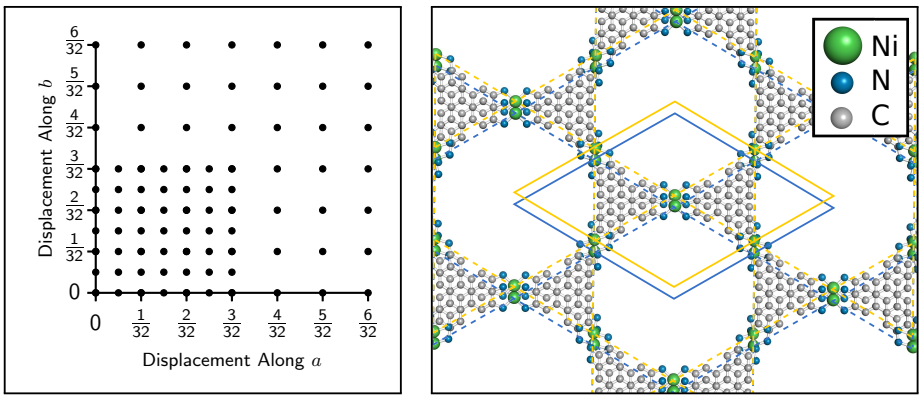

Figure 1.2: Left: The two grids of fractional coordinate translations in the *ab*-plane that were sampled by DFT calculations. **Right:** Example of a structure that is produced by a 1/16th lattice vector relative displacement along both the *a* and *b* axes. The solid lines show the unit cell (blue) and displaced unit cell (yellow), while the dashed lines highlight the Kagome lattices that are formed by the Ni atoms. Notice that this relative displacement pattern produces typical staggered benzene ring arrangement in the connector fragment.

for consistency with the PXRD signal. To consider parallel-displaced structures the *c*-axis was doubled to 6.6 Å.

A total of 82 different model unit cells for parallel-displaced structures were generated from the two grids of relative translations in the *ab*-plane shown in the left-hand panel of Figure 1.2. DFT single-point energy calculations were carried out on all 82 of these structures in VASP v5.29[175–180] using the following three exchange-correlation functionals: LDA (local density approximation of Perdew & Zugner),[181] and PBE (Perdew-Burke-Ernzerhof),[182,183] both with and without Grimme's second-generation (D2) dispersion correction.[49] Details of these computations can be found in the supplemental information of Ref. 160. The total energy of each of these structures was then used as a sample point for the energy of a potential energy surface (PES) that was interpolated using 2D Lagrange polynomials over a tensor product grid of Chebyshev points which were subsequently mapped back to the grid of original equally spaced translations (cf. Ref. 184 for a modern treatment of Lagrange polynomial interpolation.). Interpolation over the finer grid is expected to yield a more accurate representation of the potential energy surface in the region. The resulting interpolated PESs are shown in Figure 1.3. As shown in the top left-hand panel, the PBE functional showed strongly repulsive behavior making the fully eclipsed AA structure (zero displacement) energetically unfavorably by more than 2 eV. PBE predicts such a significant repulsion that that the energy should keep decreasing moving out to the largest sampled displacements of ~ 4 Å in the *ab*-plane. Simulations of the PXRD spectrum of these translated

structures indicated that such large parallel displacements would result in very distinct spectral features that were absent from the experimental spectrum. We therefore concluded that dispersion interactions must be stabilizing a structure with less significant displacement.

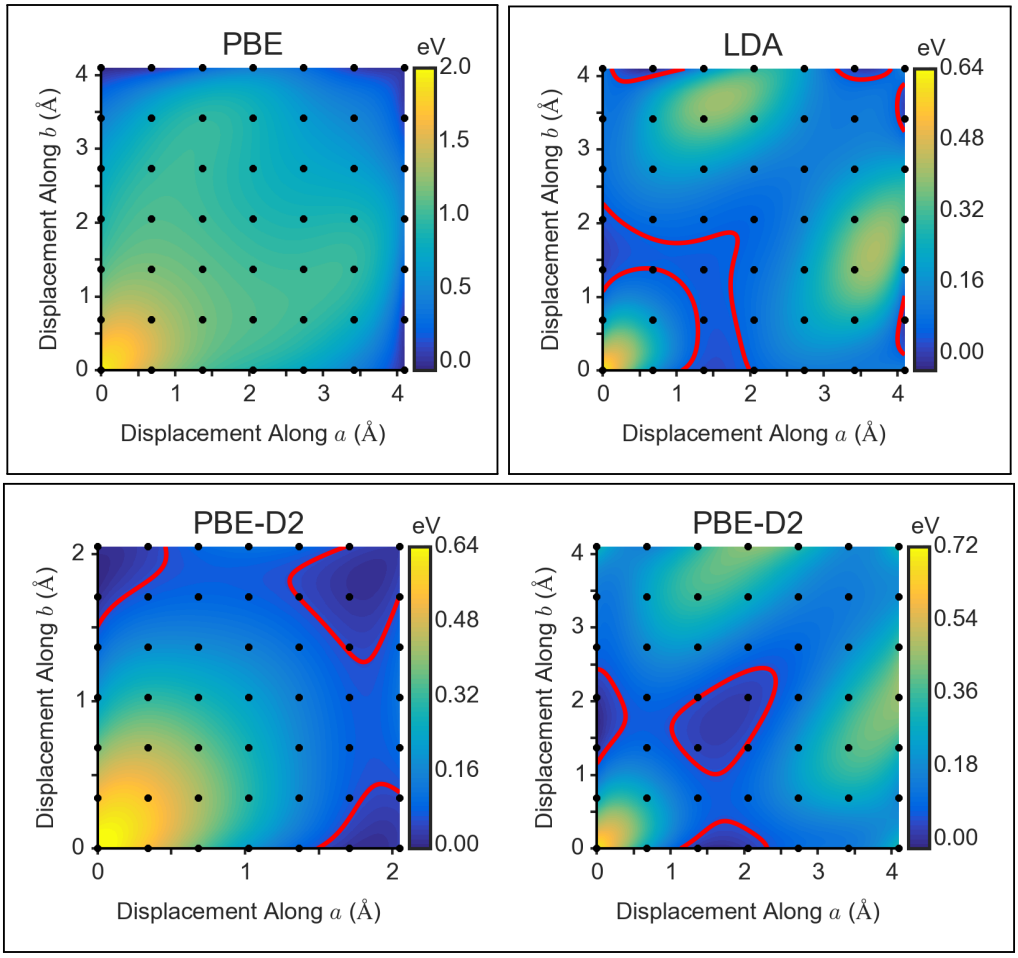

Figure 1.3: Contour maps of the potential energy surface induced by different translations between A and B layers of $Ni_3(HITP)_2$. Black dots correspond to locations of DFT single-point calculations. The surface was produced by interpolation with 2D Lagrange polynomials on a grid of Chebyshev points. The energy is normalized to zero at the minimum. Red lines indicate the 'thermally accessible' region within $2k_BT \approx 0.051$ eV of the minima. **Top Left:** Potential energy surface of the PBE functional without dispersion correction. **Top Right:** Potential energy surface of the LDA functional. **Bottom:** Potential energy surface of the PBE-D2 functional. Note that the minimum obtained from the fine interpolation grid at left is closer to a displacement of ~ 1.8 Å in contrast to the minimum at ~ 1.7 Å on the larger grid at right.

In contrast to the uncorrected PBE functional, both LDA and the dispersion corrected PBE-D2 predict that the AB parallel-displaced sequence is the most stable.These functionals suggested that the fully eclipsed AA structure is energetically unfavorable by $\sim 0.5 - 0.6$ eV. It is well known that

the LDA functional tends to over-bind and as a result can mimic attractive dispersion interactions, such as the prediction of stable minimum between two graphite planes. As shown in the top right and bottom panels of Figure 1.3, both LDA and PBE-D2 predict minima in the PES for relative displacements of $\sim 1.6 - 1.9$ Å along the a and/or b axis. In particular, an AB model wherein the 2D unit cell of one layer is slipped relative to a neighboring layer by slightly more than 1/16th of a cell edge (~ 1.8 Å) along the a or b vectors gave the lowest energy on the PBE-D2 PES. The locations of these minima are consistent with the minima on the PES provided by the van der Waals component of the Allinger MM2-1991 force field,[185] shown in Figure 1.4. Note that since we are plotting only the van der Waals component, the repulsion away from AA stacking is less significant. The full MM2 forcefield PES showed a strong repulsion favoring a relative displacement of ~ 3.5 Å between the A and B layers. We concluded that the point-charge model being used for the Ni center was overly repulsive since the location of these potential energy minima correspond to displacements that are clearly inconsistent with the experimental PXRD spectrum in addition to the LDA and PBE-D2 functionals. Both LDA and PBE-D2 show fairly flat minima, suggesting that the structure likely contains a disordered mixture of displacements to these 'parallel-displacement minima', which is consistent with the PXRD signal indicating poorer long-range order along the c direction.

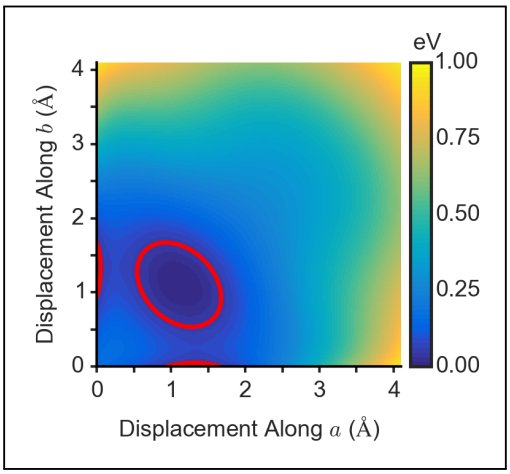

Figure 1.4: Contour map of the potential energy surface of the van der Waals component of the MM2 force field for different translations between A and B layers of $Ni_3(HITP)_2$. The surface was produced by interpolation with 2D Lagrange polynomials on a grid of Chebyshev points. The energy is normalized to zero at the minimum. Red lines indicate the 'thermally accessible' region within $2k_BT \approx 0.051$ eV of the minima. For details about these calculations see the supplemental information of Ref. 160.

Altogether, the PXRD, EXAFS, and DFT data evidence a hexagonal $Ni_3(HITP)_2$ structure with slipped-parallel stacking and unit cell parameters $a = b = 21.75$ Å and $c = 6.66$ Å. Determining a consistent structural model required the use of van der Waals inclusive DFT since the incorrect form of the PBE correlation potential at long-range resulted in predictions that significantly disagreed with the experimental evidence. The success of LDA for this system should be regarded as a happy accident since there are no terms in its exchange-correlation potential that correspond to dispersion interactions. Having seen that accounting for van der Waals interactions is crucial for modeling the structural properties of organic materials, we now turn to an example where the balance between dispersion and hydrogen-bonding interactions has an impact on the functional properties of organic semiconductors.

1.3 Charge Transport in Hydrogen-Bonded Diketopyrrolopyrrole Pigments

Many electronics applications, from photovoltaics to light emitting diodes to transistors, depend on one or more layers having high charge carrier mobility. Carrier transport in organic materials is extremely sensitive to the phase of the wavefunction and the degree of overlap between frontier orbitals on neighboring molecules, and as such the mobility acquires sensitive dependence on the relative positioning of nearest neighbor molecules (Excellent reviews of this subject may be found in Refs. 186–189). For many years the conventional wisdom in the organic semiconductor community has been that maximizing charge carrier mobility requires maximizing intramolecular π-conjugation, since delocalized charges are more mobile along the molecular backbone. Therefore, many researchers in the field avoid the use of amine and carbonyl groups when designing new materials as they interrupt conjugation.[190,191] Recently, studies of hydrogen-bonded pigments, such as indigo and its derivatives,[192–195] diketopyrrolopyrrole-thiophene co-oligomers,[196] epindolidiones,[197,198] quinacridone,[197,199,200] and numerous azo-pigments have questioned this paradigm, suggesting that equally high charge transport, and much greater stability, can be achieved by appropriate use of hydrogen-bonding.

Many factors influence the charge carrier mobility of organic materials, including disorder/morphology, molecular packing, charge-carrier density, temperature, and the presence of impurities.[186] Many π-conjugated molecules crystallize into a layered herringbone arrangement, which leads to effective 2D transport within the plane containing $\pi - \pi$ stacking interactions, while transport between layers is limited by the weak electronic coupling between head-to-tail

contacts.[186] In highly crystalline samples of small molecule organic semiconductors, transport through the $\pi - \pi$ stacking pathways is often the mobility-limiting consideration, therefore maximizing the charge transfer integrals between neighboring molecules can lead to the largest practical increases in mobility.[186] In this respect H-bond mediated crystal engineering can be used to improve performance.

The family of diketopyrrolopyrrole (DPP) pigments was first developed for industrial dye applications,[201] but have gained significant attention in the organic electronics community in recent years as building-blocks for high-performance transistors and photovoltaics.[202–204] The polymers and small molecule DPP derivatives used in these applications typically eliminate hydrogen-bonding by functionalizing the core with solubilizing alkyl chains, although both Yanagisawa *et al.*[199] and Lee *et al.*[205] have recently reported measurements on DPPs containing hydrogen-bonding NH groups. DPPs are used extensively as building blocks for semiconducting polymers. However, relatively little attention has been paid to the semiconducting properties of their native hydrogen-bonded pigment forms. The pigment form is particularly interesting because it is produced at low cost at the industrial scale (*e.g.* DPP and chlorinated DPP are commercially available for < 50 ¢/g).

To examine the semiconducting properties of DPPs in their native H-bonding form, we studied three archetypical DPP pigments, diphenyl-DPP (also called Pigment Red 255, hereafter abbreviated DPP), di(*p*-chlorophenyl)-DPP (also called Pigment Red 254, hereafter abbreviated *p*-Cl DPP), and di(*p*-bromophenyl)-DPP (hereafter abbreviated *p*-Br DPP). *p*-Cl DPP is perhaps most famously known as 'Ferrari Red' for its use in automobile coatings. The H-bonded crystal lattice of these pigments supports close and relatively cofacial $\pi - \pi$ stacking. H-bonded DPP pigments crystallize in linear H-bonded chains, with each molecule displaying head-to-tail double hydrogen-bonds to two neighbors.[163,206,207] In DPP for example, these chains run parallel to each other along the $\langle \bar{1}12 \rangle$ plane, while brick-wall type $\pi - \pi$ stacking is visible perpendicular to the $\langle \bar{1}12 \rangle$ plane. The para-halogenated DPP derivatives show a sightly staggered H-bonding motif with two linear H-bonded chains running along the $\langle 001 \rangle$ plane, and another two chains along the $\langle 002 \rangle$ plane. The H-bond length in all DPP pigments here, $1.7 - 1.8$ Å, is very short in comparison to other pigment-forming molecules. For example, quinacridones have ~ 2 Å, and indigos $2.1 - 2.8$ Å. The interplanar spacing and intermolecular centroid-centroid distances for $\pi - \pi$ stacking for all three materials are shown in Table 1.1. Considering the crystalline packing in the π-stacking and H-bonding plane (*i.e* the "charge transport plane"), all three materials are quite similar, though

Table 1.1: Data on the single-crystal X-ray diffraction determined bulk structures of H-bonded DPP pigments. The intermolecular $\pi - \pi$ distance $d_{\pi-\pi}$ is computed centroid–centroid.

Material	Interplanar $d_{\pi-\pi}$ (Å)	Intermolecular $d_{\pi-\pi}$ (Å)	$-\mathrm{NH}\cdots\mathrm{O}=$ bond length (Å)	Packing pattern	Space group
DPP	3.3 (along a) 3.0 (along b)	3.82 (along a) 6.52 (along b)	1.82	brick-wall	$P\bar{1}$
p-Cl DPP	3.0 (along a) 3.3 (along c)	5.66 (along a) 5.59 (along c)	1.74	pseudo brick-wall	$P21/n$
p-Br DPP	3.2 (along a) 3.2 (along b)	5.63 (along a) 5.63 (along b)	1.77	pseudo brick-wall	$C2/c$

the intermolecular centroid-centroid distances for $\pi - \pi$ stacking become more symmetric moving from DPP to the halogenated species. For intermolecular packing arrangements such as this, one would expect a transport anisotropy, with charge transport favorably occurring along the $\pi - \pi$ stacking direction, *i.e.* perpendicular to the H-bonding direction.[186] Thus, considerable experimental effort has been devoted to studying low surface energy hydrophobic substrates that encourage the van der Waals contacts of the H-bonded pigment molecules to interact with the surface and align in a "standing" orientation. This places the $\pi - \pi$ stacking direction parallel to the gate dielectric, encouraging high transport in transistors.[208,208] In this respect, anodically-grown AlO_x passivated with tetratetracontane ($C_{44}H_{90}$, TTC) is an ideal dielectric for H-bonded pigments, including DPPs.[197,209,210] Despite the preferential orientation occurring when DPPs are grown on TTC/AlO_x, charge transport may still be limited by the polycrystalline morphology of such films. When incorporated into thin film organic field-effect transistors, all three pigments showed carrier mobilities in the range $0.01 - 0.06$ cm^2/V $\cdot$ s.[163]

1.3.1 Charge transfer integrals

Since organic materials are principally held together by weak noncovalent interactions, many electronic properties are determined by the structure of an isolated molecule, together with a description of electron-phonon coupling and polaronic effects.[211] Weak overlap of molecular orbitals causes organic materials to have narrow electronic bands, and a site-based description of transport based on the concept of small polarons becomes appropriate.[212–218] Many effects, such as electronic polarization and static disorder, dynamic disorder due to electron-phonon coupling, thermal broadening, trap states, and the role of charge injection and charge carrier density, all

contribute to the complex phenomenology of charge transport in organic semiconductors.[186,187,219–221] However, at the microscopic level, one of the principle parameters governing charge transport is the amplitude of the charge transfer integral between adjacent molecules, which describes the rate of incoherent tunneling.[222–224] Transfer integrals are highly anisotropic, reflecting the low symmetry of the molecular packing environment and a high sensitivity to the overlap and phase of frontier molecular orbitals.

A fully *ab initio* prediction of carrier mobility for organic materials thus requires: (a) a model of the transport mechanism relevant for that material including the effects of temperature, carrier density, and impurities, (b) a model of the microscopic morphology, and (c) dynamical simulations, or a model of dynamical disorder. To separate out the effects of impurities and morphology, it is often useful to model the *intrinsic* mobility of a perfectly crystalline material. At room temperature, charge carriers in organic semiconductors are expected to be localized to a single or a few molecules due to strong electron-phonon coupling. As a result, transport is frequently described as a thermally activated hopping process where charges move from one molecule to another through incoherent electron tunneling and the uncorrelated sequence of such charge transfer events is well described by diffusion.[225] In this regime, fluctuations of the transfer integral due to thermal motion are often the same order of magnitude as the average value,[226] making it necessary to average over the trajectories of molecular dynamics simulations to achieve a high quality prediction of intrinsic mobility.

In the following we will analyze a simplified static model that addresses the simulation procedure for computing the transfer integrals and associated charge transfer rates at a given geometry. We have found that this simple static model is often sufficient to produce an order of magnitude estimate of a material's intrinsic carrier mobility and is also suggestive of the relative importance of different molecular contacts. In the case where charge carriers are localized to a single molecule, the transport of an electron (or hole) from one molecule to another can be modeled using the Marcus theory semiclassical rate k for non-adiabatic charge transfer (*i.e.* the high temperature limit),[186,219,227] which is calculated as:

$$k_i = t_i^2 \sqrt{\frac{\pi}{\hbar^2 k_B T \lambda}} \exp\left[-\frac{(\lambda + \Delta\varepsilon_i)^2}{4\lambda k_B T}\right], \tag{1.1}$$

where λ is the internal reorganization energy calculated as the geometric relaxation energy of the charged species, and t is the intermolecular transfer integral, and $\Delta\varepsilon$ is the difference in site

energies (cf. Refs.[186,219] for more discussion of this model). We calculate the charge transfer integrals using the projective molecular orbital approximation.[228,229] In the Marcus theory model of charge transport, the contribution of different "hopping pathways" may be evaluated from the relative probability, $\mathcal{P}_i = k_i / \sum_i k_i$, of hopping to the i^{th} nearest neighbor molecule.

To better understand how the observed semiconducting properties correlate with the crystal structure of the three DPP materials, we performed transfer integral calculations to estimate mobilities in their X-ray determined bulk crystal structures. It is important to note that the bulk crystal structure may differ quite significantly from the packing in the polycrystalline transistors. Indeed, pentacene is a well-known example that crystallizes in a surface-induced polymorph that is different from the known bulk polymorph.[230] To address this concern, we performed out-of-plane X-ray diffraction (XRD) measurements on vacuum evaporated films: $\omega - 2\theta$ XRD shows a single low-angle peak which corresponds, based on single-crystal diffraction data, to peaks from the $\langle 001 \rangle$ planes of the DPPs. This is a necessary but not sufficient condition to conclude that a thin film has the same crystal phase as the "bulk" structure. Since the molecules orient anisotropically with respect to the substrate ("standing" orientation with the longest lattice parameter perpendicular to the substrate), a standard $\omega - 2\theta$ XRD scan will only show peaks corresponding to that orientation. However, out-of-plane scans of films provide data consistent with the known "bulk" crystal phase. For example, for DPP, the $\langle 001 \rangle$ peak dominates the thin-film XRD spectrum, which is consistent with the prediction based on the single-crystal data. Likewise the other peaks are weaker due to preferential anisotropic growth. For further discussion, see the supplemental information in Ref. 163.

Transfer integral calculations were performed at the DFT level with the B3LYP,[231,232] PW6B95,[233] revPBE,[234,235] and revPBE0 functionals[234–238] using the Ahlrichs def2-TZVP basis set[239] coupled with an auxiliary Ahlrichs TZVP basis set[240] for the RI-JK approximation* to the Coulomb and exchange terms.[242,243] (See section A.2 of Appendix A for an explanation of these DFT functional abbreviations.) All calculations were performed in the Orca v3 software package.[244] The transport properties collected in Table 1.2 (as well as Tables B.1 & B.2 in Appendix B) also include corrections for dispersion computed self-consistently with the VV10 nonlocal correlation functional[71] as implemented in Orca for the B3LYP, revPBE, and revPBE0 functionals. The exchange-correlation functionals were evaluated on a grid4 integration grid, while the VV10 nonlocal correlation functional was evaluated with a vv10_grid3 integration grid.

*Calculations with the PW6B95 functional employed the RIJCOSX approximation.[241]

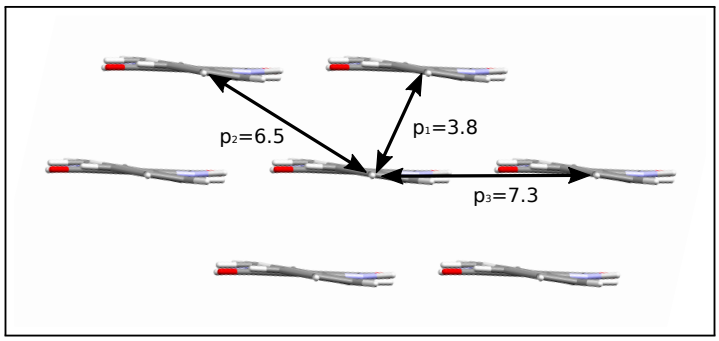

Figure 1.5: Dominant charge hopping pathways for DPP considered in density functional theory transport calculations. Distances between centroids are in units of Å. The calculated charge transfer integrals show that both pathways along $\pi - \pi$ stacking and H-bonding contribute significantly to charge transport.

By examining the charge transfer integrals we can determine which pathways, or nearest-neighbor pairs, will contribute most strongly to the predicted mobility. The results of this analysis for the B3LYP functional are presented in Table 1.2, while and results for the revPBE and revPBE0 functionals are given in Tables B.1 and B.2 in Appendix B. The dominant contribution to hopping transport in hydrogen-bonded DPP pigments occurs in the π-stacking and H-bonding plane where the greatest overlap between frontier orbitals of neighboring molecules occurs. The packing arrangement of this plane is very similar across all three pigments even though DPP forms a more linear head-to-tail arrangement than *p*-Cl DPP and *p*-Br DPP. In Figure 1.5, we label the hopping pathways that are the dominant transport directions in DPP. Paths 1 and 2 are $\pi - \pi$ interactions and path 3 is a hydrogen-bond interaction. The same labeling scheme is used for the pathways in the transport plane of *p*-Cl DPP and *p*-Br DPP and the relevant distances are given in Table 1.1. The structural and electronic perturbations introduced by Cl and Br substitutions alter which pathway is dominant. For instance, these transfer integrals suggest that the electron mobility of DPP will be dominated by the H-bond pathway, while *p*-Cl DPP and *p*-Br DPP show stronger coupling in the $\pi - \pi$ pathways. An important observation is that a substantial contribution (12-70%) is made by pathways along the H-bonding direction in all three compounds.

The edge-to-edge contacts in molecular semiconductors normally have very low transfer integrals and contribute negligibly to transport, in the case of DPPs, however, these values are considerably higher. This is potentially significant, as not only $\pi - \pi$ stacking contacts are expected to contribute to conduction, but also the H-bonding contacts. This implies that the prevailing understanding concerning orientation of $\pi - \pi$ stacking domains, as described above, may require

reconsideration with respect to H-bonded systems. Therefore, in the design of future H-bonded derivatives of DPP, increasing H-bonding interactions may be a favorable approach. Though the mobility values remain modest in comparison with more optimized DPP-containing polymeric systems, in the $10^{-2} - 10^{-1}$ $\mathrm{cm}^2/\mathrm{V} \cdot \mathrm{s}$ range, our results suggest that H-bonded crystal engineered materials deserve additional attention.

Table 1.2: Transport properties (calculated at the B3LYP/def2-TZVP level) for diketopyrrolopyrrole pigments broken down into the dominant hopping pathways. d is the length of the pathway. $\mathcal{P}$ is the relative probability of hopping along the i^{th} pathway and m_i is its multiplicity, *i.e.* the number of symmetry related pathways. $|t|$ is the absolute value of the transfer integral. Values in parentheses have been calculated with VV10 applied self-consistently. Results for the revPBE and revPBE0 functionals are given in Tables B.1 and B.2 in Appendix B.

Pathway	d (Å)	m	$\lvert t_e \rvert$ (meV)	$\mathcal{P}_e$ (%)	$\lvert t_h \rvert$ (meV)	$\mathcal{P}_h$ (%)
			DPP			
p_1	3.8	2	6.3 (7.4)	2.7 (3.6)	82.7 (84.4)	40.3 (40.2)
p_2	6.5	2	13.8 (13.7)	12.9 (12.3)	23.4 (24.0)	3.2 (3.3)
p_3	7.3	2	22.4 (22.8)	34.1 (33.8)	33.2 (34.0)	6.5 (6.5)
			p-Cl DPP			
p_1	5.6	2	16.8 (16.2)	8.3 (7.9)	16.1 (16.3)	1.4 (1.3)
p_2	5.7	2	23.4 (24.1)	16.3 (16.8)	88.6 (90.9)	41.2 (41.1)
p_3	7.3	2	20.9 (21.2)	12.9 (12.6)	33.1 (33.7)	5.7 (5.7)
			p-Br DPP			
p_1	5.6	4	31.2 (31.6)	18.8 (18.8)	21.5 (21.8)	8.9 (8.8)
p_3	7.3	2	23.1 (23.4)	10.3 (10.3)	40.2 (41.0)	31.0 (31.1)

One feature of transfer integral predictions is that they are extremely sensitive to both the overlap of the frontier orbitals of the dimer of interest and also to the relative phase of those orbitals. As a result, they can be quite sensitive to small changes in either nuclear coordinates or the long-range behavior of an exchange-correlation functional. For materials such as H-bonded pigments, whose properties depend on a balance between two noncovalent interactions, namely hydrogen-bonding and $\pi - \pi$ interactions, errors in both the exchange and correlation potential can have significant impact. (The balance between dispersion and exchange effects is especially well documented in the extensive literature on *ab initio* predictions of the structure of liquid water, *e.g.*, see Refs.[245–247] For a recent perspective on the accuracy of different DFT functionals, with and without dispersion corrections, for describing H-bonds see Ref. 248.) Since transfer integrals are a density derived property, only a density dependent correction scheme will alter the predicted

transport rate.

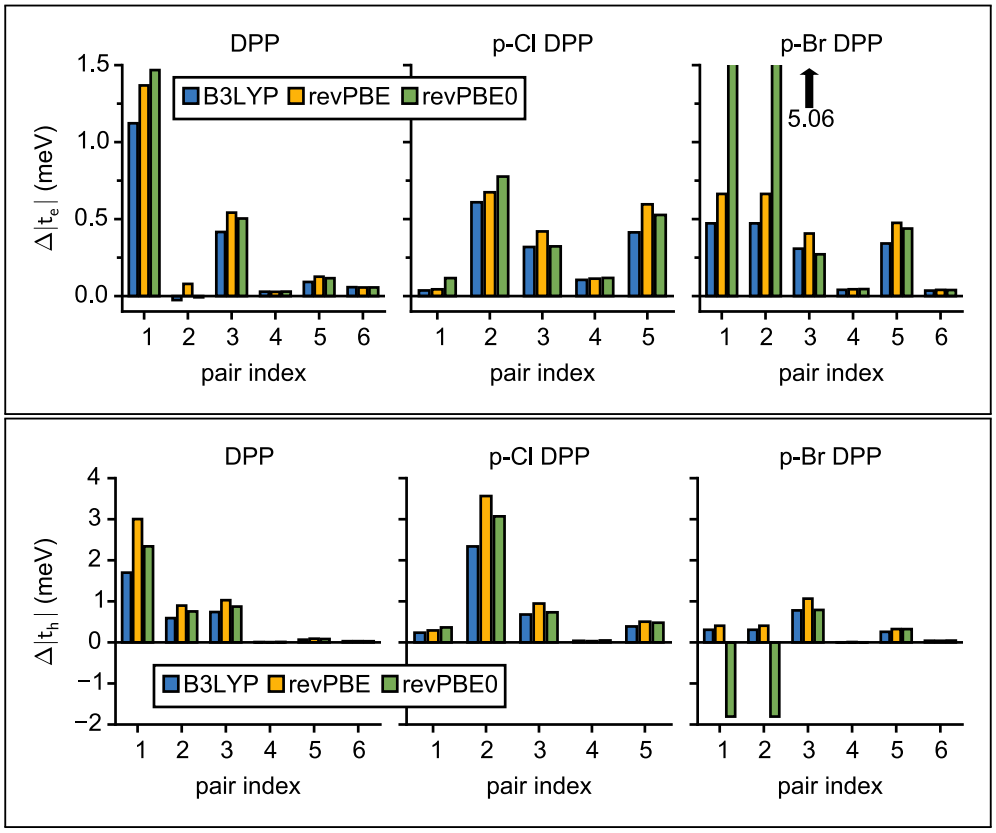

Figure 1.6: Change in the amplitude of transfer integrals (|t|) for diketopyrrolopyrrole pigments upon self-consistent application of the VV10 nonlocal correlation functional dispersion correction. Positive values indicate that DFT+VV10 predicted a larger transfer integral than the uncorrected DFT functional. **Top:** electron transfer integrals. **Bottom:** hole transfer integrals.

To investigate how important changes to the intermolecular density arising from dispersion and exact exchange are for charge transport in H-bonded pigments, we repeated the transfer integral calculations with a self-consistent implementation of the VV10 nonlocal correlation functional dispersion correction. The results are given in parentheses in Table 1.2 as well as Tables B.1 and B.2 in Appendix B. Figure 1.6 shows the change to the transfer integrals for each hopping pathway when self-consistent dispersion is included, while Figure 1.7 shows the same breakdown for the impact of including exact exchange. Although the impact of the self-consistent dispersion correction is small ($\sim 0.5 - 3$ meV), it is worth noting that this is only about half the difference between changing from a GGA functional, revPBE, to the hybrid variant, (revPBE0), which includes 25% exact exchange. Both the self-consistent application of VV10 and the inclusion of exact exchange alter the transfer integrals for close-contact pairs ($\pi - \pi$ and H-bonded) more

significantly than they do the head-to-tail contacts since the frontier orbital overlap for these contacts is greater. However, the relative percentage change due to dispersion is typically larger for the head-to-tail contacts since the transfer integrals for these long distance pathways are much smaller and are dominated by long-range interactions. Self-consistent application of VV10 has a larger impact for the dominant $\pi - \pi$ pathway (either p_1 or p_2) than it does for the H-bonded pathway (p_3), in accordance with our expectations. Given the small magnitude of these changes to the transfer integrals and the large computational cost of applying VV10 self-consistently, we would not recommend widespread adoption of self-consistent VV10 for exploratory transfer integral calculations. However, since noncovalent interactions play a crucial role in determining the structure of many organic semiconductors, and since transfer integrals are often very sensitive to small changes in the nuclear coordinates, it may be worth investigating how self-consistent dispersion corrections alter the electron-phonon coupling in these materials. Overall, we find that noncovalent interactions play a surprisingly large role in determining the dominant transport pathways in H-bonded DPP pigments. The linear hydrogen-bonding chains in these materials suggests that nonlocal electron-phonon coupling effects are likely to play a larger role in the charge transport properties than is typically observed in other π-conjugated small molecule organic electronics crystals.[186]

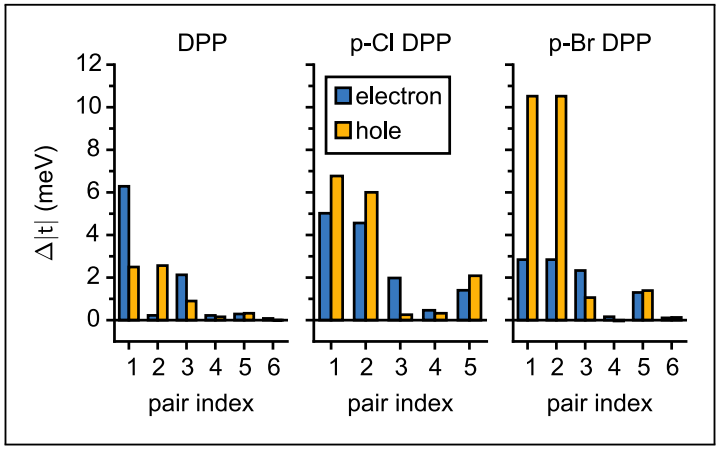

Figure 1.7: Change in the amplitude of transfer integrals (|t|) for diketopyrrolopyrrole pigments in changing from a GGA functional (revPBE) to a hybrid variant (revPBE0) of the same functional, which contains 25% exact exchange. Positive values indicate that the hybrid functional predicted a larger transfer integral than the GGA functional. No dispersion correction has been applied.

1.4 Conclusions

In this chapter we have highlighted examples of the role that non-covalent interactions can play in determining the structure and electronic properties of organic electronics materials. These brief investigations made use of two types of popular dispersion corrections presently available for use with DFT, namely, a nonlocal correlation functional (VV10) and a C_6 based semiempirical correction (D2). The application of DFT-D type semiempirical corrections often prove sufficient for many structural investigations, since they offer computationally cheap vdW forces, but they typically do not allow for robust correction of density-dependent properties. Such schemes are typically limited to pairwise or three-body dispersion corrections, which can be a significant drawback for studying low-dimensional structures or highly polarizable extended systems. On the other hand, nonlocal correlation functionals methods may be applied either non-self-consistently (typically at a fraction of the computational cost of a GGA calculation), or self-consistently (typically at greater computational cost than the underlying GGA calculation) if one wishes to study density dependent properties. The ability to compute forces (*i.e.*, energy gradients) and interrogate how a method impacts density dependent properties are central tasks for many investigations, and should be regarded as desirable features for a vdW correction scheme in DFT. For instance, many of the optoelectronic properties of organic materials are strongly modulated by electron-phonon coupling, which often has a significant nonlocal or many-body contribution. This is especially true in two-dimensional materials such as graphene.[249] Investigating these properties typically requires the use of a linear response formalism or the ability to run a dynamical simulation and subsequently use spectral methods to extract the relevant quantities from the correlation functions computed on the trajectory. With the ever expanding list of low-dimensional materials, such as vdW heterobilayers, being studied by researchers in physics, chemistry, and materials science, there are many systems of interest that are dominated by vdW interactions and require large-scale density-dependent simulation methodologies. With these considerations in mind, Chapters 2, 3, and 4 will be devoted to further developing the many-body dispersion model for use in structural and optoelectronic studies of both isolated and condensed phase systems.

2

Analytical Gradients for the Many-Body Dispersion Model of Noncovalent Interactions

2.1 Introduction

Thus far we have seen that accurate treatment of the long-range electron correlation energy, including dispersion, is essential for describing the structure and function of a wide variety of systems and have discussed a few approaches for correcting these terms in density functional theory (DFT). In recent years it has become increasingly apparent that accounting for the true many-body nature of dispersion is beneficial when developing models for treating van der Waals interactions in DFT.[87] One of the most successful models for incorporating these many-body effects into DFT is the many-body dispersion (MBD) model of Tktatchenko *et al.*[80,81,141] which approximates the long-range correlation energy using the zero-point energy of a model system of quantum harmonic oscillators fully coupled to one another in the dipole approximation. Deriving dispersion interactions from screened collections of quantum harmonic oscillators was a popular technique in the 1970s and 1980s, and much of the formalism that is used in the MBD model is due to Langbein,[134,135] and Thole.[118] The correlation energy derived from diagonalizing the Hamiltonian of these oscillators is provably equivalent to the random-phase approximation (RPA) correlation energy in the dipole limit (through the adiabatic-connection fluctuation-dissipation theorem), and thus this scheme provides a computationally efficient mechanism for evaluating the RPA correlation energy.[84,88] Ambrosetti *et al.* further improved the model by incorporating a range-separation scheme to avoid double counting the short-range correlation energy; this method is termed range-separated many-body dispersion (MBD@rsSCS).[88] Although the MBD model has been very successful as an *a posteriori* energy correction after the solution of the nonlinear Kohn-Sham equations (*i.e.* a post-self-consistent field correction), computing the gradient of the

MBD energy has previously been limited to finite difference techniques, which require calculations at multiple nuclear configurations. In this chapter, we seek to extend the applicability of the MBD model by developing analytical gradients of the MBD@rsSCS energy with respect to nuclear coordinates, including all implicit coordinate dependencies arising from the partitioning of the electron density into Hirshfeld effective atomic volumes.* This gives an accurate and efficient scheme for MBD inclusive geometry optimizations and molecular dynamics simulations.

This chapter is principally divided into a theoretical discussion of the MBD model (section 2.2), and a discussion of the first applications of analytical MBD forces to the optimization of isolated molecular systems (section 2.4). We start by presenting a self-contained summary of the MBD framework to clarify notation and highlight the different dependencies on nuclear coordinates (sections 2.1.1-2.2.1). We then derive analytical nuclear gradients of the MBD correlation energy (section 2.2.2).

Subsequently, we demonstrate the efficiacy of MBD forces for treating several representative systems displaying intermolecular, intramolecular, and supramolecular interactions (sections 2.4.1-2.4.3). For intermolecular and intramolecular interactions we consider conformers of the benzene dimer and isolated small peptides with aromatic side-chains. We find excellent agreement with the wavefunction theory reference geometries of these systems at a fraction of the computational cost. To demonstrate the performace of our method on a larger system that would be truly intractable to optimize with numerical gradient techniques, we optimized the $C_{60}@C_{60}H_{28}$ buckcatcher supramolecular host–guest complex.

We finally examine the role of the implicit nuclear coordinate dependence that arises from the partitioning of the electron density into effective atomic volumes (section 2.4.4) by comparing the magnitude of MBD forces with and without these implicit derivatives. We find that the Hirshfeld volume gradients contribute strongly to MBD forces and therefore negelecting them yields large relative errors and is a wholly unacceptable approximation, despite previous assertions to the contrary that have been made in the literature.[88,251]

*Tktatchenko *et al.* employ a Hirshfeld partitioning of the charge density to assign the parameters of the coupled quantum harmonic oscillators in MBD,[250] but Silvestrelli has recently shown that maximially localized Wannier functions offer a competitive alternative.[86]

2.1.1 Notation employed in this work

As the theory comprising the MBD model has evolved over the past few years, several notational changes have been required to accommodate the development of a more complete formalism to account for the various contributions to the long-range correlation energy in molecular systems and condensed-phase materials. In this section, we provide a current and self-contained review of the MBD model followed by a detailed derivation of the corresponding analytical nuclear gradients (forces). Our discussion most closely follows the notation employed in Refs. 88 and 87 To assist in the interpretation of these equations, we have also furnished a glossary of symbols utilized in this chapter as part of the accompanying Appendix A. For a more thorough discussion of the MBD model (including its approximations and physical interpretations), we refer the reader to the original works[80,88] as well as a recent review[87] on MBD interactions in molecules and condensed matter.

Throughout this chapter, all equations are given in Hartree atomic units ($\hbar = m_e = e = 1/4\pi\epsilon_0 = 1$) with tensor (vector and matrix) quantities denoted by bold typeface. In this regard, one particularly important bold/normal typeface distinction that will arise below is the difference between the 3×3 dipole polarizability tensor,

$$\boldsymbol{\alpha} = \begin{pmatrix} \alpha_{xx} & \alpha_{xy} & \alpha_{xz} \\ \alpha_{yx} & \alpha_{yy} & \alpha_{yz} \\ \alpha_{zx} & \alpha_{zy} & \alpha_{zz} \end{pmatrix}, \tag{2.1}$$

and the "isotropized" dipole polarizability, a scalar quantity obtained *via*

$$\alpha = \tfrac{1}{3}\mathrm{Tr}\big[\boldsymbol{\alpha}\big]. \tag{2.2}$$

The Cartesian components of tensor quantities are indicated by superscript Latin indices ijk, *i.e.*, T^{ij} is the $i^{\mathrm{th}}, j^{\mathrm{th}}$ component of the tensor $\mathbf{T}$. Likewise, Cartesian unit vectors are indicated by $\hat{\mathbf{e}}_i$. Atom indices are denoted by subscript Latin indices abc. The index p will be used as a dummy index for summation. The imaginary unit is indicated with blackboard bold typeface, $\mathbb{i}$, to distinguish it from the Cartesian component index i. Quantities that arise from the solution of the range-separated self-consistent screening (rsSCS) system of equations introduced by Ambrosetti *et al.*[88] will be denoted by an overline, *i.e.*, $X \to \overline{X}$. This range-separated form of the MBD model

has been termed MBD@rsSCS (which has also been denoted as MBD* elsewhere). For brevity we will refer to this model as simply MBD.

The MBD model requires keeping track of several different quantities that are naturally denoted with variants of the letter "R", so we highlight these quantities here for the benefit of the reader. Spatial position, such as the argument of the electron density, $\rho(\mathbf{r})$, is indicated by $\mathbf{r}$. The nuclear position of an atom a (or QHO mapped to that nucleus) is indicated by $\boldsymbol{\mathcal{R}}_a$. The internuclear vector is denoted $\mathbf{R}_{ab} = \boldsymbol{\mathcal{R}}_a - \boldsymbol{\mathcal{R}}_b$, such that the internuclear distance is given by $R_{ab} = \|\mathbf{R}_{ab}\|$. It follows that the i^{th} Cartesian component of this internuclear vector is R^i_{ab}. Finally, the effective van der Waals radius of an atom a is indicated by $\mathcal{R}^{\text{vdW}}_a$.

The dependence of the long-range MBD correlation energy, E_{MBD}, on the underlying nuclear positions, $\{\boldsymbol{\mathcal{R}}\} = \boldsymbol{\mathcal{R}}_a, \boldsymbol{\mathcal{R}}_b, \boldsymbol{\mathcal{R}}_c, \ldots$, will arise both *explicitly* through the presence of internuclear distance terms, R_{ab}, and *implicitly* through the presence of effective atomic volume terms, $V_a = V_a[\{\boldsymbol{\mathcal{R}}\}]$, obtained *via* the Hirshfeld partitioning[250] of $\rho(\mathbf{r})$ (see section 2.2.1.1). As such, these distinct types of dependence on nuclear positions will be clearly delineated throughout the review of the MBD model and the derivation of the corresponding MBD ionic forces below. For notational convenience, we will often use $\boldsymbol{\partial}_c$ rather than $\boldsymbol{\nabla}_{\boldsymbol{\mathcal{R}}_c}$ to indicate a derivative with respect to the nuclear position of atom c.

2.2 Model Specification

2.2.1 Review of the many-body dispersion (MBD) model

The MBD formalism is based on a one-to-one mapping of the N atoms comprising a molecular system of interest to a collection of N QHOs centered at the nuclear coordinates, each of which is characterized by a *bare* isotropic frequency-dependent dipole polarizability, $\alpha_a(\mathbb{i}\omega)$. Derived from the electron density, *i.e.*, $\alpha_a = \alpha_a[\rho(\mathbf{r})]$, these polarizabilities describe the unique local chemical environment surrounding a given atom by accounting for hybridization (coordination number), Pauli repulsion, and other non-trivial exchange-correlation effects (see section 2.2.1.1). To account for anisotropy in the local chemical environment as well as collective polarization/depolarization effects, the solution of a range-separated Dyson-like self-consistent screening (rsSCS) equation is used to generate *screened* isotropic frequency-dependent dipole polarizabilities for each QHO, $\overline{\alpha}_a$ (see section 2.2.1.2). The MBD model Hamiltonian is then constructed based on these *screened* frequency-dependent dipole polarizabilities. Diagonalization of this Hamiltonian couples this

collection of QHOs within the dipole approximation, yielding a set of interacting QHO eigenmodes with corresponding eigenfrequencies $\{\lambda\}$. The difference between the zero-point energy of these *interacting* QHO eigenmodes and that of the input *non-interacting* modes ($\{\overline{\omega}\}$), is then used to compute the long-range correlation energy at the MBD level of theory (see section 2.2.1.3), *i.e.*,

$$E_{\mathrm{MBD}} = \frac{1}{2}\sum_{p=1}^{3N}\sqrt{\lambda_p} - \frac{3}{2}\sum_{a=1}^{N}\overline{\omega}_a. \tag{2.3}$$

2.2.1.1 The MBD starting point: bare dipole polarizabilities

Mapping the N atoms comprising a molecular system of interest onto a collection of N QHOs is accomplished via a Hirshfeld partitioning[‖] of $\rho(\mathbf{r})$, the ground state electron density. Partitioning $\rho(\mathbf{r})$ into N spherical effective atoms enables assignment of the *bare* frequency-dependent dipole polarizabilities $\boldsymbol{\alpha}_a(\mathbb{i}\omega)$ used to characterize a given QHO. Within the MBD formalism, this assignment is given by the following 0/2-order Padé approximant applied to the scalar dipole polarizability:[253]

$$\alpha_a(\mathbb{i}\omega) = \frac{\alpha_a(0)}{1 - (\mathbb{i}\omega/\omega_a)^2}, \tag{2.4}$$

in which $\alpha_a(0)$ is the *static* dipole polarizability and ω_a is the characteristic excitation (resonant) frequency for atom a. The dependence of the *bare* frequency-dependent dipole polarizability in Eq. (2.4) on $\rho(\mathbf{r})$ is introduced by considering the direct proportionality between polarizability and atomic volume,[16] an approach that has been very successful in the Tkatchenko-Scheffler (TS) dispersion correction,[62] *i.e.*,

$$\alpha_a[\rho(\mathbf{r})](0) = \left(\frac{V_a[\rho(\mathbf{r})]}{V_a^{\mathrm{free}}}\right)\alpha_a^{\mathrm{free}}(0) = \left(\frac{\int \mathrm{d}\mathbf{r}\, w_a(\mathbf{r})\rho(\mathbf{r})r^3}{\int \mathrm{d}\mathbf{r}\, \rho_a^{\mathrm{free}}(\mathbf{r})r^3}\right)\alpha_a^{\mathrm{free}}(0), \tag{2.5}$$

in which V_a^{free} and α_a^{free} are the volume and *static* dipole polarizability of the *free* (isolated) atom in vacuo, respectively, obtained from either experiment or high-level quantum mechanical calculations. *Explicit* dependence on $\rho(\mathbf{r})$ resides in the *effective* "atom-in-a-molecule" volume, $V_a[\rho(\mathbf{r})]$, obtained *via* Hirshfeld partitioning[250] of $\rho(\mathbf{r})$ into atomic components, in which the

[‖] Although there are numerous schemes for partitioning the electron density, the Hirshfeld prescription[250] has been shown to result in atomic partitions that most closely resemble the densities of the corresponding free (isolated) atoms (by minimizing the Kullback-Leibler entropy deficiency of information theory).[252]

weight functions,

$$w_a(\mathbf{r}) = \rho_a^{\text{free}}(\mathbf{r}) / \sum_b \rho_b^{\text{free}}(\mathbf{r}), \tag{2.6}$$

are constructed from the set of spherical *free* atom densities, $\{\rho_b^{\text{free}}(\mathbf{r})\}$. At present, we compute the Hirshfeld partitioning and subsequently the MBD energy and forces as an *a posteriori* update to the solution of the non-linear Kohn-Sham equations, *i.e.*, without performing self-consistent updates to $\rho(\mathbf{r})$. Future work will address the impacts of computing the Hirshfeld partitioning iteratively[254] and using the MBD potential to update the Kohn-Sham density self-consistently. In this regard, recent work on the self-consistent application of the TS method indicates that self-consistency can have a surprisingly large impact on the charge densities, and corresponding work functions, of metallic surfaces,[114] so we anticipate that self-consistent MBD will be particularly interesting for the study of surfaces and polarizable low-dimensional systems. For later convenience, we rewrite Eqs. (2.4) and (2.5) to collect all quantities that *do not* implicitly depend on the nuclear coordinates through $V_a[\rho(\mathbf{r})]$ into the quantity $\Upsilon_a(\mathbb{i}\omega)$:

$$\begin{aligned} \alpha_a[\rho(\mathbf{r})](\mathbb{i}\omega) &= \left[\frac{1}{1-(\mathbb{i}\omega/\omega_a^{\text{free}})^2}\frac{\alpha_a^{\text{free}}(0)}{V_a^{\text{free}}}\right] V_a[\rho(\mathbf{r})] && (2.7)\\ &\equiv \Upsilon_a(\mathbb{i}\omega)\; V_a[\rho(\mathbf{r})]. && (2.8) \end{aligned}$$

2.2.1.2 Range-separated self-consistent screening (rsSCS)

Let $\mathbf{A}$ be a $3N \times 3N$ block diagonal matrix formed from the frequency-dependent polarizabilities in Eq. (2.7):**

$$\mathbf{A}(\mathbb{i}\omega) = \bigoplus_{b=1}^{N} \boldsymbol{\alpha}_b(\mathbb{i}\omega) = \text{diag}[\boldsymbol{\alpha}_1,\ \boldsymbol{\alpha}_2,\ \ldots,\ \boldsymbol{\alpha}_N]. \tag{2.9}$$

This quantity will be referred to as the *bare* system dipole polarizability tensor. For a given frequency, range-separated self-consistent screening (rsSCS) of $\mathbf{A}(\mathbb{i}\omega)$ is then accomplished by solving the following matrix equation[87,118] (see Appendix C for the detailed derivation of Eq. (2.11)):

$$\begin{aligned} \overline{\mathbf{A}} &= \mathbf{A} - \mathbf{A}\,\mathbf{T}_{\text{SR}}\,\overline{\mathbf{A}} && (2.10)\\ \Rightarrow \overline{\mathbf{A}} &= \left[\mathbf{A}^{-1} + \mathbf{T}_{\text{SR}}\right]^{-1}, && (2.11) \end{aligned}$$

**The dipole polarizability tensor $\boldsymbol{\alpha}_a$ for a given atom or QHO is formed by populating the diagonal elements $(\alpha_{xx}, \alpha_{yy}, \alpha_{zz})$ with the *isotropic* dipole polarizability in Eq. (2.7).

where $\mathbf{T}_{\mathrm{SR}}$ is the short-range dipole–dipole interaction tensor, defined below in Eq. (2.34) and section 2.2.1.4. The matrix $\overline{\mathbf{A}}$ is the (dense) *screened* non-local polarizability matrix, sometimes called the relay matrix.[‡‡]

Partial internal contraction over atomic sub-blocks of $\overline{\mathbf{A}}$ yields the screened and anisotropic *atomic* polarizability tensors (the corresponding *molecular* polarizability is obtained by total internal contraction), *i.e.*,

$$\overline{\boldsymbol{\alpha}}_a(\mathbb{i}\omega) = \sum_{b=1}^{N} \overline{\mathbf{A}}_{ab}(\mathbb{i}\omega). \tag{2.12}$$

The static "isotropized" screened polarizability scalars, $\overline{\alpha}_a(0)$, that appear in the MBD Hamiltonian in Eq. (2.17) and section 2.2.1.3 below are then calculated from $\overline{\boldsymbol{\alpha}}_a(0)$ *via*

$$\overline{\alpha}_a(0) = \frac{1}{3}\mathrm{Tr}\Big[\overline{\boldsymbol{\alpha}}_a(0)\Big] \tag{2.13}$$

as described above in Eq. (2.2). Note that Eqs. (2.11)-(2.12) can be solved at any imaginary frequency, $\mathbb{i}\omega$, so we do not require the Padé approximant given in Eq. (2.4) to bootstrap from $\overline{\alpha}_a(0)$ to $\overline{\alpha}_a(\mathbb{i}\omega)$. However, the relationship between $\overline{\omega}_a$ and $\overline{C}_{6,aa}$, given in Eq. (2.15), is one that is derived from the Padé approximant for the bare polarizability $\alpha(\mathbb{i}\omega)$.

In the non-retarded regime, the Casimir-Polder integral relates the effective $C_{6,ab}$ dispersion coefficient to the dipole polarizabilities of QHOs a and b *via* the following integral over imaginary frequencies:[21]

$$C_{6,ab} = \frac{3}{\pi}\int_0^\infty \mathrm{d}\omega\ \alpha_a(\mathbb{i}\omega)\alpha_b(\mathbb{i}\omega). \tag{2.14}$$

By solving Eqs. (2.11-2.12) on a grid of imaginary frequencies $\{\mathbb{i}y_p\}$, a set of screened effective C_6 coefficients, $\{\overline{C}_6\}$, can be determined by a Gauss-Legendre quadrature estimate of the integral in Eq. (2.14). The screened QHO characteristic excitation frequency, $\overline{\omega}_a$, is then calculated as

$$\overline{\omega}_a = \frac{4}{3}\frac{\overline{C}_{6,aa}}{[\overline{\alpha}_a(0)]^2} = \frac{4}{\pi}\sum_p g_p \left[\frac{\overline{\alpha}_a(\mathbb{i}y_p)}{\overline{\alpha}_a(0)}\right]^2, \tag{2.15}$$

where g_p and y_p are the quadrature weights and abscissae, respectively. Scaling of the usual Gauss-Legendre abscissae from $[-1,1]$ to the semi-infinite interval $[0,\infty)$ is discussed in the accompanying Appendix C.

[‡‡] At this point, it is very important to note a difference in the notation relative to Refs. 87 and 84: our matrix $\overline{\mathbf{A}}$ is equivalent to their $\overline{\mathbf{B}}$ or B, which was keeping with Thole's original notation[118] for the relay matrix.

2.2.1.3 The MBD model Hamiltonian

The central concept in the MBD model is the Hamiltonian for a set of N coupled dipoles that fluctuate within an isotropic harmonic potential $U(\mathbf{x}_a) = \frac{1}{2} m_a \omega_a^2 \mathbf{x}_a^2$, and acquire instantaneous dipole moments, $\mathbf{d}_a = q_a \mathbf{x}_a$, that are proportional to the displacement $\mathbf{x}_a$ from an equilibrium position and charge q_a on each oscillator. This Hamiltonian defines the so-called coupled fluctuating dipole model (CFDM),[30] and is given by:

$$\boldsymbol{\mathcal{H}}_{\mathrm{CFDM}} = -\sum_{a=1}^{N} \frac{\boldsymbol{\nabla}_{\mathbf{x}_a}^2}{2m_a} + \sum_{a=1}^{N} \frac{1}{2} m_a \omega_a^2 \mathbf{x}_a^2 + \sum_{a>b}^{N} \mathbf{d}_a^\dagger \mathbf{T}_{ab} \mathbf{d}_b, \tag{2.16}$$

where $\mathbf{T}_{ab}$ is the dipole–dipole interaction tensor that couples dipoles a and b.

In the range-separated MBD model,[88] $\mathbf{T}$ is replaced by a long-range screened interaction tensor, $\overline{\mathbf{T}}_{\mathrm{LR}}$ (as defined in section 2.2.1.4 and Eq. (2.36) below), and the fluctuating dipoles are mapped onto QHOs, with effective masses $m_a = \left(\overline{\alpha}_a(0)\, \overline{\omega}_a^2\right)^{-1}$ obtained from their respective static polarizabilities and excitation frequencies. The corresponding range-separated MBD model Hamiltonian is therefore:[88]

$$\boldsymbol{\mathcal{H}}_{\mathrm{MBD}} = -\sum_{a=1}^{N} \frac{\boldsymbol{\nabla}_{\boldsymbol{\mu}_a}^2}{2} + \frac{1}{2} \sum_{a=1}^{N} \overline{\omega}_a^2 \boldsymbol{\mu}_a^2 + \sum_{a>b}^{N} \overline{\omega}_a \overline{\omega}_b \sqrt{\overline{\alpha}_a(0) \overline{\alpha}_b(0)}\; \boldsymbol{\mu}_a^\dagger \overline{\mathbf{T}}_{ab}^{\mathrm{LR}} \boldsymbol{\mu}_b, \tag{2.17}$$

in which $\boldsymbol{\mu}_a = \sqrt{m_a}\, \boldsymbol{\xi}_a$ is the mass-weighted dipole moment[††] of QHO a that has been displaced by $\boldsymbol{\xi}_a$ from its equilibrium position. The first two terms in Eq. (2.17) represent the kinetic and potential energy of the individual oscillators, respectively, and the third term is the two-body coupling due to the long-range dipole–dipole interaction.

By considering the single-particle potential energy and dipole–dipole interaction terms in Eq. (2.17), we can construct the $3N \times 3N$ MBD interaction matrix, which is comprised of 3×3 subblocks describing the coupling of each pair of QHOs a and b:

$$\mathbf{C}_{ab}^{\mathrm{MBD}} = \delta_{ab} \overline{\omega}_a^2 + (1 - \delta_{ab}) \overline{\omega}_a \overline{\omega}_b \sqrt{\overline{\alpha}_a(0) \overline{\alpha}_b(0)}\; \overline{\mathbf{T}}_{ab}^{\mathrm{LR}}, \tag{2.18}$$

where δ_{ab} is the Kronecker delta of QHO indices.

The eigenvalues $\{\lambda_p\}$ obtained by diagonalizing $\mathbf{C}^{\mathrm{MBD}}$ correspond to the *interacting* (or

[††]Since each QHO is assigned a unit charge ($e = 1$), the dipole moment $\boldsymbol{\mu}$ is thereby equivalent to the displacement vector $\boldsymbol{\xi}$

"dressed") QHO modes, while $\overline{\omega}_a$ correspond to the modes of the *non-interacting* reference system of screened oscillators. The MBD correlation energy is then evaluated *via* Eq. (2.3) as the zero-point energetic difference between the interacting and non-interacting modes.

For periodic systems, we would replace all instances of the dipole–dipole interaction tensor by

$$\mathbf{T}_{ab} \to \mathbf{T}_{ab} + \sum_{b'} \mathbf{T}_{ab'} \tag{2.19}$$

where the sum over b' indicates a lattice sum over the periodic images of atom b. Since this is an additive modification of $\mathbf{T}$, it will not qualitatively modify the expressions for the analytical nuclear derivatives of the MBD energy. Hence, the derivation of the ionic forces presented herein (and the accompanying chemical applications) will focus on the case of a non-periodic (or isolated) systems. We note in passing here that the current implementation of the MBD energy and ionic forces in Quantum ESPRESSO (QE) is able to treat both periodic and non-periodic systems. In this regard, a chapter 3 and a forthcoming paper [255] will describe the details of the implementation and discuss the subtleties required to make the computation of well-converged MBD ionic forces efficient for periodic systems.

2.2.1.4 The range-separated dipole–dipole interaction

Prior to range-separation, the 3×3 sub-block $\mathbf{T}_{ab}$ of the dipole–dipole interaction tensor $\mathbf{T}$, which describes the coupling between atoms a and b, is defined as:

$$\mathbf{T}_{ab} = \boldsymbol{\nabla}_{\boldsymbol{\mathcal{R}}_a} \otimes \boldsymbol{\nabla}_{\boldsymbol{\mathcal{R}}_b} v_{ab}, \tag{2.20}$$

where v_{ab} is the frequency-dependent Coulomb interaction between two spherical Gaussian charge distributions. [256] This interaction arises due to the fact that the ground state of a (singly-occupied) QHO has a Gaussian charge density:

$$v_{ab}(R_{ab}, \mathbb{i}\omega) = \frac{\operatorname{erf}\left[\zeta_{ab}(\mathbb{i}\omega)\right]}{R_{ab}}, \tag{2.21}$$

where $\zeta_{ab}(\mathbb{i}\omega) \equiv R_{ab}/\Sigma_{ab}(\mathbb{i}\omega)$, $R_{ab} = \|\boldsymbol{\mathcal{R}}_a - \boldsymbol{\mathcal{R}}_b\|$, and

$$\Sigma_{ab}(\mathbb{i}\omega) = \sqrt{\sigma_a(\mathbb{i}\omega)^2 + \sigma_b(\mathbb{i}\omega)^2} \tag{2.22}$$

is the effective correlation length of the interaction potential defined by the widths of the QHO Gaussians, as defined directly below in Eq. (2.23). As such, the dependence of $\mathbf{T}$ on the frequency and (implicitly) on the nuclear coordinates both originate from $\Sigma_{ab}(\mathbb{i}\omega)$ (see also Eqs. (2.7)-(2.8)).

In terms of the bare dipole polarizability, the width of the QHO ground-state Gaussian charge density is given by:

$$\sigma_a(\mathbb{i}\omega) = \left[\tfrac{1}{3}\sqrt{\tfrac{2}{\pi}}\alpha_a(\mathbb{i}\omega)\right]^{1/3} \tag{2.23}$$

$$= \left[\tfrac{1}{3}\sqrt{\tfrac{2}{\pi}}\Upsilon_a(\mathbb{i}\omega)\right]^{1/3}[V_a]^{1/3}, \tag{2.24}$$

where $\alpha_a(\mathbb{i}\omega) = \frac{1}{3}\mathrm{Tr}\left[\boldsymbol{\alpha}_a\right]$ is the "isotropized" *bare* dipole polarizability and Eq. (2.8) was used to make the effective volume dependence more explicit.

The Cartesian components of the dipole–dipole interaction tensor (with QHO indices suppressed) are given by:

$$\mathbf{T}^{ij}(\mathbb{i}\omega) = \left[\mathrm{erf}[\zeta] - \frac{2\zeta}{\sqrt{\pi}}\exp\left[-\zeta^2\right]\right]\mathbf{T}^{ij}_{\mathrm{dip}} + \frac{4}{\sqrt{\pi}}\frac{R^iR^j}{R^5}\zeta^3\exp\left[-\zeta^2\right], \tag{2.25}$$

where $R^i = \mathbf{R}_{ab}\cdot\hat{\mathbf{e}}_i$ is the i^{th} Cartesian component of $\mathbf{R}_{ab}$, and $\mathbf{T}_{\mathrm{dip}}$ is the frequency-*independent* interaction between two point dipoles:

$$\mathrm{T}^{ij}_{ab,\,\mathrm{dip}} = \frac{-3R^i_{ab}R^j_{ab} + R^2_{ab}\delta_{ij}}{R^5_{ab}}, \tag{2.26}$$

with δ_{ij} indicating the Kronecker delta of Cartesian indices.

The range-separation of the dipole–dipole interaction tensor is accomplished by using a Fermi-type damping function[49,56,62]

$$f(Z_{ab}) = \left[1 + \exp\left[-Z_{ab}\right]\right]^{-1}, \tag{2.27}$$

which depends on Z_{ab}, the ratio between the inter-oscillator separation, and S_{ab}, the scaled sum of the effective van der Waals radii, $\mathcal{R}^{\mathrm{vdW}}_a$ and $\mathcal{R}^{\mathrm{vdW}}_b$:

$$Z_{ab} \equiv 6\left[\frac{R_{ab}}{S_{ab}} - 1\right] \tag{2.28}$$

$$S_{ab} \equiv \beta\left[\mathcal{R}^{\mathrm{vdW}}_a + \mathcal{R}^{\mathrm{vdW}}_b\right]. \tag{2.29}$$

Here, the parameter β is fit once for a given exchange-correlation functional by minimizing energy deviations with respect to highly accurate reference data.[88] The short- and long-range components of the dipole–dipole interaction tensor are then separated according to:

$$\mathbf{T}_{\mathrm{SR}} = [1 - f(Z)]\,\mathbf{T} \tag{2.30}$$

$$\mathbf{T}_{\mathrm{LR}} = f(Z)\mathbf{T} \tag{2.31}$$

However, at long-range, the frequency-dependence in $\mathbf{T}$ dies off quickly, so when evaluating the MBD Hamiltonian we replace Eq. (2.31) with the approximation

$$\mathbf{T}_{\mathrm{LR}} \simeq f(Z)\mathbf{T}_{\mathrm{dip}} \tag{2.32}$$

which is equivalent to taking $\mathrm{erf}\,[\zeta] \simeq 1$ and $\exp[-\zeta^2] \simeq 0$. This has the added benefit of improved computational efficiency since special functions such as the error function and exponential are relatively costly to compute. As shown in Figure 3.2 in Chapter 3, these approximations hold true to within machine precision for $\zeta > 6$, and thus in practice by the time $f(Z)$ has obtained a substantial value, the frequency dependence in $\mathbf{T}$ has vanished, thereby justifying Eq. (2.32). Likewise, for $Z > 35$, the Fermi damping function equals one to within machine precision. To avoid numerical issues of underflow, our implementation of the short- and long-range dipole–dipole interaction tensors checks Z and ζ, and where appropriate replaces $\mathbf{T}$ with $\mathbf{T}_{\mathrm{dip}}$ or $f(Z)$ with one.

The rsSCS procedure described in section 2.2.1.2 adds a further subtlety in that it modifies the effective van der Waals radii in the definition of the S_{ab} and Z_{ab} quantities above (see Refs. 80,87 for a more detailed discussion of these definitions). For the short-range interaction tensor (*i.e.*, the tensor used in the rsSCS procedure) the damping function utilizes effective van der Waals (vdW) radii calculated at the Tkatchenko-Scheffler (TS) level:[62]

$$\mathcal{R}_a^{\mathrm{vdW,\,TS}} \equiv \left(\frac{V_a}{V_a^{\mathrm{free}}}\right)^{1/3} \mathcal{R}_a^{\mathrm{vdW,\,free}} \tag{2.33}$$

where $\mathcal{R}_a^{\mathrm{vdW,\,free}}$ is the free-atom vdW radius defined in Ref. 62 using an electron density contour, not the Bondi[257] radius that corresponds to the "atom-in-a-molecule" analog of this quantity. To indicate that the TS-level effective vdW radii are being used, the argument of the damping

function for the short-range interaction tensor will be denoted with Z^{TS}:

$$\mathbf{T}_{\mathrm{SR}} = \left[1 - f\left(Z^{\mathrm{TS}}\right)\right]\mathbf{T}. \tag{2.34}$$

For the long-range dipole–dipole interaction tensor used in the MBD Hamiltonian in Eq. (2.17), the damping function utilizes the self-consistently screened effective van der Waals radii:[80]

$$\overline{\mathcal{R}}_a^{\mathrm{vdW}} \equiv \left(\frac{\overline{\alpha}_a(0)}{\alpha_a^{\mathrm{free}}(0)}\right)^{1/3} \mathcal{R}_a^{\mathrm{vdW,\,free}}, \tag{2.35}$$

wherein the ratio $\overline{\alpha}(0)/\alpha^{\mathrm{free}}(0)$ takes the place of V/V^{free} thereby exploiting the proportionality between polarizability and volume.[16,87] To indicate that the screened effective vdW radii are being used, the argument of the damping function for the long-range interaction tensor will be denoted with $\overline{Z}$:

$$\overline{\mathbf{T}}_{\mathrm{LR}} = f\left(\overline{Z}\right)\mathbf{T}_{\mathrm{dip}}. \tag{2.36}$$

This dependence on $\overline{Z}$ is why we use an overline on $\mathbf{T}_{\mathrm{LR}}$ above, and in Eqs. (2.17,2.18).

2.2.2 Derivation of the MBD ionic forces

With the above definitions in hand, we are now ready to proceed with the derivation of the analytical derivatives of the MBD correlation energy with respect to the nuclear (or ionic) position $\boldsymbol{\mathcal{R}}_c$ of an arbitrary atom c.[†] These MBD forces are added to the DFT-based forces as calculated by the Hellmann–Feynman theorem. As mentioned above in section 2.1.1, two distinct types of nuclear coordinate dependence will arise: *explicit* dependence through $\mathbf{R}_{ab} = \boldsymbol{\mathcal{R}}_a - \boldsymbol{\mathcal{R}}_b$ and *implicit* dependence through $V[\{\boldsymbol{\mathcal{R}}\}]$ (as moving a neighboring atom c will slightly alter the effective volume assigned to atom a). Future work will address the effects of the MBD contribution to the external potential when applied self-consistently, which will ultimately impact the electron density. Our current work neglects these effects, and computes the MBD corrections *non*-self-consistently.

Having carefully separated out the implicit dependence on V in the relevant quantities above,

[†]It is very important to note that in this work we have only computed the Hellmann-Feynman derivative of the total DFT+MBD energy. Specifically, when the MBD energy is computed non-self-consistently (*i.e.* as an *a posteriori* correction), there is an additional force component that results from the gradient of the molecular orbital coefficients (*i.e.*, the non-self-consistency correction).[258–260] This term can be treated by directly computing the "response" of the density by solving the coupled-perturbed-Kohn-Sham equations. Alternatively, this term exactly vanishes if MBD is computed self-consistently, which is our recommended approach.

the derivation proceeds largely by brute force application of the chain and product rules. The derivative of the MBD correlation energy given in Eq. (2.1.1) is governed by:

$$\boldsymbol{\partial}_c E_{\mathrm{MBD}} = \frac{1}{2}\sum_{p=1}^{3N} \boldsymbol{\partial}_c \sqrt{\lambda_p} - \frac{3}{2}\sum_{a=1}^{N} \boldsymbol{\partial}_c \overline{\omega}_a, \tag{2.37}$$

hence requiring derivatives of the screened excitation frequencies as well as the eigenvalues of the matrix $\mathbf{C}^{\mathrm{MBD}}$.

Since $\mathbf{C}^{\mathrm{MBD}}$ is real and symmetric, it has $3N$ orthogonal eigenvectors. We therefore do not concern ourselves with repeated eigenvalues (see Appendix C for discussion) and take derivatives of λ_p as:[261]

$$\boldsymbol{\partial}_c \sqrt{\lambda_p} = \frac{\boldsymbol{\partial}_c \lambda_p}{2\sqrt{\lambda_p}} \tag{2.38}$$

$$\boldsymbol{\partial}_c \lambda_p = \left[\boldsymbol{\mathcal{X}}^{\mathsf{T}} \boldsymbol{\partial}_c \mathbf{C}^{\mathrm{MBD}} \boldsymbol{\mathcal{X}}\right]_{pp} \tag{2.39}$$

$$\Rightarrow \sum_{p=1}^{N} \boldsymbol{\partial}_c \sqrt{\lambda_p} = \frac{1}{2}\mathrm{Tr}\left[\boldsymbol{\Lambda}^{-1/2} \boldsymbol{\mathcal{X}}^{\mathsf{T}} \boldsymbol{\partial}_c \mathbf{C}^{\mathrm{MBD}} \boldsymbol{\mathcal{X}}\right]. \tag{2.40}$$

where $\boldsymbol{\mathcal{X}}$ is the matrix of eigenvectors of $\mathbf{C}^{\mathrm{MBD}}$ and $\boldsymbol{\Lambda} = \mathrm{diag}[\lambda_p]$ is the diagonal matrix of eigenvalues. To evaluate this last line we require the appropriate derivative of the ab block of $\mathbf{C}^{\mathrm{MBD}}$, *i.e.*,

$$\begin{aligned}
\boldsymbol{\partial}_c \mathbf{C}^{\mathrm{MBD}}_{ab} = {} & 2\delta_{ab}\overline{\omega}_a \boldsymbol{\partial}_c \overline{\omega}_a \\
& + (1-\delta_{ab})\left[\overline{\omega}_a \boldsymbol{\partial}_c \overline{\omega}_b + \overline{\omega}_b \boldsymbol{\partial}_c \overline{\omega}_a\right] \sqrt{\overline{\alpha}_a(0)\overline{\alpha}_b(0)}\ \overline{\mathbf{T}}^{\mathrm{LR}}_{ab} \\
& + (1-\delta_{ab})\,\overline{\omega}_a\overline{\omega}_b \frac{\left[\overline{\alpha}_a(0)\,\boldsymbol{\partial}_c\overline{\alpha}_b(0) + \overline{\alpha}_b(0)\,\boldsymbol{\partial}_c\overline{\alpha}_a(0)\right]}{2\sqrt{\overline{\alpha}_a(0)\overline{\alpha}_b(0)}}\ \overline{\mathbf{T}}^{\mathrm{LR}}_{ab} \\
& + (1-\delta_{ab})\,\overline{\omega}_a\overline{\omega}_b \sqrt{\overline{\alpha}_a(0)\overline{\alpha}_b(0)}\ \boldsymbol{\partial}_c \overline{\mathbf{T}}^{\mathrm{LR}}_{ab}.
\end{aligned} \tag{2.41}$$

To proceed any further we now need the derivatives of $\overline{\omega}$, $\overline{\alpha}$, and $\overline{\mathbf{T}}_{\mathrm{LR}}$. From Eq. (2.15), we find that the derivative of the screened excitation frequency, $\overline{\omega}$, requires us to evaluate derivatives of $\overline{\alpha}(\mathbb{i}\omega)$ (with $\overline{\alpha}(0)$ as a specific case) as follows:

$$\boldsymbol{\partial}_c \overline{\omega}_a = \frac{8}{\pi}\sum_{p=1}^{n} g_p \left[\frac{\overline{\alpha}_a(\mathbb{i}y_p)\boldsymbol{\partial}_c\overline{\alpha}_a(\mathbb{i}y_p)}{[\overline{\alpha}_a(0)]^2} - \frac{[\overline{\alpha}_a(\mathbb{i}y_p)]^2\,\boldsymbol{\partial}_c\overline{\alpha}_a(0)}{[\overline{\alpha}_a(0)]^3}\right]. \tag{2.42}$$

The derivative of the screened polarizability, $\overline{\alpha}$, is calculated from the "isotropized" partial

contraction of $\overline{\mathbf{A}}$ (with the frequency dependence suppressed):

$$\boldsymbol{\partial}_c \overline{\alpha}_a = \frac{1}{3}\mathrm{Tr}\left[\sum_{b=1}^{N} \left[\boldsymbol{\partial}_c \overline{\mathbf{A}}\right]_{ab}\right]. \tag{2.43}$$

Using Eq. (2.11) and expanding the derivative of the inverse of a non-singular matrix, we have

$$\boldsymbol{\partial}_c \overline{\mathbf{A}} = -\overline{\mathbf{A}}\left[-\mathbf{A}^{-1}\left[\boldsymbol{\partial}_c \mathbf{A}\right]\mathbf{A}^{-1} + \boldsymbol{\partial}_c \mathbf{T}_{\mathrm{SR}}\right]\overline{\mathbf{A}}. \tag{2.44}$$

Using Eqs. (2.8) and (2.9), we compute $\boldsymbol{\partial}_c \mathbf{A}$ as:

$$\boldsymbol{\partial}_c \mathbf{A} = \bigoplus_{a=1}^{N} \mathrm{diag}\left[\Upsilon_a \, \boldsymbol{\partial}_c V_a\right]. \tag{2.45}$$

In Eq. (2.45) we have terminated our chain-rule with $\boldsymbol{\partial}_c V_a$, which has remaining *implicit* dependence on nuclear coordinates. We regard $\boldsymbol{\partial}_c V_a$ as one of our three fundamental derivatives since the Hirshfeld partitioning is typically computed separately from the rest of the MBD algorithm. Discussion of how to compute $\boldsymbol{\partial}_c V_a$ may be found in Appendix C.

In considering the derivatives of the dipole–dipole interaction tensors we will encounter both implicit and explicit nuclear position dependence through ζ_{ab}. The derivatives of $\mathbf{T}_{\mathrm{SR}}$ and $\overline{\mathbf{T}}_{\mathrm{LR}}$ are fairly complicated, so it will help to consider first the damping function in isolation. Here,

$$\begin{aligned}
\boldsymbol{\partial}_c f(R_{ab}) &= \frac{\exp\left[-Z_{ab}\right]}{\left[1+\exp\left[-Z_{ab}\right]\right]^2}\,\boldsymbol{\partial}_c Z_{ab} && (2.46)\\
\boldsymbol{\partial}_c Z_{ab} &= 6\left[\frac{\boldsymbol{\partial}_c R_{ab}}{S_{ab}} - \frac{R_{ab}\boldsymbol{\partial}_c S_{ab}}{S_{ab}^2}\right] && (2.47)\\
\boldsymbol{\partial}_c S_{ab} &= \beta\left[\boldsymbol{\partial}_c \mathcal{R}_a^{\mathrm{vdW}} + \boldsymbol{\partial}_c \mathcal{R}_b^{\mathrm{vdW}}\right], && (2.48)
\end{aligned}$$

where $\boldsymbol{\partial}_c R_{ab}$ is calculated as

$$\boldsymbol{\partial}_c R_{ab} = \boldsymbol{\nabla}_{\mathcal{R}_c}\|\mathbf{R}_{ab}\| = (\delta_{ac} - \delta_{bc})\,\frac{\mathbf{R}_{ab}}{\|\mathbf{R}_{ab}\|}, \tag{2.49}$$

and the effective van der Waals radii have only implicit nuclear coordinate dependence. For $\mathbf{T}_{\mathrm{SR}}$ we require the derivative of the TS effective vdW radii:

$$\boldsymbol{\partial}_c \mathcal{R}_a^{\mathrm{vdW,\,TS}} = \frac{\mathcal{R}_a^{\mathrm{vdW,\,free}}}{\left[V_a^{\mathrm{free}}\right]^{1/3}} \frac{\boldsymbol{\partial}_c V_a}{3\left[V_a\right]^{2/3}}, \tag{2.50}$$

while for $\overline{\mathbf{T}}_{\mathrm{LR}}$, we require the derivative of the screened effective vdW radii:

$$\boldsymbol{\partial}_c \overline{\mathcal{R}}_a^{\mathrm{vdW}} = \frac{\mathcal{R}_a^{\mathrm{vdW,\,free}}}{\left[\alpha_a^{\mathrm{free}}(0)\right]^{1/3}} \frac{\boldsymbol{\partial}_c \overline{\alpha}_a(0)}{3\left[\overline{\alpha}_a(0)\right]^{2/3}}, \tag{2.51}$$

which was evaluated using Eqs. (2.43)-(2.45).

In the following we suppress the a, b, c atom indices where possible so that the Cartesian indices i, j are highlighted. First we consider the derivative of $\mathbf{T}_{\mathrm{dip}}$, which is given by:

$$\boldsymbol{\partial} \mathrm{T}_{\mathrm{dip}}^{ij} = -3\left[\frac{\delta_{ij}}{R^4}\boldsymbol{\partial} R + \frac{R^j \boldsymbol{\partial} R^i + R^i \boldsymbol{\partial} R^j}{R^5} - \frac{5R^i R^j}{R^6}\boldsymbol{\partial} R\right], \tag{2.52}$$

where $\boldsymbol{\partial} R^i$ is evaluated as:

$$\boldsymbol{\partial}_c R_{ab}^i = \boldsymbol{\nabla}_{\boldsymbol{\mathcal{R}}_c}\left((\boldsymbol{\mathcal{R}}_a - \boldsymbol{\mathcal{R}}_b)\cdot \hat{\mathbf{e}}_i\right) = (\delta_{ac} - \delta_{bc})\hat{\mathbf{e}}_i. \tag{2.53}$$

Since the long-range dipole–dipole interaction tensor is approximated with the frequency-independent $\mathbf{T}_{\mathrm{dip}}$ (thereby eliminating ζ), Eqs. (2.46)-(2.51) and (2.52) provide us with all of the quantities needed to evaluate $\boldsymbol{\partial}_c \overline{\mathbf{T}}_{\mathrm{LR}}$ as:

$$\boldsymbol{\partial}_c \overline{\mathrm{T}}_{ab,\,\mathrm{LR}}^{ij} = \mathrm{T}_{ab,\,\mathrm{dip}}^{ij}\,\boldsymbol{\partial}_c f\left(\overline{Z}_{ab}\right) + f\left(\overline{Z}_{ab}\right)\boldsymbol{\partial}_c \mathrm{T}_{ab,\,\mathrm{dip}}^{ij}. \tag{2.54}$$

The derivative of $\mathbf{T}_{\mathrm{SR}}$ is more complex since $\mathbf{T}$ depends on ζ:

$$\boldsymbol{\partial}_c \mathrm{T}_{ab,\,\mathrm{SR}}^{ij} = -\mathrm{T}_{ab}^{ij}\,\boldsymbol{\partial}_c f\left(Z_{ab}^{\mathrm{TS}}\right) + \left[1 - f\left(Z_{ab}^{\mathrm{TS}}\right)\right]\boldsymbol{\partial}_c \mathrm{T}_{ab}^{ij}, \tag{2.55}$$

in which the derivative of T^{ij} is given below (see Appendix C for a detailed derivation):

$$\begin{aligned}\boldsymbol{\partial}\mathrm{T}^{ij} &= -3\left[\mathrm{erf}\left[\zeta\right] - \frac{h(\zeta)}{2\zeta}\right]\boldsymbol{\partial}\mathrm{T}^{ij}_{\mathrm{dip}} + \zeta\, h(\zeta)\left[-\frac{1}{3}\boldsymbol{\partial}\mathrm{T}^{ij}_{\mathrm{dip}} - \frac{\delta_{ij}}{R^4}\boldsymbol{\partial}R\right] \\ &\quad + \left[\mathrm{T}^{ij}_{\mathrm{dip}} + \frac{R^i R^j}{R^5}\left[3 - 2\zeta^2\right]\right] h(\zeta)\,\boldsymbol{\partial}\zeta,\end{aligned} \tag{2.56}$$

wherein we have defined the following function for compactness,

$$h(\zeta_{ab}) \equiv \frac{4\zeta_{ab}^2}{\sqrt{\pi}}\exp[-\zeta_{ab}^2]. \tag{2.57}$$

The derivative of ζ_{ab} is given by (with QHO indices restored to express $\boldsymbol{\partial}_c\Sigma_{ab}$ from Eq. (2.22)):

$$\boldsymbol{\partial}_c\zeta_{ab} = \frac{\zeta_{ab}}{R_{ab}}\boldsymbol{\partial}_c R_{ab} - \frac{\zeta_{ab}^3\left[\sigma_a\boldsymbol{\partial}_c\sigma_a + \sigma_b\boldsymbol{\partial}_c\sigma_b\right]}{R_{ab}^2}, \tag{2.58}$$

where $\boldsymbol{\partial}_c\sigma_a$ is computed from Eq. (2.24) as

$$\boldsymbol{\partial}_c\sigma_a = \left[\frac{1}{3}\sqrt{\frac{2}{\pi}}\Upsilon_a\right]^{1/3}\frac{\boldsymbol{\partial}_c V_a}{3\left[V_a\right]^{2/3}}. \tag{2.59}$$

We have now reduced the analytical nuclear derivative of the MBD correlation energy to quantities that depend on three fundamental derivatives: $\boldsymbol{\partial}_c R_{ab}$, $\boldsymbol{\partial}_c R^i_{ab}$ and $\boldsymbol{\partial}_c V_a$. The expressions for $\boldsymbol{\partial}_c R_{ab}$ and $\boldsymbol{\partial}_c R^i_{ab}$ have been given above in Eqs. (2.49, 2.53), and are straightforward to implement. The computation of $\boldsymbol{\partial}_c V_a$ is outlined briefly in Appendix C.

2.3 Computational Details

2.3.1 Calculations in Quantum ESPRESSO

We have implemented the MBD energies and analytical nuclear gradients (forces) in a development version of Quantum ESPRESSO v5.1rc2 (QE).[262] Chapter 3 and a forthcoming publication will discuss the details of our implementation, including the parallelization and algorithmic strategies required to make the method efficient for treating condensed-phase systems.[255] All calculations were performed with the Perdew,

Burke, and Ernzerhof (PBE) exchange-correlation functional,[182,183] and Hamann-Schlueter-Chiang-Vanderbilt (HSCV) norm-conserving pseudopotentials[263–265] obtained from the FPMD pseudopotential repository[266] (and converted to UPF format using a modified version of QSO2UPF V1.2[267]). As a point of completeness, it should be noted that, presently, the Hirshfeld partitioning in QE has only been implemented for norm-conserving pseudopotentials, and thus the MBD method cannot be used with ultrasoft pseudopotentials or projector-augmented wave methods (implementing the charge density partioning for these methods would require careful treatment of both the free atom reference volumes and compensation for the augmentation charges). All geometry optimizations were performed using the quasi-Newton Broyden-Fletcher-Goldfarb-Shanno (BFGS) algorithm,[268–271] with default parameters.

Cartesian coordinate geometry opmizations were performed in the PWSCF module in large simple cubic unit cells. Table 2.1 gives details of the convergence tolerances, wavefunction kinetic energy cutoffs (E_{cut}), and unit cell sizes used for each system. Since QE uses Rydberg energy units (1 Ry = $\frac{1}{2}$ $\mathrm{E_h}$), we report the tolerances in these units. All QE calculations were run Γ point only using a charge density cutoff of $4 \times \mathrm{E_{cut}}$. PBE+MBD@rsSCS jobs used 20 quadrature points for the Casimir-Polder integration. To ensure a fair comparison with our implementation of the MBD model, all TS calculations were performed as *a posteriori* corrections to the solution of the non-linear Kohn-Sham equations, *i.e.* we turned off the self-consistent density updates from TS. In Figure 2.1 we present the results of convergence testing with respect to the kinentic energy cutoff in the planewave basis set expansion, showing that the total energy per atom was converged to better than 0.3 meV/atom for each system.

2.3.2 Calculations in Orca

For comparison with the D3(BJ) dispersion correction of Grimme *et al.*[66,77] we also optimized structures using Orca v3.03.[244] Redundant internal coordinate geometry optimizations were performed with the PBE functional[182,183] with the atom-pairwise

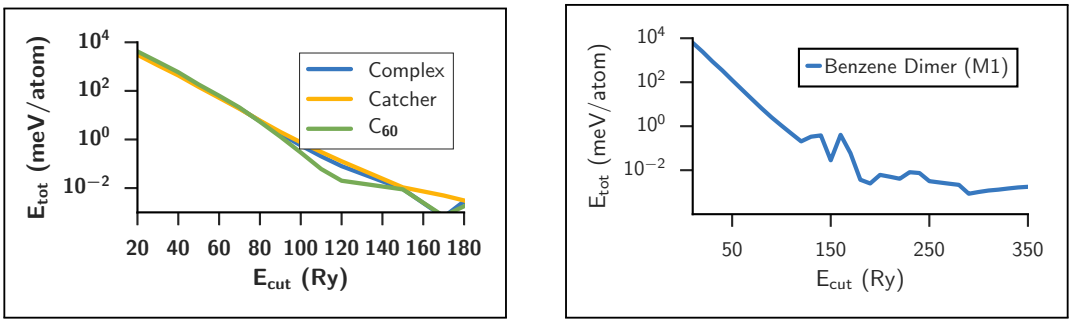

Figure 2.1: Convergence of the total energy per atom with respect to kinetic energy cutoff (E_{cut}) of the planewave basis expansion for **Top:** simulations of the C_{60} catcher complex, **Bottom:** the benzene dimer (M1 configuration).

Table 2.1: Convergance tolerances and unit cell sizes used in PWSCF geometry optimizations, reported in Rydberg atomic units ($1\ \mathrm{Ry} = \frac{1}{2}\ \mathrm{E_h}$).

	Benze Dimer	Peptides	C_{60} Catcher
E_{scf} (Ry)	10^{-8}	10^{-8}	10^{-8}
E_{cut} (Ry)	400	145	110
E_{tot} (Ry)	10^{-8}	5×10^{-7}	5×10^{-7}
F_{tot} (Ry/a_0)	10^{-4}	5×10^{-4}	5×10^{-4},
Cell Size (a_0)	30	30	50
Grid Spacing (Å)	0.04	0.07	0.12

version of the D3 dispersion correction of Grimme *et al.*,[66] using Becke-Johnson damping.[77] ORCA v3.03 implements D3 in the DFTD3 v2.1R6 software, which does not contain analytical gradients of the three-body term, so only atom-pairwise D3 was considered. The geometric counterpoise correction (gCP) of Kruse *et al.* was employed in all ORCA calculations.[272] We employed the Ahlrichs def2-TZVP basis set[239] coupled with an auxiliary Ahlrichs TZVP basis set[273,274] for the RI-J approximation.[275–277] All calculations used the G4 final ingegration grid. All calculations used 'tight' SCF tolerances; calculations on the benzene dimer and C_{60} catcher used 'tight' optimization tolerances, while those of the peptides used default optimization tolerances. Table 2.2 lists the tolerances corresponding to these two settings.

Table 2.2: Convergance tolerances used in ORCA geometry optimizations, reported in Hartree atomic units.

	Benze Dimer	Peptides	C_{60} Catcher
E_{scf} (E_h)	10^{-8}	10^{-8}	10^{-8}
E_{tot} (E_h)	10^{-6}	5×10^{-6}	10^{-6}
F_{Max} (E_h/a_0)	10^{-4}	3×10^{-4}	10^{-4}
F_{RMS} (E_h/a_0)	3×10^{-5}	10^{-4}	3×10^{-5}
Max Disp. (a_0)	10^{-3}	4×10^{-3}	10^{-3}
RMS Disp. (a_0)	6×10^{-4}	2×10^{-3}	6×10^{-4}

2.4 Results and Discussion

To verify our implementation of the MBD energy in QE, we compared against the implementation of the MBD@rsSCS model in the FHI-aims code[278,279] by computing the MBD energy of a single water molecule in a $(10\ a_0)^3$ simple cubic unit cell. We find agreement with the FHI-aims MBD code to within 10^{-11} E_h. These initial implementation tests used a large kinetic energy cutoff ($E_{cut} = 400$ Ry or greater) for the planewave basis set expansion as this cutoff directly corresponds to the density of grid points employed to describe $\rho(\mathbf{r})$, thereby defining the accuracy of the Hirshfeld partitioning. We next verified the analytical nuclear gradients by computing numerical derivatives *via* the centered difference formula for a strained conformation of the same water molecule. We find agreement between our analytical forces and the numerical derivatives to within 10^{-4} E_h/a_0, which is the level of accuracy that we expect for error propagation of finite differences of the Hirshfeld effective volumes given the finite spacing between the grid points describing $\rho(\mathbf{r})$. We emphasize that 10^{-4} E_h/a_0 is the approximate error threshold of the centered difference numerical derivatives, not our analytical treatment.

To demonstrate the performance of this implementation of analytical MBD nuclear gradients, we performed geometry optimizations on representative systems for intermolecular interactions (benzene dimer), intramolecular interactions (polypeptide secondary structure), and supramolecular interactions (C_{60}@$C_{60}H_{28}$ buckycatcher host-guest complex). We subsequently examined the importance of the implicit nuclear coordinate dependence that arises from the Hirshfeld effective volume gradient $\boldsymbol{\partial V}$ for the

computation of the MBD forces.

2.4.1 Intermolecular interactions: stationary points on the benzene dimer potential energy surface

As the prototypical example of the $\pi - \pi$ interaction, there have been a large number of theoretical studies on the benzene dimer, using very high-level wavefunction theory methods.[95,280–300] Since the intermolecular attraction between the benzene dimer arises primarily from a balance between dispersion interactions and quadrupole-quadrupole interactions (depending on the intermolecular binding motif), the interaction energy is quite small ($\sim 2 - 3$ kcal/mol) and the potential energy surface (PES) is very flat. Consequently, resolving the stationary points of this PES is quite challenging for both theory and experiment. The prediction of the interaction energy in the benzene dimer represents a stringent test of the ability of a given electronic structure theory method to capture and accurately describe non-bonded *intermolecular* interactions. Historically, three conformers of the dimer have received the most attention, namely the 'sandwich,' 'parallel-displaced,' and 'T-shaped' structures. Using the high-level benchmark interaction energy calculations as a guide, several studies have used a variety of more approximate methods to examine the PES more broadly.[291,293,298,300] By scanning the PES of the benzene dimer with DFT-based symmetry adapted perturbation theory (DFT-SAPT), Podeszwa *et al.*[291] identified 10 stationary points, *i.e.*, either minima (M) or saddle points (S) of the interaction energy (see Figure 2.2). Most wavefunction studies of the benzene dimer PES have used a fixed monomer geometry, assuming that the weak interactions will produce very little relaxation of the rigid monomer.[288] Using the highly accurate *fixed* benzene monomer geometry of Gauss and Stanton,[286] Bludský *et al.*[95] performed counterpoise-corrected geometry optimizations of these 10 configurations at the PBE/CCSD(T) level of theory, with an aug-cc-pVDZ basis set. The resulting geometries are among the largest molecular dimers to be optimized with a CCSD(T) correction to date and represent the most accurate available structures for the dimer of this classic

aromatic system.

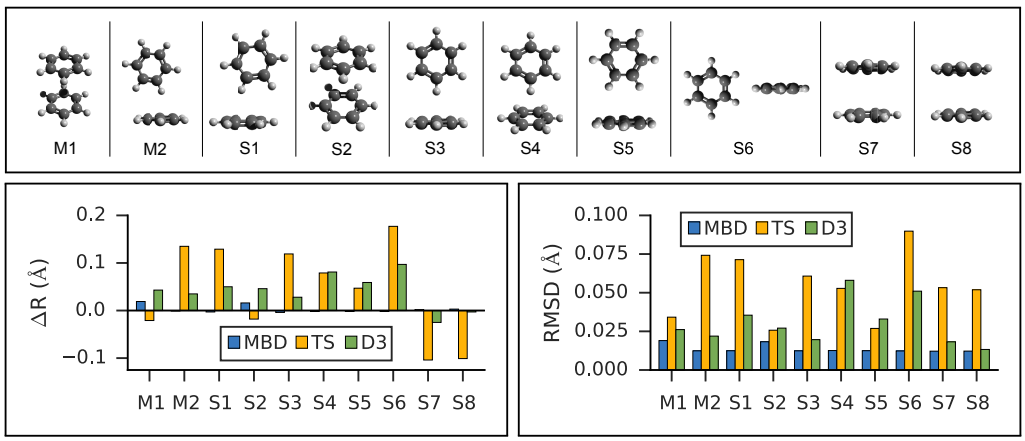

Figure 2.2: Top: Graphical depictions of the 10 configurations that correspond to stationary points on the benzene dimer PES, following the nomenclature of Podeszwa *et al.*[291] (Mn = minima; Sn = saddle points). **Left:** Change in inter-monomer distance R relative to the PBE/CCSD(T) reference for geometries optimized with PBE+vdW methods: MBD (shown in blue), TS (shown in yellow) and D3 (shown in green). PBE+MBD consistently predicts the correct inter-monomer distance. For the stacked configurations (M1, S2, S7, and S8) PBE+TS shortens the inter-monomer distance, while for T-shaped configurations (M2, S1, S3, S4, S5, and S6) the inter-monomer distance is elongated. For all configurations except the stacked S7 and S8 structures PBE+D3 predicts too long an inter-monomer distance. **Right:** Root-mean-square-deviations (RMSD) in Å between the PBE+vdW and PBE/CCSD(T)[291] optimized geometries of these 10 benzene dimer configurations. The RMSD between the PBE+MBD and reference PBE/CCSD(T) geometries (shown in blue) are uniformly small and consistent across all minima and saddle points on the benzene dimer PES. For several Mn and Sn configurations, the PBE+D3 optimized geometries (shown in green) agree quite well with the PBE/CCSD(T) reference, while the PBE+TS optimized geometries (shown in yellow) have more significant deviations.

As a first application of the MBD analytical nuclear gradients derived and implemented in this chapter, we performed geometry optimizations on these 10 benzene dimer configurations at the PBE+MBD, PBE+TS, and PBE+D3 levels of theory. All of the geometry optimizations performed herein minimized the force components on all atomic degrees of freedom according to the thresholds and convergence criteria specified in section 2.3 (*i.e.*, frozen benzene monomers were not employed in these geometry optimizations). The root-mean-square-deviations (RMSD in Å) between the PBE+MBD, PBE+TS, and PBE+D3 optimized geometries with respect to the reference PBE/CCSD(T) results are depicted in Figure 2.2.

From this figure, it is clear that the PBE+MBD method, with a mean RMSD value of 0.01 Å (and a vanishingly small standard deviation of 3×10^{-4} Å) with respect to the

reference PBE/CCSD(T) results, was able to provide uniformly accurate predictions for the geometries of all of the benzene dimer configurations considered. These findings are encouraging and consistent with the fact that the PBE+MBD method yields significantly improved binding energies for the benzene dimer as well as a more accurate quantitative description of the fractional anisotropy in the static dipole polarizability of the benzene monomer.[87] This is also consistent with the finding of von Lilienfeld and Tkatchenko that the three-body ATM term contributes $\sim 25\%$ of the binding energy of the benzene dimer in the parallel displaced configuration.[121]

With a mean RMSD value of 0.03 ± 0.01 Å and 0.05 ± 0.02 Å respectively, the PBE+D3 and PBE+TS methods both yielded a less quantitative measure of the benzene dimer geometries with respect to the reference PBE/CCSD(T) data. Of the 7 benzene dimer configurations for which the PBE+TS RMSD values were greater than 0.05 Å (namely M2, S1, S3, S4, S6, S7, and S8), it is difficult to identify a shared intermolecular binding motif among them. Intriguingely, PBE+D3 seems to fare better on sandwiched geometries and it is only the T-shaped S4 and S6 which have RMSDs above 0.05 Å.

However, analysis of the inter-monomer distance (see Figure 2.2) reveals that PBE+TS tends to shorten the inter-monomer distance, R, for stacked geometries (M1, S2, S7, and S8) by an average of 0.03 Å relative to the PBE/CCSD(T) results, while it elongates the inter-monomer distance by an average of 0.09 Å for T-shaped structures.

We believe that these observations can be explained by the fact that the frequency-dependent dipole polarizability (FDP) in the TS model is approximated by an isotropic scalar instead of an anisotropic tensor quantity. A consequence of this approximation is that the in-plane components of the FDP in the benzene monomer are underestimated while the out-of-plane component is overestimated. In the stacked benzene dimer configurations, the inter-monomer distances are primarily determined by the coupling of the induced dipole moment in the direction of the out-of-plane component of one monomer with the induced dipole moment in the direction of the out-of-plane component of the other monomer. As such, the interaction along the inter-monomer axis,

R, is overestimated, which leads to TS predicting an inter-monomer distance that is too short with respect to the available reference data. This effect is more apparent in the sandwich-stacked configurations (S7 and S8) than the parallel-displaced-stacked configurations (M1 and S2), which is also consistent with the fact that the argument above would affect configurations in which the monomers are directly aligned (*i.e.*, have a rise and no run) to a much larger degree than those that are displaced (*i.e.*, have a rise and a run). For the T-shaped configurations, the situation is slightly more complicated (and less clear than in the stacked cases). Here, the intermolecular binding motif balances several components, *e.g.*, the out-of-plane component on one monomer with the in-plane component of the other monomer. From Figure 2.2, we also observed that D3, like TS, shortens the inter-monomer distance for both S7 and S8. However, PBE+D3 elongates the inter-monomer distance by an average of 0.06 Å for all other dimer geometries.

For both stacked and T-shaped structures, PBE+MBD performs much more consistently, elongating the inter-monomer distance by a scant 5×10^{-3} Å and 1×10^{-3} Å for stacked and T-shaped configurations, respectively. This is believed to be because PBE+MBD captures the anisotropy (and screening) in the FDP of the benzene monomer. The MBD model essentially fixes the issues with TS described above and is able to yield consistent results for all inter-monomer binding motifs of the benzene dimer. In the MBD case, the beyond-pairwise dispersion interactions might also play a role here, but their effect is harder to estimate without explicitly calculating the decomposition of the MBD energy and forces into individual n-body terms ($n = 2, 3, \cdots, N$).

We note that RMSD values in the range of 0.03–0.08 Å, and errors on inter-monomer distances of 0.05-0.10 Å, in the geometries of small molecular dimers (as found here with the PBE+TS and PBE+D3 methods) are not unacceptably large in magnitude; however, these differences will become even more pronounced as the sizes and polarizabilities of the monomers continue to increase. In this regime, the MBD method—by accounting for both anisotropy and non-additivity in the polarizabilities as well as beyond-pairwise many-body contributions to the long-range correlation energy—is expected to yield accurate and

consistent equilibrium geometries for such molecular dimers. As such, the combination of DFT+MBD has the potential to emerge as a computationally efficient and accurate electronic structure theory methodology for performing scans of high-dimensional PES for molecular systems whose overall stability is primarily dictated by long-range intermolecular interactions.

2.4.2 Intramolecular interactions: secondary structure of polypeptides

As a second application, we considered the *intramolecular* interactions that are responsible for the secondary structure in small polypeptide conformations. In particular, we studied 76 conformers of 5 isolated polypeptide sequences (GFA, FGG, GGF, WG, and WGG), which are comprised of the following four amino acids: glycine (G), alanine (A), phenylalanine (F), and tryptophan (W). This set of peptide building blocks includes the simplest amino acids, glycine and alanine (with hydrogen and methyl side chains, respectively), as well as the larger aromatic amino acids, phenylalanine and tryptophan (with benzyl and indole side chains, respectively). Although each of these polypeptides are relatively small (with 34-41 atoms each), a significant amount of conformational flexibility is present due to the non-trivial intramolecular binding motifs found in these systems, such as non-bonded side chain–backbone interactions and intramolecular hydrogen bonding. In fact, it is the presence of these interactions that leads to the formation of α-helices and β-pleated sheets—the main signatures of secondary structure in large polypeptides and proteins.

Following a benchmark study by Valdes *et al.*,[301] in which the geometries of these 76 conformers were optimized using second-order Møller-Plesset perturbation theory[302] (MP2) within the resolution-of-the-identity approximation[275–277,303–307] (RI-MP2) and the fairly high-quality cc-pVTZ atomic orbital basis set,[308] we performed geometry optimizations on this set of conformers with several vdW-inclusive DFT approaches, namely, PBE+D3(BJ),[66,77] PBE+TS, and PBE+MBD. All of the geometry optimizations performed in this section minimized the force components on all atomic degrees of

freedom according to the thresholds and convergence criteria specified in section 2.3. Treating the MP2 geometries as our reference, Figure 2.3 displays box-and-whisker plots and cumulative distribution functions of the distributions of RMSDs (in Å) obtained from geometry optimizations employing the aforementioned vdW-inclusive DFT methodologies. In the top of Figure 2.4, the RMSDs for each peptide conformer are visualized as a bar chart. Our starting geometries were taken from www.begdb.com, corresponding to the RI-MP2/cc-pVTZ optimized structures given in the supplemental information of Valdes *et al.*[301] Table D.1 in Appendix D gives the correspondence between the structure indexing scheme used in this work, the nomenclature of the BEGDB database (www.begdb.com) and the nomenclature of Valdes *et al.*[301]

Here we find that the PBE+MBD method again yields equilibrium geometries that are consistently in closer agreement with the reference MP2 data than both the PBE+TS and PBE+D3 methodologies. For instance, the RMSDs between the PBE+MBD and MP2 conformers are smaller than 0.12 Å for all but one GGF conformer (**34**: GGF04), with an overall mean RMSD value of 0.07 ± 0.03 Å. In contrast to the intermolecular case of the benzene dimer, the PBE+TS method performs significantly better than PBE+D3 on the same benchmark set of polypeptides, with overall mean RMSD values of 0.11 ± 0.07 Å and 0.20 ± 0.17 Å, respectively. In this regard, the whiskers in Figure 2.3 extend to RMSD values that are within 1.5 times the interquartile range (*i.e.*, following the original, though arbitrary, convention for determining outliers suggested by Tukey[309]), which highlights the fact that there are several conformers for which both PBE+TS and PBE+D3 predict equilibrium geometries that are significantly different than MP2.

Although MP2 is the most economical wavefunction-based electronic structure method that can describe dispersion interactions, MP2 does not properly account for long-range many-body effects and tends to grossly overestimate C_6 dispersion coefficients,[310] which in general leads to an overestimation of the binding energies of dispersion-bound complexes such as the benzene dimer. Since PBE+MBD should bind less strongly than MP2, we expect the side-chain to backbone distance to elongate slightly for bent conformers.

Conformers where the side chain is extended away from the backbone are expected to show less deviation between MP2 and PBE+MBD as the side-chain backbone dispersion interaction will be less significant for the geometry of the conformer.

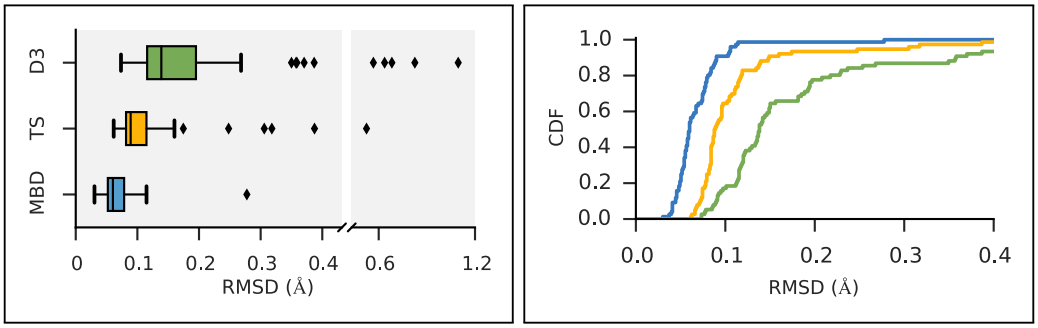

Figure 2.3: **Left:** Box-and-whisker plots showing the distribution of root-mean-square-deviations (RMSDs) in Angstrom between 76 conformers of 5 isolated small polypeptides optimized with PBE+MBD (blue), PBE+TS (yellow) and PBE+D3 (green) compared against the MP2 reference geometries of Valdes *et al.*[301] Whiskers extend to data within 1.5 times the interquartile range.[309] Note the need for a broken axis to show the largest RMSDs of PBE+D3. PBE+MBD consistently outperforms both PBE+TS and PBE+D3 in terms of yielding optimized geometries closer to the MP2 reference. Median (maximum) values are: 0.06 (0.28) Å for PBE+MBD, 0.09 (0.52) Å for PBE+TS, and 0.14 (1.10) Å for PBE+D3. **Right:** Empirical cumulative distribution function (CDF) showing the percentage of the 76 peptide conformers on which a given PBE+vdW optimization method achieves a RMSD below the value on the horiztal axis. Once again PBE+MBD is shown in blue, PBE+TS is shown in yellow and PBE+D3 is shown in green.

Aside from the noticeable outliers, the PBE+vdW structural deviations in most of the conformers correspond to small rotations or deflections of terminal groups and side chains due to dispersion-based interactions, in contrast to the backbone which is constrained by non-rotatable bonds. In the bottom of Figure 2.4 we present representative overlays of this rearrangement, showing the MP2 (blue), PBE+MBD (red), and PBE+D3 (yellow) geometries. In a) structure **17** (GFA03) is a conformer for which both PBE+MBD and PBE+D3 give small/moderate RMSDs with MP2. Both PBE+MBD and PBE+D3 open the cleft between the alanine and phenylalanine, also causing the amine on the backbone to slightly rotate. The relative positioning of these structures is expected, given MP2's tendency to over-bind dispersion interactions and PBE+D3's tendency to under-bind. In b) structure **48** (WG03), again shows PBE+MBD agreeing well with MP2, but slightly opening the backbone-side chain distance. However, PBE+D3 performs unfavorably on this structure, yielding an RMSD of 1.10 Å.

Structures where the side-chain lies farther off to the side of the backbone, such as **4** (FGG215) shown in panel d), show the smallest RMSDs between the PBE+MBD and reference MP2 geometries with the PBE+MBD geometry lying almost exactly on top of the MP2 geometry. However, FGG215 is again a structure where D3 does a poor job, this time yielding an RMSD of 0.64 Å.

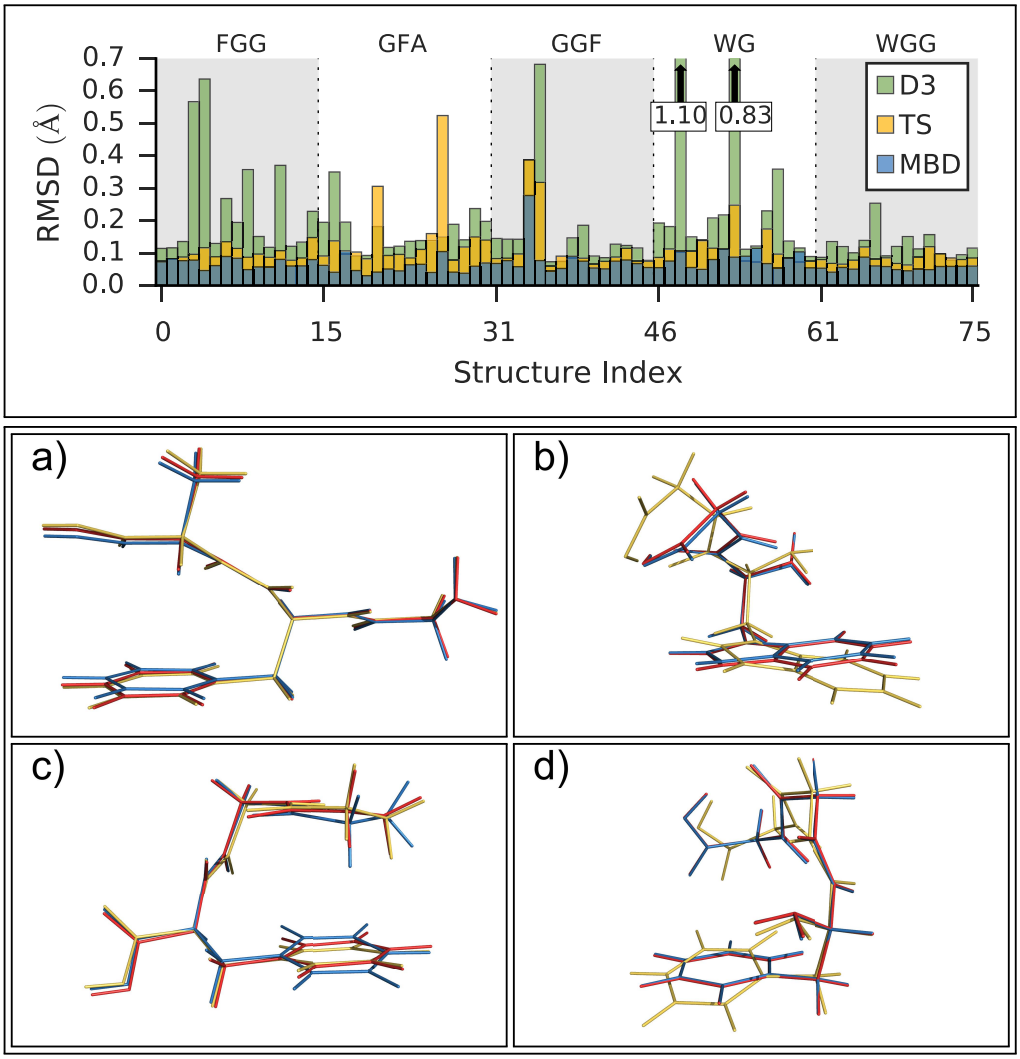

Figure 2.4: Top: Bar chart of the root-mean-square-deviations (RMSDs) in Angstrom between 76 conformers of 5 isolated small polypeptides optimized with PBE+MBD (blue), PBE+TS (yellow) and PBE+D3 (green) compared against the MP2 reference geometries of Valdes *et al.*[301] **Bottom:** Overlays of the geometries obtained from geometry optimization with MP2 (blue) and PBE+MBD (red) and PBE+D3 (yellow). In both **a)** GFA03 and **b)** WG03, the MBD correction opens the cleft between the backbone and aromatic side-chain because MP2 over-binds dispersion interactions. **c)** In GGF04, PBE+MBD rotates the phenylalanine and alanine groups together. **d)** In FGG215, since the side-chain is farther away from the backbone, PBE+MBD matches the MP2 geometry almost exactly.

The structure for which the PBE+MBD method has the largest RMSD, at 0.28 Å is **34** (GGF04), shown in panel c). As opposed to opening a cleft like in GFA03, PBE+MBD rotates the phenylalanine and alanine groups together. This rotation occurs because the terminal hydrogen on the glycine is attracted to the π-system on the phenylalanine. The rigid nature of the glycine combined with the rotatable bond in the phenylalanine, forces the phenylalanine to slightly rotate in response. The motion of the middle glycine solely attempts to minimize molecular strain from these other two interactions. Both PBE+TS and PBE+D3 methods show a similar rotation for this structure, though PBE+D3 rotates the structure even farther than PBE+MBD. This concerted rotation is associated with a very flat potential energy surface, as indicated by the fact that a second optimization run with the same tolerances resulted in a slightly greater rotation.

Following Valdes *et al.*, we classified the structures by the existence of an intramolecular hydrogen-bond between the -OH of the terminal carboxyl group and the C=O group of the preceding residue. The mean RMSD is strongly influenced by the high outliers, so the median RMSD is a more representative measure for comparing these two groups of conformers. The median RMSD for CO_2H_{free} (CO_2H_{bonded}) structures is: 0.06 (0.07) Å for PBE+MBD, 0.09 (0.09) Å for PBE+TS, and 0.14 (0.14) Å for PBE+D3. Overall, we find that the presence of this intramolecular hydrogen bond does not strongly correlate with which structures deviate more from the MP2 geometries. This finding was somewhat unexpected since Valdes *et al.* asserted that dispersion interactions are more important in determining the structure of the CO_2H_{free} family of conformers due to the peptide backbone's tendency to lie over the aromatic side chain.

Overall, we find excellent agreement between the MP2 and PBE+MBD geometries. Where PBE+MBD deviates, we find agreement with physical and chemical intuition when we take into account the well known tendency of MP2 to overestimate the magnitude of dispersion interactions. The agreement between PBE+MBD and MP2 geometries is a marked contrast to the inconsistent performance of PBE+D3 and PBE+TS which both yielded numerous outliers. Although computational cost is not directly comparable

between a Gaussian-type-orbital code and a planewave code, we are greatly encouraged by the accuracy of our PBE+MBD geometry optimizations since optimizations with a generalized gradient approximation functional such as PBE are substantially cheaper than RI-MP2. Future work will explore the performance of MBD applied to hybrid functionals to evaluate the role of error cancellation in the underlying GGA.[311] In addition, analytical gradients of the three-body term in D3 are now available in more recent versions of DFTD3, and this term should be included for a more thorough comparison of the role played by beyond-pairwise dispersion interactions.

2.4.3 Supramolecular interactions: buckyball catcher host–guest complex

Noncovalent interactions are particuarly important in supramolecular chemistry, where nonbonded interactions, such as dispersion, stabilize molecular assemblies. The large size of supramolecular host-guest complexes typically places them outside the reach of high-level quantum chemical methodologies and necessitates the use of DFT for geometry optimizations and energy computations. However, the large polarizable surfaces that interact in these systems requires a many-body treatment of dispersion to achieve a chemically accurate description of supramolecular binding energies.[106,312] The C_{60} 'buckycatcher' host–guest complex (also referred to as $C_{60}@C_{60}H_{28}$) in particular has received considerable attention as a benchmark supramolecular system in the hope that it is prototypical of dispersion-driven supramolecular systems, and it has been studied extensively both experimentally[313–316] and theoretically.[105,106,312,314,317–321] The C_{60} buckycatcher (denoted as **4a** by Grimme) is one of the most well studied members of the S12L test set of noncovalently bound supramolecular complexes.[320] This system has also stimulated interest in novel hosts for fullerenes[321–325] and scaffolding for endohedral fullerenes.[326]

Much of the past computational work has focused on modeling the interaction energy of the C_{60} buckycatcher complex and comparing these results to the experimental data on thermodynamic association constants that have been extracted from titration

Table 2.3: Selected distances of DFT+vdW optimized geometries of the $C_{60}@C_{60}H_{28}$ host–guest complex and conformer **a** of the host alone compared to X-ray crystal structures of $C_{60}@C_{60}H_{28}$·2PhMe[313] and the unsolvated buckycatcher.[316] The TPSS functional does not identify conformer **a**, so these entries are left blank.

	Complex			Host **a**	
Method	R_c (Å)	R_p (Å)	R_t (Å)	R_p (Å)	R_t (Å)
PBE+MBD	8.312	12.992	6.303	13.263	6.394
PBE+TS	8.361	12.974	6.337	12.969	6.080
PBE+D3	8.454	12.987	6.286	11.640	6.215
TPSS+D3	8.392	12.748	6.288	–	–
TPSS+D3[a]	8.361	12.822	6.303	–	–
B97-D2[b]	8.335	12.798	6.299	11.152	6.216
M06-2L[c]	8.136	12.703	6.382	11.844	6.322
X-ray[d,e]	8.484(3)	12.811(4)	6.418(5)	9.055(2)	6.44(3)

[a] Ref. 320, [b] Ref. 314, [c] Ref. 317, [d] Ref. 313, [e] Ref. 316

experiments.[313–315] This complex is a challenging system for most dispersion correction methods since the three-body term contributes approximately 10% of the interaction energy.[105,106] Motivated by this large contribution of beyond-pairwise dispersion, we optimized the $C_{60}@C_{60}H_{28}$ complex with PBE+MBD, PBE+TS and PBE+D3 to see how significantly MBD effects impact the geometry. With 148 atoms this system also represents a structure that would be too large to optimize with numerical MBD gradients.

The buckycatcher host is made of a tetrabenzocyclooctatetraene (TBCOT) tether and two corannulene pincers (see inset of Figure 2.5). The conformation of the catcher is determined by a competition between the attractive dispersion interactions between the corannulene pincers and the strain induced by deformation of the TBCOT tether.[314] The two lowest energy 'open' conformers of the catcher have the corannulene bowls in a convex–convex 'catching' motif or in a convex–concave 'waterwheel' motif; following the notation of Refs. 313,314,318, we term the 'catching' motif **a** and the 'waterwheel' motif **b**. Mück-Lichtenfeld *et al.*[314] identified two additional conformations **c**, where the corannulene bowls face out, and **d**, where the pincers are 'closed' and there is a strong $\pi - \pi$ interaction between nested corannulene bowls (see Figure 1 of Ref. 314). Interestingly, several of the functionals that have been used to study the buckycatcher do

not identify some conformers. Notably, B3LYP does not identify conformer **d**, and TPSS-D3 is prone to drive conformer **a** to a closed variant that has $R_p = 5.53$ Å. With regard to the balance between dispersion and strain, conformer **a** is the conformer that results when the C_{60} is removed from the pincers and the host is allowed to relax. We will focus our discussion on the relaxed conformer **a** and the optimized complex.

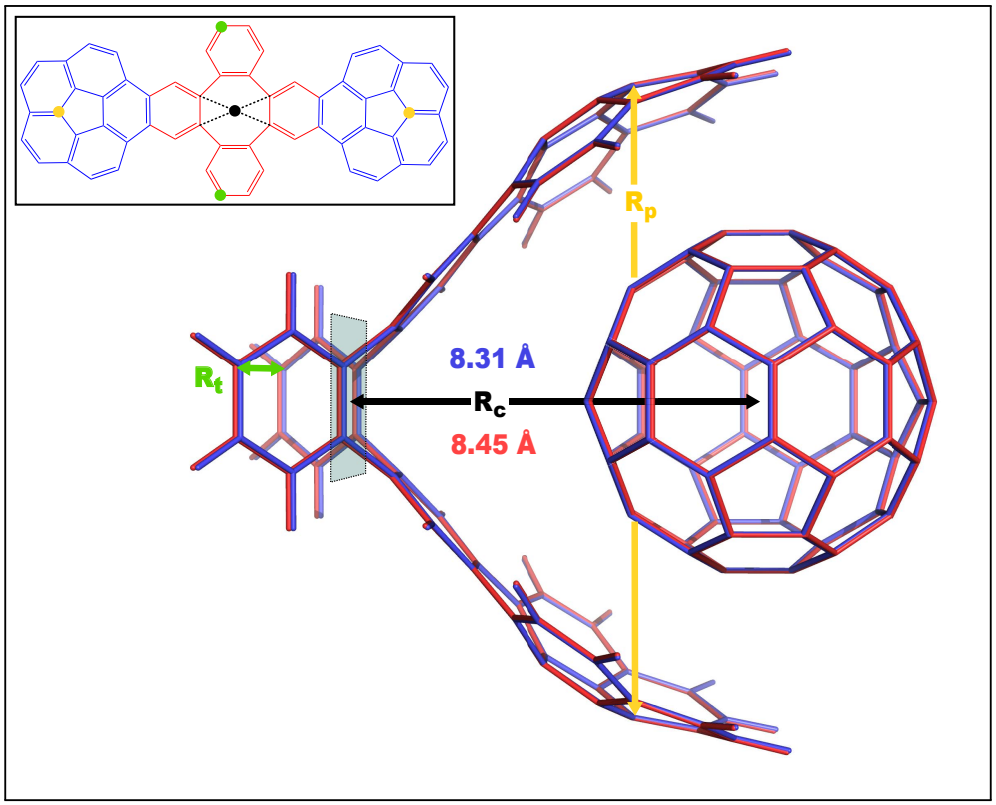

Figure 2.5: Overlay between the geometry of the C_{60}@$C_{60}H_{28}$ host–guest complex optimized with PBE+D3 (red) and PBE+MBD (blue). The distance R_c between the C_{60} centroid and the plane bisecting the tetrabenzocyclooctatetraene (TBCOT) tether (transparent green) is reduced from 8.45 Å with D3 to 8.31 Å with MBD. The green arrow shows that the R_t distance is measured between terminal carbon atoms on the TBCOT tether. The yellow arrow shows that the R_p distance is measured between the most separated carbon atoms of the central five-membered rings of both corannulene subunits.
Inset: The 2D molecular structure of the $C_{60}H_{28}$ buckycatcher host, with corannulene subunits shown in blue and the TBCOT tether shown in red. Atoms used to define the R_t and R_p distances are marked in green and yellow respectively. The black dot shows the centroid of the four atoms on the TBCOT tether used to define the R_c distance.

To compare the size of the cleft between the corannulene pincers when the buckycatcher is optimized with various DFT+vdW methods, we report the distance between the most separated carbon atoms of the central five-membered rings of both corannulene subunits

as a measure of the size of the cleft; we denote this distance as R_p (see Figure 2.5). Closing of the cleft tends to be accompanied by outward deflection of the TBCOT tether, so we also measure the distance between terminal carbons on the tether; we denote this distance as R_t (see Figure 2.5). Likewise, we measure the distance between the centroid of the C_{60} and the plane that bisects the TBCOT tether at the base of the buckycatcher (see Figure 2.5); we denote this distance as R_c. In Figure 2.5 the 2D molecular structure of the buckycatcher host and the 3D structure of the $C_{60}@C_{60}H_{28}$ host–guest complex with the three distances R_c, R_p, and R_t are highlighted.

Upon optimization with PBE+MBD we find that the corannulene pincers deflect outward, as seen by the increased R_p distance relative to the starting TPSS+D3/def2TZVP geometry from the S12L dataset.[320] The R_p distance predicted by PBE+MBD is larger than other results from vdW inclusive functionals (see Table 2.3), which may be consistent with previous reports of three-body and higher order terms substantially decreasing the binding energy of the $C_{60}@C_{60}H_{28}$ host–guest complex.[105,106] However, this deflection is accompanied by a reduction of the buckyball–catcher distance R_c, which would suggest a tighter binding. Just as with the reduced cleft distances in the peptides and the inter-monomer distance in the benzene dimer, we find that the host–guest distance predicted by PBE+MBD ($R_c = 8.31$ Å) is smaller than that predicted by PBE+D3 ($R_c = 8.45$ Å) and PBE+TS ($R_c = 8.36$ Å). For comparison, we also optimized the complex with TPSS+D3/def2TZVP and found a buckyball–catcher distance of $R_c = 8.39$ Å, which is slightly larger than the $R_c = 8.36$ Å in the previously reported TPSS+D3/def2TZVP geometry in the S12L dataset.[320] These results are reported in Table 2.3 together with a comparison to previous vdW inclusive DFT results and the corresponding distances from the X-ray determined crystal structures.

The X-ray structure for the complex is taken from $C_{60}@C_{60}H_{28}$ co-crystallized with two disordered toluene molecules, *i.e.* $C_{60}@C_{60}H_{28}{\cdot}2PhMe$.[313] In the solid state the fullerenes form columns along the *a*-axis, while the buckycatcher aligns back-to-back in the *bc*-plane. These back-to-back interactions have fewer atoms that are in van der Waals contact, but

could still push the corranulene units together slightly. Zabula *et al.* recently obtained an X-ray crystal structure of the unsolvated buckycatcher which adopts an inter-locked structure of conformer **a**.[316] This inter-locked structure provides an attractive van der Waals interaction between corranulene units, which causes cleft to close, and yields an R_p distance of 9.055(2) Å with a corresponding outward deflection of the TBCOT tether ($R_t = 6.44(3)$ Å).

Perhaps the most unusual trend in Table 2.3 is the substantial opening of the cleft between the corranulene subunits, and accompanying outward deflection of the TBCOT tether, when the isolated host is optimized with the PBE+MBD method. Comparing the R_p and R_t distances we find an ordering of PBE+MBD > PBE+TS > PBE+D3. Mück-Lichtenfeld *et al.* previously found that the TBCOT tether is quite flexible, resulting in a shallow bending potential (see Figure 2 of Ref. 314) as the R_p distance is varied; using the B97-D functional and 6-31G* basis set, the energy of conformer **b** varies by only ~ 1.3 kcal/mol as R_p is scanned from 10-14 Å.[314] Comparing the energy of the buckycatcher in the strained conformer that it adopts when hosting the buckyball, to its energy when fully relaxed, we see that at the PBE+D3/def2TZVP level this strain energy is 1.02 kcal/mol. This is consistent with the shallow bending potential found by Mück-Lichtenfeld *et al.* Given how flat this potential energy surface is, it is less surprising that the three van der Waals corrections considered give such different relaxed R_p distances for the isolated host.

The structure of the C_{60} buckyball does not vary significantly between different vdW inclusive functionals. The PBE+MBD optimized structure of C_{60} has C-C bond lengths of 1.45192(5) Å for bonds within five-membered rings (fusing pentagons and hexagons), and 1.39804(3) Å for bonds fusing hexagonal rings; which compares favorably to the well known gas-phase electron diffraction results of 1.458(6) Å and 1.401(10) Å.[327] This result is consistent with the short-range behavior of the range-separated PBE+MBD method essentially reducing to the bare PBE functional, which does a good job of predicting C-C bond lengths.

On the whole we find that the PBE+MBD method yields structures that are comparable to other vdW inclusive functionals but deviate more significantly from X-ray determined crystal structure than the PBE+D3 results. Since we do not have ane experimentally determined gas-phase structure or a wavefunction theory reference for the $C_{60}@C_{60}H_{28}$ host–guest complex, the deviation of the gas-phase PBE+MBD optimization from the experimental crystal structure should not be seen as too damaging. Future work will address the optimization of this full crystal structure.

In light of the lack of wavefunction theory geometries to compare against, we concluded with a few comments about the computational efficiency of our method. Starting from the TPSS/def2TZVP structures from the S12L dataset, we were able to optimize the 148 atom complex with the PBE+MBD method in 68 bfgs steps in about 415 cpu hours, while the PBE+D3 optimization in Orca took 34 bfgs steps in about 450 cpu hours.[‡] Given that Orca uses redundant internal coordinates for geometry optimizations and the D3 correction is almost instantaneous to calculate, it is worth noting that the Cartesian coordinates optimization in QE with the much more costly MBD correction is roughly competitive.

2.4.4 The importance of Hirshfeld effective atomic volume gradients

Our derivation of the ionic MBD forces placed considerable emphasis on the importance of including the implicit coordinate dependence arising from the gradients of the Hirshfeld effective atomic volumes. To test how large a contribution $\boldsymbol{\partial} V$ terms make to the MBD forces, we re-optimized the benzene dimers, this time setting $\boldsymbol{\partial} V = 0$ explicitly. As shown in Figure 2.6, neglect of the Hirshfeld volume gradients does not have a large impact for this system where the dispersion forces are intermolecular; the mean RMSD becomes $(16 \pm 5) \times 10^{-4}$ Å. However, the numerical stability of the method was significantly degraded and the optimization of M1 with $\boldsymbol{\partial} V = 0$ proved unable to converge after several hundred iterations.

[‡]The PBE+MBD optimization was run in about 2.75 hours on 170 Intel Xeon E5-2680 processors while the PBE+D3 optimization was run in about 14 hours on 32 cores AMD Opteron 6376 Abu Dhabi processors.

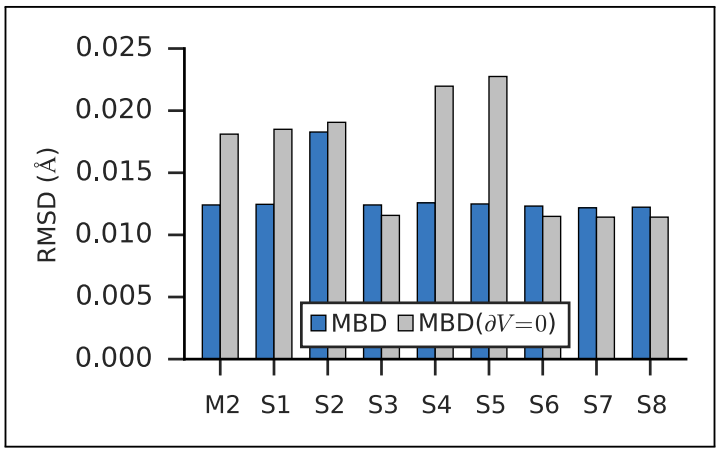

Figure 2.6: Root-mean-square-deviations (RMSD) in Å between the PBE+MBD and PBE/CCSD(T)[291] optimized geometries of 9 benzene dimer configurations using the full MBD gradient (shown in blue), and the approximation where ∂V contributions are set explicitly to zero (shown in grey). Numerical instability when $\partial V = 0$ prevented the optimization of M1 from converging.

The fact that the Hirshfeld gradients have mostly negigible impact on the benzene dimer optimizations is expected since the Hirshfeld effective atomic volumes only change when neighboring atoms are moved. Not only is the benzene monomer fairly rigid, but the range separation that is employed to avoid double counting the correlation energy at short range means that the long-range tensor $\mathbf{T}_{\mathrm{LR}}$, and correspondingly the MBD correction, is largely turned off within the benzene monomer (see Figure 3.2 in Chapter 3).

We expect a larger impact of Hirshfeld volume gradients for systems that are flexible and large enough for the damping function to have 'turned on' the MBD correction. The case of polypeptide intramolecular dispersion interactions matches both of these criteria. The peptide structures are much more flexible than the benzene monomer and also have the opportunity for cooperative addition of the Hirshfeld volume gradients along the chain, *i.e.* the local Hirshfeld volume gradients acting at the nearest neighbor level can propagate along the peptide chain and result in a larger change. We computed the MBD forces on the final optimized geometries of all 76 peptide structures and analyzed the atom-by-atom difference in forces computed with and without the Hirshfeld volume gradients. [§] As shown in Figure 2.7, negelct of the Hirshfeld gradient causes a significant

[§]Since the TS method is also based on Hirshfeld partitioning, the Hirshfeld volume gradients are also expected to be significant when computing the TS nuclear forces.

shift in the distribution of MBD forces in the peptides, with a tendency to increase the forces from the lower peak from $\sim 2 \times 10^{-4}$ $\mathrm{E_h}$/a.u. to $\sim 4 \times 10^{-4}$ $\mathrm{E_h}$/a.u. Comparing the Cartesian components of the MBD forces across all atoms in all 76 structures we find that the deviations between forces with and without the Hirshfeld volume gradients ($\mathbf{F} - \mathbf{F}_{\partial V=0}$) are approximately normally distributed with zero mean and a standard deviation of 2×10^{-4} $\mathrm{E_h}$/a.u.. This leads to the norm of the force difference ($\Delta\|\mathbf{F} - \mathbf{F}_{\partial V}\|$) having a mean of $(3.2 \pm 1.7) \times 10^{-4}$ $\mathrm{E_h}$/a.u., and a mean of the difference of norms of $\|\mathbf{F}\| - \|\mathbf{F}_{\partial \mathrm{V}=0}\| = (-5 \pm 17) \times 10^{-5}$ $\mathrm{E_h}$/a.u. Overall, neglect of the Hirshfeld gradients increases forces and causes a long-tailed distribution of relative error, that is peaked at $\sim 20\%$, but extends up to 400%. This large distribution of relative errors has the potential to significantly impact the predictive nature of *ab initio* molecular dynamics (AIMD) simulations run at the MBD level of theory that do not properly account for the analytical gradients of the Hirshfeld effective volumes. Given that this error would accumulate at every time step, combined with the fact that the MBD correction was found to be quite important in the geometry optimizations of the systems considered herein, we find the neglect of the Hirshfeld effective volume gradients to be an unacceptable approximation in AIMD. This finding is particularly true for large flexible molecular systems with significant intramolecular dispersion interactions since this error can cooperatively increase along any extended direction, *i.e.*, along an alkane chain or polypeptide backbone.

2.5 Conclusions

By developing analytical energy gradients of the range-separated MBD energy with respect to nuclear coordinates, we have enabled the first applications of MBD to full ionic relaxations. By treating gradients of the MBD energy correction analytically, rather than numerically, we have reduced the number of self-consistent calculations that must be performed from $2 \times (3N - 6)$ to 1, enabling treatment of much larger systems. Our derivation and implementation includes all implicit coordinate dependencies arising from the Hirshfeld charge density partitioning. In the isolated molecule optimizations that we

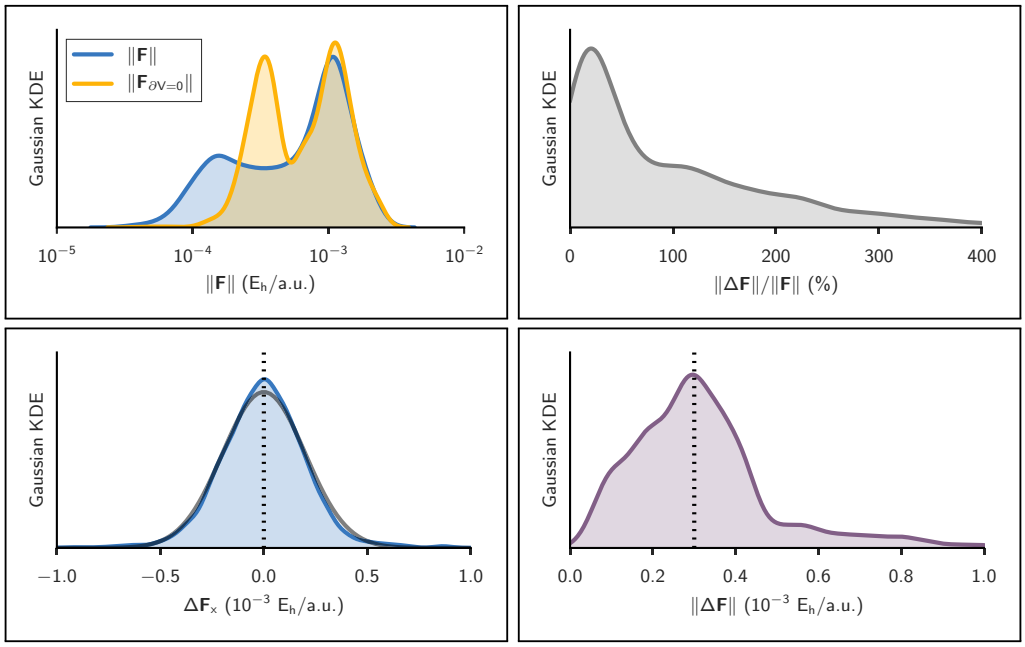

Figure 2.7: Top Left: Gaussian kernel density estimate of the distributions of the norm $\|\cdot\|$ of MBD forces $\mathbf{F}_{\mathrm{MBD}}$ acting on each atom at the optimized geometries of 76 polypeptide structures. In blue the forces are computed with full Hirshfeld gradients; in yellow forces were computed with Hirsheld gradients ∂V set to zero. **Top Right:** Gaussian kernel density estimate of the distribution of relative percentage error $\|\Delta\mathbf{F}\|/\|\mathbf{F}\|$ where $\Delta\mathbf{F}$ is the error incurred by setting $\partial V = 0$. The distribution is peaked at approximately 20% but extends to values much greater than 100%. **Bottom Left:** Difference of force components $\Delta\mathbf{F}_x = \mathbf{F}_x - \mathbf{F}_{x,\partial V=0}$, with normal distribution $\mathcal{N}(0, 0.2)$ superposed and dotted line indicating zero mean. The distributions for $\Delta\mathbf{F}_y$ and $\Delta\mathbf{F}_z$ are similar. **Bottom Right:** Norm of the difference of forces, $\|\Delta\mathbf{F}\| = \|\mathbf{F} - \mathbf{F}_{\partial V=0}\|$, with dotted line indicating the peak at 0.3×10^{-3} $\mathrm{E_h/a.u.}$

consider, the implicit coordinate dependencies that arise from the Hirshfeld volume gradients results in significant changes to the MBD forces. The long-tailed distribution of relative error that we observed indicates that any future AIMD simulations employing MBD forces must include full treatment of the Hirshfeld volume gradients, or the accumulation of error will negatively impact the simulation dynamics. Our careful treatment of these volume gradients paves the wave for future work to address how a self-consistent implementation of the MBD model will impact the electronic band structures of layered materials and intermolecular charge transfer couplings in molecular crystals.

Consistent with previous findings that a many-body description of dispersion improves the binding energies of even small molecular dimers,[87] we find that MBD forces significantly improve the structures of isolated dispersively bound molecular systems. In this regard, we find excellent agreement between PBE+MBD optimized structures and the available reference data in our investigation of both the stationary points on the benzene dimer potential energy surface and the secondary structure of polypeptides. Notably, PBE+MBD consistently out-performed the the pairwise PBE+D3, and effectively pairwise PBE+TS optimizations.

Many-body effects have previously been shown to be very significant in modeling solvation and aggregation in solution[30] and can lead to soft collective fluctuations that impact hydrophobic association[328] and the entropic stabilization of hydrogen-bonded molecular crystals.[112] We therefore anticipate that our many-body forces will be of interest for solvated simulations, such as estimates of the thermodynamic properties of metabolites[329] and modeling novel electrolytes,[330–332] and for numerous condensed phase simulations of organic molecular crystals.

The first applications of MBD forces in this chapter were restricted to gas-phase systems because computation of MBD gradients in the condensed phase, where periodic images of the unit cell must be considered, is substantially more challenging from a computational perspective. Converging the MBD energy in the condensed phase is

substantially more memory and compute intensive due to a real-space supercell procedure that is required to support long-wavelength normal modes of $\mathbf{C}^{\mathrm{MBD}}$. The next chapter describes the details of our implementation for periodic systems, including careful treatment of parallelization and convergence criteria, and demonstrates the utility of MBD forces for unit-cell optimizations.

3

Many-Body Dispersion Forces for Condensed Phase Simulations

3.1 Introduction

To date, much of the work on MBD has focused on the energetics of various molecules and crystalline materials.[80,81,87,88,111–113,119,141,142] In the previous chapter we presented the first implementation of the relevant analytic gradients with respect to nuclear displacements, which permitted fast and accurate MBD inclusive geometry optimizations of gas-phase systems. Since dispersion energies largely scale with system size, dispersion becomes extremely important when considering properties like the cohesive energy of organic solids. In the present chapter we will describe a more efficient implementation of the MBD energy and analytic gradients, which has enabled their application to larger simulations of condensed phase systems. The infinite periodicity of solids, in contrast to isolated gas-phase systems, raises several issues for the computation and convergence of MBD energies and forces. In particular, convergence of the dipole interactions between periodic images of the atoms in the unit cell, and the real-space supercell procedure that is required to support long-wavelength collective dipole modes, have been discussed only briefly in other treatments of range-separated MBD.[88] Additionally, very little attention has been paid to the numerical stability of the MBD algorithm when implemented for extended systems. In this chapter we will carefully examine the MBD algorithm and discuss our approach for parallelizing it for optimization of periodic systems. We start with a brief overview of the MBD algorithm as it applies to condensed phase systems, this

time placing an emphasis on numerical aspects rather than the equations which define the model. Subsequently, we will delve into numerical analysis of the MBD algorithm. The chapter concludes with a few applications of MBD inclusive optimizations of extended systems.

3.2 Algorithm Overview and Control Flow

As we saw in section 2.2.1 the MBD correlation energy is divided into two terms, corresponding to the difference between the zero-point energy of the *interacting* QHO eigenfrequencies ($\{\sqrt{\lambda}\}$) and that of the screened *non-interacting* modes ($\{\overline{\omega}\}$). To facilitate discussion of the algorithm, we call these two terms the interacting and non-interacting energies (or forces) respectively:

$$E_{\mathrm{MBD}} = \underbrace{\frac{1}{2}\sum_{p=1}^{3N}\sqrt{\lambda_p}}_{E_{\mathrm{int.}}} - \underbrace{\frac{3}{2}\sum_{a=1}^{N}\overline{\omega}_a}_{E_{\mathrm{non-int.}}} \tag{3.1}$$

$$\mathbf{F}_{\mathrm{MBD}} = -\boldsymbol{\partial}E_{\mathrm{MBD}} = \underbrace{-\boldsymbol{\partial}E_{\mathrm{int.}}}_{\mathbf{F}_{\mathrm{int.}}} + \underbrace{\boldsymbol{\partial}E_{\mathrm{non-int.}}}_{-\mathbf{F}_{\mathrm{non-int.}}} \tag{3.2}$$

Broadly stated, the MBD algorithm begins by initializing arrays with free atom reference quantities. These quantities are then used to compute the Tkatchenko-Scheffler (TS) level frequency-dependent terms, by weighting the free atom quantities by the Hirshfeld volumes. The TS-level quantities are computed on an imaginary frequency grid to perform the range-separated self-consistent screening (rsSCS) procedure used to compute the screened dynamic polarizabilities, $\overline{\alpha}_a(\mathbb{i}\omega)$. The non-interacting energy requires $\overline{\omega}_a$, a screened excitation frequency, which is computed from the screened dynamic polarizability via the Casimir-Polder integral for the screened effective C_6 coefficient:

$$\overline{\omega}_a = \frac{4}{3}\frac{\overline{C}_{6,aa}}{[\overline{\alpha}(0)_a]^2} = \frac{4}{\pi\,[\overline{\alpha}_a(0)]^2}\int_0^\infty \overline{\alpha}_a(\mathbb{i}\omega)\overline{\alpha}_a(i\omega)\,\mathrm{d}(\mathbb{i}\omega). \tag{3.3}$$

Since this integral does not have an analytic solution, we numerically evaluate it with Gauss-Legendre quadrature scaled to the semi-infinite interval $[0, \infty)$.

$$\overline{\omega}_a = \frac{4}{\pi \left[\overline{\alpha}_a(0)\right]^2} \sum_{p=1}^{n} g_p \left[\overline{\alpha}_a(\mathbb{i} y_p)\right]^2 \tag{3.4}$$

where g_p and y_p are the quadrature weights and abscissae respectively. These quadrature frequencies are returned in the subroutine GENERATE_GRID.

On each pass through the quadrature loop (see the bold arrow in Figure 3.1) the running quadrature sums for $\overline{\omega}_a$ and $\boldsymbol{\partial}_c \overline{\omega}_a$ are updated after the self-consistent screening and contraction of the $\overline{\mathbf{A}}$ matrix has computed $\overline{\alpha}_a$ at frequency $\mathbb{i} y_p$. At the end of the frequency integration loop (exit diamond decision point in Figure 3.1), the final screened excitation frequencies and their derivatives are summed over the atom index a to give the non-interacting energy and forces, Eqs. (3.1) and (3.2).

Having computed the screened quantities, the interaction Hamiltonian (matrix $\mathbf{C}^{\mathrm{MBD}}$) is then built from the screened quantities and the long-range dipole–dipole interactions are converged periodically. This Hamiltonian is then diagonalized and the interacting energy and forces are computed, Eqs. (2.41,3.1, 3.1). Finally, the MBD energy and forces are computed by taking the difference between interacting and non-interacting quantities.

The algorithm described above has been implemented with our gradients code in a development version of the Quantum ESPRESSO (QE) software package,[262] which was chosen for its preexisting implementation of the Hirshfeld partitioning and the derivatives of these volumes. We have written the code in a modular fashion to allow ease of incorporation into other packages: the only necessary inputs are the Hirshfeld volumes, Hirshfeld volume derivatives, lattice vectors, and atomic coordinates. At the time of writing, an energy-only variant of this module has been incorporated into the OCTOPUS software package,[333,334] and we are working to distribute the module to developers of FHI-aims[278] and Q-CHEM.[335] We will release this code with QE, and separately as a stand-alone module.

Since the computation of the MBD energy and gradients entails several layers of nested subroutines and requires complex parallelization strategies, we present a flowchart in Figure 3.1 that graphically shows the program flow. The blue boxes in Figure 3.1 denote parallelization over force components (atomic index c), and the yellow boxes denote parallelization over independent 3×3 sub-blocks of the dipole tensors (atomic indices a, b). We refer to this later strategy as "ab" parallelization since we are distributing quantities coupling "ab" pairs of QHOs. These two separate, but complementary, parallelization strategies will be discussed in the remainder of this section, where we provide an in-depth discussion of each algorithmic step with pseudocode and references to the relevant equations from Chapter 2.

3.3 The Non-Interacting Energy

In the subections below we will describe the various subroutines used to compute the non-interacting energy. In subsection 3.3.1 we describe the initialization from free atom quantities. In subsection 3.3.2 we discuss the range-separated self-consistent screening procedure used to compute screened quantities. In subsection 3.3.3 we discuss periodic convergence of the dipole-dipole interaction. Finally, in subsection 3.3.4 we discuss the quadrature scheme used to evaluate the Casimir-Polder integral.

3.3.1 Initialization and component decomposition

We begin by initializing arrays with free atom quantities and Hirshfeld effective atomic volumes, and then assigning force components to each MPI process. The free atom quantities are stored in a precomputed lookup table, and the Hirshfeld effective volumes and their derivatives are computed using code in the TS-vdW module of QE. Because each component is independent, for an N atom system communication is limited to syncing a force vector of size $3N$ across all processes. In Figure 3.1 this parallelization scheme is represented with the blue boxes. In instances where there are more MPI processes than atoms, only the first N processes are assigned force components.

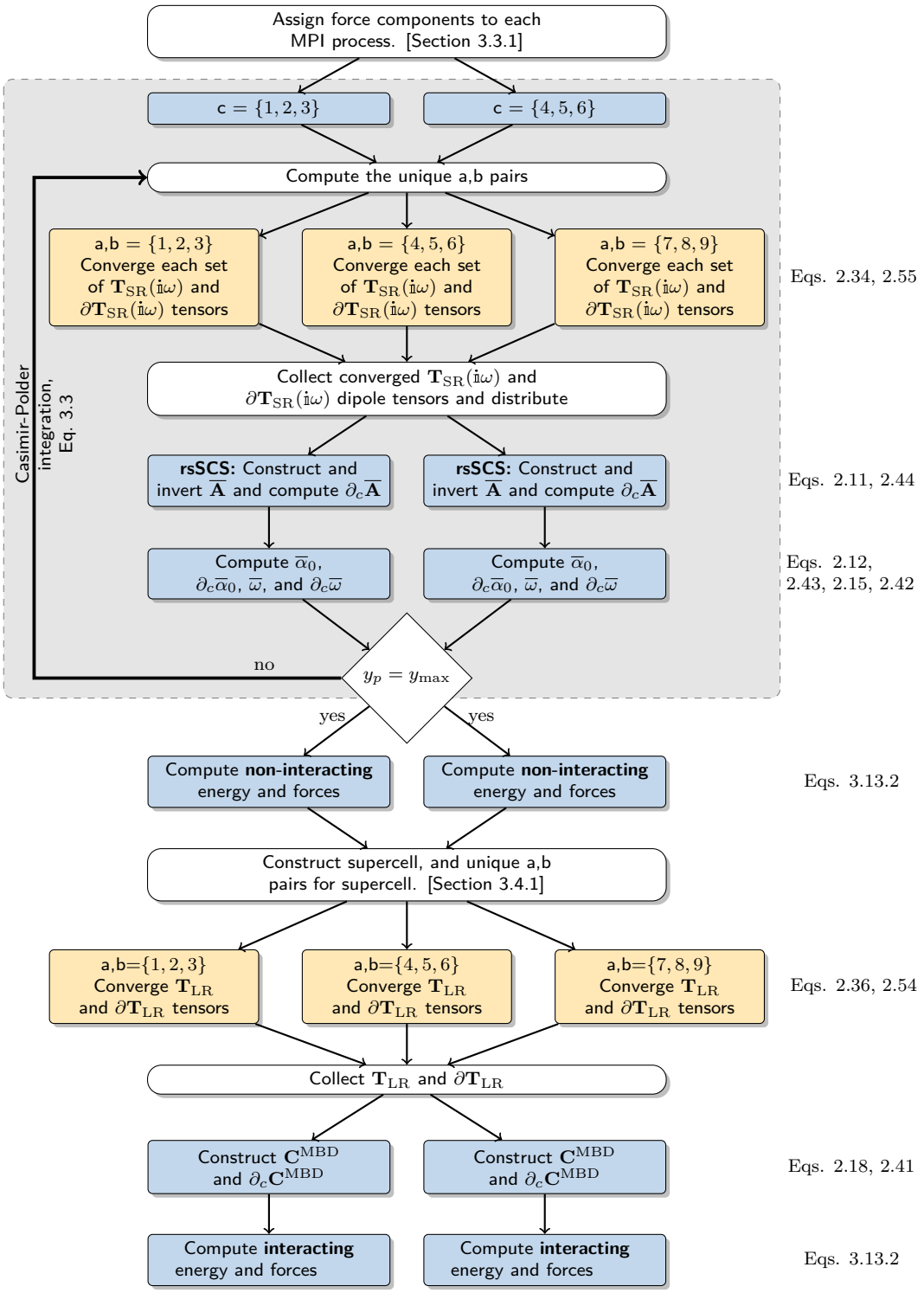

Figure 3.1: Parallelization flowchart for our MBD implementation. Blue and yellow cells indicate parallelization over force components (c index) and independent dipole tensors (ab indices) respectively. White cells indicate tasks on the head node.

3.3.2 Self-consistent screening (rsSCS)

After initialization and assignment of force component MPI processes, the processes summarized in the grey box in Figure 3.1 accomplish both the rsSCS procedure and numerical evaluation of the Casimir-Polder integral to compute the screened oscillator frequencies and atomic polarizabilities. Our implementation uses an algebraic scaling of Gauss-Legendre quadrature abscissae to the semi-infinite interval $[0, \infty)$, but numerous other schemes are possible. In section 3.3.4 we will examine the errors incurred by various alternative schemes. Looping over the quadrature frequencies y_p, (represented in the flowchart by the loop testing if $y_p = y_{\max}$), we compute the screened atomic polarizabilities at each frequency by constructing a relay matrix, $\overline{\mathbf{A}}$, and inverting it, Eq. 2.12.

This construction requires the computation of frequency-dependent polarizabilities $\alpha(\mathbb{i}y_p)$, QHO widths $\sigma(\mathbb{i}y_p)$, and vdW radii at the TS-level, $\mathcal{R}^{\text{vdW, TS}}$, all of which is wrapped in a subroutine called EffectiveQuantities. While this subroutine involves

1: **function** EffectiveQuantities(α^{free}, ω^{free}, y_p)
2: Compute $\Upsilon_a(\mathbb{i}y_p)$ with $\left[\frac{1}{1+(\omega/\omega_a^{\text{free}})^2}\frac{\alpha_a^{\text{free}}(0)}{V_a^{\text{free}}}\right]$
3: Compute $\alpha(\mathbb{i}y_p)$ with $\Upsilon_a(\mathbb{i}\omega)V_a$
4: Compute $\boldsymbol{\partial}\alpha^{TS}(\mathbb{i}y_p)$ with $\Upsilon_a(\mathbb{i}\omega)\partial_c V_a$
5: Compute $\mathcal{R}^{\text{vdW, TS}}$ with $\frac{\mathcal{R}_a^{\text{vdW, free}}}{[V_a^{\text{free}}]^{1/3}}[V_a]^{1/3}$
6: Compute $\boldsymbol{\partial}\mathcal{R}^{\text{vdW, TS}}$ with $\frac{\mathcal{R}_a^{\text{vdW, free}}}{[V_a^{\text{free}}]^{1/3}}\frac{\boldsymbol{\partial}_c V_a}{3[V_a]^{2/3}}$
7: Compute $\sigma(\mathbb{i}y_p)$ with $\left[\frac{1}{3}\sqrt{\frac{2}{\pi}}\Upsilon_a(\mathbb{i}\omega)\right]^{1/3}[V_a]^{1/3}$
8: Compute $\boldsymbol{\partial}\sigma(\mathbb{i}y_p)$ with $\left[\frac{1}{3}\sqrt{\frac{2}{\pi}}\Upsilon_a\right]^{1/3}\frac{\boldsymbol{\partial}_c V_a}{3[V_a]^{2/3}}$
9: **end function**

computing quite a few quantities, it is extremely quick. For a system of 200 atoms, we have seen that computing the effective quantities typically takes less than 0.01 seconds on a single core of an Intel Xeon E5-2680 processor.

The rsSCS procedure is accomplished in a subroutine called Screen. This subroutine builds the TS-level matrices $\mathbf{A}$ and $\mathbf{T}_{\text{SR}}$ and solves for the screened polarizability through matrix inversions. Derivatives of all quantities are computed as they become available,

and collected in a manner that avoids extra loops. We have employed parallelism over force components for $\partial_c\overline{\mathbf{A}}$, and "$ab$ parallelism" for $\mathbf{T}_{\mathrm{SR}}$ and $\partial_c\mathbf{T}_{\mathrm{SR}}$ since each ab sub-block is an independent 3×3 matrix coupling QHOs a and b. These sub-blocks are synchronized to the root process, which then distributes the correct derivative components to each MPI process. It is important to note that while the force component based parallelization cannot utilize more than N processes, the ab parallelization can.

function SCREEN(σ, $\mathcal{R}^{\mathrm{TS}}$, y_p)
    Compute work distribution map for $\mathbf{T}_{\mathrm{SR}}$ and $\boldsymbol{\partial}\mathbf{T}_{\mathrm{SR}}$
    Build $\mathbf{T}_{\mathrm{SR}}$ and $\boldsymbol{\partial}\mathbf{T}_{\mathrm{SR}}$ with Eqs. (2.34, 2.25, 3.5, 2.55) (periodic convergence)
    Gather $\mathbf{T}_{\mathrm{SR}}$ and $\boldsymbol{\partial}\mathbf{T}_{\mathrm{SR}}$
    Distribute $\mathbf{T}_{\mathrm{SR}}$ and $\boldsymbol{\partial}\mathbf{T}_{\mathrm{SR}}$
    Build $\overline{\mathbf{A}}$ with $\left[\mathbf{A}^{-1}(\mathbb{i}\omega) + \mathbf{T}_{\mathrm{SR}}(\mathbb{i}\omega)\right]^{-1}$
    Build $\boldsymbol{\partial}\overline{\mathbf{A}}$ with $-\overline{\mathbf{A}}\left[-\mathbf{A}^{-1}\left(\partial_c\mathbf{A}\right)\mathbf{A}^{-1} + \partial_c\mathbf{T}_{\mathrm{SR}}\right]\overline{\mathbf{A}}$
end function

3.3.3 Periodic convergence of dipole-dipole interactions

Since $\mathbf{T}_{\mathrm{SR}}$ acquires frequency dependence through the QHO width $\sigma(\mathbb{i}\omega)$, this tensor and its derivative must be converged over the periodic lattice for each quadrature frequency. In computing the elements of $\mathbf{T}^{\mathrm{SR}}_{ab}(\mathbb{i}y_p)$ with Eq. (2.34) we account for interactions with periodic images of atoms in the simulation unit cell by considering the coupling between atom a and all of the periodic images b' of atom b,

$$\mathbf{T}^{\mathrm{SR}}_{ab} \rightarrow \mathbf{T}^{\mathrm{SR}}_{ab} + \sum_{b'} \mathbf{T}^{\mathrm{SR}}_{ab'} \tag{3.5}$$

and similarly for the forces,

$$\boldsymbol{\partial}\mathbf{T}^{\mathrm{SR}}_{ab} \rightarrow \boldsymbol{\partial}\mathbf{T}^{\mathrm{SR}}_{ab} + \sum_{b'} \boldsymbol{\partial}\mathbf{T}^{\mathrm{SR}}_{ab'}. \tag{3.6}$$

The sum over periodic images b' is accomplished by adding successive shells of the simulation unit cell (see Figure 3.5 a), until each 3×3 ab sub-block is converged to within

a tolerance, δ, (typically 10^{-6} or 10^{-7}):

$$\left\|\Delta\mathbf{T}^{\mathrm{SR}}\right\|_{\mathrm{max}} = \max_{ij}\left\{|\Delta \mathrm{T}_{ij}|\right\} \leq \delta, \tag{3.7}$$

where ij are Cartesian indices, the ab' indices on $\mathbf{T}^{\mathrm{SR}}$ have been suppressed for clarity, Δ indicates the change due to adding a new shell, and $\|\cdot\|_{\mathrm{max}}$ is the max norm, *i.e.* the element-wise infinity norm. Once the max norm falls below δ, we assume that we have reached convergence. It is well known that the spectrum of a Hermitian matrix, such as $\mathbf{C}^{\mathrm{MBD}}$, is stable against small perturbations (cf. Refs. 336–338). Since the interacting energy is built from a sum of $\sqrt{\lambda_p}$, where $\{\lambda_p\}$ are the eigenvalues of $\mathbf{C}^{\mathrm{MBD}}$, by converging $\overline{\mathbf{T}}_{\mathrm{LR}}$ until the max norms of all 3×3 sub-blocks fall below δ, we are guaranteed that the MBD energy will achieve a related convergence. See section C.5 of Appendix C We perform this analysis in lieu of an energy convergence cutoff, which would be prohibitively expensive given that each energy computation requires a full matrix diagonalization in addition to lattice summation of both the short- and long-range dipole tensors.

In considering how to converge the dipole-dipole tensor in the frequency-dependent range-separated formulation, there is one additional subtlety that was overlooked in the original FHI-aims implementation of MBD. The error function in Eq. (2.25) gives rise to terms proportional to $\zeta \exp\left[-\zeta^2\right]$ and $\zeta^3 \exp\left[-\zeta^2\right]$ in $\mathbf{T}_{\mathrm{SR}}$. These terms, and the exponential in the Fermi damping function, raise an important issue, namely avoiding arithmetic underflow. The finite precision of floating point numbers means that when evaluating functions like $\exp[-\zeta^2]$, it is easy to run into values that are smaller in magnitude than the computer can actually store in memory. This can lead to loss of precision as subnormal numbers are used to fill the "underflow gap" around zero. For numerical stability, we therefore evaluate the Fermi damping function as:

$$1 - f(Z_{ab}) = \begin{cases} 1 - \left[1 + \exp\left[-Z_{ab}\right]\right]^{-1} & Z_{ab} < 35 \\ 0 & Z_{ab} \geq 35 \end{cases} \tag{3.8}$$

and likewise for $f(\overline{Z})$. The cutoff $Z \geq 35$ is chosen since $f(Z) = 1$ to within machine precision ($\epsilon_{\text{mach}} \simeq 2 \times 10^{-16}$) for $Z \gtrsim 36$. Restated in terms of Eq. (2.28) this condition is,

$$Z_{ab} = 6\left[\frac{R_{ab}}{\beta\left[\mathcal{R}_a^{\text{vdW}} + \mathcal{R}_b^{\text{vdW}}\right]} - 1\right] \geq 35 \tag{3.9}$$

$$\Rightarrow R_{ab} \geq \frac{41}{6}\beta\left[\mathcal{R}_a^{\text{vdW}} + \mathcal{R}_b^{\text{vdW}}\right]. \tag{3.10}$$

Since $\beta \simeq 0.83$ for the PBE functional, this means that for interatomic distances $R_{ab} \gtrsim 60$ times the sum of the vdW radii of atoms a and b, the Fermi damping function has completely turned the short-range dipole tensor "off" and the long-range dipole tensor "on". Similarly, we evaluate the frequency-dependent terms in Eq. (2.25) in such a way that:

$$\mathbf{T} = \begin{cases} \mathbf{T}(\mathbb{i}\omega) & \zeta < 6 \\ \mathbf{T}_{\text{dip}} & \zeta \geq 6. \end{cases} \tag{3.11}$$

In addition to being sound practice numerically, these two cutoffs have a quite substantial computational benefit since the exponential and error function are both substantially more expensive than floating point multiplication or division and $\overline{\mathbf{T}}_{\text{SR}}$ is called on the order of $10^7 - 10^8$ times in a typical condensed phase MBD computation.

Note that since $\mathbf{T}_{\text{SR}}$ is damped by the Fermi function, $f(Z_{ab}) = \left[1 + \exp\left[-Z_{ab}\right]\right]^{-1}$, the underflow condition (Eq. (3.8)) often occurs within the simulation cell or within only a few periodic images. Furthermore, since all the frequency dependence in $\mathbf{T}_{\text{SR}}$ is contained in ζ_{ab}, and this cutoff condition is met much earlier than that on Z_{ab}, $\mathbf{T}_{\text{SR}}$ reduces to the frequency-*independent* $f(Z^{\text{TS}})\mathbf{T}_{\text{dip}}$ long before the Fermi function has turned "off" the short-range tensor. In Figure 3.2 we show that this frequency independence is achieved at quite short-range within a benzene molecule and plot contours of the various damping functions on a graphene sheet. For graphene $S_{ab} = 2.96$, so the underflow condition $Z \geq 35$ corresponds to $R_{ab} \geq 20.7$ Å. Before underflow is reached, the Fermi function becomes competitive with the max norm tolerance δ, e.g. for graphene $f(Z) \leq 10^{-6}$ for $R_{ab} \geq 9.8$ Å, which means that we cut off lattice summation for $\mathbf{T}_{\text{SR}}$ at shorter length

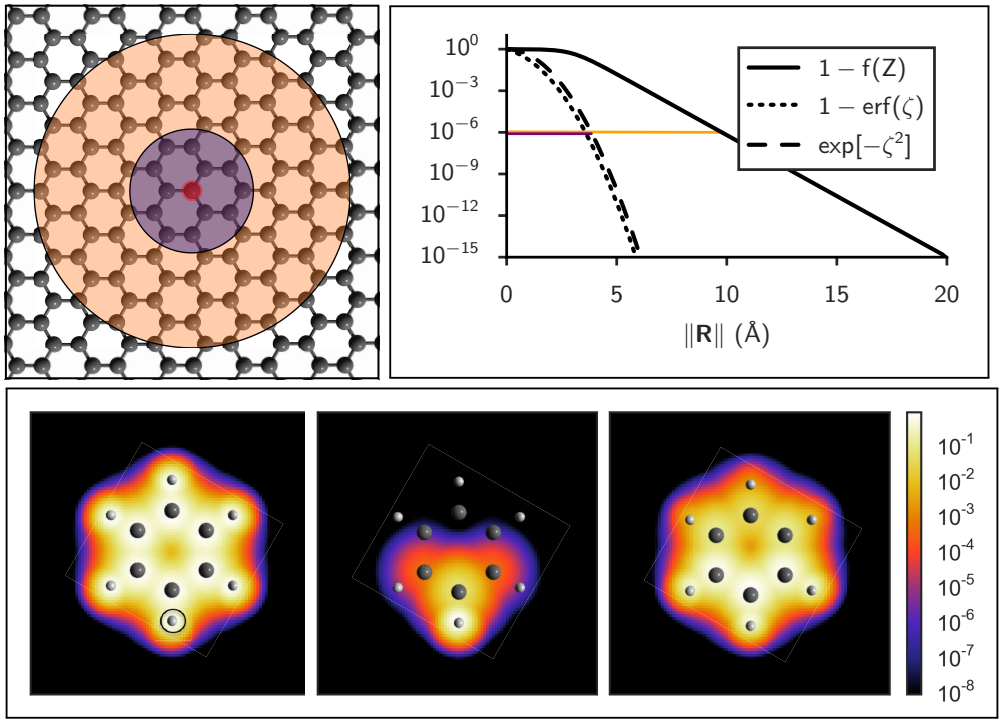

Figure 3.2: Top Left: Contours at 10^{-6} for damping functions $\exp\left[-\zeta^2\right]$ (purple) and $(1 - f\,[Z])$ (orange), with $\|\mathbf{R}\|$ relative to the atom marked in red. Damping parameters $\tilde{\Sigma} \simeq 1.03$ and $S \simeq 2.96$ were computed for a graphene nanoflake with the PBE functional. **Top Right:** Comparison of the three damping functions with the same 10^{-6} contour indicated. The rapid decay of $\exp\left[-\zeta^2\right]$ relative to the Fermi damping function demonstrates that the short-range dipole-dipole interaction tensor $\mathbf{T}_{\mathrm{SR}}$ reduces to the frequency-independent $\mathbf{T}_{\mathrm{dip}}$ well before the long-range tensor $\mathbf{T}_{\mathrm{LR}}$ has been fully "turned on" by the Fermi damping function. **Bottom:** At left, the Gaussian charge densities of the QHO oscillators assigned to each atom in benzene have been superposed and plotted on a logarithmic colorscale. One hydrogen atom is circled. In the middle panel, the frequency-dependent portion of $\mathbf{T}_{\mathrm{SR}}$, computed relative to the circled hydrogen atom, has been applied to the sum of QHO charge densities and quickly dies out moving away from the hydrogen atom of interest. On the right, the frequency-independent portion of $\mathbf{T}_{\mathrm{SR}}$, is applied to the QHO charge density and dies off much more slowly.

scales than the underflow condition. Even with these cutoffs, the convergence of each $\mathbf{T}_{\mathrm{SR}}$ block is the most computationally intensive part of the rsSCS loop.

After $\mathbf{T}_{\mathrm{SR}}$ and $\boldsymbol{\partial}\mathbf{T}_{\mathrm{SR}}$ have been converged, the ab parallelized components are gathered on the root process and redistributed to enable computation of $\overline{\mathbf{A}}(\mathbb{i}y_p)$ and $\boldsymbol{\partial}\overline{\mathbf{A}}(\mathbb{i}y_p)$. These are the principle output of SCREEN and are fed into CONTRACT to compute the scalar quantities $\overline{\alpha}(\mathbb{i}y_p)$ and $\boldsymbol{\partial}\overline{\alpha}(\mathbb{i}y_p)$ to update the running sums of $\overline{\omega}$ and $\boldsymbol{\partial}\overline{\omega}$.

1: **function** CONTRACT($\overline{\mathbf{A}}$,$\boldsymbol{\partial}\overline{\mathbf{A}}$)
2: Compute $\overline{\alpha}_a$ with $\sum_{b=1}^{N} \overline{\mathbf{A}}_{ab}(\mathbb{i}\omega)$
3: Compute $\boldsymbol{\partial}_c\overline{\alpha}_a$ with $\sum_{b=1}^{N} \partial_c\overline{\mathbf{A}}_{ab}(\mathbb{i}\omega)$
4: Update $\overline{\omega}_a$ with $\frac{4}{\pi}\sum_{p=1}^{n} g_p \left[\frac{\overline{\alpha_a}(\mathbb{i}y_p)}{\overline{\alpha_a}(0)}\right]^2$
5: Update $\boldsymbol{\partial}_c\overline{\omega}_a$ with $\frac{8}{\pi}\sum_{p=1}^{n} g_p \left[\frac{\overline{\alpha}_a(\mathbb{i}y_p)\boldsymbol{\partial}_s\overline{\alpha}_a(\mathbb{i}y_p)}{[\overline{\alpha}_a^0]^2} - \frac{[\overline{\alpha}_a(\mathbb{i}y_p)]^2\boldsymbol{\partial}_s\overline{\alpha}_a^0}{[\overline{\alpha}_a^0]^3}\right]$
6: **end function**

We present the convergence of our MBD correlation energy as a function of δ in the left-hand panel of Figure 3.3. These numerical tests were run on a three atom strained water unit cell with quadrature size n, supercell cutoff r_s, and DFT convergence thresholds kept constant for all calculations. After roughly a cutoff of 10^{-4}, every order of magnitude decrease in δ appears to yield an order of magnitude improvement in energy accuracy. While we only present results for a unit cell of strained water, similar trends are observed in other systems. The implementation allows us to essentially set a desired energy cutoff, and force the algorithm satisfy this bound. This stands in contrast to previous schemes, which required the user to set two fixed cutoff distances heuristically. Our implementation sets 10^{-6} as the default cutoff, which is used for all calculations in this chapter unless otherwise stated.

3.3.4 Casimir-Polder quadrature

To transform Gauss-Legendre quadrature from the interval $x_p \in [-1, 1]$, to the semi-infinite interval $y_p \in [0, \infty)$, we map the abscissa $x_p \to y_p$ and weights $w_p \to g_p$ with an algebraic scaling:

$$y_p \in [0, \infty) \qquad y_p = L\frac{(1 + x_p)}{(1 - x_p)} \qquad x_p \in [-1, 1] \tag{3.12}$$

$$g_p = -\frac{2L}{(1 - x_p)^2} w_p \tag{3.13}$$

There are many different possible transformations to $[0, \infty)$, but the algebraic mapping is quite robust for quadrature of functions that decay algebraically in $|x|$ as $x \to \infty$.[339] Depending on the properties of the integrand, different mappings will yield optimal quadrature, and indeed the subject of improving quadrature or spectral methods with the use of conformal mappings is an active area of research (cf. Refs. 340,341). Since the isolated atom dynamic polarizability is expected to decay as $\alpha(\mathbb{i}\omega) \propto \frac{1}{\omega^2}$,[342] we found the algebraic scaling to be preferable. We examined several numerical quadrature schemes to assess the most accurate method of performing the Casimir-Polder integral. Unsurprisingly, we found that Gauss-Legendre quadrature was more accurate than Gauss-Laguerre or Gauss-Lobatto schemes.

The quadrature error can be adjusted by tuning both the scale parameter, L, and the number n of quadrature points. Based on the available atomic dynamic polarizability reference data in Derevianko et al.[342] and the free atom reference quantities used in the TS method, the quadrature method used in MBD should be able to integrate a response function with excitation frequencies in the range of $\omega_a \sim 0.06$ (potassium) to $\omega_a \sim 1.2$ (neon) (see Figure 3.4). We found that a scaling parameter of $L = 0.6$ worked best across a wide range of isolated atomic systems in numerical tests and also performed well when integrating an analytic trial function corresponding to the Casimir-Polder integral of a

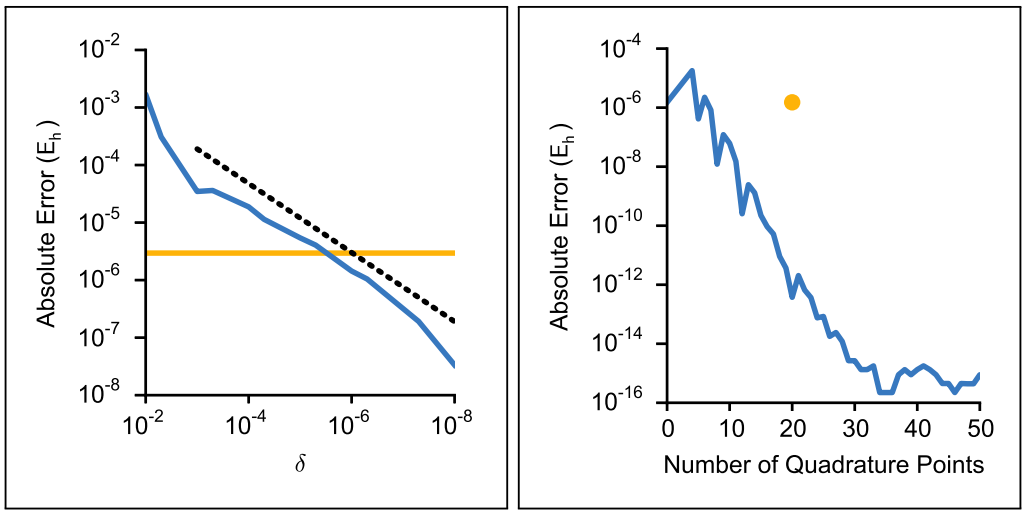

Figure 3.3: Absolute error in the total MBD correlation energy for a periodic simulation of strained water **Left:** as a function of changing the max-norm cutoff, δ, shown in blue. For reference we provide a linear relationship with slope 0.6 (dotted line), and a horizontal yellow line showing the error achieved by using a fixed 200 Å radius supercell cutoff as is done in the FHI-aims implementation of MBD. **Right:** as a function of the number of quadrature points included in our scaled Gauss-Legendre scheme, shown in blue. The energy converges to machine precision at 30 quadrature points. For reference we provide a yellow point showing the error achieved with the 20-point quadrature scheme used in the FHI-aims implementation of MBD. Our quadrature scheme achieves the same error with fewer than half the number of quadrature points.

single frequency dipole oscillator:

$$C_6(\omega_a) = \frac{3}{\pi}\int_0^\infty \left[\frac{f}{[\omega_a^2 - (\mathbb{i}\omega)^2]}\right]^2 \mathrm{d}(\mathbb{i}\omega) = \frac{3}{4}\frac{f^2}{\omega_a^3}. \tag{3.14}$$

Using this scaling factor, we have explored the energy convergence as a function of number of quadrature points. Our point of comparison for the quadrature convergence is the MBD correlation energy computed with 450 quadrature points. In the right-hand panel of Figure 3.3, we present a plot of the convergence for a periodic simulation of a single strained water molecule in a small cubic unit cell. The correlation energy appears to converge to machine precision with just 30 quadrature points. In integrating the trial function of Eq. (3.14) we observed similar sharp dips and recoveries in the quadrature error, corresponding to optimal tuning conditions where a small n quadrature scheme happens to exactly integrate a given function. This tends to occur when the scale factor and excitation frequency are equally balanced. To achieve convergence of $10^{-12}E_h$, we see

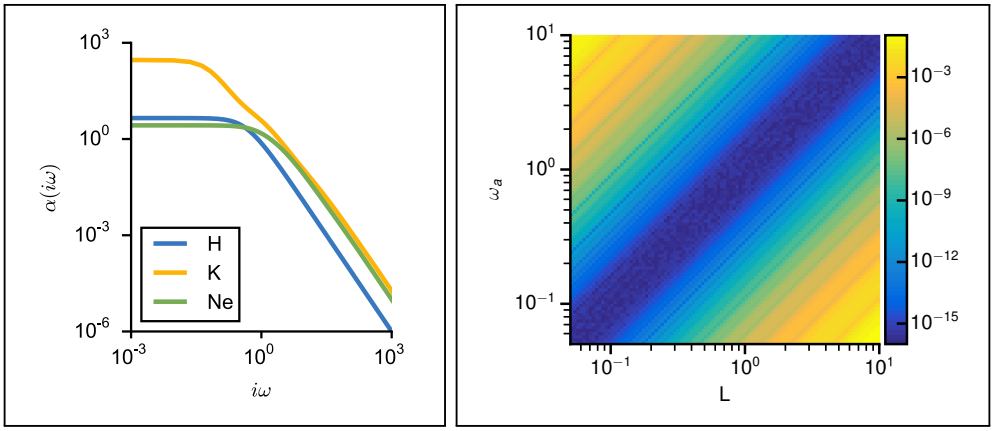

Figure 3.4: Left: Dynamic polarizability $\alpha(\mathbb{i}\omega)$ for hydrogen, potassium and neon. Notice the decay at large imaginary frequency obeys the expected $\left(\frac{1}{\omega}\right)^2$ behavior. Data from Ref. 342. **Right:** Quadrature error achieved on the Casimir-Polder integral for a dipole oscillator (Eq. (3.14)) with $n = 23$ algebraically scaled Gauss-Legendre points as a function of scale parameter L and excitation frequency ω_a.

that we only need 20 quadrature points. Given how cheap this integral is in comparison to the real-space supercell construction and diagonalization of $\mathbf{C}^{\mathrm{MBD}}$, $n = 20$ quadrature points represents a nice balance of accuracy and efficiency for the program default. It may be desirable to use fewer quadrature points for larger clusters, gas phase molecular dynamics calculations, where the Casimir-Polder integration loop will be a significant portion of the MBD computation cost; in these cases the user may select a different value of n through the keyword `mbd_vdw_n_quad_pts`.

While some quadrature schemes omit the zero point, $y_p = 0$, it is important to involve this frequency in the rsSCS loop since the MBD Hamiltonian requires the screened static dipole polarizabilities $\{\overline{\alpha}(0)\}$. It is also important to check whether any of these static polarizabilities have become negative, because this is unphysical and usually indicates that at the vdW radii of at least two nuclei overlap and the geometry should be checked. If even one element of the $\overline{\alpha}(0)$ array becomes negative, our MBD implementation terminates the calculation. At the end of the frequency integration loop (cf. Figure 3.1), we have the final set of $\overline{\omega}$, and $\boldsymbol{\partial}\overline{\omega}$, which through summation yield the non-interacting energy and forces.

3.4 The Interacting Energy

With the computation of the non-interacting energies completed, our next task is to construct the interaction Hamiltonian, $\mathbf{C}^{\mathrm{MBD}}$. Construction of this matrix starts with converging the long-range dipole-dipole interaction tensor, $\overline{\mathbf{T}}_{\mathrm{LR}}$, for all atom-atom pairs using the same max-norm cutoff procedure that we described above for $\mathbf{T}_{\mathrm{SR}}$ (cf. Eqs. 3.5, 3.7). With the converged dipole tensors, we then loop over the upper triangle of the Hamiltonian and fill it with the relevant precomputed screened static polarizabilities, $\overline{\alpha}(0)$, and screened excitation frequencies, $\overline{\omega}$. Finally, the interacting energy is computed in the subroutine InteractingEnergy by diagonalizing $\mathbf{C}^{\mathrm{MBD}}$ and summing the square root of the eigenvalues $\{\lambda\}$. The interacting forces require multiplying the derivative of the Hamiltonian by the eigenvectors of the Hamiltonian, $\boldsymbol{\mathcal{X}}$, and their transpose, $\boldsymbol{\mathcal{X}}^{\top}$, on either side, (cf. Eqs. 2.40 and 2.41). In pseudocode, the construction of $\mathbf{C}^{\mathrm{MBD}}$ and the computation of the interaction energy proceed as follows:

function ConstructHamiltonian($\overline{\alpha}_0$, $\overline{\omega}$)
    Compute work distribution map for $\mathbf{T}_{\mathrm{LR}}$ and $\boldsymbol{\partial}\mathbf{T}_{\mathrm{LR}}$
    Build $\mathbf{T}_{\mathrm{LR}}$ and $\boldsymbol{\partial}\mathbf{T}_{\mathrm{LR}}$ with Eqs. (2.36, 2.26, 2.54) (periodic convergence)
    Gather $\mathbf{T}_{\mathrm{LR}}$ and $\boldsymbol{\partial}\mathbf{T}_{\mathrm{LR}}$
    Distribute $\mathbf{T}_{\mathrm{LR}}$ and $\boldsymbol{\partial}\mathbf{T}_{\mathrm{LR}}$
    Build $\mathbf{C}^{\mathrm{MBD}}$ with Eq. (2.18)
    Build $\boldsymbol{\partial}\mathbf{C}^{\mathrm{MBD}}$ with Eq. (2.41)
end function
function InteractingEnergy($\mathbf{C}^{\mathrm{MBD}}$,$\boldsymbol{\partial}\mathbf{C}^{\mathrm{MBD}}$)
    Diagonalize $\mathbf{C}^{\mathrm{MBD}}$
    Sum $\sqrt{\lambda}$ [interacting energy]
    Sum $\boldsymbol{\partial}\lambda$ with $\frac{1}{2}\mathrm{Tr}\left[\boldsymbol{\Upsilon}^{-1/2}\boldsymbol{\mathcal{X}}^{\top}\boldsymbol{\partial}_c\boldsymbol{C}^{\mathrm{MBD}}\boldsymbol{\mathcal{X}}\right]$ [interacting forces]
end function

After InteractingEnergy has computed the energy and forces due to the interacting modes, the final expressions for E_{MBD} and $\mathbf{F}_{\mathrm{MBD}}$ are evaluated by summing interacting and non-interacting terms. Because these interacting modes can be thought of as normal modes of the coupled fluctuating dipole model Hamiltonian, to converge the MBD energy for a periodic system we need to construct a supercell that supports long-wavelength,

delocalized, modes. Ideally this procedure should be performed in k-space, but in the present implementation we use a real-space construction.

3.4.1 The real-space supercell procedure

We now turn our attention to the construction of the supercell that is used to build $\mathbf{C}^{\mathrm{MBD}}$ and $\overline{\mathbf{T}}_{\mathrm{LR}}$. If the simulation cell is less than r_s on a side, a supercell is constructed from the simulation cell, to enable long-wavelength normal modes of $\mathbf{C}^{\mathrm{MBD}}$.

The supercell is constructed by tiling the simulation cell into the positive octant as shown in Figure 3.5 c. The number of tilings in each direction are chosen by taking the integer ceiling of the supercell cutoff r_s divided by the lattice vector lengths:

$$\begin{aligned} n_a &= \lceil r_s/\|\mathbf{a}\| \rceil \\ n_b &= \lceil r_s/\|\mathbf{b}\| \rceil \\ n_c &= \lceil r_s/\|\mathbf{c}\| \rceil \end{aligned} \tag{3.15}$$

Some materials, such as graphite, have marked anisotropy in terms of which crystallographic directions support collective dipole modes most strongly due to the layered structure. In graphite $\|\mathbf{c}\|$ is larger than $\|\mathbf{a}\|$, so this tiling scheme will result in more copies of the unit cell in the ab plane. As the supercell size is increased, it will tend toward equal side-lengths, while maintaining the angular parameters of the simulation unit cell, in contrast to a spherical cutoff construction. Since we do not know *a priori* which crystal directions will support the most important long wavelength normal modes, this tendency of the supercell toward equal side lengths is beneficial.

While we have no rigorous relationship between r_s and the numerical uncertainty in the MBD energy, we have observed that r_s values in the range of $\sim 25 - 30$ Å are typically sufficient to converge the MBD energy to within about 10^{-4} $\mathrm{E_h}$ (10 meV) for 3D systems. However, Tkatchenko and coworkers have observed that 2D systems such as graphene, can support much longer wavelength collective dipole oscillations, and may require a larger

cutoff to appropriately resolve all modes. They attribute the difference in required supercell size between two and three dimensional systems to the damping that is introduced in 3D systems by coupling to the out-of-plane atoms.*

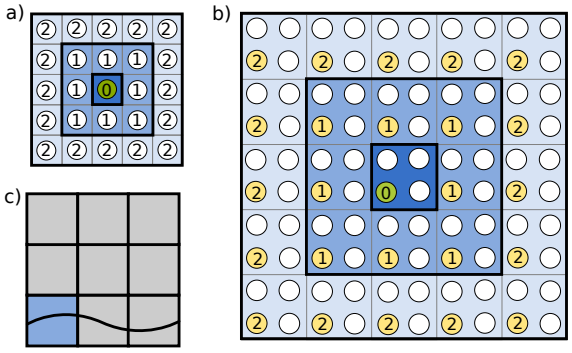

Figure 3.5: **a)** Lattice summation over successive shells of the unit cell to converge $\mathbf{T}_{\mathrm{SR}}$. Periodic images of the central green atom are numbered with their shell index. **b)** Lattice summation over successive shells of a 2×2 supercell to converge $\overline{\mathbf{T}}_{\mathrm{LR}}$. Periodic images of the atom marked in green are shown in yellow and numbered with their shell index. **c)** Schematic showing that a 3×3 supercell (grey) is built by tiling the unit cell (blue) into the positive octant, and will allow for longer wavelength normal modes.

We previously asserted that this supercell construction dominates the computational cost of MBD because the most computationally expensive aspect is the matrix diagonalization. We are now able to make this statement more concrete. Because the system is periodic, the tiled atoms will have the same polarizabilities and characteristic frequencies as their counterparts in the original unit cell. There are $N_{\mathrm{sc}} = n_a \times n_b \times n_c \times N$ atoms in the supercell, where N is the number of atoms in the simulation unit cell. Given that matrix-matrix operations generally scale as N^3, the super-lattice construction carries an asymptotic computational cost of $\mathcal{O}(9N_{\mathrm{sc}}^3)$ and a memory cost of $\mathcal{O}(9N_{\mathrm{sc}}^2)$. The memory cost for the ionic forces on the N atoms in the original unit cell is then $\mathcal{O}(9N_{\mathrm{sc}}^2 \times 3N)$. For moderately sized systems (fewer than 10,000 atoms in the supercell), this memory cost is not a problem for our implementation when run on computer clusters with 2GB or more of available memory per node. However, this memory cost can represent a significant problem for smaller computer clusters or when an insufficient number of MPI processes are requested. Future work will address a

*Personal communications, May 2015.

reciprocal-space algorithm for avoiding this real-space supercell procedure. Briefly, one would construct a $3N \times 3N$ matrix for each **k**-point of interest in the Brillion zone and diagonalize each of them to compute the relevant contribution to the MBD energy (for a total of $(n_a \times n_b \times n_c)^3$ diagonalizations of a $3N \times 3N$ matrix, rather than the single $3N_{\text{sc}} \times 3N_{\text{sc}}$ matrix diagonalization corresponding to the real-space supercell).[137]

Convergence with respect to the the supercell size is more difficult to automate than the dipole-dipole interaction, because bigger unit cells cannot simply be added onto old ones as a test for convergence. This means that the supercell cutoff radius r_s is a very significant adjustable parameter that should be investigated independently for any periodic material that is studied with MBD. We have explored the convergence of the MBD energy as a function of supercell size, and present the results for graphite and graphene in Figure 3.6.

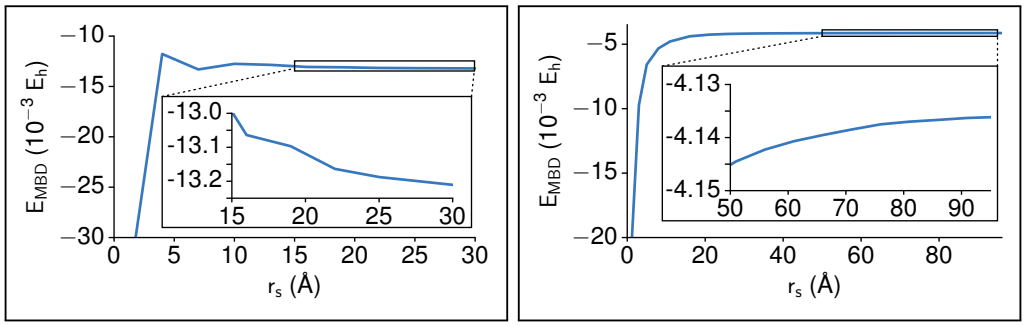

Figure 3.6: Convergence of the total MBD correlation energy as a function of supercell cutoff radius, r_s, for periodic simulations of graphite (**left**) and graphene (**right**). A tight max-norm cutoff of $\delta = 10^{-7}$ was required to achieve numerical stability for $r_s \gtrsim 30$ Å.

These results seem to indicate that the MBD energy approaches $2 - 5$ mE$_\text{h}$ of the converged value within the first 10 Å tiling, but still trends downward for graphite and upward for graphene. We extended the supercell cutoff for graphene out to much larger distances than in graphite both because of past assertions that 2D systems support longer-wavelength collective polarization modes than 3D materials (conveniently, the computational cost of a 2D supercell is dramatically reduced since the number of atoms in the cell only grows quadratically). At large supercell cutoffs the fluctuations occur on the scale of hundredths of a milliHartree, which can usually be neglected given the convergence tolerances used in the self-consistent field cycle of many simulations.

3.5 The MBD Energy

We conclude our tour of the MBD algorithm with a brief comment about cancellation error. Since the MBD correlation energy is computed by subtracting two large and nearly equal quantities, namely the interacting and non-interacting energies, it is a textbook example of a quantity that is subject cancellation, an error that occurs in floating-point arithmetic in which the relative error committed in subtraction can be so large that most of the digits become meaningless. In practice we observe that the MBD energy can be converged to $\sim 10^{-4}$ $\mathrm{E_h}$ without too much difficulty. Furthermore, the system size for which one would suffer serious loss of precision in the MBD energy is so large that one would first encounter instability in diagonalizing $\mathbf{C}^{\mathrm{MBD}}$, since for a large supercell $\mathbf{C}^{\mathrm{MBD}}$ has columns that are close to linearly dependent. However, to get a feel for the MBD algorithm it is useful to realize that both the interacting and non-interacting energy sums grow linearly with system size (see Figure 3.7). If Bloch wave summation is used to replace the real-space supercell construction in future MBD implementations, thereby enabling application to much larger system sizes, it may become necessary to readdress this issue of cancellation error and apply compensated summation techniques such as cascading accumulators,[343] pair summation, or Kahan summation.[344]

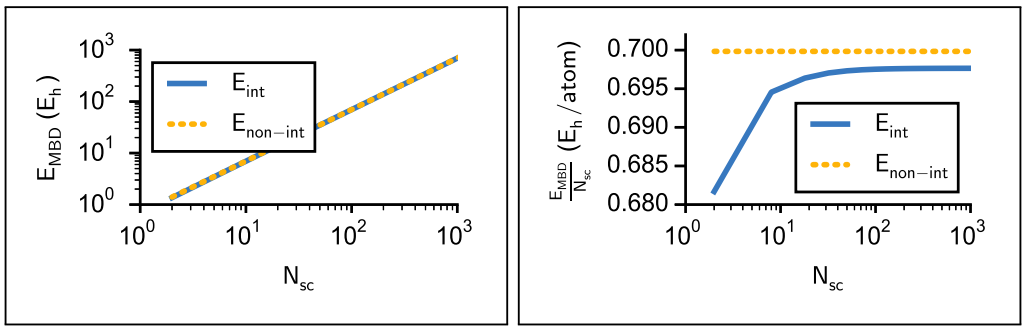

Figure 3.7: Left: Interacting and non-interacting energy for graphene as a function of N_{sc}, the number of atoms in the supercell. Both component of the MBD energy grow linearly with the number of atoms in the supercell. **Right:** Interacting and non-interacting energy per atom for graphene as a function of N_{sc}, the number of atoms in the supercell. As every atom in the supercell has identical non-interacting screened frequencies $\overline{\omega}_a$, the non-interacting energy per atom is perfectly constant. The interacting energy per atom converges quickly as the supercell grows to include hundreds of atoms.

3.6 Unit Cell Forces and Stress

Thus far, we have limited our discussion of MBD forces to the gradients of E_{MBD} with respect to the nuclear coordinates, *i.e.* the ionic forces $\mathbf{F}_{\mathrm{MBD}} \equiv -\boldsymbol{\nabla}_{\boldsymbol{\mathfrak{R}}} E_{\mathrm{MBD}}$. For a periodic system, the Cartesian coordinates $\boldsymbol{\mathfrak{R}}_c$ of an atom c in the unit cell are written in terms of the unit-cell vectors, stored in the matrix $\mathbf{h}$, and the fractional coordinates, $\mathbf{x}_c$, as:

$$\mathfrak{R}_c^i = \sum_j h^{ji}\, x_c^j \tag{3.16}$$

Gradients of the MBD energy with respect to the unit-cell vectors are required to enable MBD inclusive unit-cell optimization. These "unit-cell forces" will be labeled $\mathbf{H}_{\mathrm{MBD}} \equiv -\boldsymbol{\nabla}_{\mathbf{h}} E_{\mathrm{MBD}}$.

In the context of evaluating the forces on a periodic system's unit cell, we must consider both changes in the size and shape of the cell. Since the fractional coordinates of the atoms remain fixed while the lattice vectors change, we use the chain rule to convert the Cartesian coordinate ionic MBD forces into gradients with respect to h^{ji} in fractional coordinates,

$$\frac{\partial E_{\mathrm{MBD}}}{\partial h^{ji}} = \sum_{c=1}^{N} \frac{\partial E_{\mathrm{MBD}}}{\partial \mathfrak{R}_c^i} \frac{\partial \mathfrak{R}_c^i}{\partial h^{ji}} = \sum_{c=1}^{N} \frac{\partial E_{\mathrm{MBD}}}{\partial \mathfrak{R}_c^i} x_c^j \tag{3.17}$$

$$\Rightarrow \left[\mathbf{H}_{\mathrm{MBD}}\right]^{ij} = \sum_{c=1}^{N} \mathbf{F}_c^i x_c^j, \tag{3.18}$$

where $\mathbf{H}_{\mathrm{MBD}}$ is the 3×3 matrix of unit-cell forces is built from the ionic MBD force matrix $\mathbf{F}_{\mathrm{MBD}}$ by tracing out atom c.

Unit-cell optimizations are frequently performed at non-zero external pressure. The stress due to a homogeneous deformation $\mathbf{r} \to (1+\epsilon)\mathbf{r}$ is $\sigma = -\frac{1}{\Omega}\frac{\partial E}{\partial \epsilon}$, where Ω is the unit cell volume. This stress can be computed from the ground state wavefunction via the Hellman-Feynman theorem without needing to know how the electrons or the internal coordinates will re-adjust.[345–347] For evaluating the pressure in the unit-cell due to the

MBD correction, we convert the unit-cell forces into components of the stress tensor,

$$\sigma^{ij}_{\mathrm{MBD}} = -\frac{1}{\Omega}\sum_k \frac{\partial E_{\mathrm{MBD}}}{\partial h^{ik}} h^{jk} \qquad \Leftrightarrow \qquad \sigma_{\mathrm{MBD}} = \frac{1}{\Omega}\mathbf{H}_{\mathrm{MBD}}\mathbf{h}. \tag{3.19}$$

The correction σ_{MBD} is an additive correction to the usual DFT stress tensor.

3.7 Computational Details

We have implemented the periodic MBD energies, analytical ionic forces, unit-cell forces and stresses in a development version of Quantum ESPRESSO v5.1rc2 (QE).[262] All calculations were performed in the PWscf module with the Perdew, Burke, and Ernzerhof (PBE) exchange-correlation functional,[182,183] and Hamann-Schlueter-Chiang-Vanderbilt (HSCV) norm-conserving pseudopotentials[263–265] obtained from the FPMD pseudopotential repository[266] (and converted to UPF format using a modified version of qso2upf v1.2[267]). Details of the convergence tolerances, wavefunction kinetic energy cutoffs ($\mathrm{E_{cut}} = \frac{1}{2}\|\mathbf{k}+\mathbf{G}\|^2_{\mathrm{max}}$), MBD parameters, and unit cell sizes used for each system are given in tables 3.1 and 3.2. Since QE uses Rydberg energy units (1 Ry = $\frac{1}{2}$ $\mathrm{E_h}$), we report the tolerances in these units.

Table 3.1: Convergence tolerances and unit cell sizes used in PWscf MBD convergence calculations, reported in Rydberg atomic units (1 Ry = $\frac{1}{2}$ $\mathrm{E_h}$).

	Strained water	Graphene	Graphite
$\mathrm{E_{scf}}$ (Ry)	10^{-12}	10^{-10}	10^{-10}
$\mathrm{E_{cut}}$ (Ry)	150	80	80
k-points	Γ	$4\times4\times1$	$4\times4\times2$
MBD n	20 | variable	20	20
MBD δ	variable | 10^{-6}	10^{-7}	10^{-7}
MBD r_s (Å)	–	variable	variable
vacuum axis	x,y,z	z	none
Cell Size ($\mathrm{a_0}$)	$a = 4.7243$	$a = 4.6466$ $c/a = 27.134$	$a = 4.6466$ $c/a = 2.700$
Cell Shape	cubic	hexagonal	hexagonal

All geometry optimizations were performed using the quasi-Newton Broyden-Fletcher-Goldfarb-Shanno (BFGS) algorithm,[268–271] with default parameters. Variable cell relaxations were performed using the modified cutoff procedure of Bernasconi *et al.*[348] in which $(\mathbf{k}+\mathbf{G})^2$ is replaced by,

$$(\mathbf{k}+\mathbf{G})^2 \rightarrow (\mathbf{k}+\mathbf{G})^2 + q_{\text{cutz}}\left(1+\frac{\text{erf}\left((\mathbf{k}+\mathbf{G})^2 - E_{\text{cfixed}}\right)}{q_{2\sigma}}\right).$$

All calculations employing a Monkhorst-Pack k-point mesh were centered on the Γ point. All calculations were run using a charge density cutoff of $\rho_{\text{cut}} = 4\text{E}_{\text{cut}}$. Calculations on graphite and graphene used Marzari-Vanderbilt cold smearing with a Gaussian width of 0.2.[349] Since the present implementation of the Hirshfeld partitioning in the TS-vdW module can have errors with k-points, the graphite unit-cell optimization was run with a $4 \times 4 \times 2$ supercell.

Table 3.2: Convergence tolerances and unit cell sizes used in PWscf geometry optimizations, and variable cell relaxations, reported in Rydberg atomic units (1 Ry = $\frac{1}{2}$ E_h).

	Nucleobases on Graphene (7×7)	Ice Ic	Graphite ($4 \times 4 \times 2$)
E_{scf} (Ry)	10^{-8}	10^{-5}	10^{-7}
E_{cut} (Ry)	100	150	80
E_{cfixed} (Ry)	–	130	108
q_{cutz} (Ry)	–	200	30
$\text{q}_{2\sigma}$ (Ry)	–	15	3
E_{tot} (Ry)	10^{-8}	10^{-5}	10^{-7}
F_{tot} (Ry/a_0)	10^{-4}	5×10^{-4}	5×10^{-4}
k-points	Γ	Γ	Γ
MBD n	12	12	12
MBD δ	10^{-5}	10^{-5}	10^{-5}
MBD r_s (Å)	–	10	10
vacuum axis	z	none	none
Cell Size (a_0)	$a = 32.53$ $c/a = 1.594$	$a_{\text{initial}} = 24$	
Cell Shape	hexagonal	cubic	hexagonal

3.8 Results and Discussion

Having thoroughly tested all aspects of the MBD gradients for periodic simulations, and addressed their convergence with respect to numerical quadrature, periodic convergence of the dipole-dipole interactions, and periodic convergence of the MBD energy using the real-space supercell, we turn our attention to three example systems for demonstrations of the performance of our code. By optimizing the ionic positions of nucleobases on top of a 7×7 supercell of graphene, we demonstrate that the parallel implementation of MBD forces can easily handle systems of > 110 atoms and correctly accounts for reduced dimensionality. We next consider the unit-cell optimization of a $4 \times 4 \times 2$ supercell of graphite, and show that MBD gives results in closer agreement to the well known experimental answer than the pairwise TS method. Finally, we optimize both the ionic positions and unit-cell vectors of a 192 atom unit cell model of cubic ice and show that again MBD outperforms TS with regard to agreement with the experimental cell parameters. The primary purpose of these applications is to demonstrate the efficiency of our new implementation of MBD for periodic systems as the efficacy of the MBD methodology for treating molecular crystals has been discussed extensively elsewhere.[109–112,119,350]

As a point of completeness we should point out that at present, the TS-vdW module in QE, which is used to perform the Hirshfeld partitioning, has a few serious bugs when treating k-point sampling of the Brilloiun zone. As a result, we have been limited in our application of MBD gradients to unit-cell optimizations of systems with sufficiently large simulation cells to be treated as Γ point only. As soon as this issue is resolved, we anticipate benchmarking MBD gradients on unit-cell optimizations of many noncovalent interaction dominated crystal systems, such as rare gas crystals and molecular crystals from the sets of Binns *et al.*,[351] Bj orkman *et al.*,[116] and the well known X23 benchmark set.[108,109,352,353]

3.8.1 Physisorption of nucleobases on graphene

Understanding the interactions between carbon nanostructures and the DNA and RNA nucleobases adenine (A), cytosine (C), guanine (G), thymine (T), and uracil (U) attracted significant attention in recent years, with considerable effort devoted to predicting the physisorption binding energies of each nucleobase on graphene and related nanostructures .[354–368] In a comparative study of vdW inclusive DFT approaches, Le *et al.* found that although different methodologies disagree on the precise values of binding energies, most methods agree that the ordering of interaction strengths of the nucleobases on graphene follows the order G > A > T > C > U or G > A > C > T > U,[366] in agreement with the results of experimental titrations.[356,364]

Table 3.3: Binding distances d (Å) between graphene and nucleobases optimized with DFT & DFT+vdW methods.

	PBE			rPW86	M06-2X[b]	B97-D[c]
Nucleobase	MBD	TS[a,d,e]	D3[d]	vdW-DF2[d]	–	–
A	3.416	3.29, 3.28, 3.27	3.38	3.37	3.137	2.99
C	3.303	3.27, 3.31, 3.23	3.38	3.38	3.124	2.89
G	3.350	3.26, 3.25, 3.23	3.33	3.33	3.132	2.87
T	3.463	3.29, 3.34, 3.23	3.42	3.41	3.103	2.94
U	3.365	–, 3.30, –	3.38	3.37	–	2.91

[a] Ref. 363, [b] Ref. 361, [c] Ref. 365, [d] Ref. 366, [e] Ref. 357

The potential energy surface (PES) for a nucleobase physisorbed on graphene is quite shallow, with a energy differences of $\sim 0.04 - 0.10$ eV between the peak and the valley.[360,362] As a result, the equilibrium geometry adopted by the nucleobases when adsorbed on top of graphene can vary somewhat depending on the starting configuration and the method of treating dispersion interactions. For instance, Antony and Grimme found a nearly perfect AB stacking for all nucleobases using B97-D,[365] while Gowtham *et*

al. found a significantly rotated structure for guanine and cytosine (adopting more of an AA stacking pattern) using LDA[362] and Cho *et al.* found a rotated structure for thymine using PBE+TS.[357] Even for AB configurations, slight deviations from perfect AB base stacking are expected, due to both the incommensurate five- and six- membered rings of the bases with respect to the graphene lattice, as well as the presence of nitrogen heteroatoms and side groups that alter the electronic structure.[362]

All five nucleobases adopt a configuration with their planes oriented approximately parallel to the graphene sheet (the methyl groups cause a slight tilt), with a separation of $3.0 - 3.5$ Å. As we saw in Chapter 2, the equilibrium distance for $\pi - \pi$ stacked systems can be quite sensitive to the details of a vdW inclusive functional. To demonstrate that our periodic MBD gradients code works efficiently for systems of reduced dimensionality, we optimized the adsorbed structures of all five nucleobases on top of a 7×7 unit cell of graphene (resulting in 110-113 atoms in the unit cell). Since it would be safe to optimize such a system by holding the graphene plane fixed and letting only the nucleobase relax, this application is not one that would be strictly out of reach for previous MBD implementations. However, our aim here is to demonstrate that our parallelized periodic MBD code can treat a large system quickly, without demonstrating unexpected distortions, and properly accounting for the 2D periodicity of the system. The optimized structures are shown in Figure 3.8 and the binding distances are stated in Table 3.3. We find that the PBE+MBD optimized binding distances are larger than those of previously reported DFT-D methodologies and are in closer agreement with the vdW-DF method. Since there has not been an experimental or high-level wavefunction theory determination of this binding curve, we cannot regard any of these methodologies as a benchmark value. Burland *et al.* using the vdW-DF method together with the PBE functional find a binding distance for Adenine of 3.5 Å[359] while Le *et al.* find binding distances of $3.33 - 3.38$ Å.[366] It is well known that the vdW-DF and vdW-DF2 methods[†] consistently provide small overestimation of equilibrium distances for small vdW bound complexes,[72,99] so our

[†]The original vdW-DF method used the revPBE exchange functional, while vdW-DF2 uses rPW86 exchange.[42,72]

present PBE+MBD binding distances may be seen as unfavorable. However, both MP2 and hybrid functionals such as B3LYP and wB97X-D have been shown to give binding distances on the order of ~ 3.5 Å,[362,367] so while they are on the high side, our PBE+MBD distances are within the range of other predictions. Since the minima found in our optimizations are quite different from the typical AB stacking motifs found in other studies, this system should be studied more carefully with MBD, by starting optimizations from several initial configurations, before any firm conclusions can be drawn about how the many-body methodology differs from effective pairwise treatments of this system.

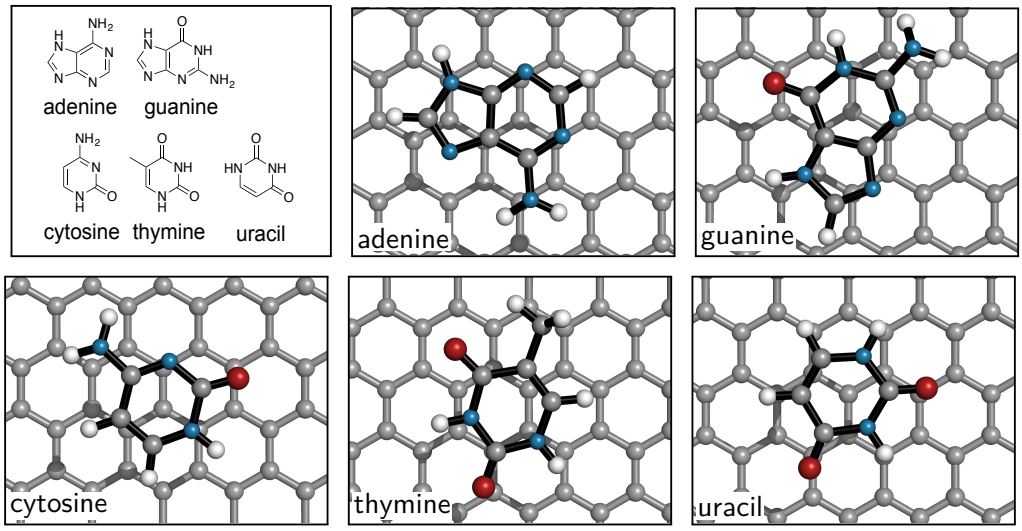

Figure 3.8: Top Left: Chemical structures of the five nucleobases. **Remaining Panels:** Top views of the optimized structures of nucleobases adsorbed on graphene with the bonds in the nucleobase shown in black for visual contrast.

3.8.2 Graphite unit cell optimization

The layers of materials such as graphite are held together purely by dispersion interactions. Since the covalent bonds within the *ab* plane are much stiffer than the van der Waals interactions in the *c* direction, graphite displays a strongly anisotropic compressibility, which varies significantly with temperature. The thermal expansion of graphite was studied quite extensively in the late 1940s and early 1970s, both as a simple system of interest for testing physical models of heat capacity and lattice dynamics, and

also for the material's importance to the nuclear industry.[369–377] More recently, graphite has received considerable attention as a material for benchmarking vdW inclusive DFT methodologies since the prediction of the interlayer binding energy (or the closely related exfoliation and cleavage energies) presents a particular challenge for many correlation methods. Graphitic nanomaterials were among the first examples of systems for which many-body vdW effects were realized to be qualitatively necessary.[26]

Dobson *et al.* have recently shown that the interaction between graphene sheets as they are separated shows many-body effects beyond those captured by the random-phase approximation (RPA).[117] In particular, they find that the long-distance graphene-graphene dispersion interaction is substantially less than the RPA prediction and is very sensitive to long-wavelength in-plane many-body modes that renormalize the velocity of the massless Dirac fermions in graphene.[117] Since MBD is formally equivalent (through the adiabatic connection fluctuation dissipation theorem) to the RPA,[84,87,88] this suggests that there may be many-body effects relevant to the properties of graphene and graphite that the DFT+MBD methodology will miss.

Since the *c*-axis of graphite expands considerably with temperature, it is important to use low temperature experimental data as a reference for comparison to electronic structure predictions of the unit cell size at 0 K. In 1970 Bailey and Yates[378] examined the anisotropic expansion of well-ordered pyrolytic graphite down to 30 K; they find that the linear coefficient of expansion in the *c*-direction is $\alpha_{\parallel} = (3.8 \pm 0.8) \times 10^{-6}$ K^{-1}. Together with the fact that $\alpha_{\parallel}$ must go to zero as temperature approaches 0 K, this indicates that a low temperature measurement of the *c*-axis spacing of graphite should be a good proxy for the zero temperature spacing without the need for significant extrapolation. Baskin *et al.* measured the lattice constants of single crystal graphite at 4.2 ± 0.3 K and 78 ± 0.3 K using Cu Kα ($\lambda = 1.5418$ Å) X-ray radiation and determined $d(4.2\text{K}) = 3.3360(5)$ AA and $d(78\text{K}) = 3.3378$ Å with $a = 2.4589(5)$ Å at both temperatures.[379] Using the expansion coefficients of Bailey and Yates, we performed a nonlinear extrapolation of the 78 K interlayer spacing and found that it is consistent with a value of 3.336 Å at zero

temperature. Therefore, we take the 4.2 K measurement as our reference value.

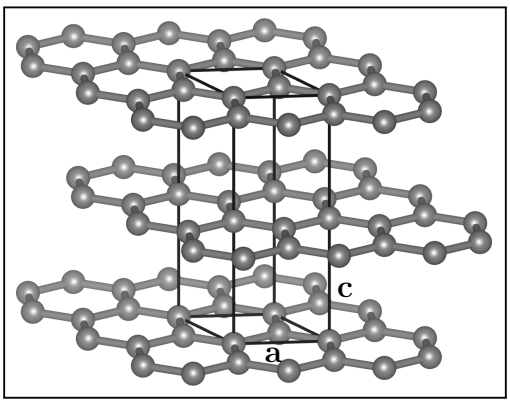

Figure 3.9: The unit cell of graphite, with the bonding atoms expanded outside the cell to show the AB stacking arrangement. The interlayer spacing is $c/2$ and the C–C bond distance is $a/\sqrt{3}$.

In considering the interlayer binding distance and exfoliation energy of graphite, GGA functionals tend to predict very weak or no binding at all, while LDA functionals predict approximately the right binding distance with too shallow a potential energy surface (though LDA yields surprisingly good predictions considering that there are no terms in LDA that should account for vdW interactions).[380] Almost all vdW inclusive treatments improve upon these deficiencies, though several authors have shown that inclusion of self-consistent screening[88,251] and many-body effects[86,88] can substantially renormalize the cohesive energy of graphite, bringing the predicted values into closer agreement with experimental[33,381,382] and quantum Monte Carlo estimates[383] than is found with nonlocal correlation approaches.[85,86,116,359,380,384]

We optimized the unit cell of graphite (shown in Figure 3.9) using a $4 \times 4 \times 2$ supercell with both PBE+MBD and PBE+TS.[‡] Since the atoms reside in positions that are constrained by the symmetry of the $P6_3/mmc$ space-group and the hexagonal bonding pattern of sp^2 hybridized carbon, the primary quantity of interest in optimizing the graphite unit cell is the interlayer spacing $d = c/2$. In Table 3.4 we compare our cell parameters to those obtained by many different authors using a variety of functionals and

[‡]When k-point integration becomes available we will check whether these results are converged since a $4 \times 4 \times 2$ supercell is somewhat smaller than desirable.

vdW correction schemes. We note that PBE is quite good at reproducing the C–C bond length of 1.42 Å and thus the a-axis length is well reproduced (results with the revPBE functional are less compelling in this regard). As previously stated, in the absence of a dispersion correction PBE predicts much too large an interlayer spacing $d \sim 3.9 - 4.9$ Å. The large variance in reported values is due to the very flat potential energy surface predicted by PBE. The revised GGAs, revPBE and PBEsol do better, but still have $> 3\%$ relative error in the interlayer spacing. The vdw-DF and vdW-DF2 nonlocal correlation methodologies tend to yield too large an interlayer spacing by $\sim 4 - 13\%$. The nonlocal correlation functional method VV10 and its revised variant both perform very well, giving relative errors of $\sim 2\%$ or less in the interlayer spacing. The outdated D2 method performs reasonably well. Since the revisions to the D3 method included parameterizing C_6 coefficients that distinguish between different hybridization states, we expect that PBE+D3 would perform as well or better than PBE+D2. We note that although the effectively pairwise PBE+TS method does extremely well, the relative error is increased when the self-consistently screened variant is used. This is surprising since the SCS procedure makes such a drastic improvement to TS for predicting many other quantities. The vdw-WF-QHO method of Silvestrelli *et al.* is, like MBD, based on coupled QHOs, but extracts its charge density partitioning using maximally localized Wannier functions rather that atomic Hirshfeld partitioning. Both vdW-WF-QHO and MBD perform extremely well relative to the experimental value and agree quite closely with the RPA result. Many more benchmarks of analytical MBD gradients for unit cell optimizations of dispersively dominated crystals should of course be performed, but we find this preliminary result quite encouraging since graphite has proven challenging for many vdW correction methods.

3.8.3 Cubic ice (Ic) unit cell optimization

Correctly reproducing the experimental phase diagram of water ice has proven to be extremely challenging for DFT because the energy differences between polymorphs are

Table 3.4: Optimized interlayer spacing, d, and lattice vector ratio, c/a, of graphite reported with various DFT and DFT+vdW methodologies. The relative percentage error ε_r is reported for both quantities. Note that we have rounded d to two decimal places since many authors did not provide greater precision and leave c/a blank where authors did not provide the optimized a value. Relative error in c/a is computed using the experimental value of $a = 2.4589(5)$ Å from Ref. 379.

d (Å)	c/a	$\varepsilon_r(d)$ (%)	$\varepsilon_r(c/a)$ (%)	Method	Reference
3.3360(5)	2.713(1)			Exp. (X-ray @ $4.2K$)	Ref. 379
3.34	–	0.1		PBE+RPA	Ref. 129
3.35	2.710	0.3	-0.1	PBE+MBD	present
3.33	–	-0.2	–	PBE+vdW-WF-QHO	Ref. 86
3.38	2.744	1.2	1.1	PBE+TS-SCS	Ref. 251
3.33	2.702	-0.1	-0.4	PBE+TS	present
3.33	2.703	-0.3	-0.4	PBE+TS	Ref. 385
3.34	2.715	0.1	0.1	PBE+TS	Ref. 251
3.23	2.622	-3.3	-3.4	PBE+D2	Ref. 386
3.37	–	1.0	–	PBE+D2	Ref. 116
3.45	–	3.3	–	PBE+vdW-DF	Ref. 116
3.91	–	17.0	–	PBE	Ref. 116
3.93	–	17.7	–	PBE	Ref. 380
4.25	3.451	27.2	27.2	PBE	Ref. 387
4.42	3.579	32.5	31.9	PBE	Ref. 386
4.90	3.982	46.9	46.8	PBE	Ref. 388
3.46	–	3.7	–	PBEsol	Ref. 380
3.58	2.877	7.2	6.1	revPBE	Ref. 384
3.55	–	6.4	–	revPBE+vdW-DF	Ref. 380
3.60	–	7.9	–	revPBE+vdW-DF	Ref. 116
3.76	–	12.7	–	revPBE+vdW-DF	Ref. 389
3.39	–	1.6		rPW86+VV10	Ref. 116
3.36	2.732	0.7	0.7	rPW86+rVV10	Ref. 85
3.41	–	2.2	–	rPW86+rVV10	Ref. 86
3.48	–	4.3	–	rPW86+vdW-DF2	Ref. 359
3.47	–	4.1	–	rPW86+vdW-DF2	Ref. 116
3.57	–	7.1	–	rPW86+vdW-DF2	Ref. 380
3.34	2.733	0.0	0.7	LDA	Ref. 388
3.34	2.738	0.1	0.9	LDA	Ref. 387
3.33	–	-0.2	–	LDA	Ref. 129
3.38	–	1.2	–	LDA	Ref. 116
3.27	–	-2.0	–	LDA	Ref. 380
3.234(3)	–	3.0		LRDMC [2x2x2]	Ref. 383

small and arise from the competing effects of hydrogen-bonding and vdW interactions.[390,391] Experimentally, the phase diagram of ice up to pressures of ~ 2 GPa is well established, but a sound theoretical description of the cohesive properties of several phases is still lacking.[390] Ice has 15 known polymorphs,[392] most of which are metastable or high pressure phases, the most recent of which was discovered in 2009.[393] Past work has shown that adding van der Waals corrections to DFT significantly improves the performance of many functionals for optimizing the unit cells and evaluating the thermodynamic stability of different polymorphs of ice, with small but significant improvements arising from three-body or many-body dispersion.[390,391,394–396]

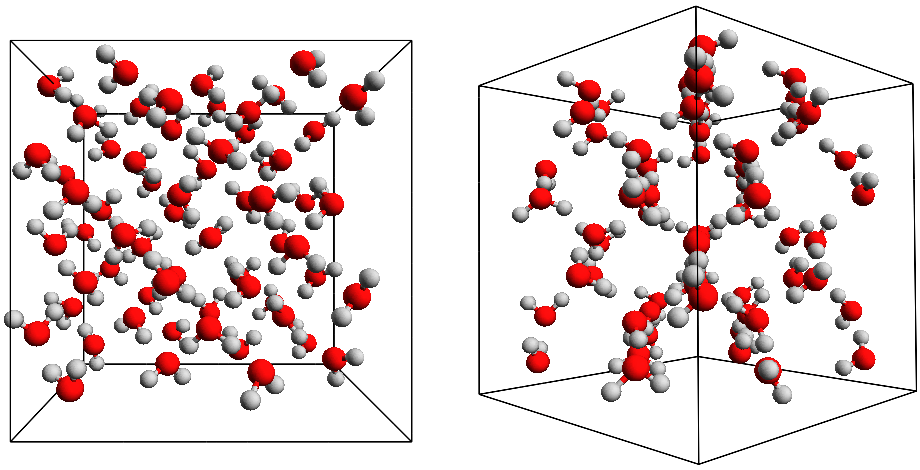

Figure 3.10: Two views of a 64 water model of the unit cell of ice I_c.

At ambient pressure, cooling water yields a hexagonal structure known as Ih. At lower temperatures, or when crystallized from supercooled water (hyperquenching),[397,398] confined in porous environments,[399,400] or heated from a vitrified state,[401,402] water crystallizes in a related metastable phase with cubic symmetry, called Ic. Ice Ic forms readily in many different environments, and is thought to exist in ice crystals in the upper atmosphere.[392,397,403–405] Structurally, Ih and Ic are quite similar, both containing layers of six-membered rings in an armchair configuration, but the stacking between these layers differs.[406] This similar lattice packing yields nearly identical static lattice and harmonic vibrational energies;[407] it is only when anharmonic effects are considered that the relative

thermodynamic stability of the I*h* over I*c* becomes apparent (I*h* is more stable by a few meV/H_2O).[408] Recently, a variety of spectroscopic and diffraction measurements, in addition to large-scale molecular dynamics calculations, have suggested that when supercooled water crystallizes to form "cubic ice," it actually forms a stacking disordered combination of ice I*c* and I*h*, rather than the pure form originally suggested by König,[409] making the relationship between these two phases a fascinating puzzle.[398,405,406,410–413] It should be noted that neither I*h* or I*c* is a proton-ordered state,[414] so any theoretical structure should be regarded as a model structure. The stacking disorder present in cubic ice is further reason to consider any model of well-ordered I*c* as a theoretical system.

Given the competition between hydrogen-bonding and dispersion forces, and the cooperativity that influences both of these interactions, we regard computing the molar volume of a metastable phase of ice to be a compelling check that our periodic MBD gradients are performing well for condensed phase simulations. In contrast to graphite, the thermal expansion of ice is small at low pressure,[415,416] *e.g.*, the cell volume of ice I*h* changes by 1.65% from 10-265 K.[417] The density of ice I*c* is almost identical to that of ice I*h* due to their similar packing structures.[418] Santra *et al.* have already thoroughly benchmarked the performance of PBE+MBD for studying the phase diagram of the proton ordered polymorphs of ice, so in this work we only report the optimization of ice I*c*.[391] Our aim is not to characterize the physical properties of ice, but rather to confirm that the behavior of our periodic MBD gradients code yields a reasonable structure for the chosen model of the I*c* system. We used a 64 water model unit cell of ice I*c*, shown in Figure 3.10, that is large enough to not require k-point integration. Containing 192 atoms, this unit cell is far larger than past numerical treatments of MBD gradients would have been able to treat. We allowed all atom positions and unit cell vectors to relax. The results of our optimizations are given in Table 3.5 and compared to the results of experimental studies and other DFT+vdW treatments. Although "pure" cubic ice likely does not exist due to the stacking faults present in the structure, the experimental molar volumes suggested for ice I*h* and ice I*c* are very similar, so we feel comfortable using the

value of $V_0 \sim 19.3$ cm^3/mol as a reference. The bare PBE functional provides too dense a structure, while various vdW corrections give larger molar volumes. We find that the MBD treatment yields a surprisingly large difference of 0.1 cm^3/mol difference in molar volume relative to TS, which is on the same order of magnitude as the increase in molar volume due to the zero-point motion of hydrogen.[394] The molar volume predicted by PBE+MBD is still considerably too small, which should not be surprising given the well known tendency of PBE to over-bind hydrogen-bonds. The larger volume predicted by vdW-DF2 is expected given the properties of both the nonlocal correlation functional and the underlying rPW86 exchange functional. We are actively investigating other phases of ice and our preliminary investigation of ice Ic with PBE+MBD suggests that there may be exciting discoveries ahead for structural investigations using analytical MBD gradients for condensed phase simulations.

Table 3.5: Unit cell parameters of ice Ic optimized with various DFT and DFT+vdW methodologies. We report both the lattice parameter a, and the molar volume V_0. The lattice parameter of our 64 H_{20} unit cell has been divided by two for comparison to the conventional 8 H_2O unit cell. Values in parentheses have been corrected for hydrogen zero-point motion.

a (Å)	V_0 (cm^3/mol)	Method	Reference
	19.30	Exp. Ih @ 13K	Ref. 415
	19.36	Exp. Ih @ 99K	Ref. 418
6.355	19.32	Exp. Ic @ 78K	Ref. 419
6.358(4)	19.35	Exp. Ic @ 89K	Ref. 418
6.350(8)	19.27	Exp. Ic @144K	Ref.[420]
6.295	18.78	PBE+MBD	present work
6.284	18.68	PBE+TS	present work
6.249 (6.257)	18.37 (18.44)	PBE	Ref. 394
6.434 (6.476)	20.05 (20.44)	rPW86+vdW-DF2	Ref. 394

3.9 Conclusions

In this chapter we have presented a new implementation of analytical MBD forces for large-scale condensed phase simulations, including all MBD corrections to unit-cell forces, stresses, and ionic forces. Our new implementation uses a quadrature scheme that is six orders of magnitude more accurate than the original FHI-aims MBD code. We have thoroughly characterized the convergence and numerical stability of our implementation and have eliminated the use of heuristic cutoffs for the dipole-dipole interaction tensors. With appropriate parallelization MBD forces may now be used to relax the structures of large (> 1000 atom) unit cells. We have made preliminary studies of the physisorption of nucleobases on graphene, the interlayer binding distance of graphite, and the structure of ice Ic and in all three cases find the performance of MBD forces to be encouraging for use in condensed phase optimizations. Once the bugs in the Hirshfeld volume partitioning for k-point sampling of the Brillion zone have been resolved, we are eager to benchmark MBD for other solid state systems. We are especially eager to compare our new implementation with the numerous numerical MBD optimizations that have been performed by the Tkatchenko group[109–112,119] since our code is substantially more numerically stable than previous MBD implementations. This is a particularly relevant issue for solids since numerical optimizations with MBD can be extremely sensitive to small perturbations of the ionic coordinates,[§] and many of the published results benchmarking MBD on molecular crystals used geometries from pairwise methods. We look forward to reexamining these systems in the future. The development of the MBD correction to the stress tensor will enable the first MBD corrections to the phase diagrams of materials such as ice or hydrogen-bonded pigments, which display competition between cooperative hydrogen-bonding and dispersion interactions. The ability to optimize unit cells and relax ionic coordinates with MBD will benefit many studies of novel functional organic materials such as layered metal-organic frameworks or vdW heterostructures.

[§]Personal discussions with Johannes Hoja, May, 2015.

4

Ongoing Developments for MBD

In Chapters 2 and 3 we presented the development and first implementation of analytical MBD forces for optimizing nuclear positions and unit-cells in isolated and condensed phase systems. Based on the successes of the MBD method for explaining many properties of organic materials, we are optimistic that these forces will be quickly adopted for use in many quantum chemical studies. However, there are three additional features that would be desirable for MBD to be a truly effective tool for modeling novel organic materials. Firstly, the range-separation parameter, β, has only been parameterized for three exchange-correlation functionals, PBE,[182,183] PBE0,[236–238] and HSE,[421–423] which limits the adoption of MBD by a wider audience. Secondly, one of the most surprising effects discovered with MBD is the entropic stabilization of aspirin by low-frequency many-body corrections to the phonon spectrum arising out of the hydrogen-bond network of one polymorph.[112] The electron-phonon coupling in materials such as graphite and graphene, can also be strongly renormalized (by up to $\sim 80\%$) by nonlocal exchange-correlation effects.[249] Since hydrogen- and halogen-bonds play such a crucial role in crystal structure engineering and since electron-phonon coupling strongly renormalizes the charge carrier mobilities of many organic semiconductors, enabling fast calculation of the MBD corrections to phonon modes is desirable. This is most easily addressed through the use of density functional perturbation theory (DFPT), which requires the analytical Hessian of the energy. Finally, density dependent properties, such as interaction energies or the transfer integrals that are commonly used to evaluate organic semiconductor materials, require a self-consistent methodology. Self-consistent density updates using MBD will also

enable the study of vdW corrections to excitation spectra by use of real-time propagation methods. In this chapter, we will describe progress that has been made toward each of these three goals and highlight a few of the remaining challenges.

4.1 Parameterizing MBD for Other Exchange-Correlation Functionals

The results presented in Chapters 2 and 3 exclusively used the Perdew-Burke-Ernzerhof (PBE)[182,183] exchange-correlation functional. Since PBE is a general purpose non-empirical GGA functional that performs reasonably well for both molecules and solids, it is a consistently ranked as one of the most popular functionals among DFT practitioners.[424] However, there are many other approximate functionals for exchange or correlation, which have been designed with different applications in mind (cf. Refs. 89,425 and references therein for a general review of DFT functionals and Ref. 426 for a discussion of popular GGAs). Unfortunately, no density functional is truly transferable in the sense that it "always" provides accurate prediction for all systems of interest.[427] As such, the development of correction schemes such as MBD is always accompanied by the need to see how "nicely" they play with the existing zoo of functionals. For instance, the exchange functional revPBE[234,235] is generally too repulsive at the equilibrium separation of dispersively bound dimers, which is why revPBE+vdW-DF tends to yield too large intermolecular separations.[428] Other popular GGA functionals have similar strengths and weaknesses. For example, Becke '88 (B88)[429] exchange is strongly over-repulsive, while LDA,[181] PW91[430–432] and PBE[182,183] give strong and weak spurious exchange binding respectively.[70,130] Previous authors have found that the non-empirical Perdew-Wang '86 (PW86)[433] exchange is perhaps the best GGA functional for describing the repulsive part of the exchange potential relevant to van der Waals interactions at short range.[70,434] Since the short range behavior of different functionals varies greatly, use of the MBD model with a new or preferred functional requires optimization of the MBD range-separation to match the properties of the underlying exchange-correlation functional.

One of the strengths of the MBD model over other vdW corrections is that there is just

a single adjustable parameter, β, which controls the damping function that range-separates MBD for coupling to the underlying DFT functional. All semi-empirical vdW correction schemes[41,49,54,66,435] use a damping function to turn off the correction at short range, both to avoid double counting the short-range correlation energy of the DFT correlation functional, and to avoid the divergence in the interaction between point dipoles. The value of the range-separation parameter, β, is determined for each exchange-correlation functional by minimizing the deviations with respect to highly accurate benchmarks for the interaction energies of noncovalently bound dimers. Ambrosetti *et al.*[88] originally optimized β for use with PBE, PBE0, and HSE against the S66×8 dataset, a collection of dissociation curves for 66 molecular dimers designed to cover the types of noncovalent interactions that occur in biomolecules ($-OH\cdots\pi$, $-CH\cdots N$, $\pi-\pi$, etc.).[436] Optimizing β against a large dataset that contains non-equilibrium geometries is preferable to avoid biasing the vdW correction toward equilibrium structures.

To enable MBD for use with other exchange-correlation functionals, we have worked with Xavier Andrade to incorporate our MBD code into the Octopus software package.[333,437,438] Octopus has several advantages over QE for this development work; principally, it uses the Libxc[439] library of exchange and correlation functionals and thereby supports a much broader range of functionals (including many that are popular in Gaussian-type orbital (GTO) based quantum chemistry programs) than most periodic simulation packages. Secondarily, since Octopus employs real-space grids,[333,440] it can more easily handle isolated systems. Finally, incorporating MBD into Octopus will pave the way for self-consistent MBD to be used with the real-time propagation scheme of time-dependent density functional theory (RT-TDDFT) and offers the potential for future development to improve the parallelism.[334,441,442] Unless otherwise specified, all calculations in Octopus employed the default Hartwigsen-Goedecker-Hutter (HGH) norm-conserving dual-space Gaussian pseudopotentials.[443]

At the time of writing, a development version of Octopus (code name Octopus tetricus), contains a working Hirshfeld volume partitioning, and support for the

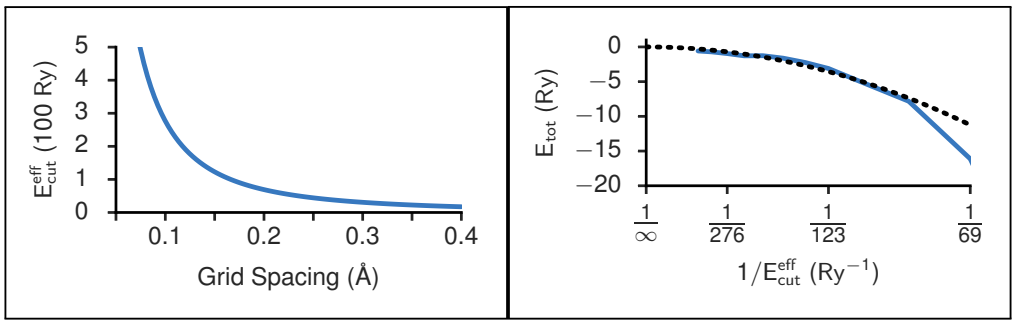

Figure 4.1: Left: Grid spacing cutoff used in Octopus versus the effective equivalent wavefunction cutoff (E_{cut}^{eff}). Note that the y-axis is in units of 100 Ry. **Right:** Total energy of an isolated benzene molecule as a function of the effective wavefunction cutoff (E_{cut}^{eff}). The dotted line shows a quadratic expansion to the complete basis set limit ($E_{cut}^{eff} = \infty$). Nonzero tick marks on the x-axis correspond to wavefunction cutoffs equivalent to grid spacings of [0.10, 0.15, 0.20] Å.

Hirshfeld gradients is actively being developed. For optimizing the range-separation parameter, β, we only need to compute interaction energies with MBD applied as an *a posteriori* correction. This means that the interaction energies need only be computed once with any given exchange-correlation functional so long as the Hirshfeld volumes computed with that functional are saved for each molecule in the dataset. With the Hirshfeld volumes on hand, the required ratios V_a/V_a^{free} can be computed and the MBD energy can be calculated independently as a function of the range-separation parameter. This scheme avoids unnecessary duplication of a large number of DFT single-point calculations. The FHI-aims MBD code accepts as input a modified `xyz` geometry file containing a column of Hirshfeld volume ratios V_a/V_a^{free}, so it is ideally suited to perform these MBD calculations on a dense grid of β values.

To enable this calculation scheme, we modified a version of the FHI-aims standalone MBD code to accept a custom value of β as an input parameter.[279] In Chapter 3 we alluded to the fact that the FHI-aims implementation of MBD@rsSCS contained several numerical instabilities and used heuristic convergence cutoffs. These instabilities only arise during computation of the MBD energy for periodic systems, so for isolated systems the energy computed by our modified FHI-aims MBD code agrees with that of our QE implementation to within 10^{-11} E_h.*

*To achieve this level of agreement with our MBD implementation it is actually necessary to modify a

Our preliminary investigation has focused on GGA functionals since they are substantially more computationally efficient than hybrid functionals in Octopus. We also considered two local density approximation (LDA) functionals, SPZ[181,444,445] and SVWN_{RPA}.[444–446] References and a list of abbreviations used to describe each functional is provided in section A.2 of Appendix A. Since the LDA exhibits spurious over-binding due to exchange,[130] adding a dispersion correction on top of LDA is expected to degrade the performance of LDA functionals, and if one insists on fitting dispersion correction parameters to the S22 set or other reference data, unphysical negative coefficients will result as the dispersion correction attempts to remove this over-binding.[447] We were therefore unsurprised to see that the mean absolute error of LDA+MBD against the S22 set decreases monotonically as β is increased and would presumably reach its minimum at $\beta \to \infty$, which would correspond to turning off the MBD correction. We note that the reference CCSD(T) interaction energies in these benchmark datasets have all been extrapolated to the complete basis set (CBS) limit. To achieve the best possible comparison of the DFT interaction energies computed in Octopus with these benchmark values, we considered a quadratic expansion to the complete basis set limit using grid spacings of $[0.2, 0.1, 0.08]$ Å. The results of such an extrapolation for an isolated benzene molecule are shown in the right-hand panel of Figure 4.1. For ease of comparison to conventional planewave codes, we convert from Octopus's grid spacing cutoff Δ (in Å) to the effective equivalent wavefunction kinetic energy cutoff $\text{E}_{\text{cut}}^{\text{eff}}$ (in Ry) as

$$\text{E}_{\text{cut}}^{\text{eff}}(\text{Ry}) = \frac{2.764}{\Delta^2}. \tag{4.1}$$

For most functionals we found that the complete basis set extrapolated results were equivalent to those computed at the grid spacing of 0.08 Å, which is effectively equivalent to a planewave kinetic energy cutoff of 432 Ry.

few errors in the FHI-aims MBD code such as unnecessary conversions between single and double precision floating-point types and errors in a few hardcoded constants. When we refer to using the FHI-aims MBD code, we actually mean using our in-house modified version of the code that has these bugs removed.

We optimized the MBD range-separation parameter β by minimizing the mean absolute error (MAE), mean absolute relative error (MARE), and mean absolute deviation (MAD), with respect to the revised S22 set[448] basis set consistent CCSD(T)/CBS benchmarks of Takatani and coworkers.[449] The resulting error curves as a function of β are displayed in Figure 4.2 for a representative set of GGA functionals. For most functionals the error surfaces are quite flat in the region of the minima. Optimal β values computed at the 0.08 Å spacing (and the corresponding minimum MAE, MAD and MARE) are given in Table 4.1 for the complete set of GGA functionals considered. Since the interaction energies in the S22 set span a large range ($-0.5 : -21$ kcal/mol), optimizing β against the relative error should avoid biasing the optimization to the strongest interactions. Some functionals display inconsistent behavior with regard to which value of β minimizes the relative error vs. the absolute error. These are the same functionals that yield the largest absolute and relative errors. This inconsistent behavior seems to occur for with functionals that have overly repulsive exchange, such as B88, optX, or revPBE, which is being compensated by turning on the attractive MBD dispersion correction at shorter range (smaller values of β). The LYP correlation functional also seems poorly suited to the MBD correction. The fact that the minimum absolute and relative errors is achieved for different values of β may also be a sign that the S22 set is too small to achieve an unbiased training. We also note that MOHLYP functional was optimized for transition metal chemistry,[450] which explains its generally poor performance on the S22 set.

Consistent with previous findings that the PW86 exchange functional avoids spurious exchange binding (and is therefore a good candidate for the foundation of a vdW corrected functional),[71,72] we find that the combination of rPW86 exchange and PBE correlation (abbreviated herein as rPW86) achieves the lowest error against the S22 set, with an optimal MARE of 8.5% and MAE of 0.5 kcal/mol. The PBE and PBEsol functionals are the next best performers. PW86 exchange pairs best with a slightly shorter-ranged MBD ($\beta = 0.76 - 0.78$) than PBE ($\beta = 0.78 - 0.81$), while the 'vdW optimized' versions of PBE, PBE$\kappa = 1$ and optPBE, yield even smaller β values. The

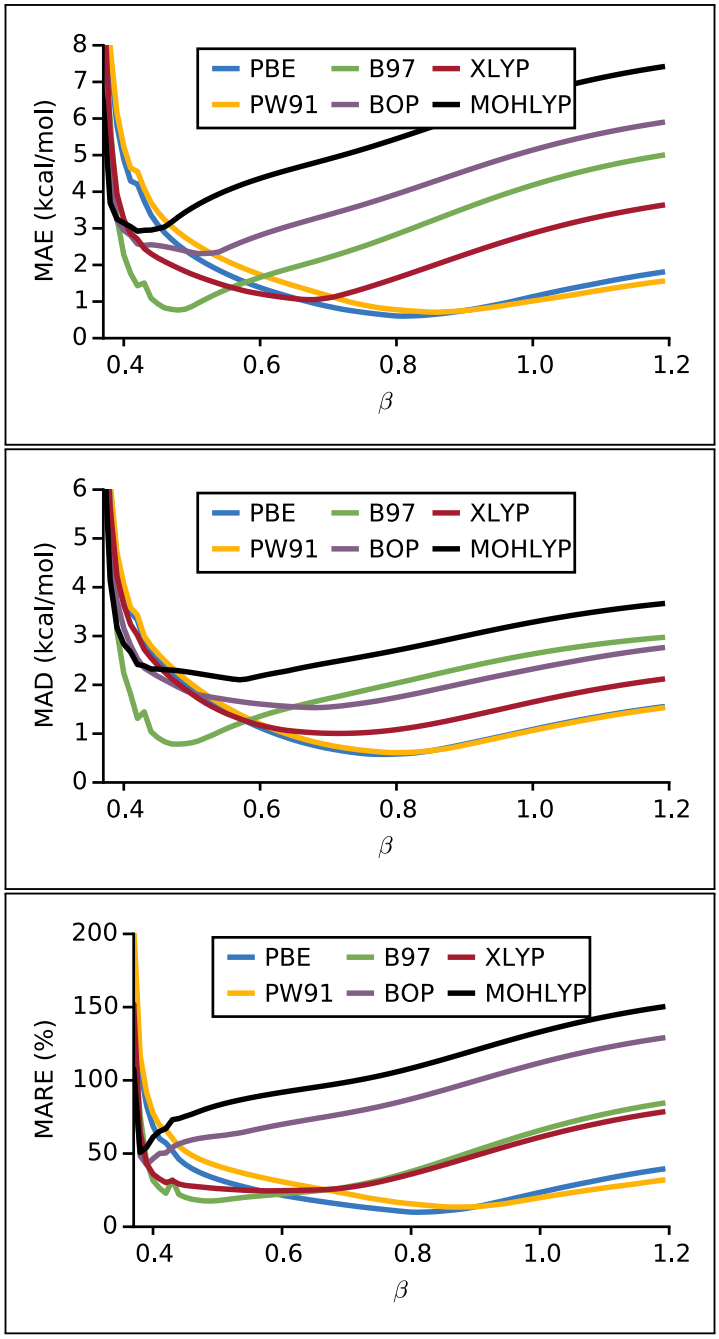

Figure 4.2: Relative to the revised S22 set interaction energies of Takatani *et al.*[449] the DFT+MBD method shown for a representative set of GGA functionals provides the following **Top:** mean absolute error (MAE) as a function of the range-separation parameter, β, **Middle:** mean absolute deviation (MAD) as a function of β, **Bottom:** mean absolute relative error (MARE) as a function of β.

large value of $\beta = 0.95$ achieved for PBEsol is likely a reflection of the adjustments that have been made to this functional to make it more compatible with condensed phase simulations. We note that the optimal values of β obtained here for PBE are somewhat smaller than the value of 0.83 reported by Ambrosetti *et al.* who optimized against the larger S66×8 set. When we optimize PBE against the S66×8 set we find $\beta_{\mathrm{opt}} = 0.87$, but the minimum is quite flat. The B97 and B97-3 functionals also perform well, but require significantly smaller $\beta \sim 0.42 - 0.49$, likely indicating a slightly more repulsive exchange. Overall, we find that the MBD model is able to compensate for the deficiencies of a wide variety of GGA functionals, with regard to their ability to describe noncovalent interaction energies. When the range-separation parameter is optimally tuned several different GGAs are able to achieve mean absolute errors well below 1 kcal/mol.

Table 4.1: Optimal MBD range-separation parameter, β, for different exchange-correlation functionals as determined by minimizing the mean absolute error (MAE), mean absolute relative error (MARE), and mean absolute deviation (MAD) relative to the S22 benchmark set using DFT+MBD interaction energies computed at a grid spacing of $\Delta = 0.08$ Å (equivalent to $\mathrm{E_{cut}} = 432$ Ry). MAE and MAD are given in kcal/mol.

Functional	$\beta_{\mathrm{opt}}^{\mathrm{MAE}}$	MAE	$\beta_{\mathrm{opt}}^{\mathrm{MARE}}$	MARE (%)	$\beta_{\mathrm{opt}}^{\mathrm{MAD}}$	MAD
rPW86	0.78	0.5	0.76	8.5	0.78	0.5
PW86	0.78	0.5	0.75	8.6	0.77	0.5
PBE	0.81	0.6	0.81	9.9	0.78	0.6
PBEsol	0.95	1.0	0.95	11	0.86	1.0
PW91	0.86	0.7	0.86	13	0.80	0.6
PBE$\kappa = 1$	0.70	0.7	0.64	15	0.71	0.8
optPBE	0.71	0.9	0.61	17	0.73	0.8
B97	0.48	0.8	0.49	18	0.48	0.8
B97-3	0.42	0.8	0.42	18	0.42	0.8
mPW91	0.71	0.9	0.62	18	0.73	0.8
HCTH/407	0.64	0.8	0.66	22	0.67	0.9
XLYP	0.67	1.1	0.58	25	0.72	1.0
BP86	0.71	1.1	0.57	26	0.74	0.9
revPBE	0.59	1.3	0.42	27	0.70	1.1
BLYP	0.65	1.3	0.42	32	0.71	1.1
BPW	0.63	1.6	0.42	35	0.70	1.2
OLYP	0.49	2.7	0.39	47	0.66	1.9
BOP	0.51	2.3	0.39	42	0.68	1.5
MOHLYP	0.42	2.9	0.38	51	0.57	2.1

We are presently working to benchmark MBD against larger datasets of noncovalent interaction energies, such as the S66×8[451] set of dimer dissociation curves and the 3B-69 set of three-body interaction energies.[104] We are eager to see how the range-separation parameter of MBD varies across a wider variety of functionals, including meta-GGAs and hybrids.

4.2 MBD Phonon Coupling: Analytical Hessians

4.2.1 Introduction

Many physical properties of solids, such as infrared and Raman spectra, heat capacity, thermal expansion, temperature dependence of optical spectra, and many more, depend on the quantum mechanical behavior of a solid's lattice dynamics. The description of these phenomena in terms of phonons dates back to the 1930s (cf. the seminal textbook of Born and Huang[452]) and has become one of the corner stones of solid state physics. In the framework of DFT, the lattice-dynamical properties of crystals are typically calculated using a form of linear response theory[453,454] called density functional perturbation theory (DFPT).[455–458] For an excellent review on this subject see Ref. 459. As usual, the electronic and vibrational degrees of freedom of a quantum solid are decoupled using the adiabatic (Born Oppenheimer) approximation.[460] The vibrational frequencies are then determined from the eigenvalues of the Hessian of the energy (also called the matrix of interatomic force constants), scaled by the atomic masses:

$$\det \left| \frac{1}{\sqrt{M_a M_b}} \frac{\boldsymbol{\partial}^2 E}{\boldsymbol{\partial} \boldsymbol{\mathcal{R}}_a \boldsymbol{\mathcal{R}}_b} - \omega^2 \right| = 0. \tag{4.2}$$

For the moment we will continue to ignore the changes in the energy that would be induced by applying the MBD correction self-consistently to update the Kohn-Sham density. In the context of DFPT, this choice to treat MBD as an *a posteriori* energy correction is important because the computation of second-order energy derivatives in DFPT requires knowledge of the first order variation in the density.

As an *a posteriori* correction, the MBD contributions to the phonon spectrum simply require second-order derivatives of the MBD correlation energy. Using numerical differentiation, Reilly *et al.* have shown that MBD corrections to the phonon density of states can have dramatic physical consequences for certain organic materials, such as introducing low-frequency many-body modes that explain the entropic stabilization of the

pharmaceutical polymorph of aspirin relative to a polymorph with a different hydrogen-bonding network.[112] Since numerical evaluation of second order MBD derivatives via finite difference methods is both extremely computationally costly and quite numerically sensitive, the analytical evaluation of the MBD Hessian is desirable.

Motivated by the potential significance of MBD phonon corrections to the study of organic materials, we now turn our attention to computing second derivatives of the MBD correlation energy with respect to the Cartesian coordinates of nuclei/ions. Just as we encountered with the derivation of the analytical forces, the layered definitions inherent in the MBD model result in rather lengthy expressions due to the chain-rule. To keep our notation as compact as possible, we will define several symbols along the way, and will focus on deriving the equations that would be necessary for implementing the MBD Hessian in code, rather than assembling a final expression in one equation. Consequently, our goal is to reduce these expressions to terms depending on either first derivative quantities that have already been addressed in Chapter 2, or to derivatives of the internuclear separation and the Hirshfeld effective volume. We adopt the notation $\boldsymbol{\partial}^2 = \boldsymbol{\partial}_c \boldsymbol{\partial}_d = \boldsymbol{\nabla}_{\boldsymbol{\mathcal{R}}_c} \otimes \boldsymbol{\nabla}_{\boldsymbol{\mathcal{R}}_d}$ to indicate the Hessian computed with respect to the nuclear positions of atoms c and d. It may be useful to refer back to the notation defined in Chapter 2 section 2.1.1 and the equations in Chapter 2 section 2.2.2 before starting to read this derivation. Just as we saw in Chapter 2 section 2.2.2, the MBD Hessian will reduce to three "fundamental" second derivatives, $\boldsymbol{\partial}^2 R_{ab}$, $\boldsymbol{\partial}^2 R_{ab}^k$, and $\boldsymbol{\partial}^2 V_a$, along with their first derivative analogues $\boldsymbol{\partial} R_{ab}$, $\boldsymbol{\partial} R_{ab}^i$, and $\boldsymbol{\partial} V_a$. We remind the reader that $R_{ab} = \|\boldsymbol{\mathcal{R}}_a - \boldsymbol{\mathcal{R}}_b\|$ is the internuclear distance and $V_a[\{\boldsymbol{\mathcal{R}}\}]$ is the Hirshfeld effective volume, which depends on the nuclear coordinates $\{\boldsymbol{\mathcal{R}}\}$ through the charge density partitioning. The derivation of the MBD Hessian proceeds in a similar fashion to the MBD ionic forces, so we will leave more of the calculus and algebra to the reader and focus on the final expression for each required quantity.

As we did in Chapter 3, we break the Hessian of the MBD correlation energy into its

interacting and non-interacting components

$$\boldsymbol{\partial}^2 E_{MBD} = \boldsymbol{\partial}^2 E_{\text{int.}}^{\text{MBD}} - \boldsymbol{\partial}^2 E_{\text{non-int.}}^{\text{MBD}} = \frac{1}{2}\sum_{p=1}^{3N} \boldsymbol{\partial}^2 \left(\sqrt{\lambda_p}\right) - \frac{3}{2}\sum_{a=1}^{N} \boldsymbol{\partial}^2 \overline{\omega}_a. \tag{4.3}$$

The basic ingredients for computing these derivatives are the same as before, but now we will have to compute the derivatives of the eigenvector matrix, $\boldsymbol{\mathcal{X}}$, in constructing the interacting term (cf. Eq. 2.40). Through the matrix $\mathbf{C}^{\text{MBD}}$, (cf. Eq. 2.18), we will encounter both first and second derivatives of the screened quantities, $\overline{\omega}_a$ and $\overline{\alpha}(\mathbb{i}\omega)$, as well as the screened long-range dipole-dipole tensor $\overline{\mathbf{T}}_{\text{LR}}$. As before, the derivatives of screened quantities appearing in both $\mathbf{C}^{\text{MBD}}$ and the non-interacting term above in Eq. 4.3 will take us through the rsSCS procedure with both $\overline{\mathbf{A}}$ and $\mathbf{T}_{\text{SR}}$. In the subsections below we will reduce the second derivatives of each of these quantities to expressions involving the six "fundamental" first and second derivatives. We start with these fundamental quantities since the implementation of Hirshfeld volume second derivatives will be one of the more demanding aspects of future efforts to develop code for MBD Hessians.

4.2.2 Fundamental quantities: $\boldsymbol{\partial}^2 R_{ab}$, $\boldsymbol{\partial}^2 R_{ab}^k$, & $\boldsymbol{\partial}^2 V$

Recall from Eq. 2.53 that the gradient of a component of the internuclear distance vector gives a difference of Kronecker deltas: $\boldsymbol{\partial}_c R_{ab}^k = (\delta_{ac} - \delta_{bc})\hat{\mathbf{e}}_k$. Making use of this relation, the Cartesian components of the second derivative $\boldsymbol{\partial}^2 R_{ab}^k$ are

$$\boldsymbol{\partial}_d^j \boldsymbol{\partial}_c^i R_{ab}^k = (\delta_{ac} - \delta_{bc}) \frac{(\boldsymbol{\mathcal{R}}_d \cdot \hat{\mathbf{e}}_j)(\hat{\mathbf{e}}_k \cdot \hat{\mathbf{e}}_i)}{\|\boldsymbol{\mathcal{R}}_d\|}. \tag{4.4}$$

Likewise, from Eq. 2.49 we have $\boldsymbol{\partial}_c \|\mathbf{R}_{ab}\| = (\delta_{ac} - \delta_{bc})\mathbf{R}_{ab}/\|\mathbf{R}_{ab}\|$, which yields the second derivative of the internuclear distance:

$$\boldsymbol{\partial}_d^j \boldsymbol{\partial}_c^i R_{ab} = (\delta_{ac} - \delta_{bc})(\delta_{ad} - \delta_{bd}) \left(\frac{(\hat{\mathbf{e}}_j \cdot \hat{\mathbf{e}}_i)}{\|\mathbf{R}_{ab}\|} - \frac{(\mathbf{R}_{ab} \cdot \hat{\mathbf{e}}_i)(\mathbf{R}_{ab} \cdot \hat{\mathbf{e}}_j)}{\|\mathbf{R}_{ab}\|^3} \right). \tag{4.5}$$

We previously (cf. Eq. (2.5)) defined the Hirshfeld effective volume as $V_a[\{\mathcal{R}\}] = \int \mathrm{d}\mathbf{r}\, w_a(\mathbf{r})\rho(\mathbf{r})\|\mathbf{r}-\mathcal{R}_a\|^3$, where

$$w_a(\mathbf{r}) = \rho_a^{\text{free}}(\|\mathbf{r}-\mathcal{R}_a\|)/\sum_b \rho_b^{\text{free}}(\|\mathbf{r}-\mathcal{R}_b\|) \tag{4.6}$$

is the Hirshfeld weight factor. We now adopt a slightly different notation (which is also used in Appendix C Eq. (C.1-C.4)) to make computing $\boldsymbol{\partial}^2 V$ more clear. The Hirshfeld weight factor and volume are re-written by defining the sum of free-atom densities,ρ_{sad}, and the Hirshfeld effective density, ρ^{eff}, as

$$\rho_{\text{sad}}(\mathbf{r}) \equiv \sum_b \rho_b^{\text{free}}(\|\mathbf{r}-\mathcal{R}_b\|) \tag{4.7}$$

$$\rho^{\text{eff}}(\mathbf{r}) = w_a(\mathbf{r})\rho(\mathbf{r}) = \frac{\rho_a^{\text{free}}(\|\mathbf{r}-\mathcal{R}_a\|)}{\rho_{\text{sad}}(\mathbf{r})}\,\rho(\mathbf{r}). \tag{4.8}$$

Then, the Hirshfeld volume becomes $V_a[\{\mathcal{R}\}] = \int \mathrm{d}\mathbf{r}\, \|\mathbf{r}-\mathcal{R}_a\|^3 \rho_a^{\text{eff}}(\mathbf{r})$. To compute the Hirshfeld volume second derivative, we start by dividing the first derivative, $\boldsymbol{\partial}_c^i V_a$, into two terms:

$$\boldsymbol{\partial}_c^i V_a = \underbrace{\int \mathrm{d}\mathbf{r}\|\mathbf{r}-\mathcal{R}_a\|^3 \boldsymbol{\partial}_c^i \rho_a^{\text{eff}}(\mathbf{r})}_{❶} - 3\delta_{ac}\underbrace{\int \mathrm{d}\mathbf{r}\Big[\hat{\mathbf{e}}_i\cdot(\mathbf{r}-\mathcal{R}_a)\,\|\mathbf{r}-\mathcal{R}_a\|\Big]\rho_a^{\text{eff}}(\mathbf{r})}_{❷} \tag{4.9}$$

So the second derivative is given by:

$$\boldsymbol{\partial}_d^j \boldsymbol{\partial}_c^i V_a = \boldsymbol{\partial}_d^j\,[❶] - 3\delta_{ac}\,\boldsymbol{\partial}_d^j\,[❷]\,, \tag{4.10}$$

where the first term is:

$$\boldsymbol{\partial}_d^j\,[❶] = \int \mathrm{d}\mathbf{r}\,\|\mathbf{r}-\mathcal{R}_a\|^3\,\boldsymbol{\partial}_d^j\boldsymbol{\partial}_c^i\rho_a^{\text{eff}}(\mathbf{r}) - 3\delta_{ad}\int \mathrm{d}\mathbf{r}\Big[\hat{\mathbf{e}}_j\cdot(\mathbf{r}-\mathcal{R}_a)\|\mathbf{r}-\mathcal{R}_a\|\Big]\boldsymbol{\partial}_c^i\rho_a^{\text{eff}}(\mathbf{r}), \tag{4.11}$$

and the second term is:

$$\begin{aligned}\boldsymbol{\partial}_d^j\,[\textbf{②}] &= \int \mathrm{d}\mathbf{r}\Big[\hat{\mathbf{e}}_i\cdot(\mathbf{r}-\boldsymbol{\mathcal{R}}_a)\,\|\mathbf{r}-\boldsymbol{\mathcal{R}}_a\|\Big]\boldsymbol{\partial}_d^j\rho_a^{\mathrm{eff}}(\mathbf{r}) \\ &\quad -\delta_{ad}\int \mathrm{d}\mathbf{r}\,\left[(\hat{\mathbf{e}}_i\cdot\hat{\mathbf{e}}_j)\|\mathbf{r}-\boldsymbol{\mathcal{R}}_a\|+\frac{[\hat{\mathbf{e}}_i\cdot(\mathbf{r}-\boldsymbol{\mathcal{R}}_a)]\,[\hat{\mathbf{e}}_j\cdot(\mathbf{r}-\boldsymbol{\mathcal{R}}_a)]}{\|\mathbf{r}-\boldsymbol{\mathcal{R}}_a\|}\right]\rho_a^{\mathrm{eff}}(\mathbf{r}).\end{aligned} \tag{4.12}$$

If we define $\boldsymbol{\imath}_a \equiv \mathbf{r}-\boldsymbol{\mathcal{R}}_a$ and suppress the argument of ρ^{eff}, we can write $\boldsymbol{\partial}^2 V$ more compactly as:

$$\begin{aligned}\boldsymbol{\partial}_d^j\boldsymbol{\partial}_c^i V_a &= \int \mathrm{d}\mathbf{r}\,\|\boldsymbol{\imath}_a\|^3\,\boldsymbol{\partial}_d^j\boldsymbol{\partial}_c^i\rho_a^{\mathrm{eff}} \\ &\quad -3\delta_{ad}\int \mathrm{d}\mathbf{r}\,\Big[(\hat{\mathbf{e}}_j\cdot\boldsymbol{\imath}_a)\,\|\boldsymbol{\imath}_a\|\Big]\boldsymbol{\partial}_c^i\rho_a^{\mathrm{eff}}-3\delta_{ac}\int \mathrm{d}\mathbf{r}\,\Big[(\hat{\mathbf{e}}_i\cdot\boldsymbol{\imath}_a)\,\|\boldsymbol{\imath}_a\|\Big]\boldsymbol{\partial}_d^j\rho_a^{\mathrm{eff}} \\ &\quad +3\delta_{ac}\delta_{ad}\int \mathrm{d}\mathbf{r}\,\left[(\hat{\mathbf{e}}_i\cdot\hat{\mathbf{e}}_j)\,\|\boldsymbol{\imath}_a\|+\frac{(\hat{\mathbf{e}}_i\cdot\boldsymbol{\imath}_a)(\hat{\mathbf{e}}_j\cdot\boldsymbol{\imath}_a)}{\|\boldsymbol{\imath}_a\|}\right]\rho_a^{\mathrm{eff}}.\end{aligned} \tag{4.13}$$

To construct the first term we need the Hessian of the Hirshfeld effective atomic density, ρ^{eff}. Noting that the only term in the sum of atomic densities that depends on $\boldsymbol{\mathcal{R}}_c$ is the corresponding free atom density, ρ_c^{free}, the gradient of ρ_{sad} simply picks out the relevant free atom density gradient

$$\boldsymbol{\partial}_c^i\rho_{\mathrm{sad}} = \sum_{b=1}^{N}\boldsymbol{\partial}_c^i\rho_b^{\mathrm{free}} = \boldsymbol{\partial}_c^i\rho_c^{\mathrm{free}}. \tag{4.14}$$

The present implementation of MBD forces combines Eq. (4.14) with the free atom density gradient, $\boldsymbol{\partial}\rho^{\mathrm{free}}$, in spherical coordinates to compute $\boldsymbol{\partial}\rho^{\mathrm{eff}}$. However, to keep the notation more compact, in the following we represent the gradient of the Hirshfeld density with $\boldsymbol{\partial}_c\rho^{\mathrm{free}}$ in Cartesian coordinates:

$$\boldsymbol{\partial}_c^i\rho_a^{\mathrm{eff}} = \frac{1}{\rho_{\mathrm{sad}}}\Big[\rho_a^{\mathrm{eff}}-\rho\,\delta_{ca}\Big]\,\boldsymbol{\partial}_c^i\rho_c^{\mathrm{free}} \tag{4.15}$$

$$= \mathcal{J}_{ca}\,\boldsymbol{\partial}_c^i\rho_c^{\mathrm{free}}, \tag{4.16}$$

where, in the first line we have suppressed the arguments of ρ_a^{free}, ρ_c^{free} and ρ_{sad}, and in the third line we define $\mathcal{J}_{ca}(\mathbf{r})$ to collect unperturbed density terms. The Hessian of the

Hirshfeld effective density then follows as:

$$\boldsymbol{\partial}_d^j \boldsymbol{\partial}_c^i \rho_a^{\text{eff}} = \boldsymbol{\partial}_d^j \Big[\mathcal{J}_{ca}\Big] \boldsymbol{\partial}_c^i \rho_c^{\text{free}} + \mathcal{J}_{ca}\, \boldsymbol{\partial}_d^j \boldsymbol{\partial}_c^i \rho_c^{\text{free}} \tag{4.17}$$

$$= \frac{1}{\rho_{\text{sad}}} \left[\frac{\rho}{\rho_{\text{sad}}}\, \boldsymbol{\partial}_d^j \rho_a^{\text{free}} - \left[\mathcal{J}_{ca} + \frac{\rho_a^{\text{eff}}}{\rho_{\text{sad}}} \right] \boldsymbol{\partial}_d^j \rho_d^{\text{free}} \right] \boldsymbol{\partial}_c^i \rho_c^{\text{free}} + \mathcal{J}_{ca}\, \boldsymbol{\partial}_d^j \boldsymbol{\partial}_c^i \rho_c^{\text{free}}. \tag{4.18}$$

Since the free atom density, ρ_c^{free}, is spherically symmetric, it can be evaluated in much the same fashion as is used for the present Hirshfeld gradient code, where the derivative of ρ^{free} is evaluated by numerical differentiation in spherical coordinates of the splined free atom density. The greater challenge for a future MBD Hessian implementation will be evaluation of Eq. (4.13), where the spatial integration will need to be performed for each Cartesian component of $\boldsymbol{\partial}_d^j \boldsymbol{\partial}_c^i V_a$. However, this integral will be quite local and could likely be evaluated on a truncated radial grid. These integrations will likely be much easier to perform in real-space grid or GTO based quantum chemistry codes. Having taken care of the fundamental quantities, we now turn our attention to building up the Hessian of quantities appearing in the rsSCS procedure. In the discussion that follows we will place a box around any of the six fundamental derivatives $\boldsymbol{\partial} V$, $\boldsymbol{\partial}^2 V$, $\boldsymbol{\partial} R_{ab}$, $\boldsymbol{\partial}^2 R_{ab}$, $\boldsymbol{\partial} R_{ab}^i$, or $\boldsymbol{\partial}^2 R_{ab}^i$ to highlight terms that need not be further reduced.

4.2.3 The screened excitation frequency, $\overline{\omega}_a$

To evaluate the second derivative of the non-interacting energy we simply require $\boldsymbol{\partial}^2 \overline{\omega}_a$. Recall from Eq. (2.42) that the first derivative $\boldsymbol{\partial}_c \overline{\omega}_a$ is

$$\boldsymbol{\partial}_c \overline{\omega}_a = \frac{8}{\pi} \sum_{p=1}^{n} g_p \Bigg[\underbrace{\frac{\overline{\alpha}_a(\mathbb{i} y_p)}{[\overline{\alpha}_a(0)]^2} \boldsymbol{\partial}_c \overline{\alpha}_a(\mathbb{i} y_p)}_{\text{❶}} - \underbrace{\frac{[\overline{\alpha}_a(\mathbb{i} y_p)]^2}{[\overline{\alpha}_a(0)]^3} \boldsymbol{\partial}_c \overline{\alpha}_a(0)}_{\text{❷}} \Bigg]. \tag{4.19}$$

For compactness we suppress the atomic index a as well as the imaginary frequency quadrature argument $(\mathbb{i} y_p)$. Then, considering the derivatives of the first interior term we

have:

$$\boldsymbol{\partial}_d\,[\textbf{❶}] = \frac{\overline{\alpha}\boldsymbol{\partial}_d\boldsymbol{\partial}_c\overline{\alpha} + \boldsymbol{\partial}_d\overline{\alpha}\boldsymbol{\partial}_c\overline{\alpha}}{[\overline{\alpha}(0)]^2} - \frac{2\overline{\alpha}\boldsymbol{\partial}_d\overline{\alpha}(0)\boldsymbol{\partial}_c\overline{\alpha}}{[\overline{\alpha}(0)]^3}. \tag{4.20}$$

Likewise, the derivative of the second interior term is simply:

$$\boldsymbol{\partial}_d\,[\textbf{❷}] = \frac{[\overline{\alpha}]^2\boldsymbol{\partial}_d\boldsymbol{\partial}_c\overline{\alpha}(0) + 2\overline{\alpha}\boldsymbol{\partial}_d\overline{\alpha}\boldsymbol{\partial}_c\overline{\alpha}(0)}{[\overline{\alpha}(0)]^3} - \frac{3[\overline{\alpha}]^2\boldsymbol{\partial}_d\overline{\alpha}(0)\boldsymbol{\partial}_c\overline{\alpha}(0)}{[\overline{\alpha}(0)]^4}. \tag{4.21}$$

Grouping terms by the power of $\overline{\alpha}(0)$ in the denominator and restoring the suppressed quantities we have:

$$\begin{aligned}
\boldsymbol{\partial}_d\boldsymbol{\partial}_c\overline{\omega}_a \;=\; & \frac{8}{\pi[\overline{\alpha}_a(0)]^2}\sum_{p=1}^{n} g_p\Big[\overline{\alpha}_a(\mathbb{i}y_p)\boldsymbol{\partial}_d\boldsymbol{\partial}_c\overline{\alpha}_a(\mathbb{i}y_p) + \boldsymbol{\partial}_d\overline{\alpha}_a(\mathbb{i}y_p)\boldsymbol{\partial}_c\overline{\alpha}_a(\mathbb{i}y_p)\Big] \\
& -\frac{8}{\pi[\overline{\alpha}_a(0)]^3}\sum_{p=1}^{n} g_p\Big[[\overline{\alpha}_a(\mathbb{i}y_p)]^2\boldsymbol{\partial}_d\boldsymbol{\partial}_c\overline{\alpha}_a(0)\Big] \\
& -\frac{16}{\pi[\overline{\alpha}_a(0)]^3}\sum_{p=1}^{n} g_p\Big[\overline{\alpha}_a(\mathbb{i}y_p)\Big(\boldsymbol{\partial}_d\overline{\alpha}_a(0)\boldsymbol{\partial}_c\overline{\alpha}_a(\mathbb{i}y_p) + \boldsymbol{\partial}_d\overline{\alpha}_a(\mathbb{i}y_p)\boldsymbol{\partial}_c\overline{\alpha}_a(0)\Big)\Big] \\
& +\frac{24}{\pi[\overline{\alpha}_a(0)]^4}\sum_{p=1}^{n} g_p\Big[[\overline{\alpha}_a(\mathbb{i}y_p)]^2\boldsymbol{\partial}_d\overline{\alpha}_a(0)\boldsymbol{\partial}_c\overline{\alpha}_a(0)\Big].
\end{aligned} \tag{4.22}$$

To evaluate Eq. (4.22), we employ Eq. (2.43) from Chapter 2, and derive the Hessian of the the screened dynamic polarizability, $\overline{\alpha}(\mathbb{i}\omega)$, below. ă

4.2.4 The screened polarizability, $\overline{\alpha}(\mathbb{i}\omega)$

The principle output of the rsSCS procedure is the isotropic screened atomic polarizability, $\overline{\alpha}_a(\mathbb{i}\omega)$. As before (cf. Eq. (2.43)), we use the linearity of the trace to write

$$\overline{\alpha}_a(\mathbb{i}\omega) = \frac{1}{3}\mathrm{Tr}\left[\sum_{b=1}^{N}\left[\overline{\mathbf{A}}(\mathbb{i}\omega)\right]_{ab}\right] \qquad \Rightarrow \qquad \boldsymbol{\partial}^2\overline{\alpha}_a = \frac{1}{3}\mathrm{Tr}\left[\sum_{b=1}^{N}\left[\boldsymbol{\partial}^2\overline{\mathbf{A}}(\mathbb{i}\omega)\right]_{ab}\right]. \tag{4.23}$$

Recall from section 2.2.1.2 and Eq. 2.44 of Chapter 2, that for a given imaginary frequency the rsSCS procedure builds the screened system polarizability tensor $\overline{\mathbf{A}}(\mathbb{i}\omega)$ by inverting the short-range dipole tensor $\mathbf{T}_{\mathrm{SR}}(\mathbb{i}\omega)$ and the bare system polarizability tensor,

$\mathbf{A}(\mathbb{i}\omega)$, such that

$$\boldsymbol{\partial}_c\overline{\mathbf{A}} = -\overline{\mathbf{A}}\left[\boldsymbol{\partial}_c\mathbf{A}^{-1} + \boldsymbol{\partial}_c\mathbf{T}_{\mathrm{SR}}\right]\overline{\mathbf{A}}. \tag{4.24}$$

where we have suppressed the frequency-dependence and

$$\boldsymbol{\partial}_c\mathbf{A}^{-1} = -\mathbf{A}^{-1}\left[\boldsymbol{\partial}_c\mathbf{A}\right]\mathbf{A}^{-1}, \tag{4.25}$$

and $\boldsymbol{\partial}_c\mathbf{A}$ is evaluated as in Eq. (2.45). For compactness let $\mathbf{B} \equiv \boldsymbol{\partial}_c\mathbf{A}^{-1} + \boldsymbol{\partial}_c\mathbf{T}_{\mathrm{SR}}$ so that $\boldsymbol{\partial}_c^i\overline{\mathbf{A}} = -\overline{\mathbf{A}}\mathbf{B}^i\overline{\mathbf{A}}$. The Hessian of the screened polarizability tensor is then:

$$\boldsymbol{\partial}_d^j\boldsymbol{\partial}_c^i\overline{\mathbf{A}} = -\left[\boldsymbol{\partial}_d^j\overline{\mathbf{A}}\right]\mathbf{B}^i\overline{\mathbf{A}} - \overline{\mathbf{A}}\left[\boldsymbol{\partial}_d^j\mathbf{B}^i\right]\overline{\mathbf{A}} - \overline{\mathbf{A}}\mathbf{B}^i\left[\boldsymbol{\partial}_d^j\overline{\mathbf{A}}\right], \tag{4.26}$$

where

$$\boldsymbol{\partial}_d^j\mathbf{B}^i = \boldsymbol{\partial}_d^j\boldsymbol{\partial}_c^i\mathbf{A}^{-1} + \boldsymbol{\partial}_d^j\boldsymbol{\partial}_c^i\mathbf{T}_{\mathrm{SR}}, \tag{4.27}$$

and

$$\boldsymbol{\partial}_d^j\boldsymbol{\partial}_c^i\mathbf{A}^{-1} = -\left[\boldsymbol{\partial}_d^j\mathbf{A}^{-1}\right]\left[\boldsymbol{\partial}_c^i\mathbf{A}\right]\mathbf{A}^{-1} - \mathbf{A}^{-1}\left[\boldsymbol{\partial}_c^i\mathbf{A}\right]\left[\boldsymbol{\partial}_d^j\mathbf{A}^{-1}\right] - \mathbf{A}^{-1}\left[\boldsymbol{\partial}_d^j\boldsymbol{\partial}_c^i\mathbf{A}\right]\mathbf{A}^{-1}. \tag{4.28}$$

To evaluate Eq. (4.28), we employ Eq. (2.43) and Eq. (4.25). Then, since $\mathbf{A}$ is fully diagonal, and in Chapter 2 we carefully separated out the terms that do not depend on the effective volume, the Hessian of $\mathbf{A}$ is computed directly from $\boldsymbol{\partial}^2 V$ as

$$\boldsymbol{\partial}_d^j\boldsymbol{\partial}_c^i\mathbf{A} = \bigoplus_{a=1}^{N}\mathrm{diag}\left[\Upsilon_a\boxed{\boldsymbol{\partial}_d^j\boldsymbol{\partial}_c^i V_a}\right]. \tag{4.29}$$

The final ingredient to evaluate Eq. (4.27), is the Hessian of the short-range dipole-dipole interaction tensor. As we encountered before, derivatives of this tensor will require accounting for both the *implicit* nuclear coordinate dependence arising through the Hirshfeld volumes in the frequency-dependent QHO interaction potential, as well as the *explicit* nuclear coordinate dependence arising from the point-dipole interaction.

4.2.5 The frequency-dependent dipole-dipole tensor, $\mathbf{T}$

Since derivatives of the full frequency-dependent dipole-dipole tensor, $\mathbf{T}^{ij}(R_{ab}, \zeta_{ab})$, become quite involved, we will again use the notation of section C.3 in Appendix C and define three convenience functions, U, $\mathbf{W}^{k\ell}$, and $\mathbf{T}^{k\ell}_{\text{dip}}$ to break the derivatives of $\mathbf{T}$ into more manageable pieces. Let,

$$U \equiv \operatorname{erf}[\zeta] - \frac{2}{\sqrt{\pi}}\zeta \exp\left[-\zeta^2\right] \tag{4.30}$$

$$\mathbf{W}^{k\ell} \equiv \mathbf{\Psi}^{k\ell}\frac{4}{\sqrt{\pi}}\zeta^3 \exp\left[-\zeta^2\right] \tag{4.31}$$

$$\mathbf{\Psi}^{k\ell} \equiv \left(\frac{R^k R^\ell}{R^5}\right) \tag{4.32}$$

$$\mathbf{T}^{k\ell}_{\text{dip}} \equiv -3\mathbf{\Psi}^{k\ell} + \frac{\delta_{k\ell}}{R^3} \quad \Leftrightarrow \quad \mathbf{\Psi}^{k\ell} = -\frac{1}{3}\mathbf{T}^{k\ell}_{\text{dip}} + \frac{1}{3}\frac{\delta_{k\ell}}{R^3} \tag{4.33}$$

where all atomic ab indices have been suppressed and the function $\mathbf{\Psi}$ is used to contain the explicit nuclear coordinate dependent term that is shared in $\mathbf{W}$ and $\mathbf{T}_{\text{dip}}$. Since the derivatives of $\mathbf{T}_{\text{dip}}$ and $\mathbf{\Psi}^{k\ell}$ are closely related, we specify the conversion in Eq. (4.33). As before, ζ_{ab} is the ratio of the internuclear distance R_{ab} to the interaction potential length, Σ_{ab}. So, then the $(k,\ell)^{\text{th}}$ component of $\mathbf{T}$ (cf. Eq. (2.56)) is given by

$$\mathbf{T}^{k\ell} = U\mathbf{T}^{k\ell}_{\text{dip}} + \mathbf{W}^{k\ell}. \tag{4.34}$$

The second derivative of this quantity is then

$$\boldsymbol{\partial}^j_d\boldsymbol{\partial}^i_c\mathbf{T}^{k\ell} = \mathbf{T}^{k\ell}_{\text{dip}}\boldsymbol{\partial}^j_d\boldsymbol{\partial}^i_c U + U\boldsymbol{\partial}^j_d\boldsymbol{\partial}^i_c\mathbf{T}^{k\ell}_{\text{dip}} + \boldsymbol{\partial}^j_d U\ \boldsymbol{\partial}^i_c\mathbf{T}^{k\ell}_{\text{dip}} + \boldsymbol{\partial}^i_c U\ \boldsymbol{\partial}^j_d\mathbf{T}^{k\ell}_{\text{dip}} + \boldsymbol{\partial}^j_d\boldsymbol{\partial}^i_c\mathbf{W}^{k\ell}. \tag{4.35}$$

To evaluate Eq. (4.35), we will take the derivatives of each convenience function U, $\mathbf{\Psi}$, $\mathbf{W}$, and $\mathbf{T}_{\text{dip}}$ in turn.

In constructing the MBD forces, we previously defined a helper function $h(\zeta) = \frac{4\zeta^2}{\sqrt{\pi}} \exp\left[-\zeta^2\right]$ so that $\boldsymbol{\partial} U = h(\zeta)\boldsymbol{\partial}\zeta$. The second derivative of U is then evaluated as

$$\begin{aligned} \boldsymbol{\partial} h(\zeta) &= 2\left[\frac{1-\zeta^2}{\zeta}\right] h(\zeta)\boldsymbol{\partial}\zeta & (4.36) \\ \Rightarrow \boldsymbol{\partial}_d^j \boldsymbol{\partial}_c^i U &= h(\zeta)\boldsymbol{\partial}_d^j \boldsymbol{\partial}_c^i \zeta + 2\left[\frac{1-\zeta^2}{\zeta}\right] h(\zeta)\boldsymbol{\partial}_d^j \zeta\ \boldsymbol{\partial}_c^i \zeta, & (4.37) \end{aligned}$$

where $\boldsymbol{\partial}\zeta$ was originally evaluated in Eq. (2.58) and is repeated below in Eq. (4.38). The second derivative of ζ is then:

$$\begin{aligned} \boldsymbol{\partial}_c^i \zeta_{ab} = \boldsymbol{\partial}_c^i \left[\frac{R_{ab}}{\Sigma_{ab}}\right] &= \Sigma_{ab}^{-1} \boxed{\boldsymbol{\partial}_c^i R_{ab}} - \Sigma_{ab}^{-2} R_{ab}\ \boldsymbol{\partial}_c^i \Sigma_{ab} & (4.38) \\ \Rightarrow \boldsymbol{\partial}_d^j \boldsymbol{\partial}_c^i \zeta_{ab} &= -\Sigma_{ab}^{-2}\left[\boxed{\boldsymbol{\partial}_c^i R_{ab}} \boldsymbol{\partial}_d^j \Sigma_{ab} - \boxed{\boldsymbol{\partial}_d^j R_{ab}} \boldsymbol{\partial}_c^i \Sigma_{ab} - R_{ab}\ \boldsymbol{\partial}_d^j \boldsymbol{\partial}_c^i \Sigma_{ab}\right] & (4.39) \\ &\quad + \Sigma_{ab}^{-1} \boxed{\boldsymbol{\partial}_d^j \boldsymbol{\partial}_c^i R_{ab}} + 2\Sigma_{ab}^{-3} R_{ab}\ \boldsymbol{\partial}_c^i \Sigma_{ab}\ \boldsymbol{\partial}_d^j \Sigma_{ab}. \end{aligned}$$

To evaluate Eq. (4.39), we need the derivatives of the interaction potential length, Σ_{ab}, which are constructed from derivatives of the QHO widths σ_a and σ_b. Recall that $\Sigma_{ab} = \sqrt{\sigma_a^2 + \sigma_b^2}$, so:

$$\begin{aligned} \boldsymbol{\partial}_c^i \Sigma_{ab} &= \Sigma_{ab}^{-1}\left(\sigma_a \boldsymbol{\partial}_c^i \sigma_a + \sigma_b \boldsymbol{\partial}_c^i \sigma_b\right) & (4.40) \\ \Rightarrow \boldsymbol{\partial}_d^j \boldsymbol{\partial}_c^i \Sigma_{ab} &= \Sigma_{ab}^{-1}\left(\boldsymbol{\partial}_d^j \sigma_a\ \boldsymbol{\partial}_c^i \sigma_a + \boldsymbol{\partial}_d^j \sigma_b\ \boldsymbol{\partial}_c^i \sigma_b\right) + \Sigma_{ab}^{-1}\left(\sigma_a \boldsymbol{\partial}_d^j \boldsymbol{\partial}_c^i \sigma_a + \sigma_b \boldsymbol{\partial}_d^j \boldsymbol{\partial}_c^i \sigma_b\right) & (4.41) \\ &\quad - \Sigma_{ab}^{-1}\left(\boldsymbol{\partial}_d^j \Sigma_{ab}\ \boldsymbol{\partial}_c^i \Sigma_{ab}\right) \end{aligned}$$

To compute the Hessian of the QHO width, we recall from Eq. 2.59 that

$$\boldsymbol{\partial}_c^i \sigma_a = \left[\frac{1}{3}\sqrt{\frac{2}{\pi}}\Upsilon_a\right]^{1/3} \frac{\boxed{\boldsymbol{\partial}_c^i V_a}}{3[V_a]^{2/3}} \tag{4.42}$$

so we have:

$$\boldsymbol{\partial}_d^j \boldsymbol{\partial}_c^i \sigma_a = \left[\frac{1}{3}\sqrt{\frac{2}{\pi}}\Upsilon_a\right]^{1/3} \left(\frac{1}{3}\frac{\boxed{\boldsymbol{\partial}_d^j \boldsymbol{\partial}_c^i V_a}}{[V_a]^{2/3}} - \frac{2}{9}\frac{\boxed{\boldsymbol{\partial}_d^j V_a}\ \boxed{\boldsymbol{\partial}_c^i V_a}}{[V_a]^{5/3}}\right). \tag{4.43}$$

Combining Eq. (4.42-4.43), we can evaluate (4.39). Then, together Eqs. (4.38-4.39) are used to evaluate the second derivative of U in Eq. (4.37).

Having dealt with U, we now turn our attention to the second derivative of $\mathbf{W}^{k\ell}$. We start with the explicit nuclear coordinate derivatives that arise through $\boldsymbol{\partial}^2\boldsymbol{\Psi}^{k\ell}$:

$$\boldsymbol{\partial}_c^i\Psi^{k\ell} = -\frac{1}{3}\boldsymbol{\partial}_c^i\mathbf{T}_{\text{dip}}^{k\ell} - \frac{\delta_{k\ell}}{R^4}\boxed{\boldsymbol{\partial}_c^i R} = \frac{R^\ell\boxed{\boldsymbol{\partial}_c^i R^k} + R^k\boxed{\boldsymbol{\partial}_c^i R^\ell}}{R^5} - \frac{5R^kR^\ell}{R^6}\boxed{\boldsymbol{\partial}_c^i R} \quad (4.44)$$

$$\boldsymbol{\partial}_d^j\boldsymbol{\partial}_c^i\Psi^{k\ell} = -\frac{1}{3}\boldsymbol{\partial}_d^j\boldsymbol{\partial}_c^i\mathbf{T}_{\text{dip}}^{k\ell} + 4\frac{\delta_{k\ell}}{R^5}\boxed{\boldsymbol{\partial}_d^j R}\boxed{\boldsymbol{\partial}_c^i R} - \frac{\delta_{k\ell}}{R^4}\boxed{\boldsymbol{\partial}_d^j\boldsymbol{\partial}_c^i R}. \quad (4.45)$$

With $\boldsymbol{\partial}_c^i\boldsymbol{\Psi}^{k\ell}$ in hand, and again making use of $h(\zeta)$, the first derivative of $\mathbf{W}^{k\ell}$ is simply

$$\boldsymbol{\partial}_c^i\mathbf{W}^{k\ell} = \Psi^{k\ell}\left[3-2\zeta^2\right]h(\zeta)\boldsymbol{\partial}_c^i\zeta - \frac{1}{3}\zeta h(\zeta)\boldsymbol{\partial}_c^i\Psi^{k\ell} \quad (4.46)$$

For the second derivative, we'll need to consider terms like $\left[3-2\zeta^2\right]h(\zeta)$ and $\zeta h(\zeta)$. We start by referring to the first quantity as $g(\zeta)$, so that

$$g(\zeta) \equiv \left[3-2\zeta^2\right]h(\zeta) \quad (4.47)$$

$$\Rightarrow \boldsymbol{\partial}_c^i\mathbf{W}^{k\ell} = \Psi^{k\ell}g(\zeta)\boldsymbol{\partial}_c^i\zeta - \frac{1}{3}\Big(\zeta h(\zeta)\Big)\boldsymbol{\partial}_c^i\Psi^{k\ell}. \quad (4.48)$$

Aside from the derivatives of $g(\zeta)$ and $\zeta h(\zeta)$, we already have everything we need to construct $\boldsymbol{\partial}^2\mathbf{W}^{k\ell}$ from Eqs. (4.44), (4.45), (4.38), and (4.39):

$$\begin{aligned}\boldsymbol{\partial}_d^j\boldsymbol{\partial}_c^i\mathbf{W}^{k\ell} = {} & \Psi^{k\ell}\boldsymbol{\partial}_d^j g(\zeta)\boldsymbol{\partial}_c^i\zeta + \Psi^{k\ell}g(\zeta)\boldsymbol{\partial}_d^j\boldsymbol{\partial}_c^i\zeta + g(\zeta)\boldsymbol{\partial}_c^i\zeta\,\boldsymbol{\partial}_d^j\Psi^{k\ell} \\ & -\frac{1}{3}\boldsymbol{\partial}_d^j\Big(\zeta h(\zeta)\Big)\boldsymbol{\partial}_c^i\Psi^{k\ell} - \frac{1}{3}\zeta h(\zeta)\boldsymbol{\partial}_d^j\boldsymbol{\partial}_c^i\Psi^{k\ell}.\end{aligned} \quad (4.49)$$

Considering $\boldsymbol{\partial}g(\zeta)$, we have:

$$\boldsymbol{\partial}g(\zeta) = [3-2\zeta^2]\boldsymbol{\partial}h(\zeta)\boldsymbol{\partial}\zeta - 4\zeta h(\zeta)\boldsymbol{\partial}\zeta = \left[2g(\zeta)\left(\frac{1-\zeta^2}{\zeta}\right) - 4\zeta h(\zeta)\right]\boldsymbol{\partial}\zeta. \quad (4.50)$$

where in the second line we have employed Eq. (4.36). The utility of this definition of $g(\zeta)$

arises more clearly when considering the derivative of $\zeta h(\zeta)$:

$$\boldsymbol{\partial}\Big(\zeta h(\zeta)\Big) = g(\zeta)\boldsymbol{\partial}\zeta. \tag{4.51}$$

Thus, in terms of Eqs. (4.51) and (4.50) we can rewrite Eq. (4.49) as:

$$\begin{aligned}\boldsymbol{\partial}_d^j\boldsymbol{\partial}_c^i\mathbf{W}^{k\ell} &= \Psi^{k\ell}\left[2g(\zeta)\left(\frac{1-\zeta^2}{\zeta}\right) - 4\zeta h(\zeta)\right]\boldsymbol{\partial}_d^j\zeta\;\boldsymbol{\partial}_c^i\zeta + \Psi^{k\ell}g(\zeta)\;\boldsymbol{\partial}_d^j\boldsymbol{\partial}_c^i\zeta \\ &\quad + g(\zeta)\boldsymbol{\partial}_c^i\zeta\;\boldsymbol{\partial}_d^j\Psi^{k\ell} - \tfrac{1}{3}g(\zeta)\boldsymbol{\partial}_d^j\zeta\;\boldsymbol{\partial}_c^i\Psi^{k\ell} - \tfrac{1}{3}\zeta h(\zeta)\boldsymbol{\partial}_d^j\boldsymbol{\partial}_c^i\Psi^{k\ell}.\end{aligned} \tag{4.52}$$

We leave the expansion of $\boldsymbol{\partial}^2\mathbf{W}$ in this form since an implementation of the MBD Hessian in code is likely to benefit from the compact form offered by $g(\zeta)$ and $h(\zeta)$. It is worth noting that both $g(\zeta)$ and $h(\zeta)$ are proportional to $\exp\left[-\zeta^2\right]$, so all terms in $\boldsymbol{\partial}^2\mathbf{W}^{k\ell}$ and $\boldsymbol{\partial}^2U$ die off within the same $\zeta < 6$ radius remarked on in our discussion of floating point underflow in Chapter 3.

In considering derivatives of the point-dipole tensor $\mathbf{T}_{\text{dip}}$ we will suppress all atomic indices (a, b, c, d) as a means of highlighting the Cartesian indices (i, j, k, ℓ). Although the atomic indices are suppressed, we maintain the convention that $\boldsymbol{\partial}^i = \boldsymbol{\partial}_c^i$ and $\boldsymbol{\partial}^j = \boldsymbol{\partial}_d^j$. In contrast to the fast damping due to $\exp\left[-\zeta^2\right]$ present in $\boldsymbol{\partial}^2U$ and $\boldsymbol{\partial}^2\mathbf{W}$, the Hessian of the point-dipole tensor, $\mathbf{T}_{\text{dip}}$, depends solely on the internuclear distance R_{ab} and has terms that are of the same order as those in the first derivative. To see this dependence it is helpful to group the terms by their order in inverse powers of R_{ab}, which we will denote $\mathcal{O}(R^{-n})$. For example, all three terms in the first derivative of $\mathbf{T}_{\text{dip}}$ are of $\mathcal{O}(R^{-4})$

$$\boldsymbol{\partial}_c^i\mathbf{T}_{\text{dip}}^{k\ell} = \boldsymbol{\partial}_c^i\left(\frac{\delta_{kl}}{R^3}\right) - 3\boldsymbol{\partial}_c^i\boldsymbol{\Psi}^{k\ell} \tag{4.53}$$

$$= -3\left[\frac{\delta_{k\ell}}{R^4}\right]\boxed{\boldsymbol{\partial}_c^i R} - 3\left[\frac{R^\ell\boxed{\boldsymbol{\partial}_c^i R^k} + R^k\boxed{\boldsymbol{\partial}_c^i R^\ell}}{R^5}\right] + 15\left[\frac{R^kR^\ell}{R^6}\right]\boxed{\boldsymbol{\partial}_c^i R}. \tag{4.54}$$

The Hessian of $\mathbf{T}_{\text{dip}}$ is expanded below with term order, $\mathcal{O}(R^{-n})$, indicated in the margin.

$$
\begin{aligned}
\boldsymbol{\partial}^j\boldsymbol{\partial}^i\mathbf{T}^{k\ell}_{\text{dip}} = &-3\left[\frac{R^\ell\boxed{\boldsymbol{\partial}^j\boldsymbol{\partial}^i R^k}+R^k\boxed{\boldsymbol{\partial}^j\boldsymbol{\partial}^i R^\ell}}{R^5}\right] && \mathcal{O}(R^{-4})\\
&-3\left[\frac{\delta_{k\ell}}{R^4}\right]\boxed{\boldsymbol{\partial}^j\boldsymbol{\partial}^i R} && \mathcal{O}(R^{-5})\\
&+15\left[\frac{R^kR^\ell}{R^6}\right]\boxed{\boldsymbol{\partial}^j\boldsymbol{\partial}^i R} && \mathcal{O}(R^{-5})\\
&+12\left[\frac{\delta_{k\ell}}{R^5}\right]\boxed{\boldsymbol{\partial}^j R}\boxed{\boldsymbol{\partial}^i R} && \mathcal{O}(R^{-5})\\
&-3\left[\frac{\boxed{\boldsymbol{\partial}^j R^\ell}\boxed{\boldsymbol{\partial}^i R^k}+\boxed{\boldsymbol{\partial}^j R^k}\boxed{\boldsymbol{\partial}^i R^\ell}}{R^5}\right] && \mathcal{O}(R^{-5})\\
&+15\left[\frac{R^\ell\boxed{\boldsymbol{\partial}^i R^k}+R^k\boxed{\boldsymbol{\partial}^i R^\ell}}{R^6}\right]\boxed{\boldsymbol{\partial}^j R} && \mathcal{O}(R^{-5})\\
&+15\left[\frac{R^\ell\boxed{\boldsymbol{\partial}^j R^k}+R^k\boxed{\boldsymbol{\partial}^j R^\ell}}{R^6}\right]\boxed{\boldsymbol{\partial}^i R} && \mathcal{O}(R^{-5})\\
&-90\left[\frac{R^kR^\ell}{R^7}\right]\boxed{\boldsymbol{\partial}^j R}\boxed{\boldsymbol{\partial}^i R} && \mathcal{O}(R^{-5})
\end{aligned}
\tag{4.55}
$$

Notice that since $\boldsymbol{\partial}^2\mathbf{T}_{\text{dip}}$ contains a term of $\mathcal{O}(R^{-4})$, it can be said to be equally long-ranged as $\boldsymbol{\partial}\mathbf{T}_{\text{dip}}$. Even though the second and third terms may appear to be $\mathcal{O}(R^{-4})$, they are actually $\mathcal{O}(R^{-5})$ because $\boldsymbol{\partial}^2 R$ is $\mathcal{O}(R^{-1})$ (cf. Eqs. (4.5)). Likewise, $\boldsymbol{\partial}^2 R^k$, $\boldsymbol{\partial} R$, and $\boldsymbol{\partial} R^k$ are all $\mathcal{O}(R^0)$ (cf. Eq. (4.4) and surrounding discussion).

Through Eqs. (4.55), (4.52) and (4.37), and the equations that they depend on, we have reduced $\boldsymbol{\partial}^2\mathbf{T}$ to the six fundamental derivatives. In the next subsection we will treat the range-separation of both the short- and long-ranged dipole-dipole tensors.

4.2.6 Range-separated dipole-dipole tensors, $\mathbf{T}_{\rm SR}$ & $\overline{\mathbf{T}}_{\rm LR}$

Recall the expressions for the first derivatives of the range-separated dipole interaction tensors (cf. Eqs. (2.55) and (2.54)):

$$\boldsymbol{\partial}_c^i \mathbf{T}_{\rm SR}^{k\ell} = -\mathbf{T}^{k\ell}\boldsymbol{\partial}_c^i f(Z^{TS}) + \left[1 - f\left(Z^{TS}\right)\right]\boldsymbol{\partial}_c^i \mathbf{T}^{k\ell} \tag{4.56}$$

$$\boldsymbol{\partial}_c^i \overline{\mathbf{T}}_{\rm LR}^{k\ell} = \mathbf{T}_{\rm dip}^{k\ell}\boldsymbol{\partial}_c^i f(\overline{Z}) + f(\overline{Z})\boldsymbol{\partial}_c^i \mathbf{T}_{\rm dip}^{k\ell}. \tag{4.57}$$

The second derivatives of these quantities are then:

$$\begin{aligned}\boldsymbol{\partial}_d^j\boldsymbol{\partial}_c^i \mathbf{T}_{\rm SR}^{k\ell} &= -\mathbf{T}^{k\ell}\boldsymbol{\partial}_d^j\boldsymbol{\partial}_c^i f\left(Z^{TS}\right) - \boldsymbol{\partial}_d^j\mathbf{T}^{k\ell}\boldsymbol{\partial}_c^i f\left(Z^{TS}\right) - \boldsymbol{\partial}_d^j f\left(Z^{TS}\right)\boldsymbol{\partial}_c^i\mathbf{T}^{k\ell} \\ &\quad + \left[1 - f\left(Z^{TS}\right)\right]\boldsymbol{\partial}_d^j\boldsymbol{\partial}_c^i\mathbf{T}^{k\ell}\end{aligned} \tag{4.58}$$

$$\begin{aligned}\boldsymbol{\partial}_d^j\boldsymbol{\partial}_c^i \overline{\mathbf{T}}_{\rm LR}^{k\ell} &= \boldsymbol{\partial}_d^j\mathbf{T}_{\rm dip}^{k\ell}\boldsymbol{\partial}_c^i f(\overline{Z}) + \mathbf{T}_{\rm dip}^{k\ell}\boldsymbol{\partial}_d^j\boldsymbol{\partial}_c^i f(\overline{Z}) + \boldsymbol{\partial}_d^j f(\overline{Z})\boldsymbol{\partial}_c^i\mathbf{T}_{\rm dip}^{k\ell} \\ &\quad + f(\overline{Z})\boldsymbol{\partial}_d^j\boldsymbol{\partial}_c^i\mathbf{T}_{\rm dip}^{k\ell},\end{aligned} \tag{4.59}$$

where the appropriate effective vdW radii (cf. Eqs. (2.33), (2.50), (2.35) and (2.51)) are used in the arguments of the Fermi damping function $Z^{\rm TS}$ and $\overline{Z}$.

We have already evaluated $\boldsymbol{\partial}^2\mathbf{T}_{\rm dip}$ and $\boldsymbol{\partial}^2\mathbf{T}$, so we proceed with evaluation of the derivatives of the Fermi damping function. Suppressing the ab indices, the second derivative of the Fermi damping function is easily calculated as (cf. Eq. (2.46)):

$$\boldsymbol{\partial}_c f(Z) = \frac{e^{-Z}}{\left[1+e^{-Z}\right]^2}\,\boldsymbol{\partial}_c Z = e^{-Z}[f(Z)]^2\boldsymbol{\partial}_c Z \tag{4.60}$$

$$\Rightarrow \boldsymbol{\partial}_d\boldsymbol{\partial}_c f(Z) = e^{-Z}[f(Z)]^2\Big[\left(2e^{-Z}f(Z) - 1\right)\boldsymbol{\partial}_d Z\,\boldsymbol{\partial}_c Z + \boldsymbol{\partial}_d\boldsymbol{\partial}_c Z\Big]. \tag{4.61}$$

This is computed using the derivatives of Z (cf. Eq. (2.47)):

$$\boldsymbol{\partial}_c Z = 6\left[\frac{\boxed{\boldsymbol{\partial}_c R}}{S} - \frac{R\,\boldsymbol{\partial}_c S}{S^2}\right] \tag{4.62}$$

$$\Rightarrow \boldsymbol{\partial}_d\boldsymbol{\partial}_c Z = 6\left[\frac{\boxed{\boldsymbol{\partial}_d\boldsymbol{\partial}_c R}}{S} - \frac{\boldsymbol{\partial}_d S\,\boxed{\boldsymbol{\partial}_c R} + \boxed{\boldsymbol{\partial}_d R}\,\boldsymbol{\partial}_c S + R\,\boldsymbol{\partial}_d\boldsymbol{\partial}_c S}{S^2} + 2\frac{R\,\boldsymbol{\partial}_c S\,\boldsymbol{\partial}_d S}{S^3}\right] \tag{4.63}$$

which are constructed from the derivatives of S_{ab} (cf. Eq. (2.48)):

$$\boldsymbol{\partial}_c S_{ab} = \beta \left[\boldsymbol{\partial}_c \mathcal{R}_a^{\mathrm{vdW}} + \boldsymbol{\partial}_c \mathcal{R}_q^{\mathrm{vdW}} \right] \tag{4.64}$$

$$\Rightarrow \boldsymbol{\partial}_d \boldsymbol{\partial}_c S_{ab} = \beta \left[\boldsymbol{\partial}_d \boldsymbol{\partial}_c \mathcal{R}_a^{\mathrm{vdW}} + \boldsymbol{\partial}_d \boldsymbol{\partial}_c \mathcal{R}_q^{\mathrm{vdW}} \right] \tag{4.65}$$

The Hessians of the TS-level and rsSCS-level effective vdW radii are used to construct $\boldsymbol{\partial}^2 Z^{\mathrm{TS}}$ and $\boldsymbol{\partial}^2 \overline{Z}$ respectively:

$$\boldsymbol{\partial}_d \boldsymbol{\partial}_c \mathcal{R}_a^{\mathrm{vdW,\,TS}} = \frac{\mathcal{R}_a^{\mathrm{vdW,\,free}}}{[V_a^{\mathrm{free}}]^{1/3}} \left(\frac{1}{3} \frac{\boxed{\boldsymbol{\partial}_d \boldsymbol{\partial}_c V_a}}{[V_a]^{2/3}} - \frac{2}{9} \frac{\boxed{\boldsymbol{\partial}_d V_a} \boxed{\boldsymbol{\partial}_c V_a}}{[V_a]^{5/3}} \right) \tag{4.66}$$

$$\boldsymbol{\partial}_d \boldsymbol{\partial}_c \overline{\mathcal{R}}_a^{\mathrm{vdW}} = \frac{\mathcal{R}^{\mathrm{vdW,\,free}}}{[\alpha^{0,\,\mathrm{free}}]^{1/3}} \left(\frac{1}{3} \frac{\boldsymbol{\partial}_d \boldsymbol{\partial}_c \overline{\alpha}(0)}{[\overline{\alpha}(0)]^{2/3}} - \frac{2}{9} \frac{\boldsymbol{\partial}_d \overline{\alpha}(0)\ \boldsymbol{\partial}_c \overline{\alpha}(0)}{[\overline{\alpha}(0)]^{5/3}} \right) \tag{4.67}$$

Where the Hessian of $\overline{\alpha}(0)$ has been computed above in section 4.2.4 and $\boldsymbol{\partial}_c \overline{\alpha}_a(0)$ is computed in Eq. 2.43 of Chapter 2. We have now reduced the Hessians of all quantities required to evaluate the range-separated dipole-dipole tensors (cf. Eqs. (4.58) and (4.59)) to the fundamental derivatives or previously derived expressions. Together these expressions allow computation of $\boldsymbol{\partial}^2 \overline{\omega}$, and in turn the Hessian of the non-interacting energy:

$$\boldsymbol{\partial}^2 E_{\mathrm{non-int.}}^{\mathrm{MBD}} = \frac{3}{2} \sum_{a=1}^{N} \boldsymbol{\partial}^2 \overline{\omega}_a \tag{4.68}$$

The only remaining ingredient for the MBD Hessian is to evaluate the interacting quantities, which require the second derivative of the interaction matrix, *i.e.* $\boldsymbol{\partial}^2 \mathbf{C}^{\mathrm{MBD}}$, and of its eigenvalues, *i.e.* $\boldsymbol{\partial}^2 \lambda$.

4.2.7 Interacting quantities

We now turn our attention to the Hessian of the interacting energy

$$\boldsymbol{\partial}^2 E_{\text{int.}}^{\text{MBD}} = \frac{1}{2}\sum_{p=1}^{3N} \boldsymbol{\partial}^2 \sqrt{\lambda_p} \tag{4.69}$$

Recall from Eq. (2.40) that the interacting forces were computed from

$$\sum_{p=1}^{N} \boldsymbol{\partial}_c \sqrt{\lambda_p} = \frac{1}{2}\text{Tr}\left[\boldsymbol{\Lambda}^{-1/2}\boldsymbol{\mathcal{X}}^{\intercal}\boldsymbol{\partial}_c \mathbf{C}^{\text{MBD}}\boldsymbol{\mathcal{X}}\right], \tag{4.70}$$

where $\boldsymbol{\Lambda}$ is the diagonal matrix of eigenvalues of $\mathbf{C}^{\text{MBD}}$ and $\boldsymbol{\mathcal{X}}$ is the matrix of eigenvectors. Symbolically, the second derivative is equally straightforward,

$$\begin{aligned}\sum_{p=1}^{N} \boldsymbol{\partial}_d\boldsymbol{\partial}_c \sqrt{\lambda_p} =& \frac{1}{2}\text{Tr}\left[\boldsymbol{\partial}_d\left(\boldsymbol{\Lambda}^{-1/2}\right)\boldsymbol{\mathcal{X}}^{\intercal}\boldsymbol{\partial}_c \mathbf{C}^{\text{MBD}}\boldsymbol{\mathcal{X}}\right] + \frac{1}{2}\text{Tr}\left[\boldsymbol{\Lambda}^{-1/2}\boldsymbol{\mathcal{X}}^{\intercal}\boldsymbol{\partial}_d\boldsymbol{\partial}_c \mathbf{C}^{\text{MBD}}\boldsymbol{\mathcal{X}}\right] \\ &+ \frac{1}{2}\text{Tr}\left[\boldsymbol{\Lambda}^{-1/2}\boldsymbol{\partial}_d\left(\boldsymbol{\mathcal{X}}^{\intercal}\right)\boldsymbol{\partial}_c \mathbf{C}^{\text{MBD}}\boldsymbol{\mathcal{X}}\right] + \frac{1}{2}\text{Tr}\left[\boldsymbol{\Lambda}^{-1/2}\boldsymbol{\mathcal{X}}^{\intercal}\boldsymbol{\partial}_c \mathbf{C}^{\text{MBD}}\boldsymbol{\partial}_d\boldsymbol{\mathcal{X}}\right].\end{aligned} \tag{4.71}$$

However, the second line of the above expression requires eigenvector derivatives, $\boldsymbol{\partial}_d\boldsymbol{\mathcal{X}}$, which must be treated with some care. Since $\mathbf{C}^{\text{MBD}}$ is real, symmetric, and diagonally dominated we assume for the moment that all of its eigenvalues are distinct.[†] There is a rich literature on analytical and numerical treatments of eigenvalue and eigenvector derivatives (cf. Refs. 261,461 simple derivations, Refs. 462,463 for treatment of repeated eigenvalues and Refs. 464,465 for discussion of iterative methods for their computation). The following treatment is therefore brief and specific to the case of real, symmetric matrices with distinct eigenvalues and eigenvector derivatives. The eigensystem of interest is:

$$\left[\mathbf{C}^{\text{MBD}} - \Lambda\mathbb{I}\right]\boldsymbol{\mathcal{X}} = \mathbf{0}. \tag{4.72}$$

[†]Numerically this can become problematic in very large supercells, but Hessians will become prohibitively memory expensive faster than MBD forces, so it is likely that evaluating Hessians for periodic systems will require converging the MBD energy in reciprocal space anyway, thereby eliminating some of the concerns with diagonalizing a large $\mathbf{C}^{\text{MBD}}$ matrix.

Let $\mathbf{x}_p$ be the p^{th} column of $\boldsymbol{\mathcal{X}}$, *i.e.* the eigenvector corresponding to $\lambda_p = \Lambda_{pp}$. The derivative of this eigenvector is then:[261]

$$\begin{aligned}
\boldsymbol{\partial}\Big(\Big[\mathbf{C}^{\text{MBD}} - \lambda_p \mathbb{I}\Big]\, \mathbf{x}_p \Big) &= \mathbf{0} && (4.73)\\
\Big[\mathbf{C}^{\text{MBD}} - \lambda_p \mathbb{I}\Big] \Big(\boldsymbol{\partial}\mathbf{x}_p\Big) &= -\Big[\boldsymbol{\partial}\mathbf{C}^{\text{MBD}} - \boldsymbol{\partial}\lambda_p \mathbb{I}\Big]\, \mathbf{x}_p && (4.74)\\
&= \underbrace{\Big[\mathbf{x}_p^{\mathsf{T}} \boldsymbol{\partial}\mathbf{C}^{\text{MBD}} \mathbf{x}_p \mathbb{I}\Big]\, \mathbf{x}_p - \boldsymbol{\partial}\mathbf{C}^{\text{MBD}} \mathbf{x}_p}_{\mathbf{D}_p} && (4.75)
\end{aligned}$$

where in the last line we have defined the quantity $\mathbf{D}_p$ to collapse the right-hand side. Note that since $\mathbf{x}_p^{\mathsf{T}} \mathbf{D}_p = 0$, this system of equations is consistent even though the matrix on the left-hand side of Eq. (4.74) has rank $3N - 1$ (recalling that $\mathbf{C}^{\text{MBD}}$ is a $3N \times 3N$ matrix, where N is the number of atoms in the simulation cell or supercell, full rank would be $n = 3N$). To admit a unique solution, we then need an additional equation, which expresses $\boldsymbol{\partial}\mathbf{x}_p$ in terms of a sum of all n right eigenvectors.

$$\boldsymbol{\partial}\mathbf{x}_p = \sum_{q=1}^{3N} \eta_q \mathbf{x}_q \quad = \quad \boldsymbol{\mathcal{X}}\boldsymbol{\eta} \tag{4.76}$$

To determine the constants $\{\eta_q\}$, left multiply Eq. (4.75) by $\mathbf{x}_q^{\mathsf{T}}$:

$$\begin{aligned}
\mathbf{x}_q^{\mathsf{T}} \Big[\mathbf{C}^{\text{MBD}} - \lambda_p \mathbb{I}\Big]\, \boldsymbol{\mathcal{X}}\boldsymbol{\eta} &= \mathbf{x}_q^{\mathsf{T}} \mathbf{D}_p && (4.77)\\
\Rightarrow [\lambda_q - \lambda_p]\, \eta_q &= \mathbf{x}_q^{\mathsf{T}} \mathbf{D}_p \qquad q \neq p && (4.78)
\end{aligned}$$

So we have determined the constants for all but $q = p$ and have the expression:

$$\boldsymbol{\partial}\mathbf{x}_p = \eta_p \mathbf{x}_p + \underbrace{\sum_{q=1, q\neq p}^{3N} \frac{\mathbf{x}_q^{\mathsf{T}} \mathbf{D}_p \mathbf{x}_q}{\lambda_q - \lambda_p}}_{\mathbf{v}_p} \tag{4.79}$$

To determine the arbitrary constant η_p we consider the norm of the eigenvector. We assume that the eigenvectors of $\mathbf{C}^{\mathrm{MBD}}$ are normalized to one, so:

$$\mathbf{x}_p^\mathsf{T}\mathbf{x}_p = 1 \qquad \Rightarrow \qquad \mathbf{x}_p^\mathsf{T}\boldsymbol{\partial}\mathbf{x}_p = 0 \tag{4.80}$$

Thus, plugging Eq. (4.79) into Eq. (4.80) determines η_p:

$$\mathbf{x}_p^\mathsf{T}\boldsymbol{\partial}\mathbf{x}_p = \mathbf{x}_p^\mathsf{T}\eta_p\mathbf{x}_p + \mathbf{x}_p^\mathsf{T}\mathbf{v}_p = 0 \qquad \Rightarrow \qquad \eta_p = -\mathbf{x}_p^\mathsf{T}\mathbf{v}_p. \tag{4.81}$$

Altogether the eigenvector derivative is:

$$\boldsymbol{\partial}\mathbf{x}_p = \left(\sum_{q=1,q\neq p}^{3N} \frac{\mathbf{x}_q^\mathsf{T}\mathbf{D}_p\mathbf{x}_q}{\lambda_q - \lambda_p}\right) - \mathbf{x}_p^\mathsf{T}\left(\sum_{q=1,q\neq p}^{3N} \frac{\mathbf{x}_q^\mathsf{T}\mathbf{D}_p\mathbf{x}_q}{\lambda_q - \lambda_p}\right)\mathbf{x}_p \tag{4.82}$$

where $\mathbf{D}_p \equiv \boldsymbol{\partial}\lambda_p\mathbf{x}_p - \boldsymbol{\partial}\mathbf{C}^{\mathrm{MBD}}\mathbf{x}_p$. Since these expressions require avoiding the divergence that would occur for $q = p$ in dividing by $(\lambda_q - \lambda_p)$, we shall not re-assemble the expression for $\boldsymbol{\partial}^2\sqrt{\lambda}$ into the matrix expression of Eq. 4.71, but simply note that Eq. (4.82) provides a prescription for the necessary computations.

The only remaining elements required for the interacting energy Hessian are to compute $\boldsymbol{\partial}\lambda_p^{-1/2}$ and $\boldsymbol{\partial}^2\mathbf{C}^{\mathrm{MBD}}$. The former is trivially $-\frac{1}{2}\lambda_p^{-3/2}\boldsymbol{\partial}\lambda_p$. It will be convenient to define $K_{ab} \equiv \sqrt{\overline{\alpha}_a(0)\overline{\alpha}_b(0)}$ so that we can compress expressions appearing in $\boldsymbol{\partial}\mathbf{C}^{\mathrm{MBD}}$ and $\boldsymbol{\partial}^2\mathbf{C}^{\mathrm{MBD}}$. Employing this notation, we re-write Eq. (2.41) such that the first derivative of $\mathbf{C}^{\mathrm{MBD}}$ is

$$\begin{aligned}\boldsymbol{\partial}_c\mathbf{C}_{ab}^{\mathrm{MBD}} = &\underbrace{2\delta_{ab}\overline{\omega}_a\boldsymbol{\partial}_c\overline{\omega}_a}_{❶} + \underbrace{(1-\delta_{ab})\left[\overline{\omega}_a\boldsymbol{\partial}_c\overline{\omega}_b + \overline{\omega}_b\boldsymbol{\partial}_c\overline{\omega}_a\right]K_{ab}\,\overline{\mathbf{T}}_{ab}^{\mathrm{LR}}}_{❷} \\ &+ \underbrace{(1-\delta_{ab})\,\overline{\omega}_a\overline{\omega}_b\boldsymbol{\partial}_c K_{ab}\,\overline{\mathbf{T}}_{ab}^{\mathrm{LR}}}_{❸} + \underbrace{(1-\delta_{ab})\,\overline{\omega}_a\overline{\omega}_b K_{ab}\,\boldsymbol{\partial}_c\overline{\mathbf{T}}_{ab}^{\mathrm{LR}}}_{❹},\end{aligned} \tag{4.83}$$

where in the second line we have used the relation:

$$\boldsymbol{\partial}_c K_{ab} \;=\; \frac{[\overline{\alpha}_a(0)\,\boldsymbol{\partial}_c\overline{\alpha}_b(0) + \overline{\alpha}_b(0)\,\boldsymbol{\partial}_c\overline{\alpha}_a(0)]}{2K_{ab}}. \tag{4.84}$$

Taking the derivative of Eq. (4.84) yields:

$$\begin{aligned}\Rightarrow \boldsymbol{\partial}_d\boldsymbol{\partial}_c K_{ab} \;=\;& \frac{1}{2}K_{ab}^{-1}\Big[\boldsymbol{\partial}_d\overline{\alpha}_a(0)\,\boldsymbol{\partial}_c\overline{\alpha}_b(0) + \boldsymbol{\partial}_d\overline{\alpha}_a(0)\,\boldsymbol{\partial}_c\overline{\alpha}_b(0)\Big] \\ &+\frac{1}{2}K_{ab}^{-1}\Big[\overline{\alpha}_b(0)\,\boldsymbol{\partial}_d\boldsymbol{\partial}_c\overline{\alpha}_a(0) + \overline{\alpha}_b(0)\,\boldsymbol{\partial}_d\boldsymbol{\partial}_c\overline{\alpha}_a(0)\Big] \\ &-\frac{1}{2}K_{ab}^{-2}\boldsymbol{\partial}_d K_{ab}\Big[\overline{\alpha}_a(0)\,\boldsymbol{\partial}_c\overline{\alpha}_b(0) + \overline{\alpha}_b(0)\,\boldsymbol{\partial}_c\overline{\alpha}_a(0)\Big].\end{aligned} \tag{4.85}$$

The second derivative of $\mathbf{C}^{\mathrm{MBD}}$ simply requires brute force application of the product rule and assembling the relevant expressions computed above $\boldsymbol{\partial}^2\overline{\alpha}(0)$, $\boldsymbol{\partial}^2\overline{\omega}$, $\boldsymbol{\partial}^2\overline{\mathbf{T}}_{\mathrm{LR}}$ and the corresponding first derivatives computed in Chapter 2 (Eqs. (2.42),(2.43) and (2.54)). Although these derivatives are not especially interesting, we expand them below for the sake of having a complete derivation that will hopefully one day be implemented into functional MBD Hessian code. The derivative of the first term in Eq. (4.83) is:

$$\boldsymbol{\partial}_d\,[\textbf{❶}] \;=\; 2\delta_{ab}\,(\boldsymbol{\partial}_d\overline{\omega}_a\boldsymbol{\partial}_c\overline{\omega}_a + \overline{\omega}_a\boldsymbol{\partial}_d\boldsymbol{\partial}_c\overline{\omega}_a) \tag{4.86}$$

The derivative of the second term in Eq. (4.83) is:

$$\begin{aligned}\boldsymbol{\partial}_d\,[\textbf{❷}] \;=\; (1-\delta_{ab})\Bigg[&\boldsymbol{\partial}_d\big[\overline{\omega}_a\boldsymbol{\partial}_c\overline{\omega}_b + \overline{\omega}_b\boldsymbol{\partial}_c\overline{\omega}_a\big]K_{ab}\;\overline{\mathbf{T}}_{ab}^{\mathrm{LR}} \\ &+[\overline{\omega}_a\boldsymbol{\partial}_c\overline{\omega}_b + \overline{\omega}_b\boldsymbol{\partial}_c\overline{\omega}_a]\boldsymbol{\partial}_d K_{ab}\;\overline{\mathbf{T}}_{ab}^{\mathrm{LR}} \\ &+[\overline{\omega}_a\boldsymbol{\partial}_c\overline{\omega}_b + \overline{\omega}_b\boldsymbol{\partial}_c\overline{\omega}_a]K_{ab}\;\boldsymbol{\partial}_d\overline{\mathbf{T}}_{ab}^{\mathrm{LR}}\Bigg],\end{aligned} \tag{4.87}$$

where in the first line we have:

$$\boldsymbol{\partial}_d\big[\overline{\omega}_a\boldsymbol{\partial}_c\overline{\omega}_b + \overline{\omega}_b\boldsymbol{\partial}_c\overline{\omega}_a\big] = \boldsymbol{\partial}_d\overline{\omega}_a\boldsymbol{\partial}_c\overline{\omega}_b + \boldsymbol{\partial}_d\overline{\omega}_b\boldsymbol{\partial}_c\overline{\omega}_a + \overline{\omega}_a\boldsymbol{\partial}_d\boldsymbol{\partial}_c\overline{\omega}_b + \overline{\omega}_b\boldsymbol{\partial}_d\boldsymbol{\partial}_c\overline{\omega}_a \tag{4.88}$$

and in the second line we make use of Eq. (4.84). The derivative of the third term in Eq. (4.83) is:

$$\begin{aligned}\boldsymbol{\partial}_d\,[\textbf{❸}] \;=\; (1-\delta_{ab})\Big[&(\boldsymbol{\partial}_d\overline{\omega}_a\overline{\omega}_b+\overline{\omega}_a\boldsymbol{\partial}_d\overline{\omega}_b)\boldsymbol{\partial}_c K_{ab}\;\overline{\mathbf{T}}_{ab}^{\mathrm{LR}}+\overline{\omega}_a\overline{\omega}_b\boldsymbol{\partial}_d\boldsymbol{\partial}_c K_{ab}\;\overline{\mathbf{T}}_{ab}^{\mathrm{LR}} \\ &+\overline{\omega}_a\overline{\omega}_b\boldsymbol{\partial}_c K_{ab}\;\boldsymbol{\partial}_d\overline{\mathbf{T}}_{ab}^{\mathrm{LR}}\Big].\end{aligned} \tag{4.89}$$

And finally, the fourth term is:

$$\begin{aligned}\boldsymbol{\partial}_d\,[\textbf{❹}] \;=\; (1-\delta_{ab})\Big[&(\overline{\omega}_b\boldsymbol{\partial}_d\overline{\omega}_a+\overline{\omega}_a\boldsymbol{\partial}_d\overline{\omega}_b)K_{ab}\;\boldsymbol{\partial}_c\overline{\mathbf{T}}_{ab}^{\mathrm{LR}}+\overline{\omega}_a\overline{\omega}_b\boldsymbol{\partial}_d K_{ab}\;\boldsymbol{\partial}_c\overline{\mathbf{T}}_{ab}^{\mathrm{LR}} \\ &+\overline{\omega}_a\overline{\omega}_b K_{ab}\;\boldsymbol{\partial}_d\boldsymbol{\partial}_c\overline{\mathbf{T}}_{ab}^{\mathrm{LR}}\Big],\end{aligned} \tag{4.90}$$

where in the second line we again employ Eq. (4.84). Together Eqs. (4.86-4.90), along with the definition of K_{ab}, completely specify the Hessian of the interaction matrix $\mathbf{C}^{\mathrm{MBD}}$. We have thus reduced all terms required to compute $\boldsymbol{\partial}^2 E_{\mathrm{MBD}}$ to the six fundamental derivatives and first order derivatives from Chapter 2.

4.2.8 Conclusions

We motivated this lengthy derivation of the analytical MBD Hessian by making some broad observations about the great success of the phonon description of the quantum theory of solids and more specifically referencing the work of the Tkatchenko group in explaining the contribution of collective dispersion interactions to the phonon spectrum of organic crystals with hydrogen-bond networks. Reilly *et al.* published a particularly compelling study on polymorphism in aspirin,[112] but personal discussions with other members of the group have indicated that MBD makes large contributions ot the phonon density of states for many organic molecular crystals. Implementing the analytical MBD Hessian is likely to require several thousand lines of code and an efficient Hessian implementation for condensed phase systems may require additional development efforts

to converge the MBD energy in reciprocal space. However, given the large role that electron-phonon coupling plays in determining the charge transport properties of organic semiconductors, we are confident that there are many fascinating discoveries about many-body dispersion effects that are waiting to be made from studying the impact of MBD on phonon states in organic materials. In this respect, the MBD model is just beginning to reveal its true value.

4.3 Self-Consistent MBD

In the introduction and in Chapter 1, we motivated the discussion of many-body dispersion effects by noting that nonlocal correlation effects impact many properties of organic semiconductors and low dimensional nanostructures. In the discussion of DPP pigments, we found that self-consistent application of the VV10 nonlocal correlation correction could impact density dependent properties such as charge transfer integrals. Self-consistent dispersion corrections can potentially impact all properties that are derived from the charge density, such as the dipole moment, but the greatest impact is expected for properties that either depend very sensitively on the phase or overlap magnitude (such as a transfer integral or interaction energy), or for the excitations of systems that are dominated by dispersion interactions (such as the coupling between twisted vdW heterostructures). At very short range, dispersion corrections are damped out, while at very long range the density is so small that the effects of self-consistency are typically negligible.[92,99] It is for this reason that many vdW corrections have been applied very successfully as *a posteriori* corrections to the self-consistent field solution.[92]
Thonhauser *et al.* found that although the change in the charge density is very small ($\sim 10^{-4}$electrons/Å^3), self-consistent application of the vdW-DF nonlocal correlation functional produces significant changes to the binding energy and forces in the argon dimer.[99] This "vdW bonding charge" indicates that for systems where the fragments are pushed together more closely but the interactions are still dominated by dispersion, self-consistent treatment of the vdW corrections are likely to be most important.

Self-consistent application of nonlocal correlation functional methods such as vdW-DF or VV10 can result in greater than 200% the computational cost of a generalized gradient approximation functional such as PBE, while non-self-consistent application only cost an additional $\sim 3\%$.[366] Given this computational expense and the accuracy of using dispersion methods as *a posteriori* corrections, nonlocal functionals are rarely employed self-consistently. However, when one is interested in density dependent properties for highly polarizable systems, such as graphitic nanostructures, it is important to have self-consistent density dependent correction methodologies available. Unlike the nonlocal correlation functional corrections, which derive their correction from nonlocal correlation kernel defined at every point in space, MBD is based on a coarse-graining of the charge density, namely, the Hirshfeld partitioning and assignment of QHOs. In this sense, self-consistent MBD is more comparable to methods such as the dDsC method of Brémond *et al.*[92] or to self-consistent application of the TS correction.[114] Ferri *et al.* have found that self-consistent application of a vdW correction is particularly important for electrodynamic screening at metal surfaces.[114] Motivated by the potential for self-consistent dispersion corrections to play a crucial role in studying density dependent properties of layered materials, we have derived and implemented a self-consistent formulation of MBD. As this is an active area of method development, the results presented herein should be regarded as preliminary.

4.3.1 Derivation of self-consistent MBD

To derive the MBD correction to the self-consistent field equations it will be useful to review the basic equations of density functional theory. Within the Kohn-Sham framework of DFT,[466] non-interacting single particle states generate the same density as the true interacting electrons. The total energy of this system, E, is expressed as a functional of the density

$$E[\rho] = T[\rho] + \int \mathrm{d}\mathbf{r}\; v_{\mathrm{ext}}(\mathbf{r})\rho(\mathbf{r}) + \overbrace{\frac{e^2}{2}\int \mathrm{d}\mathbf{r}\int \mathrm{d}\mathbf{r}'\frac{\rho(\mathbf{r})\rho(\mathbf{r}')}{\|\mathbf{r}-\mathbf{r}'\|}}^{E_{\mathrm{H}}[\rho]} + E_{\mathrm{xc}}[\rho], \tag{4.91}$$

where $T[\rho]$ is the kinetic energy, $E_{\mathrm{H}}[\rho]$ is the Hartree (or Coulomb) energy, v_{ext} is the external potential arising from the electron-nuclear Coulomb interaction as well as any external electric or magnetic fields that are present, and E_{xc} is the exchange-correlation energy. Together, these last three terms make up the contribution of the local effective potential, v_{eff}, in which the non-interacting Kohn-Sham particles move. As a result, v_{eff} is called the Kohn-Sham potential, and it is given by the functional derivative with respect to the charge density of the potential energy terms above

$$v_{\mathrm{eff}} = v_{\mathrm{ext}} + e^2\int \frac{\rho(\mathbf{r}')}{\|\mathbf{r}-\mathbf{r}'\|}\mathrm{d}\mathbf{r}' + \frac{\delta E_{\mathrm{xc}}[\rho]}{\delta\rho}, \tag{4.92}$$

where the last term is called the exchange-correlation potential, v_{xc}. Since the MBD correlation energy is a linear correction to the exchange-correlation energy

$$E_{\mathrm{xc}}[\rho] \to E_{\mathrm{xc}}[\rho] + E_c^{\mathrm{MBD}}[\rho], \tag{4.93}$$

the self-consistent contribution of MBD to the density is found by computing the functional derivative of E_c^{MBD} with respect to the charge density, and adding this

"dispersion potential," $v_{\rm c}^{\rm MBD}$, to the exchange-correlation potential:

$$v_{\rm xc} \to v_{\rm xc} + v_{\rm c}^{\rm MBD} = \frac{\delta E_{\rm xc}[\rho]}{\delta\rho} + \frac{\delta E_{\rm c}^{\rm MBD}}{\delta\rho} \tag{4.94}$$

All of the density dependence in the MBD correlation energy arises through the Hirshfeld partitioning, which is why we denoted the Hirshfeld effective atomic volumes as a functional of the density, $V[\rho(\mathbf{r})]$, when they first appeared in Eq. (2.5). Having been careful in Chapter 2 to separate out terms that depended on the Hirshfeld gradients, it is a straightforward task to compute the dispersion potential by using the chain-rule to express $v_{\rm c}^{\rm MBD}$ in terms of the derivative with respect to the Hirshfeld volume

$$v_{\rm c}^{\rm MBD} = \frac{\delta E_c^{\rm MBD}}{\delta\rho} = \frac{\boldsymbol{\partial} E_{\rm c}^{\rm MBD}}{\boldsymbol{\partial} V}\frac{\delta V}{\delta\rho} \tag{4.95}$$

This is especially convenient since we reduced all gradients in Chapter 2 to the three fundamental quantities $\boldsymbol{\partial} R$, $\boldsymbol{\partial} R^i$, and $\boldsymbol{\partial} V$, which makes it easy to eliminate terms depending on $\boldsymbol{\partial}\|\mathbf{R}\|$ or $\boldsymbol{\partial}\|\mathbf{R}^i\|$ since $\boldsymbol{\partial}\mathbf{R}_{ab}/\boldsymbol{\partial}\rho = 0$. Therefore, $\boldsymbol{\partial}\mathbf{T}_{\rm dip}/\boldsymbol{\partial}\rho$ vanishes completely (cf. Eq. (2.52)), so $\boldsymbol{\partial}\overline{\mathbf{T}}_{\rm LR}$ reduces to

$$\frac{\boldsymbol{\partial}\overline{\mathrm{T}}^{ij}_{ab,\,\rm LR}}{\boldsymbol{\partial} V_c} = \mathrm{T}^{ij}_{ab,\,\rm dip}\,\frac{\boldsymbol{\partial} f\left(\overline{Z}_{ab}\right)}{\boldsymbol{\partial} V_c}. \tag{4.96}$$

Likewise, we modify terms that have mixed dependence on $\boldsymbol{\partial} V$ and $\boldsymbol{\partial} R$, such as Eqs. (2.47), (2.56), (2.54), (2.58), and (2.59). For instance, Eq. (2.56) becomes:

$$\frac{\boldsymbol{\partial}\mathrm{T}^{ij}}{\boldsymbol{\partial} V_c} = \left[\mathrm{T}^{ij}_{\rm dip} + \frac{R^i R^j}{R^5}\left[3 - 2\zeta^2\right]\right] h(\zeta)\,\frac{\boldsymbol{\partial}\zeta}{\boldsymbol{\partial} V_c}, \tag{4.97}$$

where $\boldsymbol{\partial}\zeta$ (cf. Eq. (2.58)) is reduced to

$$\frac{\boldsymbol{\partial}\zeta_{ab}}{\boldsymbol{\partial} V_c} = -\frac{\zeta_{ab}^3}{R_{ab}^2}\left[\sigma_a\frac{\boldsymbol{\partial}\sigma_a}{\boldsymbol{\partial} V_c} + \sigma_b\frac{\boldsymbol{\partial}\sigma_b}{\boldsymbol{\partial} V_c}\right]. \tag{4.98}$$

Many of the intermediate equations, such as Eq. (2.37-2.44), (2.55), (2.46), (2.51), or

(2.48), remain wholly unmodified since they are expressed in terms of non-fundamental quantities that contain Hirshfeld volume dependence. Terms that depend solely on $\boldsymbol{\partial} V$, such as Eqs. (2.50), (2.59), and (2.45) remain essentially unchanged except for canceling $\boldsymbol{\partial} V$, *e.g.* $\boldsymbol{\partial}\mathbf{A}$ (cf. Eq. (2.45)) becomes:

$$\frac{\boldsymbol{\partial}\mathbf{A}}{\boldsymbol{\partial} V_c} = \bigoplus_{a=1}^{N} \operatorname{diag}\left[\Upsilon_{\mathrm{a}}\delta_{\mathrm{ca}}\right], \tag{4.99}$$

and $\boldsymbol{\partial}\sigma$ (cf. Eq. (2.59)) becomes:

$$\frac{\boldsymbol{\partial}\sigma_a}{\boldsymbol{\partial} V_c} = \left[\frac{1}{3}\sqrt{\frac{2}{\pi}}\Upsilon_a\right]^{1/3} \frac{\delta_{ca}}{3[V_a]^{2/3}}, \tag{4.100}$$

where the Kronecker deltas arise in Eq. (4.99) and (4.100) because $\boldsymbol{\partial} V_b / \boldsymbol{\partial} V_a = \delta_{ba}$.

Finally, the "fundamental" derivative for the dispersion potential is the functional derivative of the effective volume integral. Recalling that $\rho^{\mathrm{eff}}(\mathbf{r}) = w_a \rho(\mathbf{r})$, this derivative is quite simple (cf. Sec. 4.2.2):

$$V_a = \int \mathrm{d}\mathbf{r} \|\mathbf{r} - \boldsymbol{\mathcal{R}}_a\|^3 w_a(\mathbf{r}) \rho(\mathbf{r}) \tag{4.101}$$

$$\Rightarrow \frac{\delta V_a}{\delta \rho(\mathbf{r})} = \int \mathrm{d}\mathbf{r} \|\mathbf{r} - \boldsymbol{\mathcal{R}}_a\|^3 w_a(\mathbf{r}) = \int \mathrm{d}\mathbf{r} \|\mathbf{r} - \boldsymbol{\mathcal{R}}_a\|^3 \frac{\rho_a^{\mathrm{free}}(\|\mathbf{r} - \boldsymbol{\mathcal{R}}_a\|)}{\rho_{\mathrm{sad}}(\mathbf{r})}. \tag{4.102}$$

4.3.2 Results and discussion

We have made these modifications to our MBD gradients code and implemented MBD self-consistently in the PWscf module of QE. Since this development work was only recently completed, we have not yet conducted a systematic evaluation of which properties of dispersively bound systems are impacted by the self-consistent application of MBD, nor have we conclusively eliminated all software bugs. We are also actively working to develop scMBD in Octopus, where the ability to invert the Kohn-Sham potential may offer additional insight into the scMBD method. As indicated in the introduction to this section, we expect self-consistency to be a negligible correction to most systems since the

charge density is typically small in the intermolecular region where the dispersion potential will contribute. However, dispersion dominated properties such as the interaction energies of aromatic molecules may strike the appropriate balance between being sufficiently long-range for the MBD correlation energy to have been "turned on" by the damping function while the charge density has not decayed so much that the self-consistent changes to the density cannot influence properties significantly. In the discussion below we will present our preliminary findings resulting from the first self-consistent MBD calculations.

A recent benchmark study by Řezáč *et al.* has examined the performance of many electronic structure methods for computing three-body intermolecular interaction energies on a diverse set of 69 molecular trimers selected from 23 molecular crystals, thus the benchmark set is titled "3B-69".[104] The benchmark three-body interaction energies were computed at the CCSD(T)/CBS level using the MP2+Δ CCSD(T) method.[‡] This scheme is estimated to provide results within $\sim 2\%$ of converged CCSD(T)/CBS results. The set covered structures that exhibit a variety of intermolecular interactions and packing arrangements. The two-body and three-body interaction energies are defined as:

$$\Delta E^2(AB) = E(AB) - E(A) - E(C) \tag{4.103}$$

$$\begin{aligned} \Delta E^3(ABC) = {} & E(ABC) - \Delta E^2(AB) - \Delta E^2(AC) - \Delta E^2(BC) \\ & - E(A) - E(B) - E(C) \end{aligned} \tag{4.104}$$

They found that many popular density functionals corrected with the three-body Axilrod-Teller-Muto term[14,15] as implemented in the D3 dispersion correction, performed quite poorly for reproducing these three-body interaction energies, largely due to an inability of the underlying exchange-correlation functionals to reproduce many-body exchange or polarization effects in a reliable manner.[104] This is a particularly important finding because polarization and cooperative hydrogen-bonding are often one of the

[‡]The Hartree-Fock energy is computed in an augmented correlation consistent aug-cc-pQZ basis set,[308,467] and the RI-MP2 correlation energy is extrapolated to the complete basis set limit (CBS) using aug-cc-pVQZ/aug-cc-pVTZ basis sets. Finally, a correction at the CCSD(T)/aug-cc-pDZ level with the frozen natural orbital (FNO) approximation was applied.

largest sources of many-body non-covalent interactions, *e.g.* hydrogen bond cooperativity can account for 30% or more of the binding energy of some water clusters.[468]

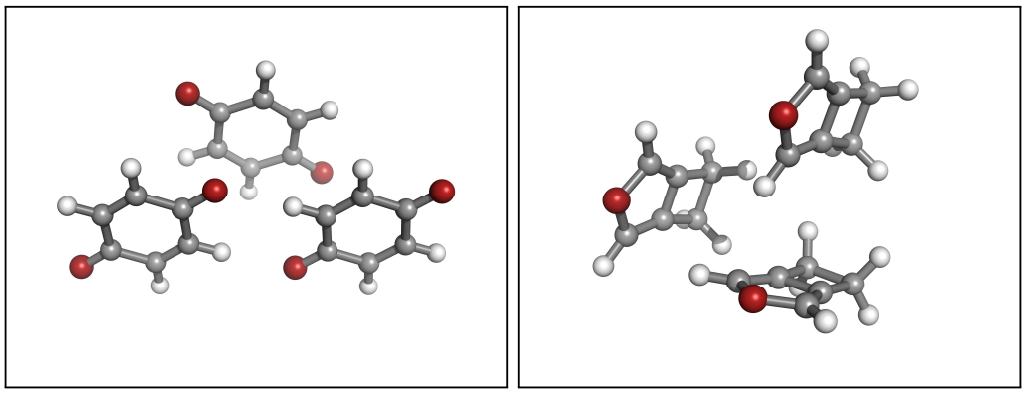

Figure 4.3: Left: Structure of the *p*-benzoquinone trimer (3B-69 ID: 21a). **Right:** Structure of the cyclobutylfuran trimer (3B-69 ID: 23a). .

As a first test of the impact of self-consistency on MBD, we have selected a *p*-benzoquinone trimer (ID: 21a) and the cyclobutylfuran trimer (ID: 23a) from the 3B-69 set since Řezáč *et al.* indicate that these are the trimers with the two largest contributions of three-body dispersion, while differing significantly in their share of three-body polarization.[104] We computed the two and three-body interaction energies for these trimers in PWSCF using the PBE functional and Hamann-Schlueter-Chiang-Vanderbilt (HSCV) norm-conserving pseudopotentials[263–265] in a simple-cubic unit cell of side length $a = 40$ a.u., with a kinetic energy wavefunction cutoff of $E_{cut} = 150$ Ry and a SCF convergence tolerance of $E_{scf} = 10^{-8}$ Ry. All calculations were run at the Γ point. Since PWSCF is a planewave code, these interaction energies do not need to be corrected for basis set superposition error. However, the planewave cutoff of 150 Ry may need to be increased to yield fully converged interaction energies. For comparison we have also computed the contributions of the two and three-body versions of the D3 dispersion correction with 'zero' damping,[66] using the standalone DFTD3 v3.1r0 program.[469]

The results of the interaction energy calculations on *p*-benzoquinone are presented in Table 4.2, while for cyclobutylfuran the results are presented in Table 4.3. We find that self-consistency has no impact on the MBD dispersion energy, both for two- and

Table 4.2: Interaction energies of *p*-benzoquinone (3B-69 ID: 21a) computed with the PBE functional employing several dispersion corrections: self-consistent MBD (scMBD), non-self-consistent MBD (MBD), self-consistent TS (scTS), non-self-consistent TS (TS), and D3 with zero damping without the three-body term (D3$(0)^{(2)}$) and with the three-body term (D3$(0)^{(3)}$). Reference CCSD(T)/CBS values are taken from Ref. 104. All energies are listed in kcal/mol. The percentage contribution due to vdW is listed in parentheses.

Method	$\Delta E^2(AB)$	$\Delta E^2(AC)$	$\Delta E^2(BC)$	$\Delta E^3(ABC)$
PBE	-0.551	-0.550	-3.997	0.428
PBE+D3$(0)^{(2)}$	-3.723 (85%)	-3.722 (85%)	-5.531 (28%)	0.429 (0.0%)
PBE+D3$(0)^{(3)}$	-3.634 (85%)	-3.633 (85%)	-5.585 (28%)	0.511 (16%)
PBE+TS	-4.123 (87%)	-4.123 (87%)	-5.418 (26%)	0.338 (-27%)
PBE+scTS	-4.127 (87%)	-4.126 (87%)	-5.419 (26%)	0.336 (-28%)
PBE+MBD	-3.847 (86%)	-3.847 (86%)	-5.833 (31%)	1.076 (60%)
PBE+scMBD	-3.847 (86%)	-3.847 (86%)	-5.833 (31%)	1.076 (60%)
CCSD(T)/CBS	-3.580	-3.580	-5.125	0.332

Table 4.3: Interaction energies of cyclobutylfuran (3B-69 ID: 23a) computed with the PBE functional employing several dispersion corrections: self-consistent MBD (scMBD), non-self-consistent MBD (MBD), self-consistent TS (scTS), non-self-consistent TS (TS), and D3 with zero damping without the three-body term (D3$(0)^{(2)}$) and with the three-body term (D3$(0)^{(3)}$). Reference CCSD(T)/CBS values are taken from Ref. 104. All energies are listed in kcal/mol. The percentage contribution due to vdW is listed in parentheses.

Method	$\Delta E^2(AB)$	$\Delta E^2(AC)$	$\Delta E^2(BC)$	$\Delta E^3(ABC)$
PBE	-0.565	-0.393	-0.393	0.219
PBE+D3$(0)^{(2)}$	-2.469 (77%)	-3.264 (88%)	-3.264 (88%)	0.221 (1.1%)
PBE+D3$(0)^{(3)}$	-2.426 (77%)	-3.196 (88%)	-3.196 (88%)	0.308 (29%)
PBE+TS	-2.880 (80%)	-4.014 (90%)	-4.014 (90%)	0.089 (-144%)
PBE+scTS	-2.883 (80%)	-4.017 (90%)	-4.017 (90%)	0.088 (-151%)
PBE+MBD	-2.889 (80%)	-3.882 (90%)	-3.883 (90%)	0.780 (72%)
PBE+scMBD	-2.889 (80%)	-3.882 (90%)	-3.883 (90%)	0.780 (72%)
CCSD(T)/CBS	-2.220	-3.093	-3.093	0.081

three-body interaction energies. Self-consistent application of the TS method (denoted scTS), yields negligible impact on the interaction energies. Consistent with the behavior observed by Řezáč *et al.* for the PBE functional, bare PBE already over estimates the three-body interaction energy due an overly repulsive description of exchange,[104] so the beyond-pairwise dispersion corrections, which are additionally repulsive, worsen the disagreement with the CCSD(T)/CBS reference. Surprisingly, TS yields a significant negative contribution to the three-body interaction energies, which corrects for PBE's the over estimation of $\Delta E^3(ABC)$. While TS is an effectively pairwise method, it does incorporate some many-body effects through its dependence on the Kohn-Sham density, which is why this method does not yield vanishing contribution to $\Delta E^3(ABC)$.

The large difference between TS and MBD arises due to both self-consistent screening and beyond-pairwise interactions. The three-body contribution to dispersion interactions is typically repulsive, as can be seen by the positive contribution to the three-body interaction energy being made by the three-body term in D3. In contrast, the TS correction is always attractive, which causes the negative contribution to the three-body interaction energies. The fact that non-self-consistent TS predicts such a large negative contribution to the three-body interaction energy suggests that the interactions between the molecules are strong enough to yield significant polarization of the dimer densities in the presence of the third molecule. To exclude the possibility of periodic interactions impacting these results we analyzed the dipole moments for *p*-benzoquinone and applied a Makov-Payne correction[470] (which corrects the electrostatics of a periodic simulation cell to reproduce an isolated system). These tests confirmed that the 40 a.u. simulation cell is large enough to isolate the system. As expected, self-consistency does not disturb the dipole moment of the *p*-benzoquinone monomer, with both scMBD and MBD predicting a negligible dipole moment to four decimal places.

Having only considered two trimers (for a total of 6 two-body interaction energies and 2 three-body interaction energies), we cannot make any general claims about the performance of any of these methods. Given the small size of these structures, it is

somewhat surprising that MBD accounts for 60-70% of the three-body interaction energy. Clearly the 3B-69 benchmark set offers a stringent test of multiple aspects of a DFT+vdW correction scheme, and the performance of MBD should be examined more carefully across the entire dataset. We are very eager to explore self-consistent MBD on a wider variety of systems, and also with functionals that have a superior description of exchange relative to PBE. It would be particularly interesting to see how MBD performs with hybrid or range-separated exchange hybrid functionals since the addition of a large portion of exact exchange can significantly improve the description of three-body interaction energies.[104] The development of scMBD also paves the way for future studies to assess the impact of dispersion corrections on linear response properties such as absorption spectra through the use of real-time TDDFT propagation techniques. Self-consistent application of MBD may yield larger changes for extended systems, such as vdW heteromaterials. These materials will be particularly interesting to study with real-time TDDFT coupled with scMBD since their optical and electronic properties are influenced strongly by their vdW coupling. The strong impact of vdW interactions on the properties of these materials, such as twist-induced van Hove singularities and second harmonic generation,[471–477] has recently gained significant attention and will be an exciting avenue for future research into the many-body nature of dispersion interactions.

Conclusion

The principle contributions of this dissertation were to extend the applicability of the MBD model by developing analytical forces, unit-cell stresses, phonon corrections, and self-consistent updates to the Kohn-Sham potential. We additionally re-parameterized MBD for use with a wide variety of GGA functionals. In Chapter 1 we motivated this method development effort by highlighting examples where gradient based information, in the form of unit-cell optimizations and self-consistent application of a non-local correlation functional, might be used in applying dispersion corrected DFT to study advanced functional organic materials. In Chapter 2, we derived and implemented MBD forces for nuclear coordinate relaxations and showed that proper accounting for the implicit coordinate dependencies that arise from the Hirshfeld volume gradients resulted in significant changes to the MBD forces. Consistent with previous findings on binding energetics, we find that MBD forces significantly improve the predicted structures of isolated dispersively bound molecular systems and consistently outperforms popular pairwise-additive DFT-D based methods with regard to agreement with high-level wavefunction-based reference geometries. By treating all gradients analytically, rather than numerically through finite difference methods, we have enabled the DFT+MBD optimizations of much larger systems.

In Chapter 3, we presented a new implementation of analytical MBD forces for large-scale condensed phase simulations, including the corrections to unit-cell forces and stresses. We eliminated the use of heuristic cutoffs for convergence of the dipole-dipole interaction tensors and improved the numerical stability of the MBD algorithm. We have made preliminary studies of the physisorption of nucleobases on graphene, the interlayer binding distance of graphite, and the structure of ice Ic; in all three cases we find the performance of MBD forces to be encouraging for use in condensed phase optimizations. In Chapter 4, we described three areas of ongoing development work for MBD, the

re-parameterization of MBD's range-separation parameter to enable application of MBD with other GGA functionals, the development of analytical second derivatives of the MBD energy for use in correcting DFPT phonon simulations, and the development of self-consistent MBD (scMBD). In agreement with the findings of Lee *et al.*, our preliminary investigation of different GGA functionals with MBD indicated that the PW86 and rPW86 exchange functionals may offer slight improvements over PBE exchange.[72] The development of self-consistent MBD is too recent to have thoroughly analyzed which properties and systems are impacted by self-consistent application of MBD. However, we are excited about the possibility of employing this methodology with real-time TDDFT propagation techniques to examine the impact of dispersion corrections on the linear response properties of systems such as twisted vdW heteromaterials. Since MBD forces are very efficient to evaluate for non-periodic systems, we are also eager to explore the application of MBD in *ab initio* molecular dynamics simulations since many-body effects often have a significant impact on aggregation in solution[30] and hydrophobic association.[328]

Although the DFT+MBD method in its present form has been remarkably successful in describing many systems where pairwise-additive models of dispersion fail, there are at least four areas that should be investigated for future improvements.

- **Improving the computational efficiency for periodic systems.** The real-space supercell procedure described in Chapter 3 represents a significant computational overhead for converging the MBD energy in condensed phase systems. Converging this energy in reciprocal space by the use of a Bloch wave expansion would significantly reduce the computational cost of MBD for periodic systems.

- **Improving the use of anisotropic response information.** The MBD interaction Hamiltonian is constructed by first computing a fully non-local screened anisotropic dipolar response matrix $\overline{\mathbf{A}}$, and then contracting down to isotropic atomic polarizabilities. This isotropization represents a significant loss of

information about the local bonding environment. In principle, it is possible to evaluate the MBD correlation energy from an integral expression for the ACFD-RPA correlation energy, which could enable use of the fully anisotropic $\overline{\mathbf{A}}$ rather than the isotropized $\overline{\alpha}$.[84,87,88] However, the range-separated Coulomb interaction must then be evaluated for anisotropic QHOs rather than the isotropic Gaussian charge densities that are currently used. This could prove computationally prohibitive and is closely related to the next challenge.

- **Incorporating higher-order multipoles.** Presently, the MBD algorithm restricts the response of the system to the dipole interaction between QHOs. Several approaches to incorporate higher-order multipoles (quadrupoles, octupoles, *etc.*), should be examined. By assigning more than one QHO to every atom it should be possible to capture higher-order multipoles, but this approach will present challenges for avoiding the unphysical behavior that occurs when trying to apply the self-consistent screening procedure to QHOs that are spaced too closely (negative response frequencies arise). Alternatively, the integral ACFD-RPA variant of evaluating the MBD correlation energy can be employed with a multipolar response function, but this is likely to encounter many of the difficulties presently associated with direct RPA correlation energy calculations. Many of the nice properties of the MBD model rely on the fact that the dipole coupling is analytically tractable. Reexamining the multipole expansion of the screened interaction tensor used by Langbein in his original oscillator model of dispersion could prove fruitful.[134] Future extensions of the MBD model to incorporate finite temperature effects may also benefit from considering Langbein's expressions for the density of states and free energies of coupled QHOs.

- **Improved coupling to the DFT correlation functional.** To reduce the empiricism present in the range-separated MBD model, the coupling between the long-range MBD correlation energy should be amended by re-deriving the DFT

correlation functional in the presence of the long-range dispersion component, as is done in the "dispersionless density functional" of Pernal and coworkers.[478] Alternatively, the correlation component of the functional could be range-separated in an analogous fashion to functionals that employ range-separated exchange.[479–482] Given that range-separated exchange functionals have been quite successful in describing charge-transfer excited states,[483] our development of self-consistent MBD in the Octopus code opens the interesting possibility of studying whether long-range corrected correlation (*i.e.* scMBD) is compatible with long-range corrected exchange (*i.e.* range-separated hybrids) and how these treatments work together to influence non-local excited states.

- **Description of metallic states.** One of the primary advantages of non-local correlation functionals over the MBD model is that they correctly reduce to the local density approximation as the electron density converges to the homogeneous electron gas. Properly treating metallic states therefore requires letting the polarizability vanish in regions of slowly-varying electron density. It may be possible to use the framework of non-local correlation functional methods to derive the parameters of the localized oscillators directly from the electron density and its gradient. This would have the advantage of eliminating the reliance on the free-atom reference data and could improve the model's ability to be extended to model screening at metallic surfaces. Recently, Silvestrelli and Ambrosetti have successfully employed a QHO based model for adsorption on metal surfaces by assigning the oscillator parameters with maximally-localized Wannier functions.[86,484] Given the importance of self-consistently accounting for dielectric screening in such systems,[114] it would be interesting to see how an extended scMBD model compares to existing approaches such as the vdWsurf model.[67,83]

Although the methodological developments for the MBD model presented herein need additional careful benchmarking, we are optimistic that these new tools will enable many

exciting discoveries of beyond-pairwise dispersive effects in future studies of organic materials.

A

Glossaries

A.1 Energy Unit Conversions

Table A.1: Conversions for units of energy commonly used in quantum chemistry (NIST CODATA 2014 recommended values rounded to 7 significant figures).

	E_h	Ry	eV	kcal/mol
E_h	1	2	27.21137	627.5095
Ry	1/2	1	13.60569	313.7547
eV	3.674932×10^{-2}	7.349864×10^{-2}	1	23.060548
kcal/mol	1.593601×10^{-3}	3.187203×10^{-3}	4.336410×10^{-2}	1

A.2 Exchange-Correlation Functional Glossary

Table A.2: Glossary of exchange-correlation functional abbreviations appearing in this work.

Abbreviation	Exchange	Correlation	References
SPW	Slater	Perdew & Wang	Refs. 444, 445, 485
SPZ	Slater	Perdew & Zugner	Refs. 181, 444, 445
$SVWN_{RPA}$	Slater	Vosko, Wilk, & Nusair (RPA variant)	Refs. 444–446
PBE	Perdew, Burke, & Ernzerhof ($\kappa = 0.804$)		Refs. 182, 183
PBEsol	Perdew, Burke, & Ernzerhof for solids		Refs. 486
optPBE	optPBE *	–	Refs. 182, 183, 487
optB88	optB88 †	–	Refs. 182, 183, 487

continued on next page

*optPBE is a combination of PBE and RPBE with enhancement factor parameters μ & κ optimized for the S22 dataset: $\mu = 0.175519$ and $\kappa = 1.04804$.

†optB88 was reparameterized against the S22 dataset, giving $\mu/\beta = 1.2$ and $\mu = 0.22$ in its enhancement factor.

Table A.2: Glossary of exchange-correlation functional abbreviations (continued).

Abbreviation	Exchange	Correlation	References
PBE$\kappa = 1$	PBE$\kappa = 1$ [‡]	–	Refs. 182, 183, 487
RPBE	revised PBE of Hammer, Hansen, & Norskov	–	Refs. 488
revPBE	revised PBE of Zhang & Yang [§]	–	Refs. 234, 235
PW86	Perdew-Wang '86	–	Refs. 433
rPW86	refitted Perdew-Wang '86	–	Refs. 433, 72
PBE0	PBE +25%exact exchange	PBE	Refs. 182,183, 236–238
revPBE0	revPBE +25% exact exchange	PBE	Refs. 234–238
BOP	Becke '88	One-Parameter Tsuneda *et al.*	Refs. 429, 489
BP86	Becke '88	Perdew '86	Refs. 429, 126
BPW	Becke '88	Perdew-Wang '91	Refs. 429–432
PW91	Perdew-Wang '91	Perdew-Wang '91	Refs. 430–432
mPW91	modified PW91	Perdew-Wang '91	Refs. 430–432, 490
B97	Becke '97	Becke '97	Refs. 491
B97-3	Becke '97	Becke '97	Refs. 492
XLYP	Xu & Goddard extended exchange	Lee, Yang & Parr	Refs. 493–495
BLYP	Becke '88	Lee, Yang & Parr	Refs. 429, 494, 495
OLYP	optX	Lee, Yang & Parr	Refs. 494–496
MOHLYP	metal-optimized OptX	50% Lee, Yang & Parr	Ref. 450
HCTH/407	Hamprecht, Cohen, Tozer, & Handy		Ref. 497
TPSS	Tao, Perdew, Staroverov, & Scuseria		Refs. 498, 499
B3LYP	Becke, three-parameter, Lee, Yang & Parr		Ref. 231, 232
AM05	Adamo & Mattsson		Refs. 500, 501

[‡]PBE exchange with the κ parameter in the enhancement factor set to 1.
[§]revPBE has $\kappa = 1.245$ in the enhancement factor.

A.3 Abbreviation Glossary

Table A.3: Glossary of frequently used abbreviations appearing in this work.

Abbreviation	Definition
vdW	van der Waals
DPP	diketopyrrolopyrrole
MOF	metal-organic framework
FDP	frequency-dependent polarizability
ACFD	adiabatic-connection fluctuation-dissipation
RPA	random phase approximation
DFT	density functinonal theory
DFT+vdW	dispersion corrected DFT
vdW-DF	van der Waals density functional (non-local correlation method)
DFT-D	pairwise-additive semiempirical dispersion correction
D3(BJ)	Grimme's third generation semiempirical pairwise dispersion correction with Becke-Johnson damping
TS	Tkatchenko-Scheffler pairwise dispersion correction
SCS	self-consistent screening
rsSCS	range-separated self-consistent screening
CFDM	coupled fluctuating dipole model
MBD	many-body dispersion, in this work we use the rsSCS variant
scMBD	self-consistent many-body dispersion
QHO	quantum harmonic oscillator
QDO	quantum Drude oscillator
QE	Quantum ESPRESSO
GGA	generalized gradient approximation
LDA	local density approximation
MARE	mean absolute relative error
MAE	mean absolute error
MAD	mean absolute deviation
TDDFT	time-dependent density functional theory
RT-TDDFT	real-time TDDFT
SAPT	symmetry adapted perturbation theory
CCSD(T)	coupled-cluster with single and double with perturbative triple excitations
MP2	second order Møller-Plesset perturbation theory

Table A.4: Glossary of symbols appearing in this work.

Symbol	Description
$E_{xc}[\rho]$	exchange-correlation energy functional
$E_x[\rho]$	exchange component of exchange-correlation energy functional
$E_c[\rho]$	correlation component of exchange-correlation energy functional
v_{xc}	exchange-correlation potential, computed from the functional derivative $\frac{\delta E_{xc}}{\delta \rho(\mathbf{r})}$
$\boldsymbol{\alpha}_a^{\text{free}}(0)$	static free-atom polarizability formed with $\alpha_a^{\text{free}}(0)$ scalars on the diagonal
$\boldsymbol{\alpha}_a(0)$	Eq. (2.5): static bare polarizability, related to $\boldsymbol{\alpha}_a^{\text{free}}(0)$ by the ratio V_a/V_a^{free}
$\boldsymbol{\alpha}_a(\mathbb{i}\omega)$	Eq. (2.7): frequency-dependent bare polarizability tensor, calculated by Padé approximant Eq. (2.4)
$\alpha_a(\mathbb{i}\omega)$	'isotropized' bare dipole polarizability scalar, calculated as $\alpha_a = \frac{1}{3}\text{Tr}[\boldsymbol{\alpha}_a]$
$\mathbf{A}(\mathbb{i}\omega)$	Eq. (2.9): bare system polarizability tensor, $3N \times 3N$ block diagonal matrix of $\boldsymbol{\alpha}_a(\mathbb{i}\omega)$
$\overline{\mathbf{A}}(\mathbb{i}\omega)$	Eq. (2.11): screened system polarizability tensor, solved at complex frequency $\mathbb{i}\omega$ using $\left[\mathbf{A}^{-1} + \mathbf{T}_{SR}\right]^{-1}$
$\overline{\boldsymbol{\alpha}}_a(0)$	Eq. (2.13): screened static polarizability, calculated by partial contraction of $\overline{\mathbf{A}}(0)$
$\overline{\boldsymbol{\alpha}}_a(\mathbb{i}\omega)$	Eq. (2.12): screened frequency-dependent polarizability, calculated by partial contraction of $\overline{\mathbf{A}}(\mathbb{i}\omega)$
ω_a^{free}	free-atom QHO excitation frequency, computed as: $\omega_a^{\text{free}} = 4/3\left(C_{6,aa}^{\text{free}}/\left[\alpha_a^{\text{free}}(0)\right]^2\right)$
$C_{6,aa}^{\text{free}}$	free-atom C_6 coefficient (also called a Hamaker constant)
$C_{6,aa}$	bare effective atomic C_6 coefficient, computed by weighting $C_{6,aa}^{\text{free}}$ with $\left(V_a/V_a^{\text{free}}\right)^2$
$\overline{C}_{6,aa}$	Eq. (2.14): screened effective atomic C_6 coefficient
ω_a	bare QHO excitation frequency, equals ω^{free} due to cancellation of V_a/V_a^{free} factors
$\overline{\omega}_a$	Eq. (2.15): screened QHO excitation frequency
y_p	frequency grid for numerical integration
g_p	weights for numerical integration
$\sigma_a(\mathbb{i}\omega)$	Eq. (2.23): QHO width, calculated from the bare polarizability scalar

continued on next page

Table A.4: Glossary of symbols (continued).

Symbol	Description
$\Upsilon_a(\mathbb{i}\omega)$	Eq. (2.24): multiplicative prefactor to V_a in defining α_a
V_a^{free}	free-atom effective volume
V_a	Eq. (C.2): Hirshfeld effective atomic volume
$\Sigma_{ab}(\mathbb{i}\omega)$	Eq. (2.22): effective correlation length of the interaction potential, defined from QHO widths of atoms a and b
$\boldsymbol{\mathfrak{R}}_a$	nuclear position of atom a
R_{ab}	internuclear distance between atoms a and b
$\mathbf{R}_{ab}$	internuclear vector $(\boldsymbol{\mathfrak{R}}_a - \boldsymbol{\mathfrak{R}}_b)$ between atoms a and b
R_{ab}^i	i^{th} Cartesian component of the internuclear vector
$\mathbf{r}$	spatial position such as the argument of the electron density
ζ	ratio between interatomic separation R and correlation length Σ
$h(\zeta)$	Eq. (2.57): function of ζ appearing in $\mathbf{T}$
$v(R, \mathbb{i}\omega)$	Eq. (2.21): Coulomb interaction between two QHO Gaussian charge densities separated by R with frequency-dependent widths
$\mathbf{T}$	Eq. (2.56): dipole interaction tensor between QHO Gaussian charge densities
$\mathbf{T}_{\text{dip}}$	Eq. (2.26): dipole interaction tensor between point dipoles
$\mathbf{T}_{SR}$	Eq. (2.34): short-range component of $\mathbf{T}$, evaluated using $f(Z^{\text{TS}})$
$\overline{\mathbf{T}}_{LR}$	Eq. (2.36): long-range component of $\mathbf{T}$, evaluated using $f(\overline{Z}_{\text{vdW}})$
$f(Z)$	Eq. (2.27): damping function for range-separation of the dipole interaction tensor
S_{ab}	sum of effective vdW radii scaled by β
Z_{ab}	ratio of interatomic separation R_{ab} and S_{ab}
$\mathcal{R}_a^{\text{vdW, TS}}$	Eq. (2.33): effective vdW radii at the TS level
$\overline{\mathcal{R}}_a^{\text{vdW}}$	Eq. (2.35): screened effective vdW radii
ρ	total electronic charge density
ρ_a^{eff}	Eq. (C.1): Hirshfeld effective electron density asigned to atom a
ρ_{sad}	sum of spherical free-atom densities $\sum_b \rho_b^{\text{free}}$
$\boldsymbol{\mathcal{H}}^{\text{MBD}}$	Eq. (2.17): MBD model Hamiltonian
$\mathbf{C}^{\text{MBD}}$	Eq. (2.18): MBD interaction Hamiltonian matrix
$\boldsymbol{\mathcal{X}}$	matrix of eigenvectors of $\mathbf{C}^{\text{MBD}}$
$\boldsymbol{\lambda}$	vector of eigenvalues of $\boldsymbol{C}^{\text{MBD}}$
$\boldsymbol{\Lambda}$	diagonal matrix of eigenvalues of $\boldsymbol{C}^{\text{MBD}}$

continued on next page

Table A.4: Glossary of symbols (continued).

Symbol	Description
L	scale factor used in algebraic scaling of Gauss-Legendre points
δ	max-norm convergence threshold used in periodic summation of $\mathbf{T}$
r_s	supercell cutoff radius
n_a	number of unit-cell tilings in the $\mathbf{a}$ lattice vector direction
n_b	number of unit-cell tilings in the $\mathbf{b}$ lattice vector direction
n_c	number of unit-cell tilings in the $\mathbf{c}$ lattice vector direction
N_{sc}	number of atoms in the supercell
$\mathbf{h}$	matrix of unit-cell vectors
Ω	unit-cell volume
σ_{MBD}	MBD contribution to the unit-cell stress tensor
$\boldsymbol{\partial}_c$	gradient with respect to nuclear position of atom c, equivalent to $\boldsymbol{\nabla}_{\boldsymbol{\mathcal{R}}_c}$
E_{MBD}	MBD correlation energy
$E_{\text{int.}}$	"interacting mode" contribution to the MBD energy
$E_{\text{non-int.}}$	"non-interacting mode" contribution to the MBD energy
$\mathbf{F}^{\text{MBD}}$	MBD ionic forces: $-\boldsymbol{\nabla}_{\boldsymbol{\mathcal{R}}} E_{\text{MBD}}$
$\mathbf{H}^{\text{MBD}}$	MBD unit-cell forces: $-\boldsymbol{\nabla}_{\boldsymbol{h}} E_{\text{MBD}}$
$\mathbf{U}^{\text{MBD}}$	MBD wavefunction forces: $-\boldsymbol{\nabla}_{\rho} E_{\text{MBD}}$
$\boldsymbol{\partial}^2 E^{\text{MBD}}$	MBD Hessian: $\boldsymbol{\nabla}_{\boldsymbol{\mathcal{R}}} \otimes \boldsymbol{\nabla}_{\boldsymbol{\mathcal{R}}} E_{\text{MBD}}$
E_{scf}	SCF energy convergence cutoff
E_{cut}	planewave basis set expansion energy cutoff
β	MBD range-separation parameter
$\mathbf{B}$	convenience function used in Eqs. 4.26 and 4.27
U	Eq. 4.30: convenience function used in computing the derivatives of $\mathbf{T}$
$\mathbf{W}$	Eq. 4.31: convenience function used in computing the derivatives of $\mathbf{T}$
$\boldsymbol{\Psi}$	Eq. 4.32: convenience function used in computing the derivatives of $\mathbf{T}$
$g(\zeta)$	function of ζ defined in Eq. 4.47 for computing the derivatives of $\mathbf{W}$
K_{ab}	convenience function first used in Eq. 4.83
$\mathbf{D}_p$	Eq. 4.75: convenience function used in computing eigenvector derivatives in Section 4.2.7
ΔE^2	Eq. 4.103: two-body interaction energy
ΔE^3	Eq. 4.104: three-body interaction energy

B

DPP Transport Properties with More Functionals

Table B.1: Transport properties (calculated at the revPBE/def2-TZVP level) for diketopyrrolopyrrole pigments broken down into the dominant hopping pathways. d is the length of the pathway. $\mathcal{P}$ is the relative probability of hopping along the i^{th} pathway and m_i is its multiplicity, *i.e.* the number of symmetry related pathways. $|t|$ is the absolute value of the transfer integral. Values in parentheses have been calculated with VV10 applied self-consistently.

Pathway	d (Å)	m	$\lvert t_e \rvert$ (meV)	$\mathcal{P}_e$ (%)	$\lvert t_h \rvert$ (meV)	$\mathcal{P}_h$ (%)
			DPP			
p_1	3.8	2	0.8 (2.2)	0.1 (0.4)	81.2 (84.2)	41.2 (41.2)
p_2	6.5	2	13.2 (13.3)	15.4 (14.8)	20.4 (21.3)	2.6 (2.6)
p_3	7.3	2	19.8 (20.3)	34.3 (34.5)	31.5 (32.5)	6.2 (6.2)
			p-Cl DPP			
p_1	5.6	2	12.4 (12.5)	6.4 (5.8)	9.9 (10.2)	0.6 (0.6)
p_2	5.7	2	18.2 (18.9)	13.8 (13.4)	82.2 (85.8)	41.5 (41.5)
p_3	7.3	2	18.6 (19.0)	14.3 (13.5)	32.2 (33.2)	6.4 (6.2)
			p-Br DPP			
p_1	5.6	4	24.7 (25.4)	17.9 (17.9)	13.9 (14.3)	5.1 (5.1)
p_3	7.3	2	20.5 (20.9)	12.3 (12.2)	38.6 (39.7)	39.0 (38.9)

Table B.2: Transport properties (calculated at the revPBE0/def2-TZVP level) for diketopyrrolopyrrole pigments broken down into the dominant hopping pathways. d is the length of the pathway. $\mathcal{P}$ is the relative probability of hopping along the i^{th} pathway and m_i is its multiplicity, *i.e.* the number of symmetry related pathways. $|t|$ is the absolute value of the transfer integral. Values in parentheses have been calculated with VV10 applied self-consistently.

Pathway	d (Å)	m	$\lvert t_e \rvert$ (meV)	$\mathcal{P}_e$ (%)	$\lvert t_h \rvert$ (meV)	$\mathcal{P}_h$ (%)
			DPP			
p_1	3.8	2	7.1 (8.6)	3.5 (4.8)	83.6 (86.0)	40.8 (40.8)
p_2	6.5	2	13.5 (13.5)	12.6 (11.9)	23.0 (23.7)	3.1 (3.1)
p_3	7.3	2	21.9 (22.4)	33.5 (33.0)	32.4 (33.3)	6.1 (6.1)
			p-Cl DPP			
p_1	5.6	2	17.4 (17.5)	8.9 (8.4)	16.7 (17.1)	1.5 (1.4)
p_2	5.7	2	22.8 (23.6)	15.2 (15.1)	88.2 (91.3)	41.1 (41.1)
p_3	7.3	2	20.5 (20.9)	12.3 (11.8)	32.5 (33.2)	5.6 (5.4)
			p-Br DPP			
p_1	5.6	4	27.5 (32.6)	17.7 (19.2)	24.4 (22.6)	10.6 (9.4)
p_3	7.3	2	22.9(23.1)	12.2 (9.7)	39.7(40.4)	27.8 (30.1)

Table B.3: Reorganization energies of diketopyrrolopyrrole pigments calculated at the DFT/def2-TZVP level of theory for the B3LYP functional. Results computed with the PW6B95 functional are given in parentheses. The value marked with a star was computed in a smaller def2-SVPD basis set.

Pigment	λ_e (meV)	λ_h (meV)
DPP	192 (210)	331 (365)
p-Cl DPP	203 (192*)	348 (376)
p-Br DPP	181 (192)	330 (360)

C

Additional Mathematical Details

C.1 Repeated Eigenvalues of $\mathbf{C}^{\mathrm{MBD}}$

In considering the derivative of λ_k, in Eq. (2.40) in Chapter 2, we assumed that $\boldsymbol{C}^{\mathrm{MBD}}$ had $3N$ distinct eigenvalues. Due to numerical perturbations it is somewhat unlikely for $\boldsymbol{C}^{\mathrm{MBD}}$ to have repeated eigenvalues, but we cannot assume this *a priori*. The procedure for taking derivatives of repeated eigenvalues of a real, symmetric matrix, like $\boldsymbol{C}^{\mathrm{MBD}}$, is essentially first order perturbation theory where the perturbation is the action of the derivative operator $\boldsymbol{\partial}_c$. Eigenvalue degeneracies are lifted by diagonalizing the perturbation in the degenerate subspace. For a more algorithmic discussion of repeated eigenvalue derivatives, see Andrew et al.[463] or Friswell.[462] Since C^{MBD} is real and symmetric, it is guaranteed to be diagonalizeable with orthogonal eigenvectors.

C.2 Computation of ∂V

Nuclear coordinate forces within a fully self-consistent $\mathcal{O}(N)$ implementation of the Tkatchenko-Scheffler scheme were previously developed in QuantumESEPRESSO by R. A. DiStasio Jr.[502] A subroutine of the tsvdw module computes the Hirshfeld partitioning into effective atomic volumes, V_a, and the derivatives of that volume, ∂V_a. The Hirshfeld effective charge density of atom a is:

$$\rho_a^{\mathrm{eff}}(\mathbf{r}) = w_a(\mathbf{r})\,\rho(\mathbf{r}) = \frac{\rho_a^{\mathrm{free}}(\|\mathbf{r}-\boldsymbol{\mathcal{R}}_a\|)}{\rho_{\mathrm{sad}}(\mathbf{r})}\,\rho(\mathbf{r}), \tag{C.1}$$

where ρ is the total molecular charge density and $\rho_{\text{sad}} = \sum_b \rho_b^{\text{free}}$ is the sum of free-atom densities. The effective volume is then:

$$V_a = \int \mathrm{d}\mathbf{r}\, \|\mathbf{r} - \mathcal{R}_a\|^3 \rho_a^{\text{eff}}(\mathbf{r}). \tag{C.2}$$

Integrations on spherical atomic domains, such as in Eq. C.2, are computed on subsets of the real-space mesh. Using reference data for the free atom volumes, a radial grid cutoff value is determined for each species such that the free atom volume obtained by numerical integration up to this cutoff does not deviate from the reference value by more than 1.0%. The effective volume derivative is evaluated as

$$\boldsymbol{\partial}_c V_a = \int \mathrm{d}\mathbf{r}\, \|\mathbf{r} - \mathcal{R}_a\|^3 \boldsymbol{\partial}_c \rho_a^{\text{eff}}(\mathbf{r}) - 3\,\delta_{ca} \int \mathrm{d}\mathbf{r}\, (\mathbf{r} - \mathcal{R}_a)\|\mathbf{r} - \mathcal{R}_a\| \rho_a^{\text{eff}}(\mathbf{r}) \tag{C.3}$$

$$\boldsymbol{\partial}_c \rho_a^{\text{eff}}(\mathbf{r}) = \left[\frac{\rho_a^{\text{free}}\rho}{[\rho_{\text{sad}}]^2} - \frac{\rho}{\rho_{\text{sad}}}\delta_{ca}\right] \left[\frac{\mathbf{r} - \mathcal{R}_c}{\|\mathbf{r} - \mathcal{R}_c\|}\right] \frac{\partial \rho_c^{\text{free}}(r)}{\partial r}. \tag{C.4}$$

Note that the free-atom density is spherically symmetric, which is why we reduce $\boldsymbol{\partial}_c \rho_c^{\text{free}}(\|\mathbf{r} - \mathcal{R}_c\|)$ to a spherical coordinate derivative $\partial \rho_c^{\text{free}}/\partial r$. Likewise, Eq. (C.2) is evaluated by mapping the radial form of ρ_a^{eff} to an linear/equispaced grid, which is then interpolated using cubic splines. After interpolation, the derivative $\boldsymbol{\partial}_c \rho_a^{\text{eff}}$ at each grid point is evaluated by numerical differentiation using Bickley's 7-point formula.[503]

C.3 Derivation of $\partial \mathbf{T}^{ij}$

To break the derivative of $\mathbf{T}^{ij}$ into smaller pieces, we define some convenience functions:

$$U \equiv \operatorname{erf}[\zeta] - \frac{2}{\sqrt{\pi}}\zeta \exp\left[-\zeta^2\right] \tag{C.5}$$

$$\mathbf{W}^{ij} \equiv \left(\frac{R^i R^j}{R^5}\right) \frac{4}{\sqrt{\pi}}\zeta^3 \exp\left[-\zeta^2\right] \tag{C.6}$$

$$\mathbf{T}^{ij}_{\text{dip}} \equiv -3\left(\frac{R^i R^j}{R^5}\right) + \frac{\delta_{ij}}{R^3} \tag{C.7}$$

So in terms of these functions, $\mathbf{T}^{ij}$ is:

$$\begin{aligned} \mathbf{T}^{ij} &= U\mathbf{T}^{ij}_{\rm dip} + \mathbf{W}^{ij} && \text{(C.8)} \\ \Rightarrow \boldsymbol{\partial}\mathbf{T}^{ij} &= U\boldsymbol{\partial}\mathbf{T}^{ij}_{\rm dip} + \mathbf{T}_{\rm dip}\boldsymbol{\partial}U + \boldsymbol{\partial}\mathbf{W}^{ij} && \text{(C.9)} \end{aligned}$$

The derivative of $\mathbf{T}^{ij}_{\rm dip}$ is given in Eq. (2.52). Note that we can write $\boldsymbol{\partial}\left(R^iR^j/R^5\right)$ in terms of $\boldsymbol{\partial}\mathbf{T}^{ij}_{\rm dip}$ as:

$$\boldsymbol{\partial}\left(\frac{R^iR^j}{R^5}\right) = -\frac{1}{3}\boldsymbol{\partial}\mathbf{T}^{ij}_{\rm dip} - \frac{\delta_{ij}}{R^4}\boldsymbol{\partial}R \qquad \text{(C.10)}$$

So the derivatives of U and $\mathbf{W}^{ij}$ are:

$$\boldsymbol{\partial}U = \frac{4}{\sqrt{\pi}}\zeta^2\exp\left[-\zeta^2\right]\boldsymbol{\partial}\zeta \qquad \text{(C.11)}$$

$$\boldsymbol{\partial}\mathbf{W}^{ij} = \left(\frac{R^iR^j}{R^5}\right)\left[3-2\zeta^2\right]\frac{4}{\sqrt{\pi}}\zeta^2\exp\left[-\zeta^2\right]\boldsymbol{\partial}\zeta - \frac{4}{\sqrt{\pi}}\zeta^3\exp\left[-\zeta^2\right]\left(\frac{1}{3}\boldsymbol{\partial}\mathbf{T}^{ij}_{\rm dip} + \frac{\delta_{ij}}{R^4}\boldsymbol{\partial}R\right) \qquad \text{(C.12)}$$

Now define $h(\zeta) \equiv \frac{4}{\sqrt{\pi}}\zeta^2\exp\left[-\zeta^2\right]$.

$$\begin{aligned} \Rightarrow \boldsymbol{\partial}U &= h(\zeta)\boldsymbol{\partial}\zeta && \text{(C.13)} \\ \Rightarrow \boldsymbol{\partial}\mathbf{W}^{ij} &= \left(\frac{R^iR^j}{R^5}\right)\left[3-2\zeta^2\right]h(\zeta)\boldsymbol{\partial}\zeta + \zeta\,h(\zeta)\left(-\frac{1}{3}\boldsymbol{\partial}\mathbf{T}^{ij}_{\rm dip} - \frac{\delta_{ij}}{R^4}\boldsymbol{\partial}R\right) && \text{(C.14)} \end{aligned}$$

In terms of $h(\zeta)$ we can then write $\boldsymbol{\partial}\mathbf{T}^{ij}$ as:

$$\begin{aligned} \boldsymbol{\partial}\mathbf{T}^{ij} &= \left[\text{erf}\left[\zeta\right] - \frac{1}{2}\frac{h(\zeta)}{\zeta}\right]\boldsymbol{\partial}\mathbf{T}^{ij}_{\rm dip} + \zeta\,h(\zeta)\left(-\frac{1}{3}\boldsymbol{\partial}\mathbf{T}^{ij}_{\rm dip} - \frac{\delta_{ij}}{R^4}\boldsymbol{\partial}R\right) && \text{(C.15)} \\ &\quad + \left[\mathbf{T}_{\rm dip} + \left(\frac{R^iR^j}{R^5}\right)\left[3-2\zeta^2\right]\right]h(\zeta)\boldsymbol{\partial}\zeta \end{aligned}$$

Where the derivative of ζ_{ab} is given in Eq. (2.58) in Chapter 2.

C.4 Self-Consistent Screening: Deriving the Matrix Inversion Formulation

Self-consistent screening (SCS) is accomplished by solving the following non-homogeneous system of linear equations at a given complex frequency $\mathbb{i}\omega$ (Eq. (17) in DiStasio et al.[87]):

$$\overline{\alpha}_a(\mathbb{i}\omega) = \alpha_a(\mathbb{i}\omega) - \alpha_a(\mathbb{i}\omega) \sum_{b \neq a}^{N} \mathbf{T}_{ab}\, \overline{\alpha}_a(\mathbb{i}\omega). \tag{C.16}$$

To accomplish a range-separated self-consistent screening (rsSCS), we replace $\mathbf{T}$ with $\mathbf{T}_{\mathrm{SR}}$ (see Ref. 88). The coupled set of equations represented by Eq. (C.16) can then be written in matrix form as:

$$\overline{\mathbf{A}} = \mathbf{A} - \mathbf{A}\,\mathbf{T}_{\mathrm{SR}}\,\overline{\mathbf{A}} \tag{C.17}$$

Note that $\zeta_{aa} = 0$ so $\mathbf{T}_{aa}$ is naturally zero (cf. Eq. (2.25)). Thus, the sum $\sum_{b \neq a} \mathbf{T}_{ab}\,\overline{\alpha}_a$ is accomplished by the product $\mathbf{T}_{\mathrm{SR}}\,\overline{\mathbf{A}}$. Rearranging Eq. (C.17) and then left multiplying by $\mathbf{A}^{-1}$ gives:

$$\begin{aligned}
\overline{\mathbf{A}} + \mathbf{A}\,\mathbf{T}_{\mathrm{SR}}\,\overline{\mathbf{A}} &= \mathbf{A} && \text{(C.18)} \\
\mathbf{A}^{-1}\left[\mathbb{I} + \mathbf{A}\,\mathbf{T}_{\mathrm{SR}}\right]\overline{\mathbf{A}} &= \mathbf{A}^{-1}\mathbf{A} && \text{(C.19)} \\
\left[\mathbf{A}^{-1} + \mathbf{T}_{\mathrm{SR}}\right]\overline{\mathbf{A}} &= \mathbb{I} && \text{(C.20)}
\end{aligned}$$

Left multiplying by the inverse of the bracketed quantity yields:

$$\overline{\mathbf{A}} = \left[\mathbf{A}^{-1} + \mathbf{T}_{\mathrm{SR}}\right]^{-1}. \tag{C.21}$$

C.5 Bounds on the MBD Energy as $\overline{\mathbf{T}}_{\mathrm{LR}}$ is Converged

In discussing periodic summation of $\mathbf{T}_{\mathrm{SR}}$ in Chapter 3, we introduced a max-norm convergene condition, Eq. (3.7). The same condition is used to judge the convergence of $\overline{\mathbf{T}}_{\mathrm{LR}}$ over the periodic lattice. To understand a little about this convergence criterion interactions impacts the MBD energy we refer to a theorem, resulting from the Weyl inequalities,[504] that bounds the spectral variations (*i.e.* eigenvalue perturbations) of Hermitiam matrices.[337]

Theorem C.5.1 *Let* $\mathbf{A}$ *and* $\mathbf{B}$ *be Hermitian matrices, with eigenvalues* $\lambda_1(\mathbf{A}) \geq \cdots \geq \lambda_n(\mathbf{A})$*, and* $\lambda_1(\mathbf{B}) \geq \cdots \geq \lambda_n(\mathbf{B})$ *respectively. Then,*

$$\max_j |\lambda_j(\mathbf{B}) - \lambda_j(\mathbf{A})| \leq \|\mathbf{B} - \mathbf{A}\|.$$

This means that the spectrum of a Hermitian matrix, such as $\mathbf{C}^{\mathrm{MBD}}$, is stable against small perturbations. In other words, if $\mathbf{B} = \mathbf{A} + \boldsymbol{\mathcal{E}}$ is a slightly perturbed version of $\mathbf{A}$, then the perturbation to any individual eigenvalue of $\mathbf{A}$ is bounded by the matrix norm of the perturbation, *i.e.*, $\|\mathbf{B} - \mathbf{A}\| = \|\boldsymbol{\mathcal{E}}\|$. Spectral variation inequalities such as the theorem above are usually proved with respect to unitarily-invariant matrix norms.[337] Although the max-norm is not unitarily-invariant, it can be used to bound unitarily-invariant norms such as the trace-norm. The trace norm (also called the $p = 1$ norm) is bounded by the max norm as

$$\|\mathbf{A}\|_1 = \sum_{j=1}^{n} \lambda_j \leq n\|\mathbf{A}\|_{\max} \tag{C.22}$$

and is closely related to the $p = \infty$ norm, which is unitarily-invariant when applied to Hermitian matrices. Since the $p = \infty$ norm is the maximum absolute row (or column) sum of a Hermitian matrix, and $\|\cdot\|_{\max}$ is the elementwise maximum absolute value, we have the following bound,

$$\|\mathbf{A}\|_{\max} \leq \|\mathbf{A}\|_{\infty} \leq n\|\mathbf{A}\|_{\max}, \tag{C.23}$$

where n is the dimension of the matrix. The elements of the MBD interaction Hamiltonian, $\mathbf{C}^{\mathrm{MBD}}$, depend on both the screened quantities $\overline{\omega}$, $\overline{\alpha}(0)$, and the long-range dipole-dipole tensor $\overline{\mathbf{T}}_{\mathrm{LR}}$. When $\overline{\mathbf{T}}_{\mathrm{LR}}$ is being converged periodically, the screened quantities have already been determined. Since each periodic image, b', of atom b will have the same $\overline{\omega}_b$ and $\overline{\alpha}_b(0)$, only the off-diagonal elements of $\mathbf{C}^{\mathrm{MBD}}$ are impacted by converging $\overline{\mathbf{T}}_{\mathrm{LR}}$, and the screened quantities are not involved in the periodic sum, *i.e.*,

$$\sum_{b'} \mathbf{C}^{\mathrm{MBD}}_{ab'} = \left[\overline{\omega}_a \overline{\omega}_b \sqrt{\overline{\alpha}_a(0)\overline{\alpha}_b(0)}\right] \sum_{b'} \overline{\mathbf{T}}^{\mathrm{LR}}_{ab'} \qquad \text{for } a \neq b \tag{C.24}$$

Furthermore, the perturbations to $\mathbf{C}^{\mathrm{MBD}}$ coming from each additional term in $\overline{\mathbf{T}}^{\mathrm{LR}}_{ab}$ preserve Hermiticity. So, the max-norm criterion applied to converging $\overline{\mathbf{T}}^{\mathrm{LR}}_{ab}$ means that the maximum error in $\mathbf{C}^{\mathrm{MBD}}$ is bounded by:

$$\|\Delta\mathbf{C}^{\mathrm{MBD}}\|_{\max} \leq \delta * \max_{ab}\{\overline{\omega}_a \overline{\omega}_b \sqrt{\overline{\alpha}_a(0)\overline{\alpha}_b(0)}\}. \tag{C.25}$$

Applying our relation to the $p = \infty$ norm and using the result of the eigenvalue perturbation theorem, we have:

$$\max|\Delta\lambda| \leq \|\Delta\mathbf{C}^{\mathrm{MBD}}\|_{\infty} \leq 3N\delta * \max_{ab}\{\overline{\omega}_a \overline{\omega}_b \sqrt{\overline{\alpha}_a(0)\overline{\alpha}_b(0)}\}. \tag{C.26}$$

Since the MBD correlation energy is built from a sum of $\sqrt{\lambda_p}$, where $\{\lambda_p\}$ are the eigenvalues of $\mathbf{C}^{\mathrm{MBD}}$, by converging $\overline{\mathbf{T}}_{\mathrm{LR}}$ until the max norms of all 3×3 subblocks fall below δ, we are guaranteed that the MBD energy will achieve a related convergence. For further discussion of this subject we refer the reader to classic texts on numerical analysis and spectral variation inequalities (see *e.g.* Refs. 336–338).

D

Structure Indexing of Polypeptide Conformers

Table D.1: Peptide naming conventions used in this work, the BEGDB database, and Ref. 301.

This work	BEGDB	Ref. 301	This work	BEGDB	Ref. 301
0	252_FGG55	FGG_055	38	228_GGF08	GGF_08
1	263_FGG80	FGG_080	39	230_GGF09	GGF_09
2	253_FGG99	FGG_099	40	225_GGF10	GGF_10
3	264_FGG114	FGG_114	41	229_GGF11	GGF_11
4	257_FGG215	FGG_215	42	224_GGF12	GGF_12
5	258_FGG224	FGG_224	43	222_GGF13	GGF_13
6	255_FGG252	FGG_252	44	221_GGF14	GGF_14
7	254_FGG300	FGG_300	45	226_GGF15	GGF_15
8	265_FGG357	FGG_357	46	214_WGG01	WGG_01
9	256_FGG366	FGG_366	47	211_WGG02	WGG_02
10	259_FGG380	FGG_380	48	209_WGG03	WGG_03
11	260_FGG412	FGG_412	49	208_WGG04	WGG_04
12	261_FGG444	FGG_444	50	210_WGG05	WGG_05
13	262_FGG470	FGG_470	51	206_WGG06	WGG_06
14	266_FGG691	FGG_691	52	215_WGG07	WGG_07
15	248_GFA01	GFA_01	53	207_WGG08	WGG_08
16	239_GFA02	GFA_02	54	217_WGG09	WGG_09
17	247_GFA03	GFA_03	55	219_WGG10	WGG_10
18	251_GFA04	GFA_04	56	216_WGG11	WGG_11
19	250_GFA05	GFA_05	57	220_WGG12	WGG_12
20	245_GFA06	GFA_06	58	218_WGG13	WGG_13
21	237_GFA07	GFA_07	59	212_WGG14	WGG_14

continued on next page

Table D.1: Peptide naming conventions (continued).

This work	BEGDB	Ref. 301	This work	BEGDB	Ref. 301
22	242_GFA08	GFA_08	60	213_WGG15	WGG_15
23	241_GFA09	GFA_09	61	195_WG01	WG_01
24	238_GFA10	GFA_10	62	194_WG02	WG_02
25	240_GFA11	GFA_11	63	191_WG03	WG_03
26	244_GFA12	GFA_12	64	204_WG04	WG_04
27	243_GFA13	GFA_13	65	205_WG05	WG_05
28	249_GFA14	GFA_14	66	193_WG06	WG_06
29	236_GFA15	GFA_15	67	197_WG07	WG_07
30	246_GFA16	GFA_16	68	202_WG08	WG_08
31	231_GGF01	GGF_01	69	198_WG09	WG_09
32	234_GGF02	GGF_02	70	192_WG10	WG_10
33	233_GGF03	GGF_03	71	203_WG11	WG_11
34	227_GGF04	GGF_04	72	201_WG12	WG_12
35	235_GGF05	GGF_05	73	200_WG13	WG_13
36	232_GGF06	GGF_06	74	196_WG14	WG_14
37	223_GGF07	GGF_07	75	199_WG15	WG_15

References

[1] A. J. Stone, *The theory of intermolecular forces*, 2nd ed. (Oxford University Press, Oxford, 2013).

[2] C. J. Van Oss, M. K. Chaudhury, and R. J. Good, Chem. Rev. **88**, 927 (1988).

[3] J. D. van der Waals, *Over de Continuïteit van den Gasen Vloeistoftoestand (On the continuity of the gaseous and liquid state)*, Doctoral thesis, Leiden University, Leiden, Netherlands (1873).

[4] W. H. Keesom, Proc. R. Acad. Sci. (Amsterdam) **18**, 636 (1915).

[5] W. H. Keesom, Proc. R. Acad. Sci. (Amsterdam) **23**, 939 (1920).

[6] W. H. Keesom, Phys. Z. **22**, 129 (1921).

[7] W. H. Keesom, Phys. Z. **22**, 643 (1921).

[8] P. Debye, Phys. Z. **21**, 178 (1920).

[9] P. Debye, Phys. Z. **22**, 302 (1920).

[10] F. London, Z. Phys. **63**, 245 (1930).

[11] D. J. Wales, *Energy landscapes*, Cambridge molecular science (Cambridge University Press, Cambridge, UK; New York, 2003).

[12] V. A. Parsegian, *Van der Waals forces: a handbook for biologists, chemists, engineers, and physicists* (Cambridge University Press, New York, 2006).

[13] J. N. Israelachvili, *Intermolecular and surface forces*, 3rd ed. (Academic Press, Burlington, MA, 2011).

[14] B. M. Axilrod and E. Teller, J. Chem. Phys. **11**, 299 (1943).

[15] Y. Muto, J. Phys.-Math. Soc. Japan **17**, 629 (1943).

[16] T. Brinck, J. S. Murray, and P. Politzer, J. Chem. Phys. **98**, 4305 (1993).

[17] T. K. Ghanty and S. K. Ghosh, J. Phys. Chem. **97**, 4951 (1993).

[18] C. Zhang, T. Andersson, S. Svensson, O. Björneholm, M. Huttula, M.-H. Mikkelä, D. Anin, M. Tchaplyguine, and G. Öhrwall, J. Phys. Chem. A **116**, 12104 (2012).

[19] H. C. Hamaker, Physica **4**, 1058 (1937).

[20] E. A. Power and T. Thirunamachandran, Phys. Rev. A **48**, 4761 (1993).

[21] H. B. G. Casimir and D. Polder, Phys. Rev. **73**, 360 (1948).

[22] E. M. Lifshitz, Zh. Eksp. Teor. Fiz. **29**, 94 (1955).

[23] E. M. Lifshitz, Sov. Phys. JETP **2**, 73 (1956).

[24] I. E. Dzyaloshinskii, E. M. Lifshitz, and L. P. Pitaevskii, Soviet Physics Uspekhi **4**, 153 (1961).

[25] V. V. Gobre and A. Tkatchenko, Nature Commun. **4**, 2341 (2013).

[26] Y. V. Shtogun and L. M. Woods, J. Phys. Chem. Lett. **1**, 1356 (2010).

[27] A. Priye and W. H. Marlow, J. Phys. D: Appl. Phys. **46**, 425306 (2013).

[28] J. E. Lennard-Jones, Trans. Faraday Soc. **28**, 333 (1932).

[29] J. F. Dobson, A. White, and A. Rubio, Phys. Rev. Lett. **96**, 073201 (2006).

[30] A. G. Donchev, J. Chem. Phys. **125**, 074713 (2006).

[31] M. W. Cole, D. Velegol, H.-Y. Kim, and A. A. Lucas, Mol. Simul. **35**, 849 (2009).

[32] R.-F. Liu, J. G. Ángyán, and J. F. Dobson, J. Chem. Phys. **134**, 114106 (2011).

[33] Z. Liu, J. Z. Liu, Y. Cheng, Z. Li, L. Wang, and Q. Zheng, Phys. Rev. B **85**, 205418 (2012).

[34] K. Rapcewicz and N. W. Ashcroft, Phys. Rev. B **44**, 4032 (1991).

[35] J. F. Dobson and B. P. Dinte, Phys. Rev. Lett. **76**, 1780 (1996).

[36] Y. Andersson, D. C. Langreth, and B. I. Lundqvist, Phys. Rev. Lett. **76**, 102 (1996).

[37] E. J. Meijer and M. Sprik, J. Chem. Phys. **105**, 8684 (1996).

[38] F. A. Gianturco, F. Paesani, M. F. Laranjeira, V. Vassilenko, and M. A. Cunha, J. Chem. Phys. **110**, 7832 (1999).

[39] X. Wu, M. C. Vargas, S. Nayak, V. Lotrich, and G. Scoles, J. of Chem. Phys. **115**, 8748 (2001).

[40] M. Elstner, P. Hobza, T. Frauenheim, S. Suhai, and E. Kaxiras, J. Chem. Phys. **114**, 5149 (2001).

[41] Q. Wu and W. Yang, J. Chem. Phys. **116**, 515 (2002).

[42] M. Dion, H. Rydberg, E. Schröder, D. C. Langreth, and B. I. Lundqvist, Phys. Rev. Lett. **92**, 246401 (2004).

[43] O. A. von Lilienfeld, I. Tavernelli, U. Rothlisberger, and D. Sebastiani, Phys. Rev. Lett. **93**, 153004 (2004).

[44] S. Grimme, J. Comput. Chem. **25**, 1463 (2004).

[45] A. J. Misquitta, R. Podeszwa, B. Jeziorski, and K. Szalewicz, J. Chem. Phys. **123**, 214103 (2005).

[46] A. D. Becke and E. R. Johnson, J. Chem. Phys. **122**, 154104 (2005).

[47] A. D. Becke and E. R. Johnson, J. Chem. Phys. **123**, 154101 (2005).

[48] E. R. Johnson and A. D. Becke, J. Chem. Phys. **123**, 024101 (2005).

[49] S. Grimme, J. Comput. Chem. **27**, 1787 (2006).

[50] A. D. Becke and E. R. Johnson, J. Chem. Phys. **124**, 014104 (2006).

[51] Y. Zhao and D. G. Truhlar, J. Chem. Phys. **125**, 194101 (2006).

[52] A. D. Becke and E. R. Johnson, J. Chem. Phys. **127**, 124108 (2007).

[53] A. D. Becke and E. R. Johnson, J. Chem. Phys. **127**, 154108 (2007).

[54] P. Jurečka, J. Černý, P. Hobza, and D. R. Salahub, J. Comput. Chem. **28**, 555 (2007).

[55] I. C. Gerber and J. G. Ángyán, J. Chem. Phys. **126**, 044103 (2007).

[56] P. L. Silvestrelli, Phys. Rev. Lett. **100**, 053002 (2008).

[57] Y. Y. Sun, Y.-H. Kim, K. Lee, and S. B. Zhang, J. Chem. Phys. **129**, 154102 (2008).

[58] J.-D. Chai and M. Head-Gordon, Phys. Chem. Chem. Phys. **10**, 6615 (2008).

[59] G. A. DiLabio, Chem. Phys. Lett. **455**, 348 (2008).

[60] I. D. Mackie and G. A. DiLabio, J. Phys. Chem. A **112**, 10968 (2008).

[61] O. A. Vydrov, Q. Wu, and T. Van Voorhis, J. Chem. Phys. **129**, 014106 (2008).

[62] A. Tkatchenko and M. Scheffler, Phys. Rev. Lett. **102**, 073005 (2009).

[63] G. Román-Pérez and J. M. Soler, Phys. Rev. Lett. **103**, 096102 (2009).

[64] O. A. Vydrov and T. Van Voorhis, Phys. Rev. Lett. **103**, 063004 (2009).

[65] E. R. Johnson and G. A. DiLabio, J. Phys. Chem. C **113**, 5681 (2009).

[66] S. Grimme, J. Antony, S. Ehrlich, and H. Krieg, J. Chem. Phys. **132**, 154104 (2010).

[67] A. Tkatchenko, L. Romaner, O. T. Hofmann, E. Zojer, C. Ambrosch-Draxl, and M. Scheffler, MRS Bull. **35**, 435 (2010).

[68] V. R. Cooper, L. Kong, and D. C. Langreth, Phys. Procedia **3**, 1417 (2010).

[69] K. E. Riley, M. Pitoňák, P. Jurečka, and P. Hobza, Chem. Rev. **110**, 5023 (2010).

[70] F. O. Kannemann and A. D. Becke, J. Chem. Theory Comput. **6**, 1081 (2010).

[71] O. A. Vydrov and T. Van Voorhis, J. Chem. Phys. **133**, 244103 (2010).

[72] K. Lee, E. D. Murray, L. Kong, B. I. Lundqvist, and D. C. Langreth, Phys. Rev. B **82**, 081101(R) (2010).

[73] S. N. Steinmann and C. Corminboeuf, J. Chem. Theory Comput. **6**, 1990 (2010).

[74] S. Grimme, WIREs Comput. Mol. Sci. **1**, 211 (2011).

[75] S. N. Steinmann and C. Corminboeuf, J. Chem. Phys. **134**, 044117 (2011).

[76] S. N. Steinmann and C. Corminboeuf, J. Chem. Theory Comput. **7**, 3567 (2011).

[77] S. Grimme, S. Ehrlich, and L. Goerigk, J. Comp. Chem. **32**, 1456 (2011).

[78] N. Marom, A. Tkatchenko, M. Rossi, V. V. Gobre, O. Hod, M. Scheffler, and L. Kronik, J. Chem. Theory Comput. **7**, 3944 (2011).

[79] S. T. Schneebeli, A. D. Bochevarov, and R. A. Friesner, J. Chem. Theory Comput. **7**, 658 (2011).

[80] A. Tkatchenko, R. A. DiStasio Jr., R. Car, and M. Scheffler, Phys. Rev. Lett. **108**, 236402 (2012).

[81] R. A. DiStasio Jr., O. A. von Lilienfeld, and A. Tkatchenko, Proc. Natl. Acad. Sci. USA **109**, 14791 (2012).

[82] E. Torres and G. A. DiLabio, J. Phys. Chem. Lett. **3**, 1738 (2012).

[83] V. G. Ruiz, W. Liu, E. Zojer, M. Scheffler, and A. Tkatchenko, Phys. Rev. Lett. **108**, 146103 (2012).

[84] A. Tkatchenko, A. Ambrosetti, and R. A. DiStasio Jr., J. Chem. Phys. **138**, 074106 (2013).

[85] R. Sabatini, T. Gorni, and S. de Gironcoli, Phys. Rev. B **87**, 041108 (2013).

[86] P. L. Silvestrelli, J. Chem. Phys. **139**, 054106 (2013).

[87] R. A. DiStasio Jr., V. V. Gobre, and A. Tkatchenko, J. Phys.: Condens. Matter **26**, 213202 (2014).

[88] A. Ambrosetti, A. M. Reilly, R. A. DiStasio Jr., and A. Tkatchenko, J. Chem. Phys. **140**, 18A508 (2014).

[89] A. D. Becke, J. Chem. Phys. **140**, 18A301 (2014).

[90] J. Klimeš and A. Michaelides, J. Chem. Phys. **137**, 120901 (2012).

[91] J. F. Dobson and T. Gould, J. Phys. Condens. Matter **24**, 073201 (2012).

[92] E. Brémond, N. Golubev, S. N. Steinmann, and C. Corminboeuf, J. Chem. Phys. **140**, 18A516 (2014).

[93] U. Zimmerli, M. Parrinello, and P. Koumoutsakos, J. Chem. Phys. **120**, 2693 (2004).

[94] M. A. Neumann and M.-A. Perrin, J. Phys. Chem. B **109**, 15531 (2005).

[95] O. Bludský, M. Rubeš, P. Soldán, and P. Nachtigall, J. Chem. Phys. **128**, 114102 (2008).

[96] O. A. Vydrov and T. Van Voorhis, J. Chem. Phys. **130**, 104105 (2009).

[97] O. A. Vydrov and T. Van Voorhis, J. Chem. Phys. **132**, 164113 (2010).

[98] O. A. Vydrov and T. Van Voorhis, Phys. Rev. A **81**, 062708 (2010).

[99] T. Thonhauser, V. R. Cooper, S. Li, A. Puzder, P. Hyldgaard, and D. C. Langreth, Phys. Rev. B **76**, 125112 (2007).

[100] E. R. Johnson, I. D. Mackie, and G. A. DiLabio, J. Phys. Org. Chem. **22**, 1127 (2009).

[101] W. Hujo and S. Grimme, J. Chem. Theory Comput. **7**, 3866 (2011).

[102] W. Hujo and S. Grimme, J. Chem. Theory Comput. **9**, 308 (2013).

[103] J. A. Barker, Phys. Rev. Lett. **57**, 230 (1986).

[104] J. Řezáč, Y. Huang, P. Hobza, and G. J. O. Beran, J. Chem. Theory Comput. **11**, 3065 (2015).

[105] T. Risthaus and S. Grimme, J. Chem. Theory Comput. **9**, 1580 (2013).

[106] A. Ambrosetti, D. Alfè, and A. Tkatchenko, J. Phys. Chem. Lett. **5**, 849 (2014).

[107] A. Tkatchenko, M. Rossi, V. Blum, J. Ireta, and M. Scheffler, Phys. Rev. Lett. **106**, 118102 (2011).

[108] A. Otero de la Roza and E. R. Johnson, J. Chem. Phys. **137**, 054103 (2012).

[109] A. M. Reilly and A. Tkatchenko, J. Chem. Phys. **139**, 024705 (2013).

[110] A. M. Reilly and A. Tkatchenko, J. Phys. Chem. Lett. **4**, 1028 (2013).

[111] N. Marom, R. A. DiStasio Jr., V. Atalla, S. Levchenko, A. M. Reilly, J. R. Chelikowsky, L. Leiserowitz, and A. Tkatchenko, Angew. Chem. Int. Ed. **52**, 6629 (2013).

[112] A. M. Reilly and A. Tkatchenko, Phys. Rev. Lett. **113**, 055701 (2014).

[113] L. Kronik and A. Tkatchenko, Acc. Chem. Res. **47**, 3208 (2014).

[114] N. Ferri, R. A. DiStasio, A. Ambrosetti, R. Car, and A. Tkatchenko, Phys. Rev. Lett. **114**, 176802 (2015).

[115] R. J. Maurer, V. G. Ruiz, and A. Tkatchenko, J. Chem. Phys. **143**, 102808 (2015).

[116] T. Björkman, A. Gulans, A. V. Krasheninnikov, and R. M. Nieminen, Phys. Rev. Lett. **108**, 235502 (2012).

[117] J. F. Dobson, T. Gould, and G. Vignale, Phys. Rev. X **4**, 021040 (2014).

[118] B. Thole, Chem. Phys. **59**, 341 (1981).

[119] A. M. Reilly and A. Tkatchenko, Chem. Sci. **6**, 3289 (2015).

[120] C. Wagner, N. Fournier, V. G. Ruiz, C. Li, K. Müllen, M. Rohlfing, A. Tkatchenko, R. Temirov, and F. S. Tautz, Nature Commun. **5**, 5568 (2014).

[121] O. A. von Lilienfeld and A. Tkatchenko, J. Chem. Phys. **132**, 234109 (2010).

[122] F. Furche and T. Van Voorhis, J. Chem. Phys. **122**, 164106 (2005).

[123] J. G. Ángyán, R.-F. Liu, J. Toulouse, and G. Jansen, J. Chem. Theory Comput. **7**, 3116 (2011).

[124] J. J. Rehr, E. Zaremba, and W. Kohn, Phys. Rev. B **12**, 2062 (1975).

[125] F. Furche, Phys. Rev. B **64**, 195120 (2001).

[126] J. P. Perdew, Phys. Rev. B **33**, 8822 (1986).

[127] J. Harl and G. Kresse, Phys. Rev. B **77**, 045136 (2008).

[128] J. Harl and G. Kresse, Phys. Rev. Lett. **103**, 056401 (2009).

[129] S. Lebègue, J. Harl, T. Gould, J. G. Ángyán, G. Kresse, and J. F. Dobson, Phys. Rev. Lett. **105**, 196401 (2010).

[130] T. Björkman, A. Gulans, A. V. Krasheninnikov, and R. M. Nieminen, J. Phys.: Condens. Matter **24**, 424218 (2012).

[131] F. Furche, J. Chem. Phys. **129**, 114105 (2008).

[132] A. Heβelmann and A. Görling, Mol. Phys. **108**, 359 (2010).

[133] A. Heβelmann, Phys. Rev. A **85**, 012517 (2012).

[134] D. Langbein, *Theory of Van der Waals Attraction*, Springer Tracts in Modern Physics, Vol. 72 (Springer-Verlag, Berlin/Heidelberg, 1974).

[135] D. Langbein, J. Adhes. **1**, 237 (1969).

[136] W. L. Bade, J. Chem. Phys. **27**, 1280 (1957).

[137] A. Jones, A. Thompson, J. Crain, M. H. Müser, and G. J. Martyna, Phys. Rev. B **79**, 144119 (2009).

[138] A. P. Jones, J. Crain, V. P. Sokhan, T. W. Whitfield, and G. J. Martyna, Phys. Rev. B **87**, 144103 (2013).

[139] V. P. Sokhan, A. P. Jones, F. S. Cipcigan, J. Crain, and G. J. Martyna, Proc. Natl. Acad. Sci. USA **112**, 6341 (2015).

[140] A. White and J. F. Dobson, Phys. Rev. B **77**, 075436 (2008).

[141] R. A. DiStasio Jr., V. V. Gobre, and A. Tkatchenko, Ψ_k Newsletter **114**, 47 (2012).

[142] A. Tkatchenko, Adv. Func. Mater. **25**, 2054 (2015).

[143] S. R. Forrest and M. E. Thompson, Chem. Rev. **107**, 923 (2007).

[144] C. W. Tang and S. A. VanSlyke, Appl. Phys. Lett. **51**, 913 (1987).

[145] J. R. Sheats, J. Mater. Res. **19**, 1974 (2004).

[146] M. C. R. Delgado, E.-G. Kim, D. A. d. S. Filho, and J.-L. Bredas, J. Am. Chem. Soc. **132**, 3375 (2010).

[147] Y. Diao, K. M. Lenn, W.-Y. Lee, M. A. Blood-Forsythe, J. Xu, Y. Mao, Y. Kim, J. A. Reinspach, S. Park, A. Aspuru-Guzik, G. Xue, P. Clancy, Z. Bao, and S. C. B. Mannsfeld, J. Am. Chem. Soc. **136**, 17046 (2014).

[148] G. Giri, E. Verploegen, S. C. B. Mannsfeld, S. Atahan-Evrenk, D. H. Kim, S. Y. Lee, H. A. Becerril, A. Aspuru-Guzik, M. F. Toney, and Z. Bao, Nature **480**, 504 (2011).

[149] R. Hiremath, J. A. Basile, S. W. Varney, and J. A. Swift, J. Am. Chem. Soc. **127**, 18321 (2005).

[150] C. B. Aakeröy and K. R. Seddon, Chem. Soc. Rev. **22**, 397 (1993).

[151] G. R. Desiraju, Cryst. Growth Des. **11**, 896 (2011).

[152] A. Mukherjee, S. Tothadi, and G. R. Desiraju, Acc. Chem. Res. **47**, 2514 (2014).

[153] S. L. James, Chem. Soc. Rev. **32**, 276 (2003).

[154] J. L. Rowsell and O. M. Yaghi, Micropor. Mesopor. Mater. **73**, 3 (2004).

[155] X. Feng, X. Ding, and D. Jiang, Chem. Soc. Rev. **41**, 6010 (2012).

[156] A. G. Slater and A. I. Cooper, Science **348**, aaa8075 (2015).

[157] M. D. Allendorf and V. Stavila, Cryst. Eng. Comm. **17**, 229 (2015).

[158] A. A. Talin, A. Centrone, A. C. Ford, M. E. Foster, V. Stavila, P. Haney, R. A. Kinney, V. Szalai, F. El Gabaly, H. P. Yoon, F. Leonard, and M. D. Allendorf, Science **343**, 66 (2014).

[159] K.-H. Low, V. A. L. Roy, S. S.-Y. Chui, S. L.-F. Chan, and C.-M. Che, Chem. Commun. **46**, 7328 (2010).

[160] D. Sheberla, L. Sun, M. A. Blood-Forsythe, S. Er, C. R. Wade, C. K. Brozek, A. Aspuru-Guzik, and M. Dincă, J. Am. Chem. Soc. **136**, 8859 (2014).

[161] X. Huang, P. Sheng, Z. Tu, F. Zhang, J. Wang, H. Geng, Y. Zou, C.-a. Di, Y. Yi, Y. Sun, W. Xu, and D. Zhu, Nature Commun. **6**, 7408 (2015).

[162] Z. Wang, Z. Liu, and F. Liu, Nature Commun. **4**, 1471 (2013).

[163] E. D. Głowacki, H. Coskun, M. A. Blood-Forsythe, U. Monkowius, L. Leonat, M. Grzybowski, D. Gryko, M. S. White, A. Aspuru-Guzik, and N. S. Sariciftci, Org. Electron. **15**, 3521 (2014).

[164] M. Hmadeh, Z. Lu, Z. Liu, F. Gándara, H. Furukawa, S. Wan, V. Augustyn, R. Chang, L. Liao, F. Zhou, E. Perre, V. Ozolins, K. Suenaga, X. Duan, B. Dunn, Y. Yamamto, O. Terasaki, and O. M. Yaghi, Chem. Mater. **24**, 3511 (2012).

[165] T. Kambe, R. Sakamoto, K. Hoshiko, K. Takada, M. Miyachi, J.-H. Ryu, S. Sasaki, J. Kim, K. Nakazato, M. Takata, and H. Nishihara, J. Am. Chem. Soc. **135**, 2462 (2013).

[166] J. Cui and Z. Xu, Chem. Commun. **50**, 3986 (2014).

[167] B. T. Koo, W. R. Dichtel, and P. Clancy, J. Mater. Chem. **22**, 17460 (2012).

[168] A. P. Cote, Science **310**, 1166 (2005).

[169] A. P. Côté, H. M. El-Kaderi, H. Furukawa, J. R. Hunt, and O. M. Yaghi, J. Am. Chem. Soc. **129**, 12914 (2007).

[170] S. Wan, J. Guo, J. Kim, H. Ihee, and D. Jiang, Angew. Chem. Int. Ed. **47**, 8826 (2008).

[171] E. L. Spitler, B. T. Koo, J. L. Novotney, J. W. Colson, F. J. Uribe-Romo, G. D. Gutierrez, P. Clancy, and W. R. Dichtel, J. Am. Chem. Soc. **133**, 19416 (2011).

[172] M. Dogru, A. Sonnauer, A. Gavryushin, P. Knochel, and T. Bein, Chem. Commun. **47**, 1707 (2011).

[173] S. Wan, J. Guo, J. Kim, H. Ihee, and D. Jiang, Angew. Chem. Int. Ed. **48**, 5439 (2009).

[174] W. J. Hehre, J. Chem. Phys. **56**, 2257 (1972).

[175] G. Kresse and J. Hafner, Phys. Rev. B **47**, 558 (1993).

[176] P. E. Blöchl, Phys. Rev. B **50**, 17953 (1994).

[177] G. Kresse and J. Hafner, Phys. Rev. B **49**, 14251 (1994).

[178] G. Kresse and J. Furthmüller, Comput. Mater. Sci. **6**, 15 (1996).

[179] G. Kresse and J. Furthmüller, Phys. Rev. B **54**, 11169 (1996).

[180] G. Kresse, Phys. Rev. B **59**, 1758 (1999).

[181] J. P. Perdew and A. Zunger, Phys. Rev. B **23**, 5048 (1981).

[182] J. P. Perdew, K. Burke, and M. Ernzerhof, Phys. Rev. Lett. **77**, 3865 (1996).

[183] J. P. Perdew, K. Burke, and M. Ernzerhof, Phys. Rev. Lett. **78**, 1396 (1997).

[184] J.-P. Berrut and L. N. Trefethen, SIAM Review **46**, 501 (2004).

[185] N. L. Allinger, J. Am. Chem. Soc. **99**, 8127 (1977).

[186] V. Coropceanu, J. Cornil, D. A. da Silva Filho, Y. Olivier, R. Silbey, and J.-L. Brédas, Chem. Rev. **107**, 926 (2007).

[187] F. Ortmann, F. Bechstedt, and K. Hannewald, Phys. Status Solidi B **248**, 511 (2011).

[188] S. Atahan-Evrenk and A. Aspuru-Guzik, in *Prediction and Calculation of Crystal Structures*, Vol. 345, edited by S. Atahan-Evrenk and A. Aspuru-Guzik (Springer International Publishing, Cham, 2014) pp. 95–138.

[189] Z. Bao and J. J. Locklin, eds., *Organic field-effect transistors*, Optical science and engineering No. 128 (CRC Press, Boca Raton, 2007).

[190] A. Facchetti, Chem. Mater. **23**, 733 (2011).

[191] A. Pron, P. Gawrys, M. Zagorska, D. Djurado, and R. Demadrille, Chem. Soc. Rev. **39**, 2577 (2010).

[192] E. D. Głowacki, L. Leonat, G. Voss, M.-A. Bodea, Z. Bozkurt, A. M. Ramil, M. Irimia-Vladu, S. Bauer, and N. S. Sariciftci, AIP Adv. **1**, 042132 (2011).

[193] E. D. Głowacki, G. Voss, L. Leonat, M. Irimia-Vladu, S. Bauer, and N. S. Sariciftci, Isr. J. Chem. **52**, 540 (2012).

[194] E. D. Głowacki, D. H. Apaydin, Z. Bozkurt, U. Monkowius, K. Demirak, E. Tordin, M. Himmelsbach, C. Schwarzinger, M. Burian, R. T. Lechner, N. Demitri, G. Voss, and N. S. Sariciftci, J. Mater. Chem. C **2**, 8089 (2014).

[195] M. Irimia-Vladu, E. D. Głowacki, P. A. Troshin, G. Schwabegger, L. Leonat, D. K. Susarova, O. Krystal, M. Ullah, Y. Kanbur, M. A. Bodea, V. F. Razumov, H. Sitter, S. Bauer, and N. S. Sariciftci, Adv. Mater. **24**, 375 (2012).

[196] Y. Suna, J.-i. Nishida, Y. Fujisaki, and Y. Yamashita, Org. Lett. **14**, 3356 (2012).

[197] E. D. Głowacki, M. Irimia-Vladu, M. Kaltenbrunner, J. Gsiorowski, M. S. White, U. Monkowius, G. Romanazzi, G. P. Suranna, P. Mastrorilli, T. Sekitani, S. Bauer, T. Someya, L. Torsi, and N. S. Sariciftci, Adv. Mater. **25**, 1563 (2013).

[198] E. D. Głowacki, G. Romanazzi, C. Yumusak, H. Coskun, U. Monkowius, G. Voss, M. Burian, R. T. Lechner, N. Demitri, G. J. Redhammer, N. Sünger, G. P. Suranna, and S. Sariciftci, Adv. Funct. Mater. **25**, 776 (2015).

[199] H. Yanagisawa, J. Mizuguchi, S. Aramaki, and Y. Sakai, Jpn. J. Appl. Phys. **47**, 4728 (2008).

[200] E. D. Głowacki, L. Leonat, M. Irimia-Vladu, R. Schwödiauer, M. Ullah, H. Sitter, S. Bauer, and N. Serdar Sariciftci, Appl. Phys. Lett. **101**, 023305 (2012).

[201] Z. Hao and A. Iqbal, Chem. Soc. Rev. **26**, 203 (1997).

[202] C. B. Nielsen, M. Turbiez, and I. McCulloch, Adv. Mater. **25**, 1859 (2013).

[203] M. Grzybowski and D. T. Gryko, Adv. Opt. Mater. **3**, 280 (2015).

[204] S. Qu and H. Tian, Chem. Comm. **48**, 3039 (2012).

[205] J. Lee, A.-R. Han, J. Hong, J. H. Seo, J. H. Oh, and C. Yang, Adv. Funct. Mater. **22**, 4128 (2012).

[206] J. Mizuguchi, A. Grubenmann, G. Wooden, and G. Rihs, Acta Crystallogr. Sect. B **48**, 696 (1992).

[207] J. Mizuguchi, A. Grubenmann, and G. Rihs, Acta Crystallogr. Sect. B **49**, 1056 (1993).

[208] H. Sirringhaus, P. J. Brown, R. H. Friend, M. M. Nielsen, K. Bechgaard, B. M. W. Langeveld-Voss, A. J. H. Spiering, R. A. J. Janssen, E. W. Meijer, P. Herwig, and D. M. de Leeuw, Nature **401**, 685 (1999).

[209] A. Opitz, M. Horlet, M. Kiwull, J. Wagner, M. Kraus, and W. Brütting, Org. Electron. **13**, 1614 (2012).

[210] M. Kraus, S. Richler, A. Opitz, W. Brütting, S. Haas, T. Hasegawa, A. Hinderhofer, and F. Schreiber, J. Appl. Phys. **107**, 094503 (2010).

[211] K.-C. Kao and W. Hwang, *Electrical transport in solids: with particular reference to organic semiconductors*, 1st ed., International series on the science of the solid state No. v. 14 (Pergamon Press, Oxford; New York, 1981).

[212] H. Fröhlich, Arch. Sci. (Geneva) **10**, 5 (1957).

[213] G. L. Sewell, Philos. Mag. **3**, 1361 (1958).

[214] H. Fröhlich and G. Sewell, Proc. Phys. Soc. **74**, 643 (1959).

[215] T. Holstein, Annals of Physics **8**, 343 (1959).

[216] D. Emin and T. Holstein, Phys. Rev. Lett. **36**, 323 (1976).

[217] A. S. Alexandrov and J. T. Devreese, *Advances in polaron physics*, Springer series in solid-state sciences No. 159 (Springer, Berlin, 2010).

[218] D. Emin, *Polarons* (Cambridge University Press, Cambridge; New York, 2013).

[219] E. F. Valeev, V. Coropceanu, D. A. da Silva Filho, S. Salman, and J.-L. Brédas, J. Am. Chem. Soc. **128**, 9882 (2006).

[220] A. Troisi and G. Orlandi, Phys. Rev. Lett. **96**, 086601 (2006).

[221] F. Ortmann, F. Bechstedt, and K. Hannewald, Phys. Rev. B **79**, 235206 (2009).

[222] J. L. Bredas, J. P. Calbert, D. A. da Silva Filho, and J. Cornil, Proc. Natl. Acad. Sci. USA **99**, 5804 (2002).

[223] J.-L. Brédas, D. Beljonne, V. Coropceanu, and J. Cornil, Chem. Rev. **104**, 4971 (2004).

[224] W.-Q. Deng and W. A. Goddard, J. Phys. Chem. B **108**, 8614 (2004).

[225] J. Nelson, J. J. Kwiatkowski, J. Kirkpatrick, and J. M. Frost, Acc. Chem. Res. **42**, 1768 (2009).

[226] A. Troisi, G. Orlandi, and J. E. Anthony, Chem. Mater. **17**, 5024 (2005).

[227] R. A. Marcus, Rev. Mod. Phys. **65**, 599 (1993).

[228] J. Kirkpatrick, Int. J. Quantum Chem. **108**, 51 (2008).

[229] B. Baumeier, J. Kirkpatrick, and D. Andrienko, Phys. Chem. Chem. Phys. **12**, 11103 (2010).

[230] S. E. Fritz, S. M. Martin, C. D. Frisbie, M. D. Ward, and M. F. Toney, J. Am. Chem. Soc. **126**, 4084 (2004).

[231] A. D. Becke, J. Chem. Phys. **98**, 5648 (1993).

[232] P. J. Stephens, F. J. Devlin, C. F. Chabalowski, and M. J. Frisch, J. Phys. Chem. **98**, 11623 (1994).

[233] Y. Zhao and D. G. Truhlar, J. Phys. Chem. A **109**, 5656 (2005).

[234] Y. Zhang and W. Yang, Phys. Rev. Lett. **80**, 890 (1998).

[235] J. P. Perdew, K. Burke, and M. Ernzerhof, Phys. Rev. Lett. **80**, 891 (1998).

[236] J. P. Perdew, M. Ernzerhof, and K. Burke, J. Chem. Phys. **105**, 9982 (1996).

[237] M. Ernzerhof and G. E. Scuseria, J. Chem. Phys. **110**, 5029 (1999).

[238] C. Adamo and V. Barone, J. Chem. Phys. **110**, 6158 (1999).

[239] F. Weigend and R. Ahlrichs, Phys. Chem. Chem. Phys. **7**, 3297 (2005).

[240] A. Schäfer, H. Horn, and R. Ahlrichs, J. Chem. Phys. **97**, 2571 (1992).

[241] F. Neese, F. Wennmohs, A. Hansen, and U. Becker, Chem. Phys. **356**, 98 (2009).

[242] F. Neese, J. Comput. Chem. **24**, 1740 (2003).

[243] F. Weigend, Phys. Chem. Chem. Phys. **4**, 4285 (2002).

[244] F. Neese, WIREs Comput. Mol. Sci. **2**, 73 (2012).

[245] R. A. DiStasio Jr., B. Santra, Z. Li, X. Wu, and R. Car, J. Chem. Phys. **141**, 084502 (2014).

[246] K. Modig, B. G. Pfrommer, and B. Halle, Phys. Rev. Lett. **90**, 075502 (2003).

[247] H.-S. Lee and M. E. Tuckerman, J. Chem. Phys. **125**, 154507 (2006).

[248] A. D. Boese, Chem. Phys. Chem. **16**, 978 (2015).

[249] M. Lazzeri, C. Attaccalite, L. Wirtz, and F. Mauri, Phys. Rev. B **78**, 081406 (2008).

[250] F. L. Hirshfeld, Theor. Chim. Acta **44**, 129 (1977).

[251] T. Bučko, S. Lebègue, J. Hafner, and Ángyán J.G., Phys. Rev. B **87**, 064110 (2013).

[252] R. F. Nalewajski and R. G. Parr, Proc. Natl. Acad. Sci. USA **97**, 8879 (2000).

[253] K. T. Tang and M. Karplus, Phys. Rev. **171**, 70 (1968).

[254] P. Bultinck, C. Van Alsenoy, P. W. Ayers, and R. Carbó-Dorca, J. Chem. Phys. **126**, 144111 (2007).

[255] T. Markovich, M. A. Blood-Forsythe, R. A. DiStasio Jr., and A. Aspuru-Guzik, "Enabling large-scale simulation of many-body dispersion forces in condensed phase systems," Unpublished.

[256] T. Helgaker, P. Jørgensen, and J. Olsen, *Molecular electronic-structure theory* (Wiley, Chichester; New York, 2000).

[257] A. Bondi, J. Phys. Chem. **68**, 441 (1964).

[258] P. Bendt and A. Zunger, Phys. Rev. Lett. **50**, 1684 (1983).

[259] G. Srivastava and D. Weaire, Adv. Phys. **36**, 463 (1987).

[260] D. Marx and J. Hutter, *Ab Initio Molecular Dynamics: Basic Theory and Advanced Methods* (Cambridge University Press, Cambridge, UK; New York, 2009).

[261] R. B. Nelson, AIAA Journal **14**, 1201 (1976).

[262] P. Giannozzi, S. Baroni, N. Bonini, M. Calandra, R. Car, *et al.*, J. Phys.: Condens. Matter **21**, 395502 (2009).

[263] D. R. Hamann, M. SchlÃijter, and C. Chiang, Phys. Rev. Lett. **43**, 1494 (1979).

[264] G. B. Bachelet, D. R. Hamann, and M. SchlÃijter, Phys. Rev. B **26**, 4199 (1982).

[265] D. Vanderbilt, Phys. Rev. B **32**, 8412 (1985).

[266] F. Gygi, "FPMD Pseudopotential Repository," (Accessed Mar. 29, 2015).

[267] F. Gygi, "qso2upf," (Accessed Mar. 29, 2015).

[268] C. G. Broyden, Notices Amer. Math. Soc. **16**, 670 (1969).

[269] D. Goldfarb, Math. Comput. **24**, 23 (1970).

[270] R. Fletcher, Comp. J. **13**, 317 (1970).

[271] D. F. Shanno, Math. Comput. **24**, 647 (1970).

[272] H. Kruse and S. Grimme, J. Chem. Phys. **136**, 154101 (2012).

[273] K. Eichkorn, F. Weigend, O. Treutler, and R. Ahlrichs, Theor. Chem. Acc. **97**, 119 (1997).

[274] F. Weigend, Phys. Chem. Chem. Phys. **8**, 1057 (2006).

[275] E. Baerends, D. Ellis, and P. Ros, Chem. Phys. **2**, 41 (1973).

[276] B. I. Dunlap, J. W. D. Connolly, and J. R. Sabin, J. Chem. Phys. **71**, 3396 (1979).

[277] R. A. Kendall and H. A. Früchtl, Theor. Chem. Acc. **97**, 158 (1997).

[278] V. Blum, R. Gehrke, F. Hanke, P. Havu, V. Havu, X. Ren, K. Reuter, and M. Scheffler, Comput. Phys. Commun. **180**, 2175 (2009).

[279] A. Tkatchenko, "MBD@rsSCS," (Accessed Oct. 1, 2014).

[280] P. Hobza, H. L. Selzle, and E. W. Schlag, J. Chem. Phys. **93**, 5893 (1990).

[281] E. Arunan and H. S. Gutowsky, J. Chem. Phys. **98**, 4294 (1993).

[282] P. Hobza, H. L. Selzle, and E. W. Schlag, J. Phys. Chem. **97**, 3937 (1993).

[283] P. Hobza, H. L. Selzle, and E. W. Schlag, J. Am. Chem. Soc. **116**, 3500 (1994).

[284] R. L. Jaffe and G. D. Smith, J. Chem. Phys. **105**, 2780 (1996).

[285] P. Hobza, H. L. Selzle, and E. W. Schlag, J. Phys. Chem. **100**, 18790 (1996).

[286] J. Gauss and J. F. Stanton, J. Phys. Chem. A **104**, 2865 (2000).

[287] S. Tsuzuki, K. Honda, T. Uchimaru, M. Mikami, and K. Tanabe, J. Am. Chem. Soc. **124**, 104 (2002).

[288] M. O. Sinnokrot, E. F. Valeev, and C. D. Sherrill, J. Am. Chem. Soc. **124**, 10887 (2002).

[289] M. O. Sinnokrot and C. D. Sherrill, J. Phys. Chem. A **108**, 10200 (2004).

[290] T. P. Tauer and C. D. Sherrill, J. Phys. Chem. A **109**, 10475 (2005).

[291] R. Podeszwa, R. Bukowski, and K. Szalewicz, J. Phys. Chem. A **110**, 10345 (2006).

[292] J. Grant Hill, J. A. Platts, and H.-J. Werner, Phys. Chem. Chem. Phys. **8**, 4072 (2006).

[293] G. R.A. DiStasio, Jr. and von Helden, R. P. Steele, and M. Head-Gordon, Chem. Phys. Lett. **437**, 277 (2007).

[294] T. Janowski and P. Pulay, Chem. Phys. Lett. **447**, 27 (2007).

[295] E. C. Lee, D. Kim, P. Jurečka, P. Tarakeshwar, P. Hobza, and K. S. Kim, J. Phys. Chem. A **111**, 3446 (2007).

[296] B. Fernández, T. B. Pedersen, A. Sánchez de Merás, and H. Koch, Chem. Phys. Lett. **441**, 332 (2007).

[297] M. Pavone, N. Rega, and V. Barone, Chem. Phys. Lett. **452**, 333 (2008).

[298] M. Pitoňák, P. Neogrády, J. Řezáč, P. Jurečka, M. Urban, and P. Hobza, J. Chem. Theory Comput. **4**, 1829 (2008).

[299] C. D. Sherrill, T. Takatani, and E. G. Hohenstein, J. Phys. Chem. A **113**, 10146 (2009).

[300] J. Gräfenstein and D. Cremer, J. Chem. Phys. **130**, 124105 (2009).

[301] H. Valdes, K. Pluháčková, M. Pitoňák, J. Řezáč, and P. Hobza, Phys. Chem. Chem. Phys. **10**, 2747 (2008).

[302] C. Møller and M. S. Plesset, Phys. Rev. **46**, 618 (1934).

[303] M. Feyereisen, G. Fitzgerald, and A. Komornicki, Chem. Phys. Lett. **208**, 359 (1993).

[304] O. Vahtras, J. Almlöf, and M. Feyereisen, Chem. Phys. Lett. **213**, 514 (1993).

[305] H. A. Früchtl, R. A. Kendall, R. J. Harrison, and K. G. Dyall, Int. J. Quant. Chem. **64**, 63 (1997).

[306] D. E. Bernholdt and R. J. Harrison, J. Chem. Phys. **109**, 1593 (1998).

[307] F. Weigend, M. Häser, H. Patzelt, and R. Ahlrichs, Chem. Phys. Lett. **294**, 143 (1998).

[308] T. H. Dunning, J. Chem. Phys. **90**, 1007 (1989).

[309] J. W. Tukey, *Exploratory data analysis*, Addison-Wesley series in behavioral science (Addison-Wesley Pub. Co, Reading, MA, 1977).

[310] A. Tkatchenko, R. A. DiStasio, M. Head-Gordon, and M. Scheffler, J. Chem. Phys. **131**, 094106 (2009).

[311] S. Grimme, J. G. Brandenburg, C. Bannwarth, and A. Hansen, J. Chem. Phys. **143**, 054107 (2015).

[312] A. Tkatchenko, D. Alfè, and K. S. Kim, J. Chem. Theory Comput. **8**, 4317 (2012).

[313] A. Sygula, F. R. Fronczek, R. Sygula, P. W. Rabideau, and M. M. Olmstead, J. Am. Chem. Soc. **129**, 3842 (2007).

[314] C. Mück-Lichtenfeld, S. Grimme, L. Kobryn, and A. Sygula, Phys. Chem. Chem. Phys. **12**, 7091 (2010).

[315] V. H. Le, M. Yanney, M. McGuire, A. Sygula, and E. A. Lewis, J. Phys. Chem. B **118**, 11956 (2014).

[316] A. V. Zabula, Y. V. Sevryugina, S. N. Spisak, L. Kobryn, R. Sygula, A. Sygula, and M. A. Petrukhina, Chem. Comm. **50**, 2657 (2014).

[317] Y. Zhao and D. G. Truhlar, Phys. Chem. Chem. Phys. **10**, 2813 (2008).

[318] M. P. Waller, H. Kruse, C. Mück-Lichtenfeld, and S. Grimme, Chem. Soc. Rev. **41**, 3119 (2012).

[319] R. Podeszwa, W. Cencek, and K. Szalewicz, J. Chem. Theory Comput. **8**, 1963 (2012).

[320] S. Grimme, Chem. Eur. J. **18**, 9955 (2012).

[321] P. A. Denis, RSC Adv. **3**, 25296 (2013).

[322] A. Sygula, Eur. J. Org. Chem. **2011**, 1611 (2011).

[323] M. C. Stuparu, Tetrahedron **68**, 3527 (2012).

[324] M. Yanney and A. Sygula, Tetrahedron Lett. **54**, 2604 (2013).

[325] C. M. Álvarez, G. Aullón, H. Barbero, L. A. García-Escudero, C. Martínez-Pérez, J. M. Martín-Álvarez, and D. Miguel, Org. Lett. **17**, 2578 (2015).

[326] J. Yang, P. Feng, A. Sygula, W. Harneit, J.-H. Su, and J. Du, Phys. Lett. A **376**, 1748 (2012).

[327] K. Hedberg, L. Hedberg, D. S. Bethune, C. Brown, H. Dorn, R. D. Johnson, and M. De Vries, Science **254**, 410 (1991).

[328] A. Godec, J. C. Smith, and F. Merzel, Phys. Rev. Lett. **111**, 127801 (2013).

[329] A. Jinich, D. Rappoport, I. Dunn, B. Sanchez-Lengeling, R. Olivares-Amaya, E. Noor, A. B. Even, and A. Aspuru-Guzik, Sci. Rep. **4**, 7022 (2014).

[330] B. Huskinson, M. P. Marshak, C. Suh, S. Er, M. R. Gerhardt, C. J. Galvin, X. Chen, A. Aspuru-Guzik, R. G. Gordon, and M. J. Aziz, Nature **505**, 195 (2014).

[331] L. F. Wan and D. Prendergast, J. Am. Chem. Soc. **136**, 14456 (2014).

[332] S. Er, C. Suh, M. P. Marshak, and A. Aspuru-Guzik, Chem. Sci. **6**, 885 (2015).

[333] X. Andrade, D. Strubbe, U. De Giovannini, A. H. Larsen, M. J. T. Oliveira, J. Alberdi-Rodriguez, A. Varas, I. Theophilou, N. Helbig, M. J. Verstraete, L. Stella, F. Nogueira, A. Aspuru-Guzik, A. Castro, M. A. L. Marques, and A. Rubio, Phys. Chem. Chem. Phys. (2015), 10.1039/C5CP00351B.

[334] X. Andrade, J. Alberdi-Rodriguez, D. A. Strubbe, M. J. T. Oliveira, F. Nogueira, A. Castro, J. Muguerza, A. Arruabarrena, S. G. Louie, A. Aspuru-Guzik, A. Rubio, and M. A. L. Marques, J. Phys.: Condens. Matter **24**, 233202 (2012).

[335] Y. Shao, L. F. Molnar, Y. Jung, J. Kussmann, C. Ochsenfeld, *et al.*, Phys. Chem. Chem. Phys. **8**, 3172 (2006).

[336] J. H. Wilkinson, *The algebraic eigenvalue problem* (Clarendon Press ; Oxford University Press, Oxford; New York, 1965).

[337] R. Bhatia, *Perturbation bounds for matrix eigenvalues* (Society for Industrial and Applied Mathematics, 2007).

[338] G. H. Golub and C. F. Van Loan, *Matrix computations*, fourth edition ed., Johns Hopkins studies in the mathematical sciences (The Johns Hopkins University Press, Baltimore, 2013).

[339] J. P. Boyd, J. Sci. Comp. **2**, 99 (1987).

[340] N. Hale and L. N. Trefethen, SIAM J. Numer. Anal. **46**, 930 (2008).

[341] J. Shen and L.-L. Wang, Commun. Comput. Phys. **5**, 195 (2009).

[342] A. Derevianko, S. G. Porsev, and J. F. Babb, At. Data Nucl. Data Tables **96**, 323 (2010).

[343] J. M. McNamee, ACM SIGSAM Bull. **38**, 1 (2004).

[344] W. Kahan, Commun. ACM **8**, 40 (1965).

[345] O. H. Nielsen and R. M. Martin, Phys. Rev. Lett. **50**, 697 (1983).

[346] O. H. Nielsen and R. M. Martin, Phys. Rev. B **32**, 3792 (1985).

[347] O. H. Nielsen and R. M. Martin, Phys. Rev. B **32**, 3780 (1985).

[348] M. Bernasconi, G. Chiarotti, P. Focher, S. Scandolo, E. Tosatti, and M. Parrinello, J. Phys. Chem. Solids **56**, 501 (1995).

[349] N. Marzari, D. Vanderbilt, A. De Vita, and M. C. Payne, Phys. Rev. Lett. **82**, 3296 (1999).

[350] B. Schatschneider, J.-J. Liang, A. M. Reilly, N. Marom, G.-X. Zhang, and A. Tkatchenko, Phys. Rev. B **87**, 060104 (2013).

[351] J. Binns, M. R. Healy, S. Parsons, and C. A. Morrison, Acta Crystallogr. Sect. B **70**, 259 (2014).

[352] J. G. Brandenburg, M. Alessio, B. Civalleri, M. F. Peintinger, T. Bredow, and S. Grimme, J. Phys. Chem. A **117**, 9282 (2013).

[353] J. Moellmann and S. Grimme, J. Phys. Chem. C **118**, 7615 (2014).

[354] D. Umadevi and G. N. Sastry, J. Phys. Chem. Lett. **2**, 1572 (2011).

[355] M. Wu, R. Kempaiah, P.-J. J. Huang, V. Maheshwari, and J. Liu, Langmuir **27**, 2731 (2011).

[356] S. J. Sowerby, C. A. Cohn, W. M. Heckl, and N. G. Holm, Proc. Natl. Acad. Sci. USA **98**, 820 (2001).

[357] Y. Cho, S. K. Min, J. Yun, W. Y. Kim, A. Tkatchenko, and K. S. Kim, J. Chem. Theory Comput. **9**, 2090 (2013).

[358] B. S. Husale, S. Sahoo, A. Radenovic, F. Traversi, P. Annibale, and A. Kis, Langmuir **26**, 18078 (2010).

[359] K. Berland, Øyvind. Borck, and P. Hyldgaard, Comput. Phys. Commun. **182**, 1800 (2011).

[360] F. Ortmann, W. G. Schmidt, and F. Bechstedt, Phys. Rev. Lett. **95**, 186101 (2005).

[361] Z. Xu, B. R. Meher, D. Eustache, and Y. Wang, J. Mol. Graphics Modell. **47**, 8 (2014).

[362] S. Gowtham, R. H. Scheicher, R. Ahuja, R. Pandey, and S. P. Karna, Phys. Rev. B **76**, 033401 (2007).

[363] J.-H. Lee, Y.-K. Choi, H.-J. Kim, R. H. Scheicher, and J.-H. Cho, J. Phys. Chem. C **117**, 13435 (2013).

[364] N. Varghese, U. Mogera, A. Govindaraj, A. Das, P. K. Maiti, A. K. Sood, and C. N. R. Rao, Chem. Phys. Chem. **10**, 206 (2009).

[365] J. Antony and S. Grimme, Phys. Chem. Chem. Phys. **10**, 2722 (2008).

[366] D. Le, A. Kara, E. Schröder, P. Hyldgaard, and T. S. Rahman, J. Phys.: Condens. Matter **24**, 424210 (2012).

[367] S. Panigrahi, A. Bhattacharya, S. Banerjee, and D. Bhattacharyya, J. Phys. Chem. C **116**, 4374 (2012).

[368] S. Mukhopadhyay, S. Gowtham, R. H. Scheicher, R. Pandey, and S. P. Karna, Nanotechnology **21**, 165703 (2010).

[369] J. B. Nelson and D. P. Riley, Proc. Phys. Soc. **57**, 477 (1945).

[370] D. P. Riley, Proc. Phys. Soc. **57**, 486 (1945).

[371] P. L. Walker, H. A. McKinstry, and C. C. Wright, Ind. Eng. Chem. **45**, 1711 (1953).

[372] E. Kellett and B. Richards, J. Nucl. Mater. **12**, 184 (1964).

[373] E. A. Smirnova, Sov. Phys. J. **14**, 519 (1971).

[374] B. Kelly and P. Walker, Carbon **8**, 211 (1970).

[375] B. Kelly, Carbon **10**, 435 (1972).

[376] W. Morgan, Carbon **10**, 73 (1972).

[377] D. Tsang, B. Marsden, S. Fok, and G. Hall, Carbon **43**, 2902 (2005).

[378] A. C. Bailey and B. Yates, J. Appl. Phys. **41**, 5088 (1970).

[379] Y. Baskin and L. Meyer, Phys. Rev. **100**, 544 (1955).

[380] A. R. Botello-Méndez, S. M.-M. Dubois, A. Lherbier, and J.-C. Charlier, Acc. Chem. Res. **47**, 3292 (2014).

[381] L. X. Benedict, N. G. Chopra, M. L. Cohen, A. Zettl, S. G. Louie, and V. H. Crespi, Chem. Phys. Lett. **286**, 490 (1998).

[382] R. Zacharia, H. Ulbricht, and T. Hertel, Phys. Rev. B **69**, 155406 (2004).

[383] L. Spanu, S. Sorella, and G. Galli, Phys. Rev. Lett. **103**, 196401 (2009).

[384] M. Birowska, K. Milowska, and J. Majewski, Acta Phys. Pol. A **120**, 845 (2011).

[385] W. A. Al-Saidi, V. K. Voora, and K. D. Jordan, J. Chem. Theory Comput. **8**, 1503 (2012).

[386] T. Bučko, J. Hafner, S. Lebègue, and J. G. Ángyán, J. Phys. Chem. A **114**, 11814 (2010).

[387] N. Mounet and N. Marzari, Phys. Rev. B **71**, 205214 (2005).

[388] M. Hasegawa, K. Nishidate, and H. Iyetomi, Phys. Rev. B **76**, 115424 (2007).

[389] H. Rydberg, M. Dion, N. Jacobson, E. Schröder, P. Hyldgaard, S. I. Simak, D. C. Langreth, and B. I. Lundqvist, Phys. Rev. Lett. **91**, 126402 (2003).

[390] B. Santra, J. Klimeš, D. Alfè, A. Tkatchenko, B. Slater, A. Michaelides, R. Car, and M. Scheffler, Phys. Rev. Lett. **107**, 185701 (2011).

[391] B. Santra, J. Klimeš, A. Tkatchenko, D. Alfè, B. Slater, A. Michaelides, R. Car, and M. Scheffler, J. Chem. Phys. **139**, 154702 (2013).

[392] C. G. Salzmann, P. G. Radaelli, B. Slater, and J. L. Finney, Phys. Chem. Chem. Phys. **13**, 18468 (2011).

[393] C. G. Salzmann, P. G. Radaelli, E. Mayer, and J. L. Finney, Phys. Rev. Lett. **103**, 105701 (2009).

[394] E. D. Murray and G. Galli, Phys. Rev. Lett. **108**, 105502 (2012).

[395] O. Kambara, K. Takahashi, M. Hayashi, and J.-L. Kuo, Phys. Chem. Chem. Phys. **14**, 11484 (2012).

[396] J. G. Brandenburg, T. Maas, and S. Grimme, J. Chem. Phys. **142**, 124104 (2015).

[397] B. J. Murray, S. L. Broadley, T. W. Wilson, S. J. Bull, R. H. Wills, H. K. Christenson, and E. J. Murray, Phys. Chem. Chem. Phys. **12**, 10380 (2010).

[398] K. Thurmer and S. Nie, Proc. Natl. Acad. Sci. USA **110**, 11757 (2013).

[399] D. C. Steytler, J. C. Dore, and C. J. Wright, J. Phys. Chem. **87**, 2458 (1983).

[400] K. Morishige and H. Uematsu, J. Chem. Phys. **122**, 044711 (2005).

[401] J. A. McMillan and S. C. Los, Nature **206**, 806 (1965).

[402] M. Sugisaki, H. Suga, and S. Seki, Bull. Chem. Soc. Jpn. **41**, 2591 (1968).

[403] B. J. Murray, D. O'Sullivan, J. D. Atkinson, and M. E. Webb, Chem. Soc. Rev. **41**, 6519 (2012).

[404] B. J. Murray, D. A. Knopf, and A. K. Bertram, Nature **434**, 202 (2005).

[405] W. F. Kuhs, C. Sippel, A. Falenty, and T. C. Hansen, Proc. Natl. Acad. Sci. USA **109**, 21259 (2012).

[406] T. H. G. Carr, J. J. Shephard, and C. G. Salzmann, J. Phys. Chem. Lett. **5**, 2469 (2014).

[407] Z. Raza, D. Alfè, C. G. Salzmann, J. Klimeš, A. Michaelides, and B. Slater, Phys. Chem. Chem. Phys. **13**, 19788 (2011).

[408] E. A. Engel, B. Monserrat, and R. J. Needs, Phys. Rev. X **5**, 021033 (2015).

[409] H. König, Z. Kristallogr. **105**, 279 (1943).

[410] T. C. Hansen, M. M. Koza, and W. F. Kuhs, J. Phys.: Condens. Matter **20**, 285104 (2008).

[411] T. C. Hansen, M. M. Koza, P. Lindner, and W. F. Kuhs, J. Phys.: Condens. Matter **20**, 285105 (2008).

[412] T. L. Malkin, B. J. Murray, A. V. Brukhno, J. Anwar, and C. G. Salzmann, Proc. Natl. Acad. Sci. USA **109**, 1041 (2012).

[413] E. B. Moore and V. Molinero, Phys. Chem. Chem. Phys. **13**, 20008 (2011).

[414] P. Geiger, C. Dellago, M. Macher, C. Franchini, G. Kresse, J. Bernard, J. N. Stern, and T. Loerting, J. Phys. Chem. C **118**, 10989 (2014).

[415] R. Brill and A. Tippe, Acta Crystallogr. **23**, 343 (1967).

[416] S. J. La Placa and B. Post, Acta Crystallogr. **13**, 503 (1960).

[417] K. Röttger, A. Endriss, J. Ihringer, S. Doyle, and W. F. Kuhs, Acta Crystallogr. Sect. B **50**, 644 (1994).

[418] L. G. Dowell and A. P. Rinfret, Nature **188**, 1144 (1960).

[419] W. F. Kuhs and M. S. Lehmann, J. Phys. Colloq. **48**, C1 (1987).

[420] M. Kumai, J. Glaciol. **7**, 95 (1968).

[421] J. Heyd, G. E. Scuseria, and M. Ernzerhof, J. Chem. Phys. **118**, 8207 (2003).

[422] A. F. Izmaylov, G. E. Scuseria, and M. J. Frisch, J. Chem. Phys. **125**, 104103 (2006).

[423] J. Heyd, G. E. Scuseria, and M. Ernzerhof, J. Chem. Phys. **124**, 219906 (2006).

[424] "Annual dft popularity poll," (Accessed Aug. 13, 2015).

[425] S. F. Sousa, P. A. Fernandes, and M. J. a. Ramos, J. Phys. Chem. A **111**, 10439 (2007).

[426] J. P. Perdew and K. Burke, Int. J. Quantum Chem. **57**, 309 (1996).

[427] M. Springborg and J.-O. Joswig, in *Chemical modelling*, Vol. 11, edited by M. Springborg and J.-O. Joswig (Royal Society of Chemistry, Cambridge, 2014) pp. 134–150.

[428] A. Puzder, M. Dion, and D. C. Langreth, J. Chem. Phys. **124**, 164105 (2006).

[429] A. D. Becke, Phys. Rev. A **38**, 3098 (1988).

[430] J. P. Perdew, P. Ziesche, and H. Eschrig, *Electronic structure of solids '91*, Vol. 11 (Akademie Verlag, Berlin, 1991).

[431] J. P. Perdew, J. A. Chevary, S. H. Vosko, K. A. Jackson, M. R. Pederson, D. J. Singh, and C. Fiolhais, Phys. Rev. B **46**, 6671 (1992).

[432] J. P. Perdew, J. A. Chevary, S. H. Vosko, K. A. Jackson, M. R. Pederson, D. J. Singh, and C. Fiolhais, Phys. Rev. B **48**, 4978 (1993).

[433] J. P. Perdew and W. Yue, Phys. Rev. B **33**, 8800 (1986).

[434] D. J. Lacks and R. G. Gordon, Phys. Rev. A **47**, 4681 (1993).

[435] K. T. Tang and J. P. Toennies, J. Chem. Phys. **80**, 3726 (1984).

[436] J. Řezáč, K. E. Riley, and P. Hobza, J. Chem. Theory Comput. **7**, 2427 (2011).

[437] M. Marques, Comput. Phys. Commun. **151**, 60 (2003).

[438] A. Castro, H. Appel, M. Oliveira, C. A. Rozzi, X. Andrade, F. Lorenzen, M. A. L. Marques, E. K. U. Gross, and A. Rubio, Phys. Status Solidi B **243**, 2465 (2006).

[439] M. A. Marques, M. J. Oliveira, and T. Burnus, Comput. Phys. Commun. **183**, 2272 (2012).

[440] X. Andrade and A. Aspuru-Guzik, J. Chem. Theory Comput. **9**, 4360 (2013).

[441] A. Castro, M. A. L. Marques, and A. Rubio, J. Chem. Phys. **121**, 3425 (2004).

[442] P. García-Risueño, J. Alberdi-Rodriguez, M. J. T. Oliveira, X. Andrade, M. Pippig, J. Muguerza, A. Arruabarrena, and A. Rubio, J. Comput. Chem. **35**, 427 (2014).

[443] C. Hartwigsen, S. Goedecker, and J. Hutter, Phys. Rev. B **58**, 3641 (1998).

[444] F. Bloch, Z. Phys. **57**, 545 (1929).

[445] P. A. M. Dirac, Math. Proc. Cam. Phil. Soc. **26**, 376 (1930).

[446] S. H. Vosko, L. Wilk, and M. Nusair, Can. J. Phys. **58**, 1200 (1980).

[447] A. Karton, D. Gruzman, and J. M. L. Martin, J. Phys. Chem. A **113**, 8434 (2009).

[448] P. Jurečka, J. Šponer, J. Černý, and P. Hobza, Phys. Chem. Chem. Phys. **8**, 1985 (2006).

[449] T. Takatani, E. G. Hohenstein, M. Malagoli, M. S. Marshall, and C. D. Sherrill, J. Chem. Phys. **132**, 144104 (2010).

[450] N. E. Schultz, Y. Zhao, and D. G. Truhlar, J. Phys. Chem. A **109**, 11127 (2005).

[451] J. Řezáč, K. E. Riley, and P. Hobza, J. Chem. Theory Comput. **7**, 3466 (2011).

[452] M. Born and K. Huang, *Dynamical theory of crystal lattices*, Oxford classic texts in the physical sciences (Clarendon Press ; Oxford University Press, Oxford; New York, 1988).

[453] P. D. DeCicco and F. A. Johnson, Proc. R. Soc. A. **310**, 111 (1969).

[454] R. M. Pick, M. H. Cohen, and R. M. Martin, Phys. Rev. B **1**, 910 (1970).

[455] N. Zein, Fiz. Tverd. Tela (Leningrad) **26**, 3024 (1984), [Sov. Phys.: Solid State 26, 1825 (1984)].

[456] S. Baroni and R. Resta, Phys. Rev. B **33**, 5969 (1986).

[457] S. Baroni, P. Giannozzi, and A. Testa, Phys. Rev. Lett. **58**, 1861 (1987).

[458] X. Gonze, Phys. Rev. A **52**, 1096 (1995).

[459] S. Baroni, S. de Gironcoli, A. Dal Corso, and P. Giannozzi, Rev. Mod. Phys. **73**, 515 (2001).

[460] M. Born and J. Oppenheimer, Ann. Phys. (Berlin) **389**, 457 (1927).

[461] C. S. Rudisill and Y.-Y. Chu, AIAA J. **13**, 834 (1975).

[462] M. I. Friswell, J. Vib. Acoust. **118**, 390 (1996).

[463] A. L. Andrew and R. C. E. Tan, SIAM J. Matrix Anal. Appl. **20**, 78 (1998).

[464] R. C. E. Tan, A. L. Andrew, and F. M. L. Hong, Commun. Numer. Meth. En. **10**, 1 (1994).

[465] A. L. Andrew, J. Comput. Phys. **26**, 107 (1978).

[466] W. Kohn and L. J. Sham, Phys. Rev. **140**, A1133 (1965).

[467] D. E. Woon and T. H. Dunning, J. Chem. Phys. **100**, 2975 (1994).

[468] M. Kamiya, S. Hirata, and M. Valiev, J. Chem. Phys. **128**, 074103 (2008).

[469] S. Grimme, "dftd3," (Accessed Aug. 19, 2015).

[470] G. Makov and M. C. Payne, Phys. Rev. B **51**, 4014 (1995).

[471] W.-T. Hsu, Z.-A. Zhao, L.-J. Li, C.-H. Chen, M.-H. Chiu, P.-S. Chang, Y.-C. Chou, and W.-H. Chang, ACS Nano **8**, 2951 (2014).

[472] J. Kang, J. Li, S.-S. Li, J.-B. Xia, and L.-W. Wang, Nano Lett. **13**, 5485 (2013).

[473] J. A. Miwa, M. Dendzik, S. S. Grønborg, M. Bianchi, J. V. Lauritsen, P. Hofmann, and S. Ulstrup, ACS Nano **9**, 6502 (2015).

[474] K. Liu, C. Jin, X. Hong, J. Kim, A. Zettl, E. Wang, and F. Wang, Nature Physics **10**, 737 (2014).

[475] K. Liu, L. Zhang, T. Cao, C. Jin, D. Qiu, Q. Zhou, A. Zettl, P. Yang, S. G. Louie, and F. Wang, Nature Commun. **5**, 4966 (2014).

[476] W. Yan, L. Meng, M. Liu, J.-B. Qiao, Z.-D. Chu, R.-F. Dou, Z. Liu, J.-C. Nie, D. G. Naugle, and L. He, Phys. Rev. B **90**, 115402 (2014).

[477] H. Kumar, D. Er, L. Dong, J. Li, and V. B. Shenoy, Sci. Rep. **5**, 10872 (2015).

[478] K. Pernal, R. Podeszwa, K. Patkowski, and K. Szalewicz, Phys. Rev. Lett. **103**, 263201 (2009).

[479] A. Dreuw, J. L. Weisman, and M. Head-Gordon, J. Chem. Phys. **119**, 2943 (2003).

[480] D. J. Tozer, J. Chem. Phys. **119**, 12697 (2003).

[481] I. C. Gerber and J. G. Ángyán, Chem. Phys. Lett. **415**, 100 (2005).

[482] O. A. Vydrov, J. Heyd, A. V. Krukau, and G. E. Scuseria, J. Chem. Phys. **125**, 074106 (2006).

[483] D. Jacquemin, B. Moore, A. Planchat, C. Adamo, and J. Autschbach, J. Chem. Theory Comput. **10**, 1677 (2014).

[484] P. L. Silvestrelli and A. Ambrosetti, Phys. Rev. B **91**, 195405 (2015).

[485] J. P. Perdew and Y. Wang, Phys. Rev. B **45**, 13244 (1992).

[486] J. P. Perdew, A. Ruzsinszky, G. I. Csonka, O. A. Vydrov, G. E. Scuseria, L. A. Constantin, X. Zhou, and K. Burke, Phys. Rev. Lett. **100**, 136406 (2008).

[487] J. Klimeš, D. R. Bowler, and A. Michaelides, J. Phys.: Condens. Matter **22**, 022201 (2010).

[488] B. Hammer, L. B. Hansen, and J. K. NÃÿrskov, Phys. Rev. B **59**, 7413 (1999).

[489] T. Tsuneda, T. Suzumura, and K. Hirao, J. Chem. Phys. **110**, 10664 (1999).

[490] C. Adamo and V. Barone, J. Chem. Phys. **108**, 664 (1998).

[491] A. D. Becke, J. Chem. Phys. **107**, 8554 (1997).

[492] T. W. Keal and D. J. Tozer, J. Chem. Phys. **123**, 121103 (2005).

[493] X. Xu and W. A. Goddard, Proc. Natl. Acad. Sci. USA **101**, 2673 (2004).

[494] B. Miehlich, A. Savin, H. Stoll, and H. Preuss, Chem. Phys. Lett. **157**, 200 (1989).

[495] C. Lee, W. Yang, and R. G. Parr, Phys. Rev. B **37**, 785 (1988).

[496] N. C. Handy and A. J. Cohen, Mol. Phys. **99**, 403 (2001).

[497] A. D. Boese and N. C. Handy, J. Chem. Phys. **114**, 5497 (2001).

[498] J. Tao, J. P. Perdew, V. N. Staroverov, and G. E. Scuseria, Phys. Rev. Lett. **91**, 146401 (2003).

[499] J. P. Perdew, J. Tao, V. N. Staroverov, and G. E. Scuseria, J. Chem. Phys. **120**, 6898 (2004).

[500] R. Armiento and A. E. Mattsson, Phys. Rev. B **72**, 085108 (2005).

[501] A. E. Mattsson, R. Armiento, J. Paier, G. Kresse, J. M. Wills, and T. R. Mattsson, J. Chem. Phys. **128**, 084714 (2008).

[502] R. A. DiStasio Jr., H.-Y. Ko, B. Santra, and R. Car, "Enabling *ab initio* molcular dynamics with a self-consistent interatomic van der waals functional," Unpublished.

[503] W. G. Bickley, Math. Gaz. **25**, 19 (1941).

[504] H. Weyl, Math. Ann. **71**, 441 (1912)

This thesis was typeset using LaTeX, which was originally developed by Leslie Lamport and based on Donald Knuth's TeX. The body text is set in 11 point Latin Modern font. A template that can be used to format a dissertation with a similar look & feel is available at http://dissertate.io/.